

New Building Blocks for Molecular Spintronics

Dissertation

zur Erlangung des akademischen Grades doctor rerum naturalium
(Dr. rer. nat.)

vorgelegt dem Rat der Chemisch-Geowissenschaftlichen Fakultät der
Friedrich-Schiller-Universität Jena

von Dipl. Chem. Eike T. Spielberg
geboren am 27. April 1981 in Rotenburg (Wümme)

Gutachter:

1. Professor Dr. Winfried Plass, Institut für Anorganische und Analytische Chemie, Friedrich-Schiller-Universität Jena, Deutschland
2. Professor Dr. Jürgen Popp, Institut für Physikalische Chemie, Friedrich-Schiller-Universität Jena, Deutschland
3. Professor Dr. Jiří Pinkas, Departement of Chemistry, Masaryk University, Brno, Tschechien

Tag der öffentlichen Verteidigung: 9. Dezember 2009

Wir müssen uns damit abfinden, dass wir vielleicht nicht alles verstehen können.

— Wir können aber versuchen, so viel wie möglich zu verstehen!

gewidmet Günter Spielberg

Danksagung

An erster Stelle möchte ich meinem Betreuer Prof. Dr. Winfried Plass danken: Für seine dauerhafte Unterstützung und seine vielfältigen Ratschläge. Dafür, dass er mir so viele Tagungsbesuche ermöglicht hat. Dafür, dass er mir Raum und Möglichkeiten gegeben hat, meine vielen Ideen auszuprobieren und auf ihre nicht immer vorhandene Alltags-tauglichkeit zu testen. Für seine zahlreichen fachlichen und nicht-fachlichen Gespräche und Ratschläge. Vielen Dank!

Des Weiteren möchte ich Prof. Dr. Jürgen Popp für die Anfertigung des Zweitgutach-tens und Prof. Dr. Jiří Pinkas für die Anfertigung des Drittgutachtens danken.

Für die finanzielle Unterstützung meiner Arbeit möchte ich neben der Universität Je-na der Deutschen Forschungsgemeinschaft im Rahmen des Sonderforschungsberei-ches 436 („Metallvermittelte Reaktionen nach dem Vorbild der Natur“), der Gradu-iertenförderung des Freistaats Thüringen, der Marie-Curie-Trainings Site „Laboratorio della Magnetismo Molecolare“ in Florenz und besonders der Carl-Zeiss-Stiftung dan-ken, ohne die diese Arbeit nicht möglich gewesen wäre. Für sonstige finanzielle Un-terstützung möchte ich zudem der Deutschen Forschungsgemeinschaft im Rahmen der Schwerpunktprogramme 1137 („Molecular Magnetism“) und 1166 („Lanthanoidspezi-fische Funktionalitäten in Molekül und Material“) danken.

Mein besonderer Dank gilt weiterhin den Studenten und Mitarbeitern des „Laboato-rio della Magnetismo Molecolare“ für die schöne und sehr lehrreiche Zeit, die ich dort verbringen durfte. Ich danke Dante Gatteschi für die Betreuung, Maria Fittipaldi für die Zusammenarbeit und ganz besonders Lorenzo Sorace für seine nimmermüden Er-klärungen, seine große Unterstützung, die vielen Diskussionen und die Hilfe bei der Präsentation der Ergebnisse. Und natürlich all denen, die mir die Zeit dort unvergess-lich haben werden lassen: Pine, Pone, Rafael, Kevin, Fabrice, Federico, Lapo und Dia-na. Andrea Caneschi möchte ich für seine gute Organisation und Hilfestellung bei allen formalen Dingen danken.

Ich möchte allen wissenschaftlichen und technischen Mitarbeitern der chemischen Institute der Universität Jena für die Durchführung der verschiedenen Analysen danken. Mein Dank gilt dabei in besonderem Maße all denen, die die vielfältigen magnetischen Messungen durchgeführt haben, zusammen mit mir experimentelle Strategien erdnen haben und trotz meiner vielen Sonderwünsche immer noch mit mir zusammengearbeitet haben. Im Besonderen danke ich Bärbel Rambach und Dr. Manfred Friedrich für die zahlreichen ESR-Sitzungen, Dr. Axel Buchholz für die gute Zusammenarbeit bei der Fehlersuche am SQUID, für die Messungen und für die Zusammenarbeit bei der Auswertung. Die größte Leidtragende meiner (oder mir geschuldeten) vielen Messaufträge war zweifellos Christa Fälbel, ihr gilt daher mein ganz besonderer Dank, haben doch immer neue Anträge, immer neue Sequenzwünsche und immer neue Verbindungen ihr eine Überstunde nach der nächsten beschert. Dafür ganz herzlichen Dank!

Ich möchte weiterhin Linda Zedler, Susann Klimas und Björn Gebser danken, die im Rahmen ihrer Forschungspraktika wertvolle Beiträge zu dieser Arbeit geleistet haben. Außerdem möchte ich mich bei der Morgengruppe (Lotte, Christa, Kristin und Jana) bedanken. Den übrigen Arbeitsgruppenmitgliedern danke ich für die ausgesprochen gute Arbeitsatmosphäre und die vielfältigen Unternehmungen. Ganz besonderer Dank gilt dabei natürlich Daniel DCDP für die sehr gute Zusammenarbeit, die vielfältigen Diskussionen, die Geduld bei synthetischen Fragen und das ein oder andere FAB. Ute und meinem Vater danke ich zudem für das Korrekturlesen dieser Arbeit.

Mein größter Dank gilt allerdings meiner Familie und meinen Freunden für die unbezahlbare Unterstützung, die ich in dieser nicht immer einfachen Zeit erfahren habe.

Contents

| | | |
|----------|--|-----------|
| 1 | Introduction | 1 |
| 1.1 | Magnetism | 1 |
| 1.1.1 | What is magnetism? | 1 |
| 1.1.2 | Where does magnetism come from? | 3 |
| 1.1.3 | And what is it good for? | 9 |
| 1.2 | Quantum Computing | 10 |
| 1.3 | Building Blocks | 14 |
| | Results | 21 |
| 2 | New Functionalities | 21 |
| 2.1 | Complexes Based on Triphenylamines | 23 |
| 2.1.1 | Synthesis and Structure | 23 |
| 2.1.2 | Electronic Properties | 27 |
| 2.1.3 | Magnetic Properties | 31 |
| 2.2 | Magnetic Anomaly in Dinuclear Copper Complexes | 35 |
| 2.2.1 | Synthesis and Structure | 35 |
| 2.2.2 | Magnetic Properties | 36 |
| 2.2.3 | ESR Spectroscopy | 40 |
| 2.2.4 | Theoretical Considerations | 41 |
| 2.3 | Outlook | 47 |
| 3 | New Building Blocks | 49 |
| 3.1 | Carbazole Containing Complexes | 52 |
| 3.1.1 | Ligand Synthesis | 52 |
| 3.1.2 | Complexes with Unsubstituted Ligand | 53 |
| 3.1.3 | Complexes with Substituted Ligand | 63 |

| | | |
|----------|--|------------|
| 3.2 | Sulfonated Mesalen-type Complexes | 69 |
| 3.2.1 | Ligand Synthesis | 69 |
| 3.2.2 | Complex Structures | 70 |
| 3.2.3 | Magnetic Properties of Copper Dimer Chain | 79 |
| 3.3 | Magnetic Properties of Substituted Triaminoguanidine Ligands | 81 |
| 3.3.1 | Properties of Unsubstituted Trinuclear Copper Complex | 81 |
| 3.3.2 | Properties of Substituted Trinuclear Copper Complex | 86 |
| 3.4 | Outlook | 96 |
| 4 | Linked Building Blocks | 99 |
| 4.1 | Highly Symmetric Copper Complex | 103 |
| 4.1.1 | Synthesis and Structure | 103 |
| 4.1.2 | Magnetic Measurements | 104 |
| 4.1.3 | ESR Spectroscopy | 105 |
| 4.2 | Magnetic Properties of 1-D Copper – Lanthanide Chains | 111 |
| 4.2.1 | Synthesis and Structure | 111 |
| 4.2.2 | Theoretical Considerations | 112 |
| 4.2.3 | Magnetic Properties — In General | 115 |
| 4.2.4 | Magnetic Properties — Without Angular Momentum | 116 |
| 4.2.5 | Magnetic Properties — With Angular Momentum | 121 |
| 4.3 | Magnetic Properties of Pentanuclear Complexes | 126 |
| 4.3.1 | Synthesis and Structure | 126 |
| 4.3.2 | Magnetic Properties | 127 |
| 4.4 | Outlook | 136 |
| 5 | Summary / Zusammenfassung | 137 |
| 5.1 | Summary | 137 |
| 5.1.1 | New Functionalities | 138 |
| 5.1.2 | New Building Blocks | 139 |
| 5.1.3 | Linked Building Blocks | 141 |
| 5.2 | Zusammenfassung | 144 |
| 5.2.1 | Neue Funktionen | 144 |
| 5.2.2 | Neue Bausteine | 146 |
| 5.2.3 | Verbrückte Bausteine | 148 |

| | |
|--|------------|
| Experimental Section | 153 |
| 6 Computational Details | 153 |
| 6.1 Simulation and Fitting Routines | 153 |
| 6.2 Quantum Chemistry Calculations | 154 |
| 7 Synthesis | 155 |
| 7.1 Instrumentation | 155 |
| 7.2 Materials | 156 |
| 7.3 Films | 156 |
| 7.4 Preparation | 157 |
| 8 X-ray Crystallography | 171 |
| 9 Electrochemical Measurements | 173 |
| | |
| Appendix | 173 |
| A.1 Synthesized Ligands | 177 |
| A.2 Synthesized Complexes | 178 |
| A.3 Investigated Complexes | 179 |
| A.4 Crystallographic Data | 180 |
| A.5 Structure of 2-Hydroxy-3-methoxy-5-sulfonato-benzyl-phenylimine (20b) | 188 |
| A.6 Deconvolution and Calculation of UV/Vis- and ESR-Spectra | 190 |
| A.7 Atom Numbering Scheme | 192 |
| | |
| Bibliography | 192 |
| | |
| Declaration of Originality | 213 |

1 Introduction

1.1 Magnetism

1.1.1 What is magnetism?

Before we can discuss the results of this work, we first have to deal with the question: What is magnetism? One may discuss it from the macroscopic world, from the effects that we experience in everyday life and which have inspired the fantasy of so many people. The idea of forces acting through space only upon a specific kind of matter has risen a lot of myths around this phenomenon. Discovered long before Christ in China, one major outcome has been the invention of the compass. In China, a needle or a spoon of magnetite, a mineral with natural ferromagnetism, was placed in a bath of water allowing free rotation. This instrument, pointing south at any place, is both interesting for navigational purposes on the seas and on the land, but it has also a pronounced spiritual component. A major improvement was the invention of the dry compass, where the needle rests upon a small tip. The abdication of the water bath made this compass more secure, especially under the rough conditions on ships in heavy storms. Up to that time, the determination of position on the sea was based on land marks or, far away from the coast, upon the sun or stars. The compass represents a crucial breakthrough for voyages of discovery, allowing the determination of south even when sun, moon and stars are not visible.

But the question remains: What is magnetism? The best visualization of the magnetic field is the aggregation of iron powder along certain so-called field lines. They gave the first indications of how the invisible force is mediated. Michael Faraday and Christian Ørsted showed that magnetic field lines are also produced by electric current. And it was James Clark Maxwell, whose famous equations related the magnetic phenomena

to the electric ones thus revealing them as being two sides of the same force. His equations determine the main properties of magnetic and electric fields as well as their propagation in space. The idea of fields filling the whole space and mediating forces over infinite distances has puzzled the scientists for a long time and has led to a number of theories like the luminiferous aether, which was proposed by Sir Isaac Newton in his book "Opticks".^[1] By now, the presence of electromagnetic waves is commonly accepted and a fundamental lesson to learn when studying science.

So a part of the answer is, magnetism is a manifestation of the electromagnetic force. It is a vector field with a distinct impact on matter. It has no sources nor sinks and is caused by moving charges. At first glance, these facts explain mainly the electromagnetism. In the case of static magnetism (as it is found in the compass needle) the question remains, where does it come from? There is no overall electrical current, so why do some minerals exhibit permanent magnetic fields? And why do different materials respond so differently?

What happens in matter exposed to magnetic fields? The material creates a magnetic dipole itself, which interacts with the external field producing a force. We can measure this force for example with Gouy's balance and use the result to determine the magnetic moment of the sample. The change of the magnetic moment $\delta\vec{M}$ upon an infinitesimal change of the applied field $\delta\vec{H}$ is called the magnetic susceptibility χ or magnetic volume susceptibility:

$$\bar{\chi} = \frac{\delta\vec{M}}{\delta\vec{H}} \quad (1.1)$$

For different applications also the mass susceptibility and the molar susceptibility are of interest. They are defined according to $\bar{\chi}_m = \bar{\chi}/\rho$ or $\bar{\chi}_M = \bar{\chi}/M$, respectively, with ρ as the mass density and M as the molar mass of the compound. Magnitude, sign and temperature dependence of the magnetic susceptibility then allow us to classify materials according to the observed magnetic behavior:

Diamagnetism: The magnetic susceptibility is constant over temperature. It is comparatively small and negative. This effect is related to normal magnetic induction within the electronic system of a given material — the magnetic field of the induced current is directed antiparallel to the external field. The field lines are less dense inside the material leading to its expulsion to smaller field strengths. Diamagnetism is an intrinsic property of all matter. Its magnitude can be estimated

and subtracted from measurements to obtain the magnitude of other magnetic effects.

Paramagnetism: The magnetic susceptibility increases upon decreasing temperature. This effect can be explained by a large number of independent, uncorrelated magnetic moments trying to orientate themselves parallel to the external field. However, their effort is hindered by the thermal movement leading to a statistic deorientation. Upon cooling the thermal movement is decreased resulting in less deorientation of the magnetic moments and thus to increasing susceptibility. Paramagnetic materials densify the magnetic field lines and are pulled into spaces with higher field strengths.

Ferromagnetism: Ferromagnetic materials have a large positive magnetic susceptibility and show hysteresis upon reversing fields. When magnetized for the first time, a saturation behavior is observed. Yet upon lowering the external field back to zero, a magnetization remains, the so-called remanence magnetization. An antiparallel field, called coercive field, is needed to zero the sample magnetization. However, with rising temperature the moment is strongly reduced at a specific temperature (at the Curie-temperature) and behaves like a paramagnet at higher temperatures.

Ferrimagnetism: Ferrimagnetic materials behave very similar to ferromagnetic materials, the differences are of microscopic nature and are discussed below.

Anitferromagnetism: Antiferromagnets behave like diamagnetic compounds up to a specific temperature. Above this temperature, which is called Néel-temperature they show paramagnetic behavior.

Metamagnetism This term is generally used to name all effects, which are not covered by the five definitions above. It is often used when dealing with spin glasses (materials which possess a short-range, but no long-range ordering) or in situations of canted moments as depicted in Figure 1.2 on the right side.

1.1.2 Where does magnetism come from?

Yet this does not explain the reason or sources of permanent magnetism. It was quantum physics that solved this problem. The answer is that there exist mechanisms producing fundamental quantum magnets. Each atomic building block, i.e. proton, neu-

tron and electron (called fermions), possesses an intrinsic magnetic moment. The explanation of this property was deduced from relativistic quantum theory for the electron by Paul Dirac from 1927 to 1928.^[2;3] He concluded, that there exists a property, which can be treated mathematically like an angular momentum, as if the particles are rotating around themselves. This property is called spin, it is $\frac{1}{2}$ for all fermions and gives rise to a magnetic moment. The overall magnetism can then be explained by the interactions of these small magnetic moments. Let us have a closer look at the sources of magnetism:

Nucleus The atomic nucleus consists of protons and neutrons with their spins oriented in parallel and antiparallel fashion. This occurs according to an intrinsic rule, leading to an overall nuclear spin in which antiparallel spins cancel each other's magnetic moment. Hence, the nuclear spin depends strongly on the number of nucleons, i.e. on the isotopes of an element. The ratio between the spin (\bar{I}), described as an angular momentum, and the resulting magnetic moment ($\bar{\mu}$) is called gyromagnetic ratio γ : $\bar{\mu} = \gamma \bar{I}$. It is connected to the gyroamgnetic factor or Landé-factor g by $\gamma = \frac{g\mu}{\hbar}$ with μ as the Bohr magneton and \hbar being the reduced Planck constant. Tables listing the nuclear spin and the gyromagnetic ratio can be found in several textbooks.^[4;5]

Electrons The interactions of electrons with the nucleus and with themselves are described by Schrödinger's equation. The resulting orbitals are then occupied according to Hund's rule and Fermi's exclusion principle. In doubly occupied orbitals the magnetic moments of the two electrons are aligned antiparallel and cancel each other. All closed shells and fully occupied orbitals give exclusively diamagnetic contributions. The other magnetic effects are caused by the unpaired electrons in open shells or orbitals. Magnetism is therefore a direct consequence of the quantum mechanistic treatment of the electronic structure.

Orbital momentum Only degeneracy of orbital energies can lead to an orbital momentum. This can easily be derived from the underlying Hamiltonian $\hat{L} = -i\hbar (\vec{r} \times \nabla)$. We see, that the operator is imaginary and only gives real solutions in the case of imaginary wave functions. In the case of non-degenerated orbitals the wave function is always real and therefore no angular momentum is obtained. However, it should be noted that the presence of degeneracy is only a

necessary criterion, not a sufficient one, since also accidental degeneracy can occur. In contrast to spin momenta, the orbital momentum is always integer and its size depends on the degree of degeneration.

Together with the applied external magnetic field these three sources of magnetism can be arranged in a magnetic square (Figure 1.1). It represents the basic interactions and effects, which we need for the discussion of magnetic properties of one magnetic center. In most cases this corresponds to one isolated transition metal or radical without further interactions. In particular the most common interactions are:

Zeeman-Effect: This effect describes the behavior of levels in an applied magnetic field. In the simplest case of a system with $S = \frac{1}{2}$ it is responsible for the splitting of the levels with $m_S = +\frac{1}{2}$ and $m_S = -\frac{1}{2}$. It is described by the Hamiltonian $\hat{H}_{\text{Zeeman}} = \bar{g}\mu_B\vec{B}\hat{S}$.

Spin-Orbit Coupling: The interaction of the orbital and spin part of a given system is called spin-orbit coupling. It is described by the Hamiltonian $\hat{H}_{\text{so}} = \lambda\hat{L}\hat{S}$.

Zero Field Splitting: The interactions of electrons with each other in a given system is called zero field splitting or fine interaction. It is described by the Hamiltonian $\hat{H}_{\text{zfs}} = \bar{D}\hat{S}^2$.

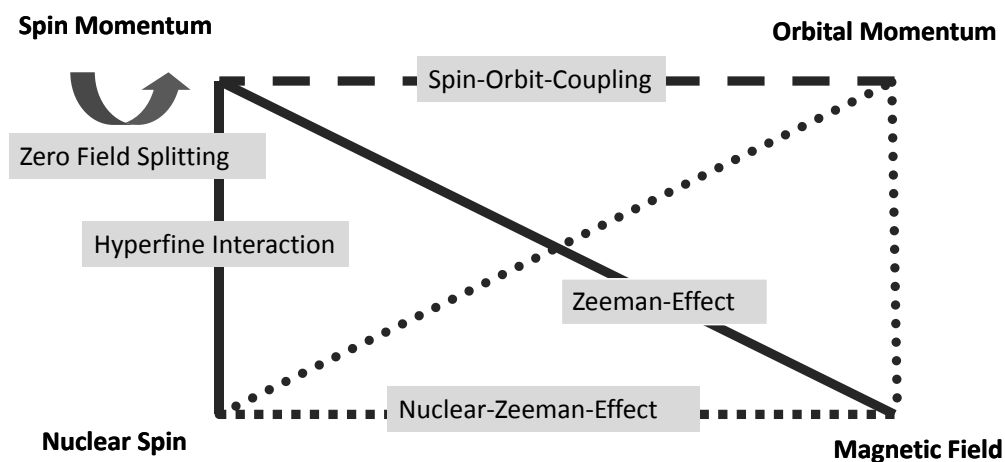


Figure 1.1: The magnetic square summarizes the sources of magnetism and the most common interactions between them.

Ligand Field: States with different orbital momentum differ in their spatial orientation. They are therefore very sensitive to the presence of charges in the nearby environment. In coordination chemistry these effects and the resulting splitting of levels is described by the ligand field. It is described by the Hamiltonian $\hat{H}_{lf} = \sum_{i=0}^k (B_i^k \hat{C}_i^k)$.

Hyperfine Interactions: The interactions of the nuclear spin I and the electron spin S is called hyperfine interaction. It is described by the Hamiltonian $\hat{H}_{hf} = A\hat{I}\hat{S}$.

The relative magnitude of these effects depends on the system we are looking at. Table 1.1 summarizes the order of magnitude for selected systems.^[6] The ligand field depends on the expansion of the orbitals and if and how they are shielded by other occupied orbitals. The hyperfine interaction depends, among other things, on the spin density at the nucleus and is therefore a good measure for the electron density distribution. Spin-orbit coupling grows more important with increasing atomic mass. In order to save computational time, the orbital momentum is neglected in most analysis and its effects are projected onto the spin S . The results are, in general, strong deviations in the g -value, which should be around the free electron value (2.00023), and a strong zero field splitting. However, these projections make a comparison of systems with different orbital momenta quite difficult.

Table 1.1: Magnitude of some relevant magnetic effects in metal ions.^[6]

| Effect | System | Energy equivalent [cm^{-1}] |
|--|------------------------|---|
| Electron-electron interaction \hat{H}_{ee} | 3d, 4d, 5d 4f, 5f | 3d > 4d > 5d $\approx 10^4$ 4f > 5f $\approx 10^4$ |
| Ligand-field potential \hat{H}_{LF} | 3d, 4d, 5d 4f 5f | 3d < 4d < 5d $\approx 2 \cdot 10^4$ $\approx 10^2$ $\approx 10^3$ |
| Spin-orbit coupling \hat{H}_{SO} | 3d, 4d, 5d 4f, 5f | 3d < 4d < 5d $\approx 10^3$ 4f < 5f $\approx 10^3$ |
| Exchange interaction \hat{H}_{ex} | nd 4f nd-4f | $\leq 10^2$ ≤ 1 ≤ 10 |
| Magnetic field \hat{H}_{Zeeman} | | ≈ 0.5 (1 T) |

Yet all these effects are located at one magnetic center. The last (and probably most important) part of this section deals with the interactions of several spin centers. The spins (and therefore the magnetic moments) are considered to be localized at specific sites, which is a fairly good approximation in the case of metal ions. Their interactions are characterized by the coupling constants $J_{i,j}$, $D_{i,j}$ and $G_{i,j}$ which tend to orient the spins in a specific manner. The energies of different orientations and therefore different multiplicities are assumed to depend only on the relative orientation of the angular momenta and are calculated using spin operator techniques. The appropriate Hamiltonian reads

$$\hat{H} = -J\hat{S}_i\hat{S}_j + \bar{D}\hat{S}_i\hat{S}_j + \bar{d}\hat{S}_i \times \hat{S}_j \quad (1.2)$$

The first term is called isotropic interaction, the second comprises the non-isotropic interactions (like dipole–dipole interactions), whereas the last one represents the anti-symmetric exchange. In cases without orbital contributions and more or less pure spin magnetism, the last two terms are commonly omitted. Furthermore, it can be shown that an inversion center mapping one magnetic center upon the other excludes anti-symmetric interactions.^[7] There are several definitions for the isotropic interactions in literature ($\hat{H} = -J\hat{S}_i\hat{S}_j$, $\hat{H} = -2J\hat{S}_i\hat{S}_j$ and $\hat{H} = J\hat{S}_i\hat{S}_j$), but only the first definition is used in this work. If the interactions favor the parallel alignment of spins, we speak of ferromagnetic interactions, whereas in the case of antiparallel alignment the interactions are called antiferromagnetic.

We apply the appropriate Hamiltonian, which accounts for all relevant effects, to the corresponding basis set of wave functions and obtain the energies and magnetic moments of each state as eigenvalues and eigenvectors of the corresponding interaction matrix. The magnetic moment of an ensemble of molecules at a given temperature is obtained by occupation of the energy levels according to the Boltzmann distribution. Via this approach the temperature dependence of the molar susceptibility can be calculated and the parameters of the interactions can be fitted to reproduce the experimental behavior. By calculating the field dependency of the energy levels also simulations of isothermal saturation measurements and — under inclusion of transition rules — also the calculation of electron spin resonance (ESR) spectra are possible.

ESR spectroscopy is a powerful tool to gain a lot of information about the energy splittings in the order up to the microwave wavelength used in the experiments (usually $0.3\text{--}3\text{ cm}^{-1}$),^[8;9] whereas determination of the magnetic moment, for example with a

SQUID-magnetometer, is very capable of gaining information about larger energy differences up to the order of the thermal energy (few hundreds cm^{-1}). A combination of these two methods allows the determination of most relevant parameters.

In rather simple cases or in well-defined boundaries, analytical expressions for magnetic properties can be derived. Examples are the Bleaney-Bowers-equation, which describes the thermal dependency of the magnetic susceptibility in $S = \frac{1}{2}$ dimers or special formula for tri- and tetranuclear complexes.^[7] However, to avoid the imposed boundaries and limitations of the model used, it is often helpful to use numerical methods to diagonalize the interactions matrix. In principle these methods are only limited by the computational power and memory available for the diagonalization routine.^[10;11]

If we need to enlarge our basis for analysis it is often very helpful to gain spatial information by measurements on oriented single crystals. It has been proven to be a powerful tool in the determination of anisotropy and anisotropic interactions.^[12-21] However, it requires the preparation of comparatively large single crystals of high quality. Advances in technology like the micro-SQUID^[22] or even the nano-SQUID^[23] have reduced the requirements, but these techniques are not yet widespread. Depending on the system also the proximity of molecules in the crystal packing can cause several problems. These range from simple line broadening in ESR experiments due to short spin-spin-relaxation times to interfering intermolecular coupling, disturbing the ground state of the molecule.^[9] Diamagnetically diluted single crystals (for example cocrystallization with a large excess of an analogous closed shell metal complex or inclusion into a host lattice of the appropriate symmetry) can solve this problems, but these crystals are very difficult to prepare, especially in the case of rather large and complex molecules.

The macroscopic effects listed above can be explained by different interactions between the spins. This is schematically depicted in Figure 1.2. The individual spin carriers are depicted as arrows and the lengths of the arrows represent the magnitude of the spin. In ferromagnets (a) all interactions are ferromagnetic leading to a large overall magnetization. In ferrimagnets (b) the alignment is antiferromagnetic, but due to different magnitudes of the spins, a net magnetic moment is observed. If both spins are of same magnitude and are arranged antiparallel, we obtain a antiferromagnet (c). Special cases are metamagnets (d) and spin glasses.

1.1.3 And what is it good for?

Nowadays magnetic materials are irreplaceable in every day live. Their applications range from motors over power generators and relays — used as electrical switches in a multitude of applications — to microphones and speakers. However, the most important application has become the storage of information in computers. From a physical point of view, the permanent storage (that means also in the absence of electrical current) requires units with two well-defined states (on and off, 1 and 0) separated by an energy barrier high enough to prevent loss of information. This is achieved using small domains of magnetic materials which can be magnetized in two directions. The read-out can be done either by measuring the polarization with a probe magnet, or by measuring the electric current in the presence of an external magnetic field. The latter one is based on the Giant Magneto Resistance (GMR) effect, discovered independently by Peter Grünberg and Albert Fert and subject of the Nobel price in 2008.^[24]

From the point of electronics the advancing size reduction in common electronic devices comes to an end in the case of single molecules showing the same properties as macroscopic materials. A lot of research is dedicated to the search for new materials, especially organic ones, that show the similar behavior like their metal containing counterparts. Examples are the development of organic solar cells,^[25–27] organic field effect transistors (OFETs)^[28–30] and organic light emitting diodes (OLEDs).^[31–35] With respect to data storage also the incorporation of spins as fundamental magnetic moments is an active field of research. A lot of stable organic radicals have been reported,^[36–38] but as π -based systems they lack the magnetic anisotropy of metal ions. The anisotropy gives rise to an energy barrier for the reversal of the magne-

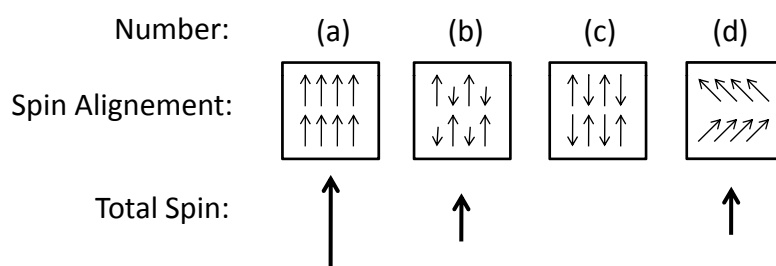


Figure 1.2: Schematic sketches of the origin of magnetic effects.

tization.^[39] Single complex molecules, that possess such a barrier are called Single Molecule Magnets (SMMs).^[40–68] Many of them contain either lanthanides^[69–79] or one of the three core structures Fe_4 ,^[17;80–85] Mn_{12} ^[39;86–92] or recently Mn_6 ^[93;94]. The arrangement of SMMs into exchange coupled one-dimensional coordination polymers, so called Single Chain Magnets (SCMs) increases the blocking temperature, i.e. the temperature where the thermal energy is equal to the energy needed for spin reversal.^[44;56;69;72;92;95] Interestingly there is also a great need for magnetic materials with just the opposite behavior — materials that behave as *superparamagnets*. Superparamagnets possess a large magnetic moment but no or only small energy barrier for its reversal.^[96;97] These materials are expected to be efficient cooling materials via the magneto-caloric effect.^[98]

1.2 Quantum Computing

But on the way to smaller and smaller devices we have already reached the area where quantum effects are no longer negligible. Indeed the loss of information by tunneling processes through energy barriers is one of the main problems in these nano-sized materials. Therefore the understanding of the basic quantum processes is crucial for avoiding them or, more elegant, use them for totally new applications. These are usually summarized under the topic *quantum computing*.^[19;99–103] Several aspects have been highlighted recently.^[104–111]

A conventional computer processes information encoded as so called bits. They can adopt two states, commonly referred to 0 and 1. Since most computers nowadays work with electronic building blocks, the state 0 is referred to if the voltage is below a given threshold and the state 1 if this threshold voltage is exceeded. More complex informations are encoded as a series of bits.

In most applications a quantum computer is not faster than a conventional computer, though distinct applications experience a dramatic acceleration. For example, there have been proposed special quantum algorithms for the factorization of large numbers and for search requests in databases (Grover algorithm^[112]). The first application is of enormous importance, since most data encryptions use this procedure nowadays (RSA-Code).

The two states 0 and 1 are replaced by the quantummechanical states $|0\rangle$ and $|1\rangle$. A quantum bit (qubit) is then defined as an normalized, arbitrary superposition of the two states $\Psi = a_0|0\rangle + a_1|1\rangle$ and more complex information as

$$\Psi_{\text{multi}} = \sum_{\chi=|0,\dots,0\rangle}^{\chi=|1,\dots,1\rangle} a_{\chi} \cdot \chi \quad (1.3)$$

The state functions χ can be defined by several quantum mechanical observables. One approach commonly discussed is based on the spin — either the nuclear spin of an element or the electron spin. The latter has been intensively studied (for example by Loss et al. [100;101]) and there have been proposed several methods of implementing quantum algorithms into molecular systems. [99;113–115] An electron possesses a spin $S = \frac{1}{2}$ and offers the two states $m_s = +\frac{1}{2}$ and $m_s = -\frac{1}{2}$ as the basis for encoding of information. [101]

The processing of informations is carried out via manipulations of the individual qubits. These manipulations are called quantum gates. [113] It was shown, that every operation can be decomposed into two different kinds of quantum gates [116]:

Single-qubit quantum gate: These are operations which change the state of one individual qubit. In the case of an $S = \frac{1}{2}$ system this would mean a single spin flip.

Two-qubit quantum gates: These operations manipulate two qubits simultaneously. This means to alter the coupling between two qubits, for example to alter the exchange coupling between two $S = \frac{1}{2}$ systems. [117;118]

In an ideal case, the interactions necessary to perform these two types of quantum gates should be the only interactions between the qubits and the environment despite the necessary initialization and the read-out. In an actual system exist a variety of additional interactions, which cause errors. In a conventional computer the threshold voltage is chosen so high, that loss of information is very improbable. In a quantum computer the impacts are much stronger and lead to a loss of informations towards the environment. This process is referred to as decoherence and is described by the coherence time. The longer this particular time is, the longer "survive" the quantum encoded information.

By choosing a system with the appropriate symmetry several pathways of decoherence can be eliminated. This exclusion leads to elongated coherence and reduces the loss of information. A subsystem is called decoherence free subsystem (DFS), if it fulfills these requirements.^[119] One class of systems, whose interaction matrix exhibits the appropriate symmetry, are antiferromagnetically coupled polynuclear transition metal complexes with an odd number of electrons and antiferromagnetic interactions between the individual centers. If all coupling constants are of exactly the same magnitude, the ground state is doubly degenerated with a total spin $S = \frac{1}{2}$. These systems are also referred to as "spin frustrated".^[19;120-127] Due to their symmetry, these states act as DFS.

The residual loss of information by decoherence can be suppressed by quantum error correction codes (QECC).^[128-131] But these codes only give satisfactory results, if the probability of an error on applying a quantum gate is well below a threshold ϵ . This threshold can be estimated by the ratio between the switching time of the corresponding quantum gate τ_{switch} and the coherence time of a given system, represented by the value of T_2 : $\epsilon = \frac{t_{\text{switch}}}{T_2}$.

From this equation it becomes obvious that there is a demand for systems combining short switching times with long coherence times. The first aspect suggest the use of electrical fields, since they can both be switched on a very short timescale and be focused on a small spatial region. One possibility to influence the coupling inside a system by electrical fields was described by Loss et al.^[132] They utilize the interactions between the electrical field and the angular momentum of the unpaired electron.^[133;134] Since the angular momentum is responsible for the antisymmetric coupling, this approach allows for the direct manipulation of the exchange interactions between the individual metal ions. Furthermore the electrical current through an STM tip could be used for the read-out of the encoded information as well.^[101]

By contrast, the second aspect is determined by the actual system serving as qubit. The main source of decoherence inside a given molecule are other spin carriers, for example nuclear spins. Replacing corresponding elements by isotopes without or with smaller nuclear moment indeed elongates T_2 . It has been shown in $\text{Cr}_7\text{Ni}/\text{Cr}_7\text{Mn}$ ring systems, that replacing hydrogen atoms by deuterium results in an elongation of the coherence time by a factor of six.^[135] Recently also it has been reported a possible way to decouple nuclear and electron spins by physical procedures.^[136]

The simplest system, which fulfills the requirements for a DFS, is build up by three spin carriers which are coupled antiferromangetically with exactly the same strength. Radicals as well as metal ions can be used as spin carriers. Several systems have been reported and have been characterized due to the characteristics of the exchange interactions.^[18;19;120–124;137–143] Since the antisymmetric exchange lifts the degeneracy of the ground state, a careful analysis of the interactions is required.

Metal complexes based on triaminoguanidines are very promising candidates for qubit storing and show several advantages. The interactions between the three metal centers are that strong, that they represent the strongest interactions even in the case of extended structures.^[144;145] This very strong couplings leads to very good thermal isolation of the degenerated ground doublet. The rigidity of the ligand backbone impedes structural distortions, which would lift the degeneracy as well. The rigid π -system favors the formations of complexes with strict C_3 -symmetry, in which the symmetry equivalence preserves the equality of the exchange interactions.

In general, the basic requirements for a quantum computer are known as the five Di-Vincenzo criteria:^[99]

- The two states must be well defined, isolated from the environment and scalable, i.e. it must be easy to add an extra qubit.
- There must exist a procedure for initializing the qubits, i.e. to prepare a defined state, for example $|0\dots0\rangle$.
- There must be the possibility to implement one- and two-qubit quantum gates.
- The coherence times need to be long enough in comparison to the switching times in order to make error corrections codes efficient.
- There must exist a possibility to read out the final state after performing the desired computations.

All of these criteria must be met in the same system at the same time and in the same measurement.

1.3 Building Blocks

The concept of designing molecular architectures by the appropriate linkage of monomeric building blocks has attracted considerable interest during recent times.^[146–150] Especially for the design of multifunctional materials it is an attractive approach to combine two units to a new molecule, exhibiting the combined properties of both original units.^[151] These starting units are commonly called building blocks. They are characterized by an intense interplay between their function and their structure. Possible functions might be

- conduction
- memory
- architectures
- switching
- combinations and new functions
- and many more

For example, if one wishes to combine electric conductivity with light absorption of a defined wavelength, one reaches into his box of molecules, picks one with a small electric resistance and another one with a defined absorption spectrum and links these two together.^[152] This simple picture also illustrates the major problems of this approach. If we are working with molecules and the interplay between molecules, slight changes of the structure can have considerable impact on the properties. Simple linkage of molecules may alter their properties in a drastic way, especially if the specific property is not exclusively located on a molecule, but is affected by intermolecular interactions. The conductivity might be drastically decreased by separating the conducting molecules by a light absorbing chromophore. And the influence of electric and magnetic fields due to electric currents might alter the energetic levels of the chromophore and therefore the absorption spectrum.

However, one function is always present: the structural one. This is mainly determined by the space occupied by the building block and the spatial arrangement of the linking groups. Linking groups in this context can either be free metal coordination sites

or free donor groups on ligand molecules. Many ligand scaffolds have been discussed according to their specific coordination mode. Providing only one or two coordination sites by blocking a defined number of coordination sites they can be connected to other building blocks by bridging ligands in a specific way.^[153;154] One example are porphyrine complexes, in which the disk shaped ligands blocks the equatorial coordination sites and leaves only the axial positions accessible for coordination.^[155] Hence, the appropriate choice of the ligand leads to a predictable geometry in the final overall structure.

For this reason the concept of building blocks is also of great interest in the design of functional materials which require higher dimensionalities. Examples are the synthesis of chain structures (one dimensional),^[156] layers (two dimensional)^[157] and three dimensional systems (for example metal organic frameworks).^[158;159] In most of these cases metal complex molecules are designed to fulfill specific structural requirements and to possess the magnetic features needed for the final application. Some of the most prominent examples in this area are coordination polymers based on Salen-type complexes.^[154;160] In these complexes the predictable and well known coordination properties of Salen ligands are used to design building blocks with predefined open coordination sites.^[161] Via introduction of additional donor atoms also heterobinuclear entities are accessible and especially lanthanide ions can be introduced into the materials.

There are several points one has to consider when working on the design of new building blocks. A building block should

- contain the functional entity.
- offer the possibility to tune the final function.
- possess linking groups for linkage to other building blocks.
- preserve the desired function even under linking and linked conditions.

Let us discuss these points in detail.

Functional Entity: A lot of effects and functions are caused by discrete and relatively small moieties. For example, carboxylic groups account for acidic properties, sulfonates with proper counter ions increase the solubility in a wide range of solvents, open shell metal ions interact with magnetic fields and triphenylamines can

be oxidized by light and act therefore as photoelectron donors. For implementing a desired function, the first step is to identify the corresponding functional group. In some cases that might be quite easy (acidity) in other cases rather complicated (conductivity). In several cases there exists a variety of molecules which are all capable of performing the function of interest. Many molecules have been described as potential photoelectron donors or acceptors.^[32;162-176] The decision, which one to use, is then guided by other criteria, for example by general facts like price, availability and toxicity.

Tuning Possibility: In many systems the possibility of fine tuning is desirable. That means that subgroups with distinct and well-known impact are introduced to gradually alter the properties. The influence of aromatic substitutions upon a variety of chemical characteristics is well understood nowadays. Ligands synthesized by Schiff-base-condensation of substituted salicylaldehydes clarify this aspect: there exists a large number of substitution pattern, changing solubility, the nature of interactions with adjacent molecules, the steric demands, the electron density and distribution and many more. However, in most cases they do not alter the principle coordination behavior of the synthesized ligand.

Linkage Groups To serve as a building block molecules must possess linking groups to build larger aggregates. The nature of these linking groups is only limited by the fantasy of the synthetic chemist — and the stability of the final system. Linkage can be performed by covalent bonds, hydrogen bonds, π - π -interaction or electrostatic interactions. In some cases, the desired functionality requires some specific linkage modes. In conducting materials the linkage should not prevent the electron flow, which mainly occurs through π -electrons. Using a saturated ethyl group leads to a break-down of the conjugation, whereas ethylene and acetylene groups extend the delocalized π -system.

Preservation of Function One of the most important points is the test, whether or not the desired function is preserved in the final composite molecule. A building block, which loses its function when linked to other building blocks, is not a suitable building block. In some cases the function preservation can be quite easy and is highly probable (an acidic group in a polymer is still acidic) but as we come to more complex properties, it might become a demanding subject to prove the preservation of function. Although the coupling constant in a small discrete

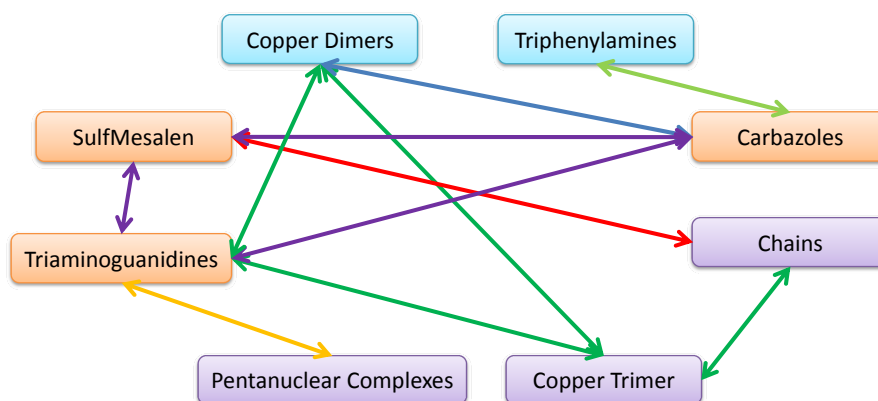


Figure 1.3: Sketch of the organization of this thesis. Blue boxes are assigned to the first step, red ones to the second and the violet ones to the last step of building block design. The colored arrows link sections which share common features: Mesalen-type ligands (red), sulfonato carrying ligands (violet), extended ESR-investigations (dark green), triaminoguanidine ligand (yellow) and triphenylamine derivatives (light green).

molecule can be determined easily by evaluation of magnetic measurements, this might be much more difficult in more extended systems, especially in the presence of additional magnetic centers with possibly even different functionalities.

In conclusion, we have to perform three general steps in the design of building blocks:

New Functionalities We have to identify an effect as a possible function of a building block, i.e. to observe an effect, identify the responsible molecular aggregates and characterize them carefully as a kind of reference system.

New Building Blocks We have to synthesize molecular aggregates, which contain the functional units but also offer the possibility of introducing anchoring groups and derivatizations for tuning the properties.

Linked Building Blocks We have to link the building blocks into oligomers, polymers and other well-defined structures and to verify that the functionality found in the monomers is preserved in the aggregates.

These three steps are used to group the various results of this thesis. The individual projects are grouped accordingly, though a lot of cross links exist. A sketch of the general organization of the thesis is depicted in Figure 1.3 to illustrate the interplay between the sections.

— Results —

2 New Functionalities

In the field of organic electronics triphenylamine derivatives are widely used due to their unique optical and electrochemical properties. They can be oxidized electrochemically to form the corresponding triphenylaminium cation radical^[177-181] and therefore act as electron donors and and/or hole transport units in organic conductors, semiconductors and other electronic devices.^[182] They can be efficiently synthesized via metal catalyzed cross coupling reactions.^[183-194] This approach gives rise to a facile derivatization of the phenyl rings and allows the tuning of the electronic properties^[195;196] as well as the introduction of linking groups to additional functionalities.^[197-199]

Since the oxidation can be light driven, too, in the run of photo electron transfer reactions,^[172;200;201] derivatives of triphenylamines also play a significant role in the design of photo-electronic devices such as organic light emitting diodes (OLEDs) and organic photo voltaic cells.^[174;176] For the former case, charge separation is induced by electrochemical oxidation and the back transfer of an electron and the hole-electron annihilation gives rise to an electro luminescence. For the latter case it is just vice versa. Here the photo electron transfer reaction results in a charge separation.

The first section of this chapter discusses how to combine these unique electrical and optical properties with open shell transition metal ions. Only few examples of ligands bearing a triphenylamine moiety are known, which are substituted with donor atoms to directly link the transition metal ions to the triphenylamine core. The interplay between the magnetically active aminium radical and the static magnetism of the metals is a promising way to new functional materials. Derivatives of triphenylamines substituted with donor atoms have therefore been synthesized as well as their corresponding copper(II) complexes. Copper(II) is most probably the best understood magnetic center and allows a classification of the obtained results.^[7;8;19;202;203] These compounds are then characterized according to their electronic structure and their magnetic properties.

Copper(II) is also known for its great variety in coordination modes.^[202] The most common coordination modes involve four to six donor atoms. Due to the d^9 system the Jahn-Teller effect leads to axial distortions in the coordination polyhedra. Octahedral complexes normally show four donor atoms forming a square and two ligands in *trans*-positions with longer metal–donor-distances. Another well-known fact is, that these positions are much more accessible to ligand exchange reaction than the equatorial ones. A nice side aspect is the fact, that it is quite easy to determine the internal z -axis of a given coordination polyhedron from the crystal structure.

Upon removing one of these axial donor atoms one ends up with a square pyramidal coordination sphere, which is very common among reported copper complexes. By a proper transformation, this coordination mode can be changed into a trigonal bipyramide. However, the impact of this transformation on the magnetic behavior is not that strong, since the energy scheme of an axially distorted trigonal bipyramide is very similar to that of an square pyramidal environment with respect to the magnetic orbital, which is the highest orbital in the energy scheme.

If the second axial donor atom is removed as well, one ends up with a square planar coordination, which can be transformed into a tetrahedral coordination by increasing the tilting angle between two planes, one spanned by two *cis* donor atoms and the copper ion and the other one spanned by the residual donor atoms and again the copper ion. The impact is much larger than in the case of a fivefold coordination, since the sequence of orbitals in the energy scheme is strongly exchanged upon deformation.^[204,205] The change of the ground state gives rise to very different ESR spectra with much greater variance in the parameters than it is found upon distortions of penta- or hexa-coordinated copper(II) ions. They show axially^[206–208] and rhombic spectra^[209] as well as very anisotropic ones.^[210] Complexes with intermediate structures should therefore be very sensitive to structural deformations, when these change the orbital contributions to the wave function of the unpaired electron. The second section of this chapter deals with an interesting effect observed in a series of dinuclear metallacycles, which exhibit precisely this described intermediate structure between square planar and tetrahedral. A combination of theoretical considerations and spectroscopic methods offers an explanation for the observed anomaly.

2.1 Complexes Based on Triphenylamines

2.1.1 Synthesis and Structure

The amine precursor *N*-(4-amino-phenyl)-diphenylamine (**2**) was synthesized by Hartwich-Buchwald-type coupling of diphenylamine and 4-nitro-bromobenzene and subsequent reduction of the *N*-(4-nitrophenyl)-diphenylamine (**1**) with hydrogen and *Raney* nickel (Figure 2.1). Reaction with salicylic aldehyde or 3,5-di-*tert*-butylsalicylic aldehyde results in the formation of the ligands HTPA (**3**) or H^{tBu} TPA (**4**), offering an NO donor set for the coordination of metal ions. Reaction of copper(II) ions with HTPA and triethylamine in an 1:1:1 ratio followed by addition of a solution of hexafluoroacetylacetonate (Hhfac), that has been already deprotonated by triethylamine, results in the formation of the neutral dimeric complex $[Cu(hfac)(TPA)]_2$ (**5**), in which the constituting $[Cu(hfac)(TPA)]$ units are bridged by the phenolic oxygens. H^{tBu} TPA reacts with copper(II) ions in a 2:1 ratio to form a neutral complex of the formula $[Cu(^{tBu}TPA)_2]$ (**6**).

The structures of these two complexes were determined by X-ray diffraction. Compound **5** crystallizes in the triclinic space group $P\bar{1}$. The copper is coordinated in a square pyramidal fashion which is elongated in the axial direction (Figure 2.2, left). Selected bond lengths and angles are depicted in Table 2.1. In the $[Cu(hfac)(TPA)]$ moieties the ligands TPA^- and $hfac^-$ give rise to the NO_3 donor set forming a plane

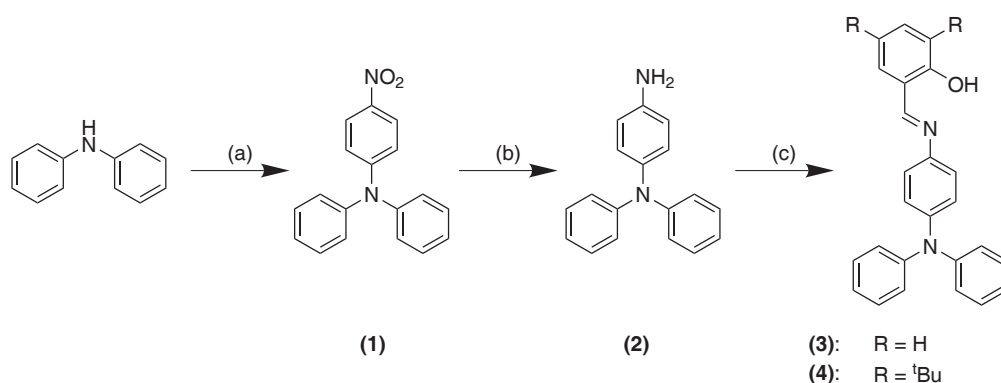


Figure 2.1: Preparation scheme for the ligand HTPA and H^{tBu} TPA; (a): 4-bromo-nitrobenzene, KO^tBu , $Pd(OAc)_2$, $P(^tBu)_3$, 80° , 3.5 h, toluene; (b): H_2 , 55bar, *Raney*-nickel, AcOEt 4 h; (c) aldehyde, MeOH, reflux, 1 h.

Table 2.1: Selected bond length in pm and bond angles in ° for [Cu(hfac)(TPA)]₂ (5)

| bond length (pm) | | bond angles (°) | |
|------------------|----------|-----------------|------------|
| Cu–O1 | 190.9(4) | N1–Cu–O2 | 169.05(18) |
| Cu–O3 | 194.6(4) | O1–Cu–O3 | 175.34(18) |
| Cu–N1 | 196.5(5) | O1–Cu–O1A | 87.17(15) |
| Cu–O2 | 198.2(4) | O2–Cu–O1A | 90.13(15) |
| Cu–O1A | 232.7(4) | O3–Cu–O1A | 95.79(16) |
| | | N1–Cu–O1A | 100.69(17) |

from which the copper ion is displaced by 12 pm. The fluorine atoms of the hfac[−] co-ligand are strongly disordered. The axial positions are mutually held by the phenolate oxygen of the second [Cu(hfac)(TPA)] moiety thus forming a Cu₂O₂ core (Figure 2.2, right). The copper–copper-distance is 310 pm and the bridging angle Cu1–O1–Cu2 is 93°. The Cu–O1-distance within a moiety is 190 pm while the one between the units is 230 pm.

The aromatic ring of the salicylidene moiety is canted by 31° against the coordination plane spanned by the donor atoms N1, O1, O2 and O3. The *para*-substituted phenyl ring between N1 and N2 is nearly orthogonal to the coordination plane ($\alpha = 83^\circ$) and forms an angle of 53° to the salicylidene moiety. The rings constituting the triphenyl amine exhibit twisting angles of 67°, 67° and 77°. One of the phenyl rings is very close

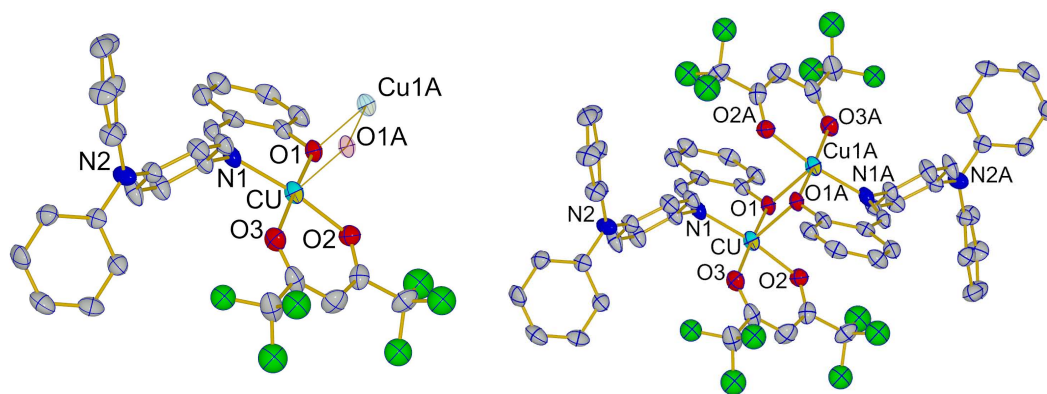


Figure 2.2: Molecular structure of the monomeric [Cu(hfac)(TPA)] unit with numbering scheme for all hetero atoms and the dimer [Cu(hfac)(TPA)]₂ (5). The ellipsoids are drawn at the 50% probability level. All hydrogen atoms have been omitted for clarity.

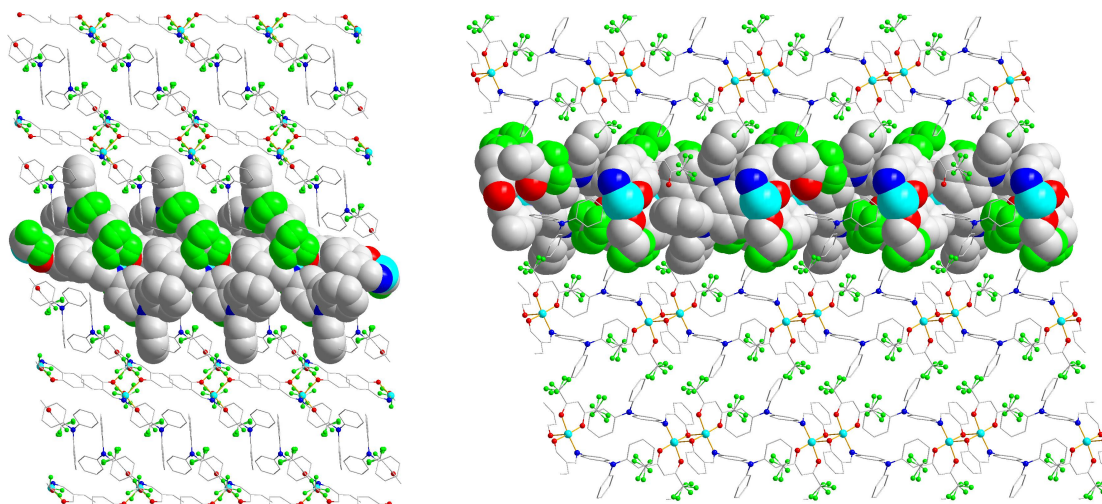


Figure 2.3: Formation of zigzag chains along the a -axis (left) and of layers in the $[101]$ -plane in the view of the c -axis in the supramolecular structure for $[\text{Cu}(\text{hfac})(\text{TPA})_2]$ (**5**).

(295 pm) and coplanar to one of the next molecule. Via these π - π interactions piles are formed along the a -axis (Figure 2.3, left), which are stacked together to form planes perpendicular to the b -axis (Figure 2.3, right).

Compound **6** crystallizes upon sequential dissolution and slow evaporation of different solvents (methanol, chloroform, ethanol) finally from acetone solutions in the monoclinic space group $P2/n$. The copper is coordinated in a N_2O_2 fashion (Figure 2.4) by two $^t\text{BuTPA}^-$ moieties. Selected bond lengths and angles are depicted in Table 2.2. There exist two molecules in the asymmetric unit, but the differences in bond lengths and angles are rather small. The angle between the planes N1A-O1A-Cu1A and N1B-O1B-Cu1A is 43° , therefore the coordination polyhedra can be regarded as an intermediate structure between square planar (0°) and tetragonal (90°). Defining a mean plane

Table 2.2: Selected bond length in pm and bond angles in $^\circ$ for $[\text{Cu}(^t\text{BuTPA})_2]$ (**6**)

| bond length (pm) | | bond angles ($^\circ$) | |
|------------------|----------|--------------------------|----------|
| CuA-O1A | 191.8(3) | N1A-Cu-N1B | 156.0(2) |
| CuA-N1A | 195.8(4) | O1A-Cu-O1B | 148.5(2) |
| CuA-O1B | 190.6(3) | N1B-Cu-N1B | 151.9(2) |
| CuA-N1B | 196.4(4) | O1B-Cu-O1B | 146.9(2) |

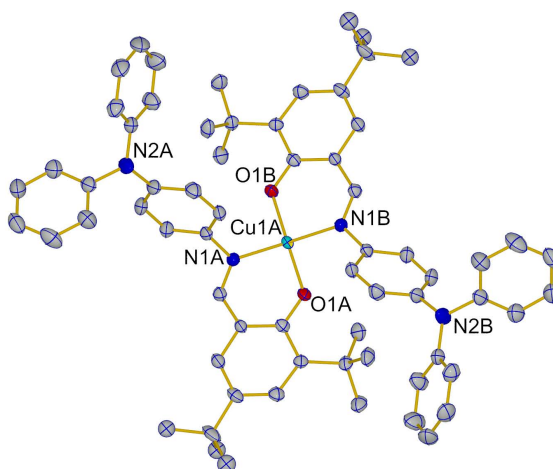


Figure 2.4: Molecular Structure of $[\text{Cu}(\text{tBuTPA})_2]$ (**6**) with numbering scheme for all hetero atoms. The ellipsoids are drawn at the 50% probability level. All hydrogen atoms have been omitted for the sake of clarity.

through the atoms N1, N2, O1, O2 and Cu, the salicylidene part of the ligand and the triphenylamines are on opposite sides of this plane. This arrangement minimizes the steric repulsion between the bulky *tert*-butyl and triphenylamine groups, thus yielding an *anti*-coordination. The angle between the salicylidene phenyl rings and the *para*-substituted bridging phenyl ring is 52° while the rings constituting the triphenyl amine moiety build up angles between 62° and 86° .

The molecules are arranged with C-H $\cdots\pi$ -interaction between the phenyl rings of the triphenyl moiety along the *c*-axis and via H $\cdots\pi$ -interaction between the *tert*-butyl groups and the phenylrings of the triphenylamine along the *a*-axis. The copper ions are ar-

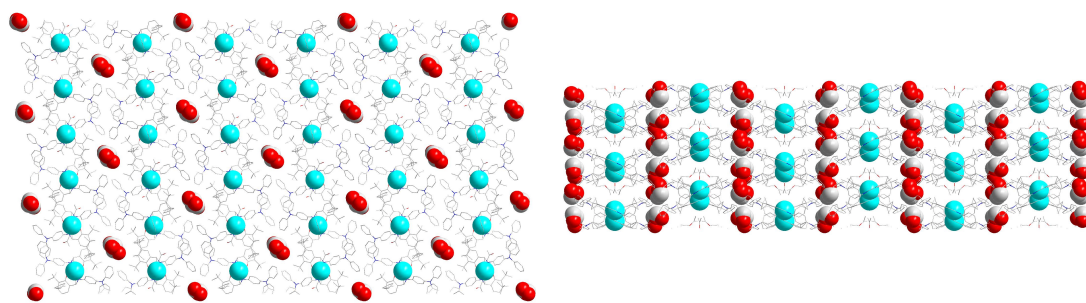


Figure 2.5: Supramolecular structure formed by $[\text{Cu}(\text{tBuTPA})_2]$ (**6**) and formation of channels as viewed along the *b*-axis (left) and *c*-axis (right). The single light balls represent the copper centers, the stacked ones the solvent molecules in the channels.

ranged in a plane forming a rhombus with angles of $\alpha_1 = 96^\circ$ and $\alpha_2 = 84^\circ$ (Figure 2.5, left). Inside the lozenge there exists a cavity which forms channels along the b -axis and is filled with strongly disordered solvent molecules (Figure 2.5, right).

2.1.2 Electronic Properties

UV-Vis spectra were recorded in commercial chloroform at ambient temperature. As it can be seen from Figure 2.6 there is a drastic change of color in solution for the ligand $H^{tBu}TPA$ during six weeks from a slight yellow to a dark violet solution. The initial spectrum was measured just after preparation of the solution and shows a series of absorption bands which can be deconvoluted by fitting multiple gaussian-shaped absorption bands to the measured spectrum (Appendix, Figure A.4). Five bands are obtained: one below 250 nm, at 279 nm ($\log \epsilon = 4.66$), at 295 nm ($\log \epsilon = 5.17$), at 363 nm ($\log \epsilon = 4.99$) and at 402 nm ($\log \epsilon = 5.15$). The spectrum recorded after six weeks (referred to as late spectrum later on) consists also of five bands in the UV (Appendix, Figure A.5): one at 256 nm ($\log \epsilon = 4.96$), at 268 nm ($\log \epsilon = 5.04$), at 292 nm ($\log \epsilon = 5.05$), at 314 nm ($\log \epsilon = 4.66$) and at 347 nm ($\log \epsilon = 4.81$). In addition there are two other broad bands in the visible region at 501 nm ($\log \epsilon = 3.04$) and at 696 nm ($\log \epsilon = 4.35$).

X-band ESR spectra recorded at 77 K on the frozen UV/Vis solution after six weeks show a small sharp Lorentz-shaped isotropic signal at $g = 2.003$ (Figure 2.6, right) with a line width of 10 G (Appendix, Figure A.6). This would be in good agreement with

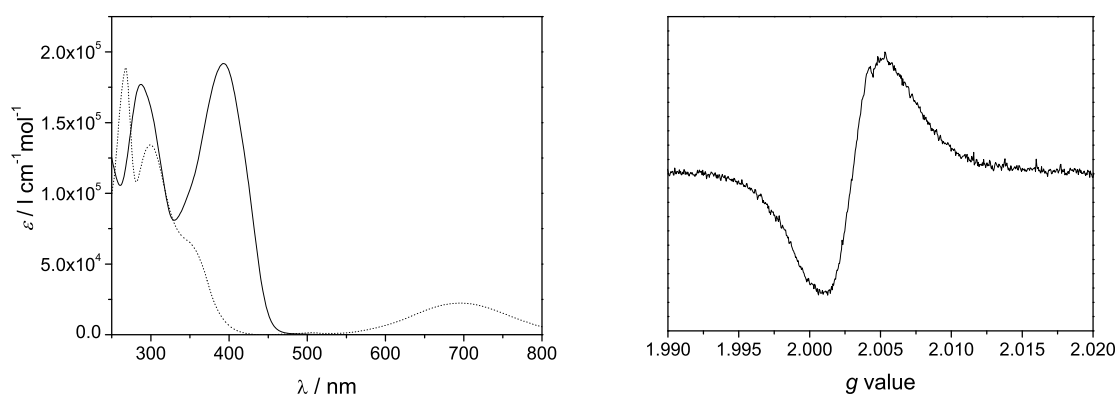


Figure 2.6: Left: Wavelength dependence of the absorption coefficient of $H^{tBu}TPA$ (**4**). Solid line: spectrum measured just after preparation, dotted line: spectrum measured after six weeks. Right: ESR spectrum recorded on a frozen solution of the UV/Vis solution after six weeks.

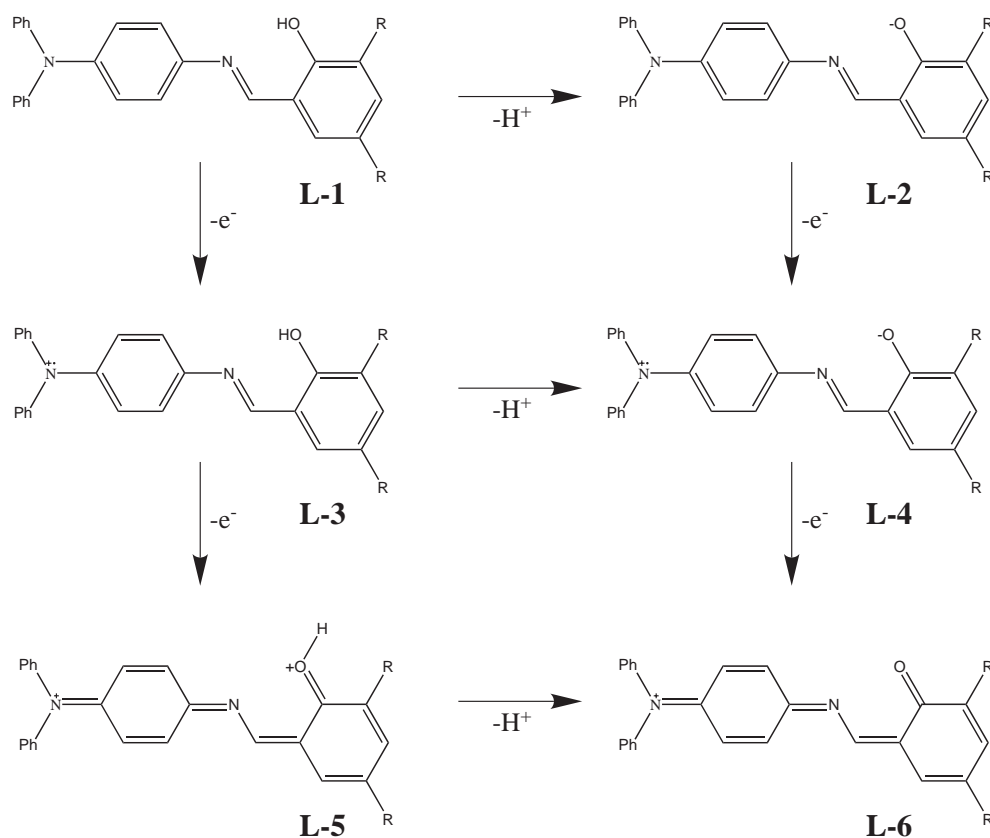


Figure 2.7: Scheme to illustrate the oxidation of $H^{tBu}TPA$ (4). Horizontal processes represent proton abstraction, vertical processes one electron oxidation. Three reaction pathways are possible: L-1 \rightarrow L-3 \rightarrow L-5 \rightarrow L-6 (mechanism 1), L-1 \rightarrow L-3 \rightarrow L-4 \rightarrow L-6 (mechanism 2), L-1 \rightarrow L-2 \rightarrow L-4 \rightarrow L-6 (mechanism 3).

a radical species obtained by one electron oxidation of the ligand. However, repeating the measurements several weeks after the first measurement, no ESR signal could be detected. At this time no further darkening of the solution could be seen, which suggests completion of further oxidation to a chinoine like system. A possible mechanism for these observations is the twofold one-electron-oxidation of the triphenylamine moiety with oxygen. Including also the abstraction of the rather acidic phenolate proton, the steps of this mechanism are depicted in Figure 2.7. For clarity only one isomer is depicted in the case of possible valence isomerism.

The twofold one electron oxidation is confirmed by square wave voltammetry. As can be seen in Figure 2.8 on the left side two well defined oxidation processes are visible with oxidation potentials of 1.155 V and 1.435 V. Both are not fully reversible, the first

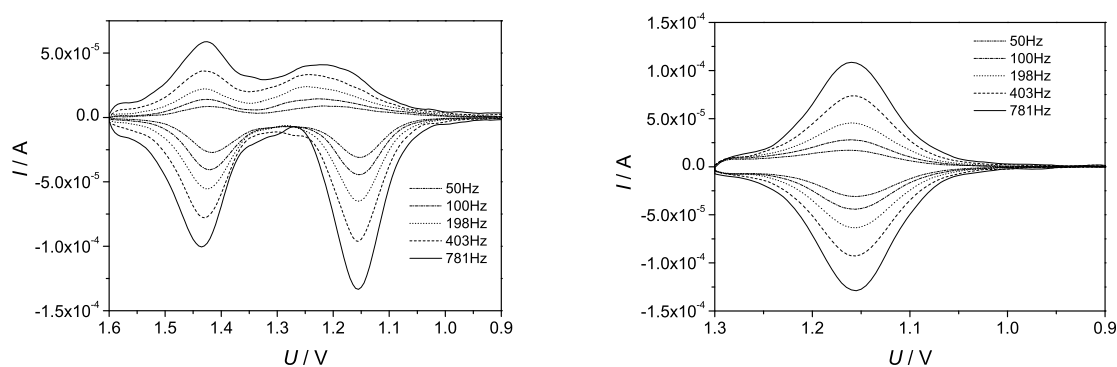


Figure 2.8: Square wave cyclic voltammetry of H^{tBu} TPA (**4**) in acetonitrile cycling from 0.9 V to 1.6 V (left) and to 1.3 V (right).

one giving only a broad and shifted current maximum upon re-reduction. However, rising the voltage only to 1.3 V, the first oxidation step becomes much more reversible (Figure 2.8, right). Assuming a simple decay reaction after oxidation (for example a deprotonation), a decomposition rate of some s^{-1} can be estimated from the frequency dependence. These observations are in very good agreement with the observed effects in solution.

Very similar observations are made measuring square wave voltammetry for the unsubstituted ligand HTPA (**3**). In this case the redox potential is slightly shifted in comparison to **4** and the reaction becomes less reversible. This is not unexpected regarding the electron donating behavior of the *tert*-butyl groups in **4**, which stabilize the radical cation. However this small difference is sufficient to prevent the aerobic oxidation under ambient conditions in solution.

The electronic structure was further investigated theoretically using density functional theory. The structures of all molecules depicted in Figure 2.7 were optimized using the BP86 functional and a def2-TZVP basis set as provided by the TurboMole program package and analyzed according to their spin densities. The results for the two open shell compounds **L-3** and **L-4** are depicted in Figure 2.9. The absorption spectra of the optimized structures were calculated using the INDO/S method as provided by the ORCA program package. The results of these calculations are depicted in Figure 2.10. To estimate the influence of a coordinated transition metal ion, spin density calculations were performed for a truncated model of **5** in the oxidized state. In this model compound, the axially coordinated second complex fragment was replaced by

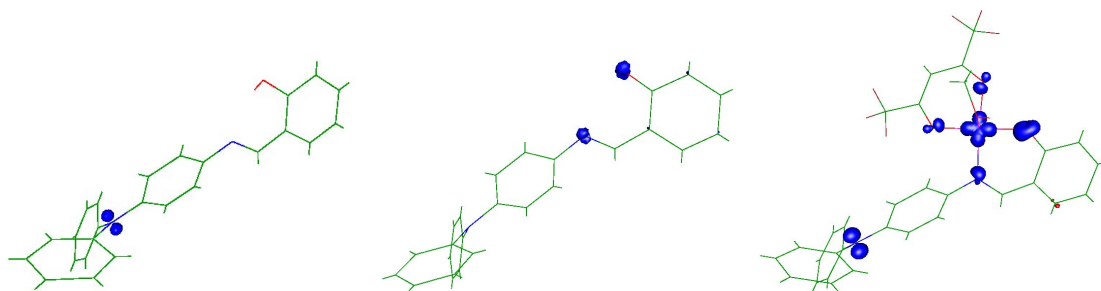


Figure 2.9: Spin densities of the oxidized ligand **L-3** (left), the deprotonated oxidized ligand **L-4** (middle) and of the triplet state of the dimer fragment $[\text{Cu}(\text{hfac})(\text{MeOH})(\text{TPA})]$ (right), in which the axial phenolate oxygen from the second half was replaced by an methanol molecule (see text). The iso-surfaces are drawn at a spin density of 0.04.

a methanol molecule. Again the structure of the radicalic ligand–copper pair was calculated using the BP86 functional and a def2-TZVP basis set as provided by the TurboMole program package and analyzed according to the spin density of the triplet state. The result is shown in Figure 2.9 on the right side.

The spin densities show an interesting change between the different species. In the protonated, oxidized ligand, the unpaired electron is located at the central nitrogen atom of the triphenylamine moiety. Upon deprotonation, the spin density is concentrated in the salicylidene binding pocket, which leads to an increase of the angle between the bridging phenyl ring and the salicylidene system from 29° in the protonated form to 54° in the unprotonated one. Upon coordination of a $[\text{Cu}(\text{hfac})(\text{MeOH})]^+$ moiety, the angle remains 54° but the spin density is now again localized on the central nitrogen of the triphenylamine moiety. It has mainly p -character and is orthogonal to the plane spanned by the nitrogen and its three closest neighboring carbon atoms. The angle between the "radical orbital" and the magnetic $d_{x^2-y^2}$ -orbital at the copper (estimated by the mean plane through the equatorial donor atoms and the copper ion) is 37° . Therefore, the coupling constant between the copper centered electron and the radical centered one is expected to be rather small.

A comparison of the calculated absorbance spectra with the experimental ones shows good agreement between the spectrum of **L-1** and the spectrum recorded just after preparation (initial spectrum). The calculated spectrum of **L-6** shows an absorption band around 517 nm and a second strong band at 702 nm. This is in good agreement with the bands observed at 501 and 696 nm in the spectrum recorded after six weeks

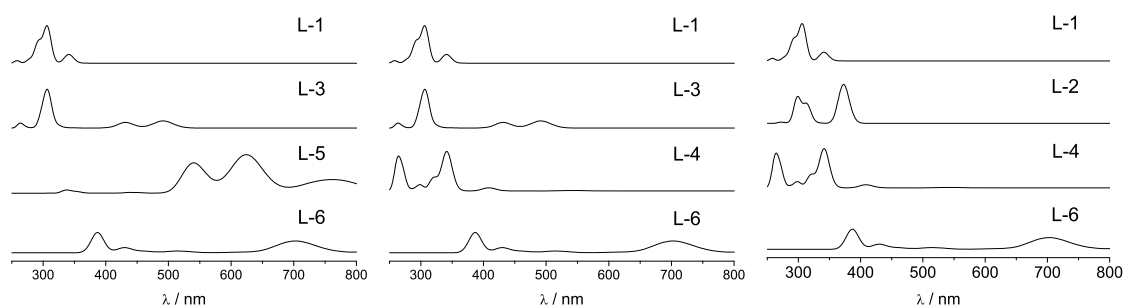


Figure 2.10: Calculated absorbance spectra of intermediates following different routes for hydrogen abstraction and one electron oxidation processes: deprotonation after (mechanism 1, left figure), between (mechanism 2, central figure) and before oxidation steps (mechanism 3, right figure).

(late spectrum) and is a further indication for the formation of a chinoine like system. The additional strong band around 400 nm in the initial spectrum can be attributed to the presence of deprotonated ligand in the solution, which would favor mechanism 3. In this case the appearing band in the late spectrum at 347 nm is probably caused by the intermediate **L-4**. This would also be in good agreement with mechanism 3.

In contrast to the results in Section 3.1 on dinuclear complexes based on carbazoles, only weak fluorescence was detectable. This is probably due to the fact, that the triphenylamine complexes presented here are more flexible than the very rigid carbazole compounds, thus providing more deactivation pathways.

2.1.3 Magnetic Properties

The temperature dependence of the magnetic susceptibility of compound **5** was determined in the temperature range between 2 and 300 K. Plots of $\chi_M = f(T)$ and $\chi_M T = f(T)$ are depicted in Figure 2.11 on the left side. At high temperatures the value of $\chi_M T$ is $1.05 \text{ cm}^3\text{K mol}^{-1}$ which is higher than the spin only value for two independent copper(II) ions ($0.75 \text{ cm}^3\text{K mol}^{-1}$ for $g = 2$). This can be explained by a temperature independent paramagnetism, which also accounts for the linear decrease upon lowering the temperature. At very low temperatures, the $\chi_M T$ increases slightly indicating weak ferromagnetic interactions. Fitting the parameters of the Bleaney-Blowers equation^[211]

$$\chi_M = \frac{N_A \mu_B}{3k_B T} \left[1 + \frac{1}{3} \exp\left(\frac{-J_{\text{CuCu}}}{k_B T}\right) \right]^{-1} + \chi_{\text{TIP}} \quad (2.1)$$

against the measured data gives the best agreement with the following parameters: $g = 2.086(4)$ and $J_{\text{CuCu}} = +0.63(7) \text{ cm}^{-1}$. With $\chi_{\text{TIP}} = 0.00085(1) \text{ cm}^3 \text{ K mol}^{-1}$ the agreement factor $R^2 = 0.988$. This corresponds well with values found for similar systems.^[212]

X-Band ESR spectra were recorded for **5** on powder samples at room temperature and at 77 K (Figure 2.11, right). They show a rather complex structure with several features, which are uncommon for copper complexes. The powder spectra of **5** show a sharp and strong perpendicular transition at $B = 3390 \text{ G}$ ($g = 2.063$) exhibiting a fine structure. The spectra show parallel transitions at around 2565 G, 2866 G and 3167 G. These might be attributed to the hyperfine interactions of the copper ions assuming an additional transition in the high field flank of the perpendicular transition. However, this assignment leads to a very large hyperfine splitting of approximately 300 G (840 MHz), which is much larger than expected.^[8] Also an additional signal at 3835 G is visible, with $g_{\text{eff}} = 1.82$ well outside the expected range for a copper(II) in a square pyramidal coordination environment.^[8] Lowering the temperature to 77 K results in a loss in intensity of the high field signal and a more complex structure on the low field side of the perpendicular transition. Additionally, the fine structure of the main signal is strongly enhanced.

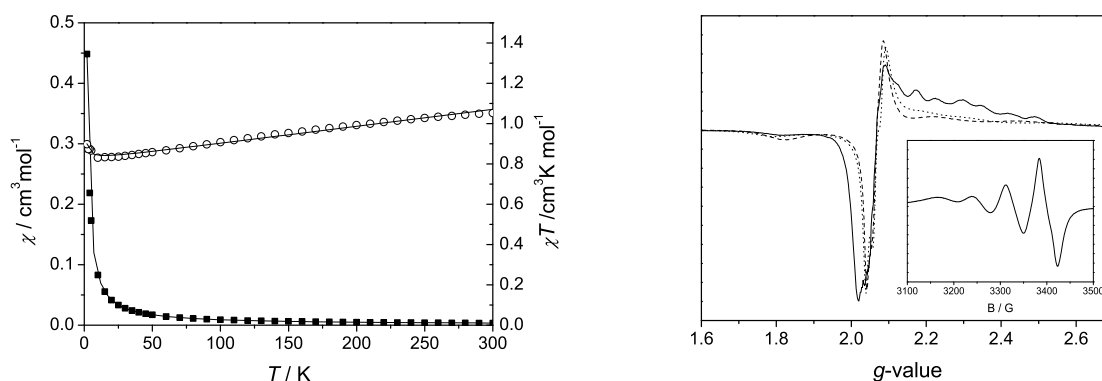


Figure 2.11: Left: Thermal dependence of the magnetic susceptibility χ_M (black squares) and $\chi_M T$ (empty circles) for $[\text{Cu}(\text{hfac})(\text{TPA})]_2$ (**5**), solid lines: simulated behavior using the values mentioned in the text. Right: X-Band ESR spectra measured on powder samples of $[\text{Cu}(\text{hfac})(\text{TPA})]_2$ (**5**) at room temperature (dashed line) and at 77 K (dotted line) as well as at 77 K in frozen solution in chloroform (solid line). The inset shows the averaged hyper fine splitting measured on a solution of **5** at room temperature in chloroform.

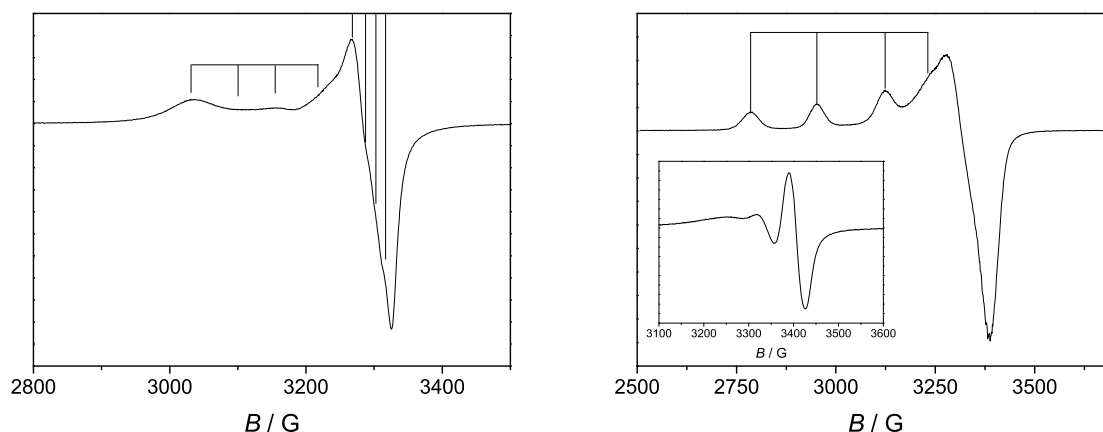


Figure 2.12: X-Band ESR spectra measured on powder samples of $[\text{Cu}(\text{}^t\text{BuTPA})_2]$ (**6**) at 77 K (left) as well as at 77 K in frozen solution in chloroform (right). The inset shows the averaged hyperfine splitting measured on a solution of **6** at room temperature in chloroform. The vertical lines represent the hyperfine splitting as discussed in the text.

The spectrum recorded at room temperature on a chloroform solution of **5** shows a signal at $g_{\text{av}} = 2.122$, which is split into four lines with $A_{\text{av}} = 71$ G. The spectrum recorded on a frozen chloroform solution of **5** at 77 K reveals a very complex hyperfine structure in the same region as the powder spectrum. Several features of the experimental spectrum can be reproduced by simulations using the following parameters: $g = [2.06, 2.08, 2.26]$, $A_{\parallel} = 525$ MHz and $J_{\text{CuCu}} = 150$ MHz. This leads to $g_{\text{av}} = 2.13$, which is in good agreement with the values observed in solution. The splitting in the hyperfine pattern in the frozen solution spectrum is caused by the very weak interactions between the two copper ions. In fact, the similarity between the powder and the frozen solution spectrum and the presence of a half-field transition prove, that the dimer stays intact upon dissolution.

For compound **6** X-Band ESR spectra were recorded on powder samples and in solution (dichloromethylen and acetone) at room temperature as well as in frozen solution at 77 K (Figure 2.12). The powder spectra at both temperatures are very similar and show a strong perpendicular transition at $g_{\perp} = 2.068$ with a hyperfine splitting $A_{\perp} \approx 23$ G and a series of four parallel transitions at $g_{\parallel} = 2.172$ with a hyperfine splitting of $A_{\parallel} \approx 110$ G. The distribution of intensity is remarkable, since the signal at lowest field is the strongest whereas the other signals are much less pronounced.

The obvious change in the spectrum upon dissolution indicates major structural changes. These might be ligand–metal dissociation, additional coordination of solvent molecules or structural rearrangements in the coordination sphere. For example, if the tilting angle between the planes spanned by the donor atoms of each ligand with the central copper atom changes it can have major impacts on the ESR spectrum as it is shown in Section 2.2. However, the well resolved hyperfine lines indicate the presence of one well-defined species in solution. The corresponding spectrum at room temperature leads to an intermediate g -value of 2.13 and an averaged hyperfine splitting of 67 G. The frozen solution spectrum gives $g = [2.048, 2.048, 2.235]$ with a hyperfine splitting of $A_{\parallel} = 190$ G. This leads to $g_{\text{av}} = 2.125$, which is in very good agreement with the parameters observed in solution at room temperature.

2.2 Magnetic Anomaly in Dinuclear Copper Complexes

2.2.1 Synthesis and Structure

The synthesis and structure of $[\text{Cu}_4(\text{L}2^{\text{t}B\text{usal}})_2(\text{hfac})_2(\text{MeOH})_2] \cdot 5\text{CHCl}_3 \cdot 3\text{MeOH}$ (**Cu4**) have been reported elsewhere.^[213] A short summary of the structural features relevant for the magnetic discussion is presented in the following paragraphs.

Bridging ligands based on substituted 1,3-diaminobenzene have been shown to build up metallacycles of the general formula $[\text{Cu}_2(\text{L})_2]$ when reacted with copper salts.^[213] Several of these complexes show an anomaly in the temperature dependence of the magnetic susceptibility measured on powder samples using standard procedures (applied fields of 1000 – 5000 Oe, equilibration times of a few minutes at every temperature step). The unexpected behavior is investigated in detail on a sample of **Cu4**. The molecular structure is depicted in Figure 2.13 on the left side. On the right side a simplified picture is shown, clarifying the two different copper sites in the molecule. While the central copper ions, forming the metallacycle, are tetra-coordinated in a distorted

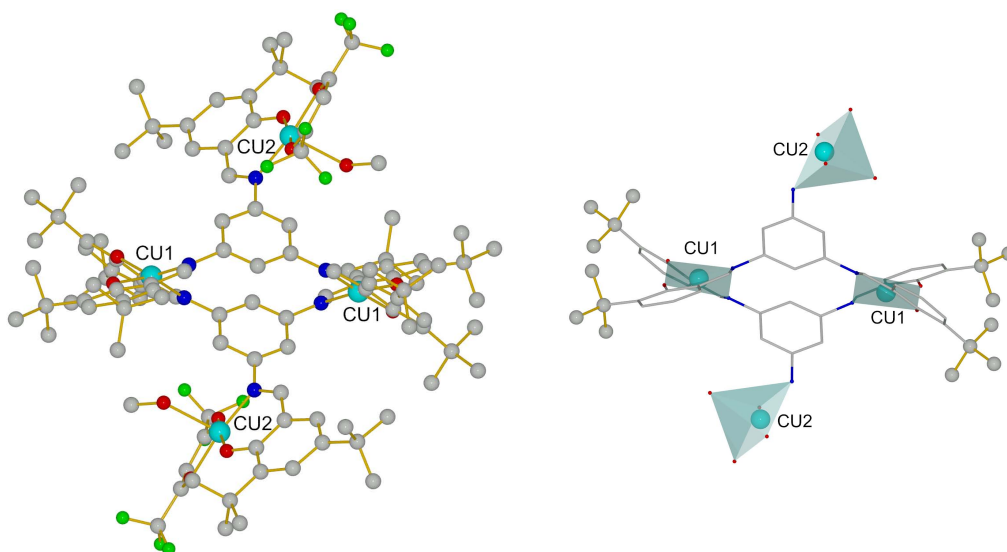


Figure 2.13: Left: Molecular structure of the tetranuclear complex **Cu4**. The central copper ions forming the metallacycle are denoted as Cu1, the outer copper ions Cu2. Right: Simplified picture showing only the connected copper polyhedra. The bridging carbon atoms are depicted as wires, the *tert*-butyl groups in ortho position to the hydroxy group as balls and sticks. All hydrogen atoms have been omitted for clarity.

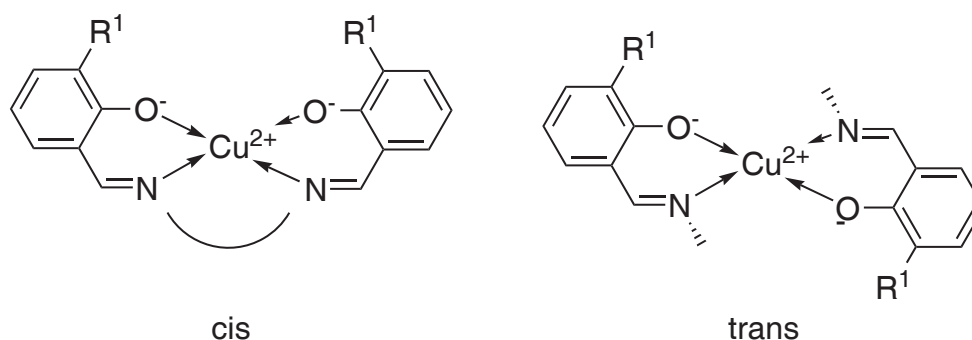


Figure 2.14: *cis* (left) and *trans* (right) coordination mode around the tetra-coordinated copper center. The metallacycle, indicated by the bent line, enforces the *cis* coordination, even in the case of sterically demanding R¹ substituents.

polyhedron, the outer copper ions are in a typical quadratic pyramidal conformation with the axial position held by a methanol oxygen atom. The crystals contain rather large amounts of chloroform molecules, which are strongly disordered. Firstly this affects the quality of the obtained crystal structures, secondly it excludes most single crystal experiments, since the crystals decay very fast when taken out of the stock solution.

Since the anomaly has been found also in dinuclear copper complexes, in which the outer copper centers are missing, the effect is related to the coordination mode of the copper ions forming the metallacycle. As mentioned above, they are tetra-coordinated. Two possible coordination modes are depicted schematically in Figure 2.14. Due to the rigid metallacycle linking the two binding pockets, a *cis* coordination is enforced, even in the case of a sterically demanding substituent R¹. In the case of non-cyclic ligands the *trans*-coordination minimizes the steric repulsion. An example for the latter case is complex **6**, which was discussed in Section 2.1. The coordination polyhedra can be described as an intermediate between square planar and tetrahedral.

2.2.2 Magnetic Properties

A plot of $\chi_M T = f(T)$ is depicted in Figure 2.15. Upon cooling $\chi_M T$ decreases due to temperature independent magnetism. Below 50 K $\chi_M T$ shows an advancing increase. Upon reheating $\chi_M T$ decreases and follows the behavior of the cooling curve up to 50 K. There it increases strongly, reaching a maximum at 120 K with a shoulder at 75 K. After

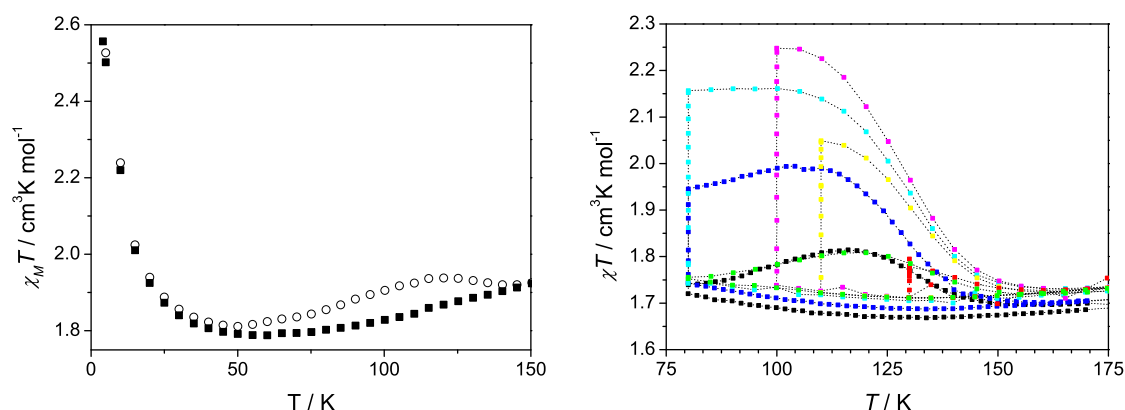


Figure 2.15: Left: Thermal dependency of $\chi_M T$ measured on powdered samples of **Cu4** using standard procedures. The black filled boxes represent the values obtained upon cooling, whereas the open circles were recorded during heating. Right: Plot of $\chi_M T = f(T)$ measured on powder samples of **Cu4** according to the procedure described in the text.

the maximum it decreases sharply reaching the cooling curve at 150 K and showing the same magnetic moments up to room temperature.

The increase at low temperature can be explained by ferromagnetic interactions between the copper ions. Sign and magnitude are both expected from the structure.^[213] The *meta*-bridged aromatic spacer gives rise to weak ferromagnetic interactions via the spin-polarization mechanism (Section 4.1). But this offers no explanation for the anomaly observed between 50 and 150 K.

The nature of this phenomenon was investigated using isothermal time dependent determination of $\chi_M T$ at 80, 100, 110 and 130 K. The sample has been cooled down to the corresponding temperature according to the standard procedure (temperature equilibration times of a few minutes) and then kept at this temperature for two hours. During this time the magnetic moment was determined every 10 minutes. After two hours the sample was warmed up to 175 K and cooled down to the subsequent temperature. The measured $\chi_M T$ values are depicted in Figure 2.15 on the right side, while the left side of Figure 2.16 depicts the temporal development of $\chi_M T$. During the isothermal measurements $\chi_M T$ increases monotonously with time. It shows a saturation behavior with sigmoidal shape, which can be seen very nicely in the data recorded at 130 K.

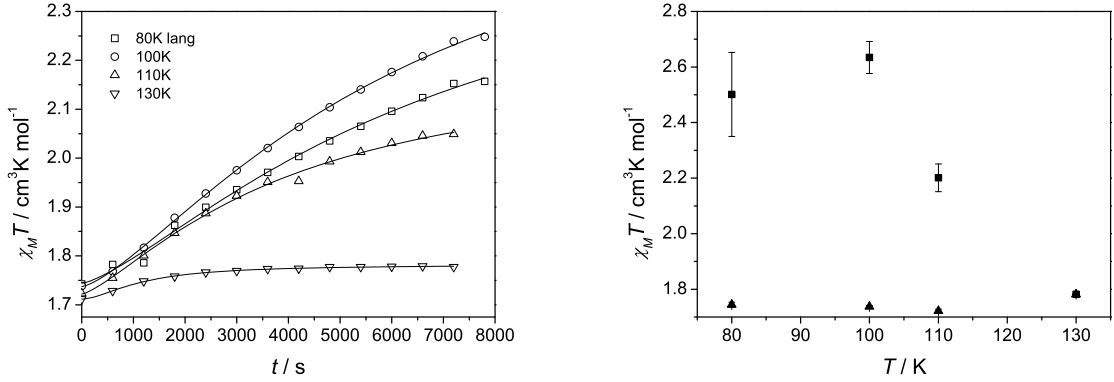


Figure 2.16: Left: Time dependence of $\chi_M T$ at 80 K (open boxes), 100 K (open circles), 110 K (open triangle) and 130 K (open diamond). The solid lines represent the simulated behavior with the parameters listed in Table 2.3 assuming logistic growth. Right: Plot of value A (filled triangles) and B (filled boxes) at 80, 100, 110 and 130 K as obtained as limit values $t \rightarrow 0$ and $t \rightarrow \infty$, respectively, of the fit of a logistic function to the time dependence of the isothermal magnetic measurements.

The difference between cooling and heating curve can therefore be attributed to a non-equilibrated system due to insufficient equilibrium time in the measurement procedure. Caused by the very long equilibrium times, it was not always possible to reach the saturation limit. To estimate these values, a logistic growth was assumed to reproduce the experimental data. The logistic growth equation reads

$$\chi_M T(t) = B + \frac{A - B}{1 + \left(\frac{t}{t_0}\right)^p} \quad (2.2)$$

where A denotes the limit for $t \rightarrow 0$ and B the limit for $t \rightarrow \infty$. t_0 and p affect the curvature of the growth function. The experimental behavior can be reproduced nicely using the parameters given in Table 2.3. The equilibrium values of $\chi_M T$ can be estimated as the limit $t \rightarrow \infty$ of the logistic curve and are depicted together with the starting values ($t \rightarrow 0$) in Figure 2.16 on the right side. While the starting values remain constant at $1.7 \text{ cm}^3 \text{K mol}^{-1}$ the values for $t \rightarrow \infty$ increase around 100 K and stay constant around $2.6 \text{ cm}^3 \text{K mol}^{-1}$ at lower temperatures.

For further insights into the electronic structures at the copper centers, the change in the magnetic susceptibility can be related to a change in the g -values. Assuming only spin magnetism of four independent copper ions, the g -value can be calculated according to

$$g = \sqrt{\frac{\chi_M T}{4} \cdot \frac{3k}{N_A \mu_B} \cdot \frac{1}{S(S+1)}} \quad (2.3)$$

2.2 Magnetic Anomaly in Dinuclear Copper Complexes

Table 2.3: Best fit parameters to reproduce the time dependency of $\chi_M T$ at 80, 100, 110 and 130 K assuming logistic growth: $\chi_M T(t) = B + (A - B)/(1 + (t/t_0)^p)$.

| T [K] | A [cm ³ K mol ⁻¹] | B [cm ³ K mol ⁻¹] | t_0 [s] | p | R^2 |
|---------|--|--|------------|---------|---------|
| 80 | 1.744(9) | 2.5(15) | 7000(1900) | 1.4(2) | 0.99479 |
| 100 | 1.737(4) | 2.63(6) | 6200(600) | 1.39(6) | 0.99935 |
| 110 | 1.722(7) | 2.20(5) | 4000(600) | 1.3(14) | 0.99587 |
| 130 | 1.7117(9) | 1.7820(9) | 1180(30) | 1.71(8) | 0.99826 |

Since the anomaly has been observed in dinuclear compounds as well, one can further assume that the g -value at the outer two copper ions remains constant. Even if there should occur changes in the coordination environment, only small changes are expected. Therefore the change from $\chi_M T \approx 1.73$ cm³K mol⁻¹ at high temperatures to $\chi_M T \approx 2.63$ cm³K mol⁻¹ at low temperatures can be expressed by an increase of the intermediate g -value from $g_{\text{high}} = 2.15$ cm³K mol⁻¹ to $g_{\text{low}} = 2.65$ cm³K mol⁻¹. The difference Δg can be related to the change $\Delta g_{\text{central}}$ at each central copper ion via

$$g_{\text{low}} = \frac{2g_{\text{outer}} + 2g_{\text{central}} + 2\Delta g_{\text{central}}}{4} \quad (2.4)$$

$$g_{\text{high}} = \frac{2g_{\text{outer}} + 2g_{\text{central}}}{4} \quad (2.5)$$

$$\Delta g = g_{\text{low}} - g_{\text{high}} = \frac{1}{2}\Delta g_{\text{central}} \quad (2.6)$$

Therefore a $\Delta g = 0.5$ gives rise to a change $\Delta g_{\text{central}}$ of approximately 1 at each copper ion. The increase of $\chi_M T$ can be attributed to an increase of the g -value of approximately 50%. It should be noted that the low temperature g -values for copper deviate strongly from the free electron value (2.0023) thus indicating the presence of rather strong orbital contributions.

The time needed for the transformation depends strongly on the preparation procedure and lengthens upon aging. The rather long timescale (hours to days) indicates structural changes as origin of the effect, whereas the change in the timescale suggests that they might be connected to a change of short-range ordering or packing effects in the powder or be related to domain growing and annihilation processes.

2.2.3 ESR Spectroscopy

X-band spectra of **Cu4** were recorded on powder samples and on frozen solutions at different temperatures between 50 and 150 K. They show only small deviation upon lowering the temperature. This might be due to unresolved g -components or due to insufficient equilibration times.

To exploit the better resolution of g -values, W-band spectra were recorded on powder samples of **Cu4**. The first spectrum was recorded at room temperature on a well equilibrated sample and is depicted in Figure 2.17 on the left side. It consists of a series of signals with a strong component at $g_x = 2.050$, a central signal at $g_y = 2.123$ and another component at $g_z = 2.160$, all indicated in the spectrum. However, the assignment is somewhat uncertain, since the spectrum shows a series of additional signals. The large separations of around 250 G exclude hyperfine interactions as origin of the splitting. They might be either due to different spin states possessing different g -values or to zero field splitting of the ground quintet.

The most striking effect upon lowering the temperature down to 10 K is an additional signal at $g_{\text{new}} = 2.253$ (Figure 2.17), which is not present in the starting spectrum. Also the g_x - and g_y -components shift towards higher g values $g_{x'} = 2.058$ and $g_{y'} = 2.156$. The spectrum does not change up to 110 K (Figure 2.18, left). When heated up to room temperature, the signal at $g = 2.253$ vanishes, however, the spectrum is not the same

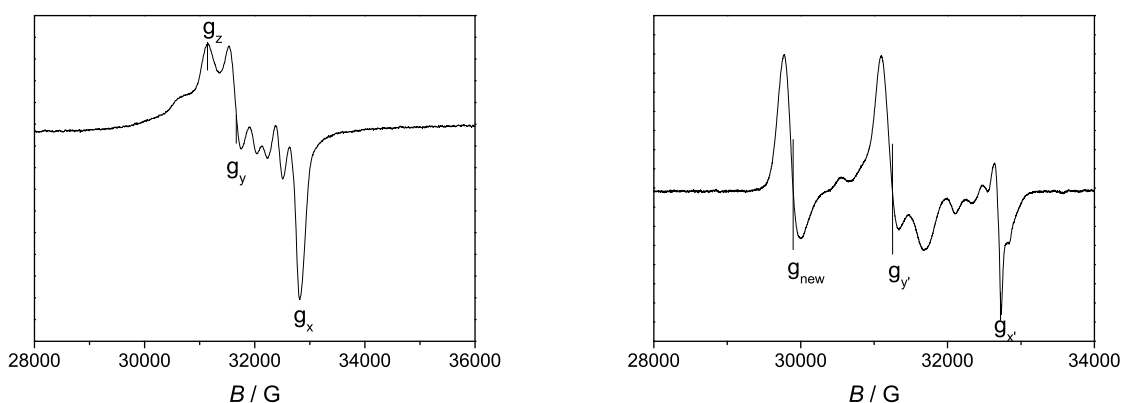


Figure 2.17: W-band ESR spectrum measured on a well equilibrated powder sample of **Cu4** at room temperature (left) and after cooling to 10 K (right). The vertical lines represent the g -components as mentioned in the text.

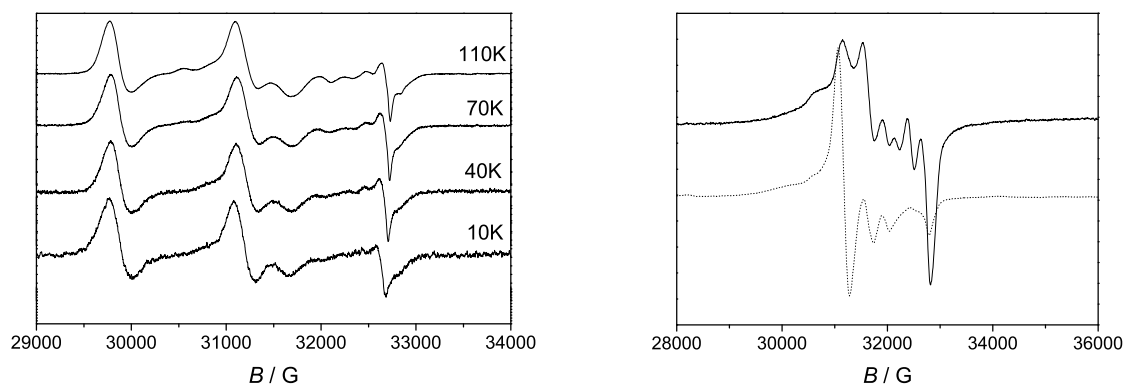


Figure 2.18: Left: Comparison of W-band ESR spectra measured while heating from 10 to 110 K on a powder sample of **Cu4**. Right: Comparison of the W-band ESR spectrum obtained before (solid line) and after the cooling/heating-cycle (dotted line).

as the well equilibrated one (Figure 2.18, right). From this spectrum one would assign $g_y = 2.158$ and g_z to the broad signal around $g = 2.195$. However, the fact that the relative intensity of the signals does not correspond with the well-equilibrated one, illustrates once more, that the conversion time is rather long.

Another explanation might be orientation of the microcrystals in the powder. Rising orbital contribution causing an increase of the magnetic moment leads to a much stronger anisotropy and therefore to much stronger forces acting on the crystallites. Thus the differences in the intensities might be caused by a not-random distribution of the molecules in the sample, like it is found for the high symmetric trinuclear copper complex in Section 4.1. Nevertheless, since the signal at $g = 2.253$ appears well outside the range of the room temperature spectrum it cannot be caused by orientational effects. It is obvious from these measurements that there is a structural change taking place at the copper center, leading to a strong increase of the g -value. The change is not as large as deduced from the susceptibility measurements, but it should be noted that there might be additional z -components which are broadened too much by the hyperfine interactions of the copper centers to be resolved.

2.2.4 Theoretical Considerations

The magnetic susceptibility measurements on **Cu4** as well as the ESR spectra indicate a structural change around the coordination sphere of the copper ion. In many re-

ported systems, the copper is either penta- or hexa-coordinated, leading to structures which can be described as distortions of an octahedral environment. Very common structure schemes are axially elongated octahedra and quadratic pyramids. The symmetry dependence of the energy scheme of the d -orbitals is depicted in Figure 2.19. The Jahn-Teller-distortions lift the degeneracy of the d -orbitals and quench the orbital contributions hence leading to g -values which are rather close to the free electron value ($2.05 < g < 2.3$). Even in the case of an undistorted octahedron, the unpaired electron would occupy an e_g -orbital with quenched orbital momentum. However, in the case of the tetracoordinated systems we are dealing with, the coordination is an intermediate between square planar (which might be seen as an octahedra with infinite axial elongation) and a tetrahedron. In a tetrahedron the sequence of orbitals is reversed, the unpaired electron occupies a t_{2g} -orbital and experiences a rather strong orbital momentum. Since the structures determined by X-ray crystallography are intermediates between these two extrema, their energy scheme is expected to be rather complex and crossing points between orbital energies might cause strong effects upon slight distortions.

The impact of tetragonal, rhombic and trigonal distortions on the energy scheme has been evaluated in detail by Hoffmann and Goslar by ligand field arguments.^[204] Taking into account the rigidity of the salicylidene binding environment and the strong preorganization caused by the metallacycle only few degrees of freedom exist. The most probable one is the torsion angle between the two salicylidene units upon rotation around the intersection line of the two planes. This is best represented by the rhombic distortions discussed by Hoffmann and Goslar^[204]. They discuss the effects on the basis of d -orbitals requiring a rotation of the axis to yield the appropriate final energy schemes and make use of constant terms for the ratio between B_2 and B_4 . For an easier adjustment of the future optical measurements and to clarify the contributions in the intersections an analysis on the basis of m_l -functions seems preferable.

To explain the effects via ligand field arguments, the central atom is described by an electron spin $S = \frac{1}{2}$ and an angular momentum of $L = 2$. Two donor atoms and the central atom form a plane each. They correspond to the angle, which is formed by the two N–Cu–O planes in the complex molecule **Cu4**. The dependence of the ligand

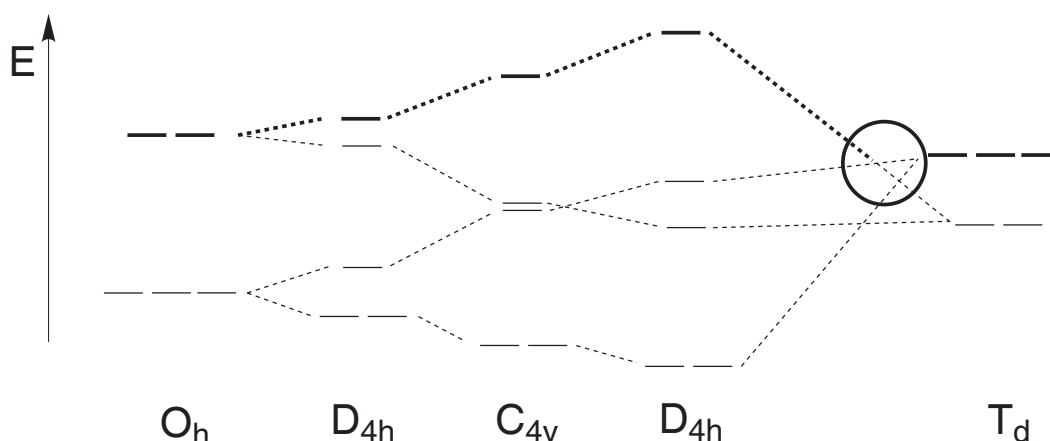


Figure 2.19: Symmetry dependence of the splitting in the d -orbitals. The energy scheme is depicted for a perfect octahedron O_h , an axially distorted octahedron (D_{4h}), quadratic pyramidal (C_{4v}), quadratic planar (D_{4h}) and tetrahedral (T_d). The bold lines depicts the magnetic orbital carrying the unpaired electron in d^9 , the bold circle indicates the intermediate structures, in which orbital crossings occur.

field parameters on the tilting angle α between these two planes is calculated using the point charge model. The relevant parameters are chosen due to symmetry considerations and are summarized in Table 2.4 together with the point group of the system.

The tilting angle α varies between zero in the case of square planar environment and $\frac{\pi}{2}$ in the case of a tetrahedron. In polar coordinates the ligand field parameters can be expressed depending on the polar angles θ and ϕ . By the choice of the coordinate system ϕ can be held constant ($\phi = \frac{\pi}{4}$), while θ can be expressed depending on α using algebraic transformations. One obtains

Table 2.4: Geometry, point group and relevant ligand field parameters for the limiting structures and the transition structures.

| geometry | point group | ligand field parameters |
|-----------------------|-------------|-------------------------|
| tetrahedron | T_D | B_4^0 |
| quadratic planar | D_{4h} | B_2^0, B_4^0, B_4^4 |
| transition structures | D_{2d} | B_2^0, B_4^0, B_4^4 |

$$\theta = \arctan\left(\frac{1}{\tan\frac{\alpha}{2}\cos\phi}\right) \quad (2.7)$$

This gives $\theta = 90^\circ$ for $\alpha = 0^\circ$ und $\theta = \arccos(\frac{1}{\sqrt{3}})$ as expected for the limiting structures. The Racah-tensors are expressed as

$$C_0^2 = \frac{1}{2} \left(3 \cos^2 \left[\arctan\left(\frac{1}{\tan\frac{\alpha}{2}\cos\phi}\right) \right] - 1 \right) \quad (2.8)$$

$$C_0^4 = \frac{1}{8} \left(35 \cos^4 \left[\arctan\left(\frac{1}{\tan\frac{\alpha}{2}\cos\phi}\right) \right] \right) + \frac{1}{8} \left(-30 \cos^2 \left[\arctan\left(\frac{1}{\tan\frac{\alpha}{2}\cos\phi}\right) \right] + 3 \right) \quad (2.9)$$

$$(C_4^4 + C_{-4}^4) = \sqrt{\frac{35}{128}} \left(\sin^4 \left[\arctan\left(\frac{1}{\tan\frac{\alpha}{2}\cos\phi}\right) \right] \cdot 2 \cos(4\phi) \right) \quad (2.10)$$

With $\phi = (\frac{1}{4} + n)\pi$ and $\cos 4\phi = \cos 4(\frac{1}{4} + n)\pi = -1$ the last term reads

$$(C_4^4 + C_{-4}^4) = -\sqrt{\frac{35}{32}} \sin^4 \left[\arctan\left(\frac{1}{\tan\frac{\alpha}{2}\cos\phi}\right) \right] \quad (2.11)$$

For $\alpha = 90^\circ$ (ideal tetrahedron) C_0^2 vanishes and the relation C_0^4 to C_4^4 becomes $\sqrt{5/14}$ as it is expected. With $k = \langle r^2 \rangle R^2 / \langle r^4 \rangle$ and $F = \langle r^4 \rangle \frac{Qe^2}{R^5}$ the ligand field parameters are calculated according to

$$\begin{aligned} B_0^2 &= \langle r^2 \rangle \frac{Qe^2}{R^3} \sum_{i=1}^4 C_0^2(\theta_i \phi_i) \\ &= k \cdot \langle r^4 \rangle \frac{Qe^2}{R^5} \sum_{i=1}^4 C_0^2(\theta_i \phi_i) \\ &= k \cdot F \cdot \sum_{i=1}^4 C_0^2(\theta_i \phi_i) \end{aligned} \quad (2.12)$$

$$\begin{aligned} B_0^4 &= \langle r^4 \rangle \frac{Qe^2}{R^5} \sum_{i=1}^4 C_0^4(\theta_i \phi_i) \\ &= F \cdot \sum_{i=1}^4 C_0^4(\theta_i \phi_i) \end{aligned} \quad (2.13)$$

$$\begin{aligned}
 B_4^4 &= \langle r^4 \rangle \frac{Qe^2}{R^5} \sum_{i=1}^4 \left(C_4^4(\theta_i \phi_i) + C_{-4}^4(\theta_i \phi_i) \right) \\
 &= F \cdot \sum_{i=1}^4 \left(C_4^4(\theta_i \phi_i) + C_{-4}^4(\theta_i \phi_i) \right)
 \end{aligned} \tag{2.14}$$

With this relations it is possible to express the energy scheme as function of the tilting angle α and the ratio k . The prefactor F contains only constant entities like the charge number Q , the electron charge e , the average $\langle r^4 \rangle$ and the radius R , which is assumed to remain constant upon the deformation. The actual size affects all ligand field parameters equally and can be neglected in the discussion of the principal properties as long as only linear terms occur. To obtain the energies the Hamiltonian

$$\hat{H} = B_0^2 C_0^2 + B_0^4 C_0^4 + B_4^4 \left(C_4^4 + C_{-4}^4 \right) \tag{2.15}$$

is applied onto the basis $|m_s m_l \rangle$ with $m_s = \pm \frac{1}{2}$ and $m_l = 0, \pm 1, \pm 2$. Diagonalization of the corresponding interaction matrix

| | | | | | |
|---------------|--|---|--|---|--|
| | $ 2 \rangle$ | $ 1 \rangle$ | $ 0 \rangle$ | $ -1 \rangle$ | $ -2 \rangle$ |
| $ 2 \rangle$ | $\frac{1}{21} B_0^4 - \frac{2}{7} B_0^2$ | | | | $\frac{\sqrt{70}}{21} B_4^4$ |
| $ 1 \rangle$ | | $-\frac{4}{21} B_0^4 + \frac{1}{7} B_0^2$ | | | |
| $ 0 \rangle$ | | | $\frac{6}{21} B_0^4 + \frac{2}{7} B_0^2$ | | |
| $ -1 \rangle$ | | | | $-\frac{4}{21} B_0^4 + \frac{1}{7} B_0^2$ | |
| $ -2 \rangle$ | $\frac{\sqrt{70}}{21} B_4^4$ | | | | $\frac{1}{21} B_0^4 - \frac{2}{7} B_0^2$ |

leads to the eigenvectors and eigenvalues^[6]

| $ \Psi \rangle$ | Energy |
|--|--|
| $\Psi_5 = \sqrt{\frac{1}{2}} (2 \rangle + -2 \rangle)$ | $-\frac{2}{7} B_0^2 + \frac{1}{21} B_0^4 + \frac{\sqrt{70}}{21} B_4^4$ |
| $\Psi_4 = \sqrt{\frac{1}{2}} (2 \rangle - -2 \rangle)$ | $-\frac{2}{7} B_0^2 + \frac{1}{21} B_0^4 - \frac{\sqrt{70}}{21} B_4^4$ |
| $\Psi_{2,3} = 1 \rangle, -1 \rangle$ | $\frac{1}{7} B_0^2 - \frac{4}{21} B_0^4$ |
| $\Psi_1 = 0 \rangle$ | $\frac{2}{7} B_0^2 + \frac{6}{21} B_0^4$ |

From these equations the energy dependence on the angle α is calculated for $k = 0.5, 0.75, 1$ and 2 . The results are depicted in Figure 2.20. For $k < 0.5$ only the shape and

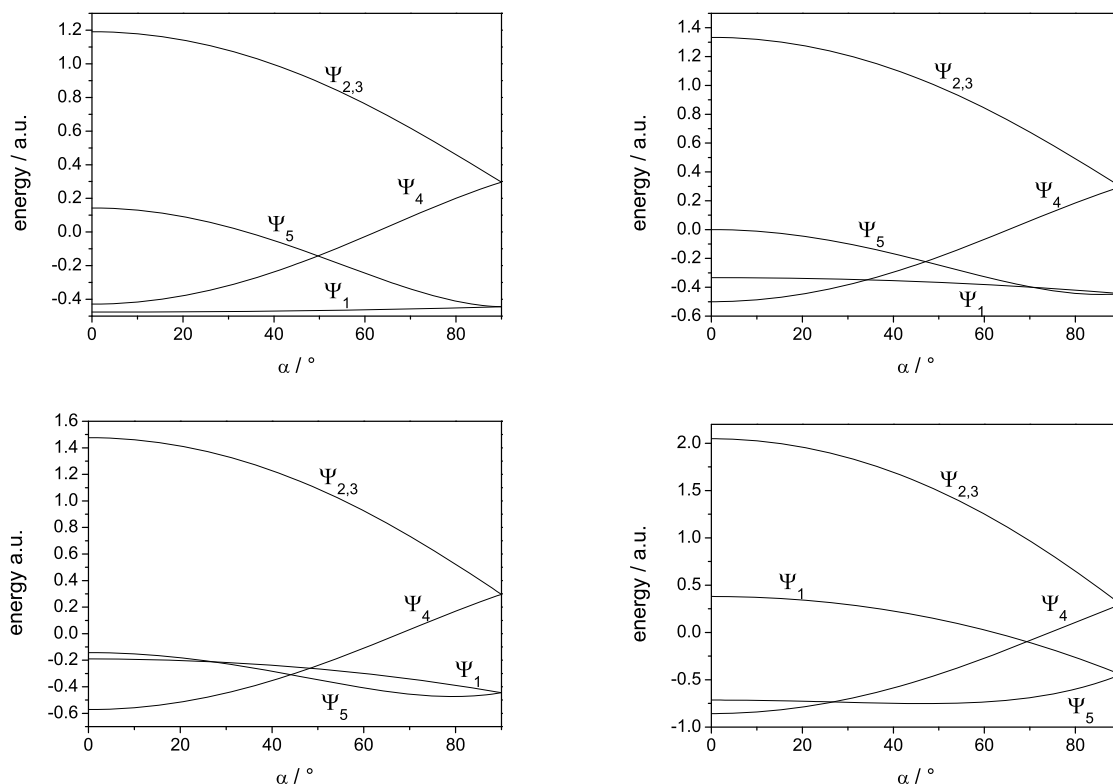


Figure 2.20: Dependence of the energy pattern on the torsion angle α for $k = 0.5$ (top left), 0.75 (top right), 1 (bottom left) and 2 (bottom right).

the expansion of the energy pattern changes, whereas values greater than 2 shift the crossing point between Ψ_4 and Ψ_5 to smaller angles until no crossing occurs and Ψ_5 stays the lowest energy over all torsion angles.

This rather simple model shows clearly, that if k is around 0.5–2, there are a lot of crossing points for α being in the region of 40–60°. Consequently one would expect the system to react very sensitive upon structural changes in this region. It should be mentioned that the results from Hoffmann and Goslar are obtained with fixed values for the radial integrals giving rise to $k = 1.47$ and hence are well within the results of this derivation.

2.3 Outlook

The combination of magnetic properties of copper(II) with the redox behavior of triphenylamines shows several points of contact for further research:

1. The stability of the formed aminium radical ion should be enhanced by substitutions on the phenyl rings. These might prevent further degradation either by steric shielding or by electronically stabilizing the positive charge.
2. Substitutions on the aromatic groups may also introduce anchoring groups to link the obtained complexes with other building blocks. Free ethynylene groups can be coupled to conductive polymers and would allow a direct interactions of the spin with the conducting electrons.
3. The replacement of the hfac^- coligand by an appropriate acceptor molecule allows the construction of donor-acceptor dyads in one molecule. They might show interesting non-linear optic responses, which might be influenced by the magnetic coupling to the central copper ion. Via this mechanism the optical response may be switched by an external magnetic field.

Furthermore it is possible to introduce amino groups on each of the three phenyl-rings.^[214] Nitration of triphenylamine with copper nitrate in acetic acid and acetic acid anhydride gives rise to the formation of 4,4',4''-Trinitrotriphenylamin (7). This can be reduced with elemental hydrogen to give the corresponding 4,4',4''-triaminotriphenylamine (8). In principle ligands derived from this core structure should be able to build up cyclophanes.^[197;215-217] They consist of two threefold rigid bridging ligands, which are connected by coordinated metal atoms in a parallel sandwich-like structure. Several of these molecules based on triaminobenzene have been reported.^[213] A cyclophane built from triphenylamines might stabilize the oxidized aminium radical via electron exchange between the closely arranged two triphenylamines.

The anomaly in the dinuclear copper metallacycles shows how putatively uninteresting metal ions become highly interesting when put in a non-convenient coordination environment. Up to now the following requirements can be formulated in order to obtain compounds showing the desired effect:

1. They possess two or more binding pockets. Two of them are needed to build up the metallacycle, but additional ones can be present in the molecule.
2. Each binding pocket offers two donor atoms each: for example a phenolate oxygen and an imine nitrogen in Schiff-base compounds.
3. The two binding pockets are linked by a rigid aromatic spacer.
4. They possess bulky substituents close to the coordination environment of the copper ion, for example in *ortho*-position to the hydroxy group in systems based on salicylidenes.

Preliminary heat capacity measurements performed by Miguel Castro from Centro Politecnico Superior in Zaragoza confirm the presence of a second order transition in the expected temperature range. As expected, it is strongly depending on the heating/cooling rate and depends furthermore upon the time given to equilibrate at low temperatures. Time and temperature depending X-ray powder diffraction studies should give additional insights into the structural changes. Investigations of the powdered samples according to the nature of the surface, size of crystallites, density and similar physical properties are needed to explain the aging effects and the broad variation of timescales found in different samples. Detailed UV/Vis studies on powder samples at low temperatures will reveal the electronic structure of the copper ion.^[205;218] Especially the maximum *d-d*-transitions have been reported to be very sensitive to structural distortions and show a linear dependence on the dihedral angle.^[206;219-221] This method also gives good access to the magnitude of the ligand field parameters. Additional inclusion of spin-orbit coupling might be necessary to describe systems with rather large orbital contributions.^[209] Finally the mechanism responsible for the structural transition needs to be identified. One possible explanation might be the freezing of rotation of the *tert*-butyl groups.^[222-229]

3 New Building Blocks

During the last years a lot of effort has been spent on the development of new magnetic materials. Especially the combination of magnetic with other properties, for example luminescence, promises new materials which may open up new fields of applications.^[230–235] On the one hand, metal ions with unpaired electrons are good carriers for the magnetic moments because of their rather large momentum assembled in a *d*- or *f*-shell, the stability of the *open shell*-compounds and the possibility to tune the properties via the choice of the metal ion and the design of the coordination sphere.

On the other hand, the optical properties can be tuned in a very distinctive way in organic compounds. The influence of various substituents on the absorbance and emission characteristics of chromophores is a well established part of organic chemistry. A vast number of chromophores is known and most have been characterized extensively regarding the nature of transitions and their other optical properties. Since a characteristic transition in carbazoles is the $n-\pi^*$ -transition, the excited state has considerable radical character, especially in photoelectron dyades.^[236] It is therefore advantageous to combine magnetic ions with photoactive ligands.

Carbazoles are well known building blocks in organic photo- and electrochemistry.^[34;237;238] Aryl substituted carbazoles constitute a subclass of triphenylamines, which have been extensively studied. The design of organic light emitting diodes,^[31–35] photo voltaic elements^[25–27] and other organic electronic devices^[30;237;239] are only three exemplary fields of interest. In addition, aryl substituted carbazoles have been studied due to their unusual fluorescence behavior, which is discussed in the terms of twisted intramolecular charge transfer (TICT)^[240–243] or other mechanisms.^[244]

The first part of this chapter deals with the synthesis and characterization of ligands based on aryl substituted carbazoles. The ligands offer two binding pockets and lead to the formation of metalla cycles. Copper(II) is probably the best understood spin

carrier,^[7;8] which makes the evaluation of the performed measurements easy. Furthermore zinc(II) ions are known to give very similar complexes in many cases. They can therefore act as a kind of reference without magnetic interactions. Using these two metal ions a distinction between the influence of an open and a close *d*-shell is possible. In addition the influence of substitution patterns is investigated. Introducing *tert*-butyl groups in the ligand gives copper complexes, which exhibit the anomaly in the temperature dependence of the magnetic susceptibility as discussed in Section 2.2.

In contrast, metal complexes based on Salen-type ligands are already well-known and have attracted considerable interest. This is due to their smooth formation, the predictable coordination geometry^[245–247] and the possible use of these complexes either as highly active catalysts^[248–270] or as building blocks for the construction of larger supramolecular assemblies.^[160;161;168;212;271–277] The last field has also led to the introduction of additional binding groups in the 3-position to form an *outer* cavity, which can coordinate additional metal ions.^[278–280] For example, a great variety of heteronuclear metal complexes are known with the so called Mesalen ligand, which carries a methoxy functionality in the 3-position.^[281–289] These ligands have been successfully applied to construct heterodinuclear fragments, for example copper-lanthanide complexes, whose properties have been extensively studied. The linkage of these complexes into one-dimensional structures gives access to interesting compounds which may be used as Single Chain Magnets (SCMs). Structures with 2,4-dicarboxy-pyrimidine have been reported^[156] and their magnetic properties are discussed in detail in Section 4.2.

A crucial point in all these applications is the solubility of the formed complexes. For many applications a system soluble in polar and/or protic environment is desirable.^[290–292;292;293] The second part of this chapter therefore deals with the synthesis and characterization of the sulfonato substituted^[294] derivative *Sulf*Mesalen and the structures of some corresponding transition metal complexes. The outer coordination cavity is not only capable of coordinating metal ions with their O₄ donor set, but is a rather good hydrogen bond acceptor environment as well. The size of the outer cavity is very well suited for protonated primary amines and the negative charge introduced by the sulfonato groups favors the interactions with the positive ammonium group. The use of diamines leads to an aggregation via hydrogen bonds, a very promising

structural scheme for the design of functional materials.^[263;272;295–297] The coordination of sulfonates known from other examples^[233;297–301] promises interesting schemes in the resulting solid state structures.

The introduction of sulfonato groups into a known ligand scaffold plays also an important role in the last section of this chapter, namely the synthesis of the sulfonated triaminoguanidine ligand $\text{Na}_2\text{H}_6^{\text{Sulf}}\text{TAG}$. Metal complexes based on triaminoguanidines are very promising candidates for qubit storage.^[302] The antiferromagnetic coupling leads to a doubly degenerated $S = \frac{1}{2}$ ground state, which should work as a decoherence free subsystem and suppress several sources of decoherence.^[119] In this context, several systems have been reported and characterized regarding the nature of their coupling interactions.^[18;19;63;120–124;126;138–143;213;303–309] Among these, the triaminoguanidine based ligands exhibit the most promising features. The coupling between the metal centers is strong, which leads to a very good thermal isolation of the computational active ground state. The rigidity of the system strongly reduces its possibility to lift the degeneracy by structural deformations and furthermore the planarity due to the π -backbone supports the C_3 -symmetry of the system.

The copper complexes of the unsubstituted ligand are known to give three-dimensional networks by linking of the trinuclear monomers,^[144;145] and the exchange interactions inside the trinuclear units are the dominating ones even in these extended structures. It was shown, that trinuclear complexes can be obtained, if the polymerization is prevented by the use of appropriate capping ligands.^[308] However, X-ray diffraction revealed the complex molecules to be stacked very closely. In addition to an extended spectroscopic and magnetic characterization of the unsubstituted trinuclear compound, the third section of this chapter deals with the synthesis and characterization of copper complexes on the basis of a sulfonato-substituted triaminoguanidine ligand. The introduction of additional charge in combination with the use of bulky counter-ions should lead to a better isolation of the molecules in the solid state. Also the preparation and characterization of polymer films containing these complex molecules is discussed here. Inclusion into the polymer matrix offers a promising way to materials for applications.

3.1 Carbazole Containing Complexes

3.1.1 Ligand Synthesis

The amino precursor *N*-(4-methoxyphenyl)-3,6-diaminocarbazole **9** was synthesized by a variation of the synthesis described by Chen et al.^[310]. After Ullmann-type coupling of carbazole with *para*-bromoanisole the amino function is introduced via nitration and subsequent reduction with elemental hydrogen. Reaction with two equivalents of salicylaldehyde derivatives in methanol gives the ligand H₂CarbOMe (**10**) in the case of unsubstituted salicyl aldehyde, H₂^{*t*Bu}CarbOMe (**13**) with 3,5-Di-*tert*-butyl-2-hydroxy-benzaldehyde and H₂^{*Sulf*}CarbOMe (**15**) using sodium 5-sulfonato-2-hydroxy-benzaldehyde as is depicted in Figure 3.1.

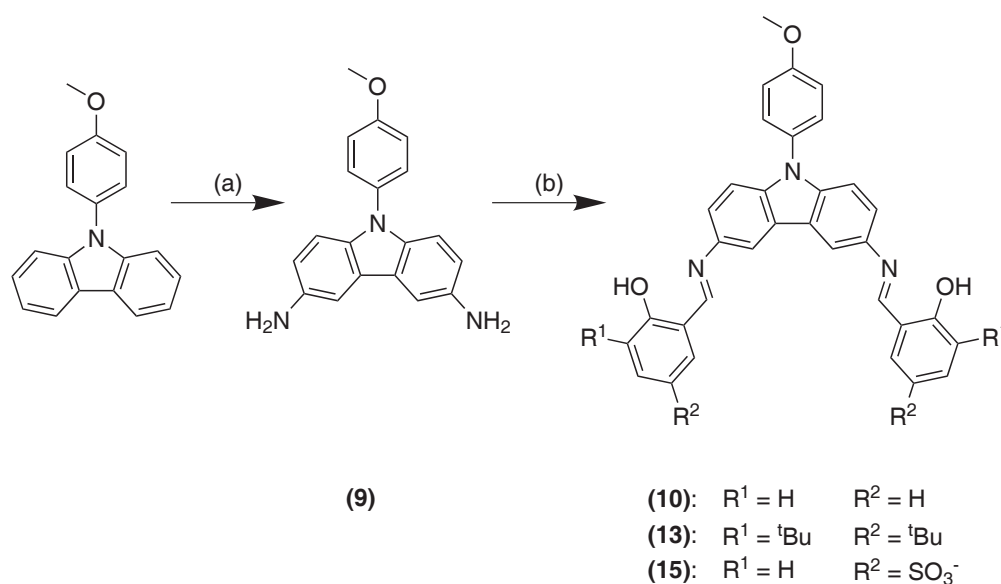


Figure 3.1: Preparation scheme for the ligand H₂CarbOMe (**10**) and its derivatives **13** and **15**; (a): Cu(NO₃)₂, AcOH, (Ac)₂O; H₂ 55 bar, *Raney* nickel, AcOEt 80°, 4h; (b): substituted salicylaldehyde, MeOH, reflux, 10min

3.1.2 Complexes with Unsubstituted Ligand

Structure

H₂CarbOMe (**10**) reacts readily with copper(II) acetate or zinc(II) acetate in 1:1 methanol/chloroform to form metallacycles of the stoichiometry [Cu₂(CarbOMe)₂] (**11**) or [Zn₂(CarbOMe)₂] (**12**), respectively. The structures of the obtained complexes were determined by X-ray crystallography. Both complexes show similar structural features, although the supramolecular structures differ. For example the copper compound contains more solvent molecules which are strongly disordered and lead to a rather rough structure description. In the case of the zinc compound the contents of solvents is much smaller and therefore the structure description is much more accurate. Because of the small differences in the molecular structure only the zinc compound is depicted in Figure 3.2.

Both complexes crystallize in the $P\bar{1}$ space group. The asymmetric unit contains two independent metal–ligand fragments, which give rise to two complex molecules due to the inversion center. The unit cell therefore contains two molecules, which differ slightly in their bond lengths and angles. However, these differences are rather small ($\Delta l < 3$ pm, $\Delta\alpha < 3^\circ$) and therefore, only one complex is discussed. Selected bond lengths and angles are summarized in Tables 3.1 and 3.2. Since the two metal centers inside one molecule are symmetry related, their coordination environment is exactly the

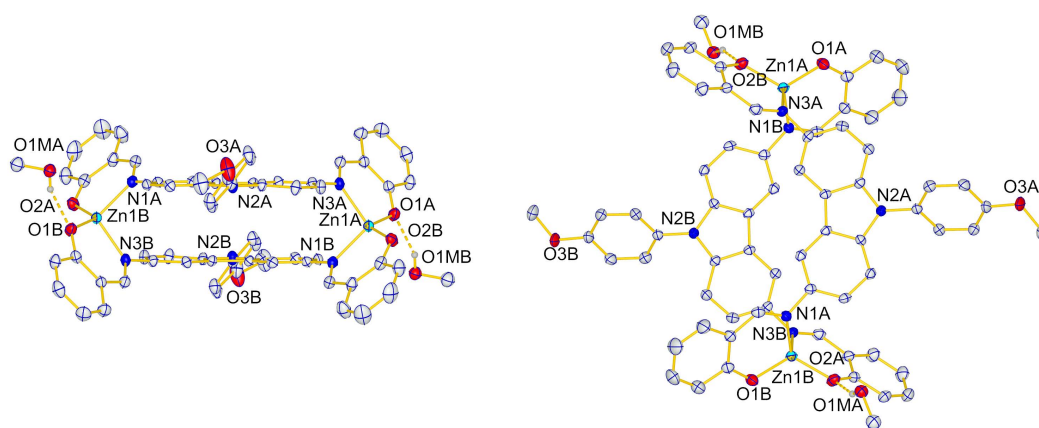


Figure 3.2: Left: Molecular structure of one of the two molecules in the unit cell of [Zn₂(CarbOMe)₂]·MeOH·CHCl₃ (**12**) with numbering scheme for all hetero atoms as seen from the side (left) and from the top (right), carbon bonded hydrogen atoms are omitted for clarity.

Table 3.1: Selected bond lengths in pm for $[\text{Zn}_2(\text{CarbOMe})_2]$ (**12**) and $[\text{Cu}_2(\text{CarbOMe})_2]$ (**11**)

| bond lengths (pm) for 12 | | bond lengths (pm) for 11 | |
|---------------------------------|----------|---------------------------------|----------|
| Zn1A–O1A | 189.2(2) | Cu1A–O2A | 189.1(6) |
| Zn1A–O2A | 190.6(2) | Cu1A–O1A | 189.9(7) |
| Zn1A–O1A | 200.4(2) | Cu1A–O1A | 194.3(7) |
| Zn1A–N3A | 201.1(3) | Cu1A–N3A | 194.3(8) |
| Zn1B–O1B | 188.1(2) | Cu1B–O1B | 188.4(6) |
| Zn1B–O2B | 189.8(2) | Cu1B–O2B | 189.1(5) |
| Zn1B–N1B | 201.5(2) | Cu1B–N1B | 194.5(7) |
| Zn1B–N3B | 201.7(3) | Cu1B–N3B | 194.7(8) |

same. They are tetracoordinated by an N_2O_2 donor set formed by one binding pocket of each ligand molecule. By filling both binding pockets the metallacycle is formed with the carbazoles coplanar at a distance of 310 pm for the zinc compound and 320 pm for the copper compound. The salicylidene unit is twisted against the carbazole plane to allow the phenolate oxygen to coordinate in a tetrahedral fashion. The zinc–zinc as well as the copper–copper distances are 1070 pm. However, there are some distinct differences due to the electronic structure of the metal centers.

The presence of Jahn-Teller-distortions in the case of the d^9 copper system leads to stronger deviation from the ideal tetrahedral coordination than it is found in the case of the d^{10} zinc system. The twisting of the salicylidene unit against the carbazole moiety is larger ($\theta_{\text{Cu}} = 47^\circ$ versus $\theta_{\text{Zn}} = 39^\circ$) and the tetrahedron is stronger distorted towards a square planar coordination. The angles between the planes spanned by O1A–M1A–N1A and O2B–M1A–N3B deviate much more from 90° expected for a tetrahedron ($\theta_{\text{Cu}} = 50^\circ$ versus $\theta_{\text{Zn}} = 78^\circ$). The same holds true for the angles between the O1A–M1A–O2B-plane (M = Cu, Zn) and the N1A–M1A–N3B-plane ($\theta_{\text{Cu}} = 50^\circ$ versus $\theta_{\text{Zn}} = 73^\circ$). As a consequence, the plane spanned by the atoms N1A, N1B, N3A, N3B, M1A and M1B is nearly orthogonal to the carbazoles in the zinc compound ($\theta_{\text{Zn}} = 83^\circ$), while it is more canted in the copper compound ($\theta_{\text{Cu}} = 74^\circ$). This effect is most probably responsible for the different supramolecular structures (*vide infra*) and the different contents of solvent molecules in the crystal structure. In general the overall structures are very similar and agree well to unsubstituted compounds reported by Paital et al. [312]

Table 3.2: Selected bond angles in ° for $[\text{Zn}_2(\text{CarbOMe})_2]$ (**12**) and $[\text{Cu}_2(\text{CarbOMe})_2]$ (**11**)

| bond angles (°) for 12 | | bond angles (°) for 11 | |
|-------------------------------|------------|-------------------------------|----------|
| O2A–Zn1A–O1A | 119.41(9) | O2A–Cu1A–O1A | 96.9(3) |
| O2A–Zn1A–N1A | 122.72(9) | O2A–Cu1A–N1A | 144.7(3) |
| O1A–Zn1A–N1A | 97.59(9) | O1A–Cu1A–N1A | 94.8(3) |
| O2A–Zn1A–N3A | 96.71(9) | O2A–Cu1A–N3A | 94.5(3) |
| O1A–Zn1A–N3A | 119.73(10) | O1A–Cu1A–N3A | 142.3(3) |
| N1A–Zn1A–N3A | 100.77(10) | N1A–Cu1A–N3A | 96.3(3) |
| O1B–Zn1B–O2B | 122.44(10) | O1B–Cu1B–O2B | 92.5(3) |
| O1B–Zn1B–N1B | 97.60(10) | O1B–Cu1B–N1B | 94.2(3) |
| O2B–Zn1B–N1B | 120.49(10) | O2B–Cu1B–N1B | 145.9(3) |
| O1B–Zn1B–N3B | 121.21(11) | O1B–Cu1B–N3B | 148.4(3) |
| O2B–Zn1B–N3B | 97.01(10) | O2B–Cu1B–N3B | 93.8(3) |
| N1B–Zn1B–N3B | 96.69(10) | N1B–Cu1B–N3B | 97.6(3) |

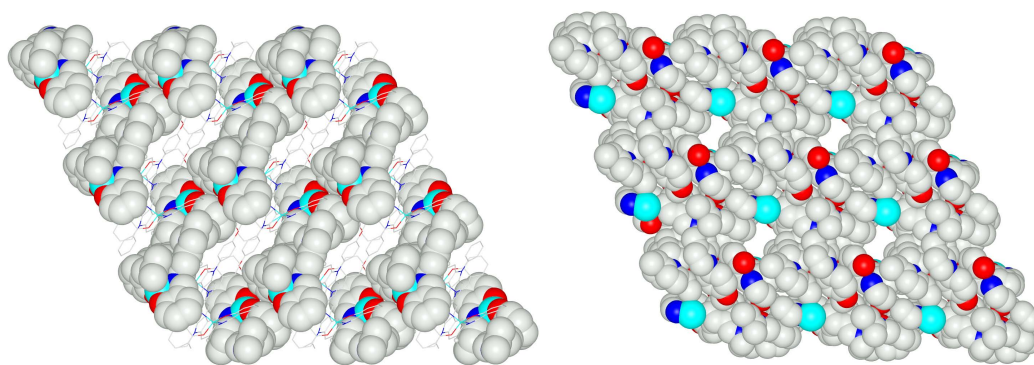


Figure 3.3: Left: Superstructure of $[\text{Zn}_2(\text{CarbOMe})_2]$ (**12**) as viewed along the c -axis. Hydrogen atoms and solvent molecules are omitted for clarity. One of the two molecules in each unit cell is depicted as wires, the other in the space filling model. Right: Superstructure of $[\text{Cu}_2(\text{CarbOMe})_2]$ (**11**) as viewed along the a -axis in the space filling model. Hydrogen atoms and solvent molecules are omitted for clarity.

Table 3.3: Summary of the metric parameters for the hydrogen bonds found in the crystal structures of $[\text{Zn}_2(\text{CarbOMe})_2] \cdot 2(\text{CHCl}_3) \cdot 2\text{MeOH}$ (**12**)

| D–H···A | $d(\text{D–H})/\text{pm}$ | $d(\text{D} \cdots \text{H})/\text{pm}$ | $d(\text{D} \cdots \text{A})/\text{pm}$ | $\alpha(\text{D–H} \cdots \text{A})/^\circ$ |
|-------------------------------------|---------------------------|---|---|---|
| O1M–H···O1A | 84 | 197 | 276 | 157 |
| C_{CHCl_3} –H···O2B | 100 | 211 | 303 | 152 |

In the copper system there are two different orientations per axis. If one looks along one crystal axis the orientations build up layers each. The closest intermolecular copper–copper distance is 830 pm and hence shorter than the distance inside the metallacycle. Along the *a*-axis there exist channels of about 500 pm build up by four molecules (Figure 3.3, right). These channels are filled with disordered solvent molecules, i.e. with methanol, water and chloroform. Additional solvent molecules are located at other sites of the crystal lattice. Along the *c*-axis the molecules are packed due to π – π -interactions between one of the six-membered carbazole rings and the five-membered carbazole ring of an neighboring molecule.

In the zinc system, the intermolecular zinc–zinc distance is even shorter (700 pm). There is an extensive network build up by π – π -interactions between different salicylidene groups and between the salicylidene moieties and the methoxy substituted phenyl rings, which leads to the formation of layers spanned by the *c*-axis and the diagonal between the *a*- and *b*-axis (Figure 3.3, left). The chloroform and methanol molecules are located near the phenolate oxygens. The metric data (Table 3.3) for the corresponding Donor–H···Acceptor suggest the presence of hydrogen bonding interactions. One molecule in the unit cell binds two methanol molecules (depicted in Figure 3.2) while the other binds two chloroform molecules. The structure therefore can be thought of as a network of $[\text{Zn}_2(\text{CarbOMe})_2(\text{CHCl}_3)_2]$ and $[\text{Zn}_2(\text{CarbOMe})_2(\text{MeOH})_2]$ units. A similar partitioned structure scheme is found in the copper compound. However, the strong disorder of solvent molecules prevents a detailed analysis. But it should be noted, that in the actual refined structure, half of the molecules do not have any hydrogen bonded solvent molecules while the others are connected to several disordered chloroform and methanol molecules.

These differences in the superstructure of the copper and the zinc system are due to the differences in their coordination environment. In the copper system the tilting of the salicylidene residues is different and therefore the π – π -interactions are no

longer able to construct the dense framework found in the zinc structure. The resulting superstructure is not as compact, leaving room for disordered molecules and other types of structural disorder, thus explaining the rather rough structure description.

Electronic Properties

Absorbance spectra were recorded in THF solution for the amino precursor **9** and the ligand **10** and in dichloromethylene for the complexes **11** and **12** (Figure 3.4, left). The nature of the absorption bands was investigated using semi-empirical INDO/S calculations on DFT-optimized structures. A comparison of simulated and measured spectra is depicted in the Appendix (Figure A.7) and a list of the nature of orbitals near to the HOMO and LUMO are provided in Table 3.4. Fluorescence spectra were recorded by irradiating at the highest aromatic absorption wavelength and are depicted in Figure 3.4 on the right side. Excitation spectra were recorded to prove that all bands originate from the desired compounds.

It should be noted here, that all compounds show a loss of fluorescence intensity with time. This effect is seen as well in solid state fluorescence spectra of the amine precursor **9**. This is probably due to photo-degradation processes. It is known that carbazoles can be coupled electrochemically, when the corresponding aminium radical starts a radical polymerization upon oxidation.^[313] Since the longest wavelength absorption of the aromatic system has $n-\pi$ -character (*vide infra*), the excited state has considerable radical character. It is therefore probable that the degradation follows a similar pathway. However, the loss of intensity, which is especially fast in halogenated solvents, impedes a quantitative analysis of the fluorescence.

The amino spectrum consists mainly of four bands: the first one with a maximum at around 390 nm ($25\,640\text{ cm}^{-1}$) with $\log \epsilon = 3.6$, the second at around 320 nm ($31\,250\text{ cm}^{-1}$) with $\log \epsilon = 4.3$, the third at 287 nm ($34\,840\text{ cm}^{-1}$) with $\log \epsilon = 4.2$ and one below 250 nm ($> 40\,000\text{ cm}^{-1}$) with $\log \epsilon > 4.6$. Fluorescence spectra recorded in THF show a strong band at around 428 nm ($23\,360\text{ cm}^{-1}$) with a shoulder at 446 nm ($22\,420\text{ cm}^{-1}$). The bands are shifted by $2\,280\text{ cm}^{-1}$ and $3\,220\text{ cm}^{-1}$, respectively, compared to the absorption. The interpretation of the spectra is hindered by the fact, that there is an obvious color dependence on the solvent used for recrystallization. Using ethanol results in a

Table 3.4: Character of orbitals obtained by the semi-empirical INDO/S calculations for the amine precursor (**9**), the ligand H₂CarbOMe (**10**), the copper complex (**11**) and the zinc complex (**12**). Abbreviations used: carb: the carbazole moiety, phenyl: the methoxy substituted phenyl ring, sal: the salicylidene moiety, O⁻: the phenolate oxygens, C-N: the imino bond.

| Orbital | amine precursor 9 | CarbOMe 10 | copper complex 11 (α/β) | zinc complex 12 |
|---------|---------------------------|------------------------|---|------------------------|
| HOMO-7 | $n(\text{amine})$ | $\pi(\text{phenyl})$ | $\pi(\text{carb})/\pi(\text{carb})$ | $n(\text{O}^-)$ |
| HOMO-6 | $n(\text{carb})$ | $\pi(\text{sal})$ | $\pi(\text{carb})/\pi(\text{carb})$ | $n(\text{O}^-)$ |
| HOMO-5 | $\pi(\text{carb})$ | $\pi(\text{sal})$ | $\pi(\text{sal})/\pi(\text{sal})$ | $n(\text{O}^-)$ |
| HOMO-4 | $\pi(\text{phenyl})$ | $\pi(\text{sal})$ | $\pi(\text{sal})/\pi(\text{sal})$ | $n(\text{O}^-)$ |
| HOMO-3 | $\pi(\text{carb})$ | $\pi(\text{carb})$ | $\pi(\text{carb})/\pi(\text{carb})$ | $\pi(\text{carb})$ |
| HOMO-2 | $\pi(\text{phenyl})$ | $\pi(\text{phenyl})$ | $\pi(\text{carb})/\pi(\text{carb})$ | $\pi(\text{carb})$ |
| HOMO-1 | $\pi(\text{carb})$ | $\pi(\text{phenyl})$ | $\pi^*(\text{C-O})/\pi^*(\text{C-O})$ | $n(\text{carb})$ |
| HOMO | $n(\text{carb})$ | $n(\text{carb})$ | $\pi^*(\text{C-O})/\pi^*(\text{C-O})$ | $n(\text{carb})$ |
| LUMO | $\pi^*(\text{carb})$ | $\pi^*(\text{C-N})$ | $d(\text{Cu})/\pi^*(\text{C-N})$ | $\pi^*(\text{C-N})$ |
| LUMO+1 | $\pi^*(\text{phenyl})$ | $\pi^*(\text{C-N})$ | $d(\text{Cu})/\pi^*(\text{C-N})$ | $\pi^*(\text{C-N})$ |
| LUMO+2 | $\pi^*(\text{phenyl})$ | $\pi^*(\text{carb})$ | $d(\text{Cu})/\pi^*(\text{sal})$ | $\pi^*(\text{C-N})$ |
| LUMO+3 | $\pi^*(\text{carb})$ | $\pi^*(\text{phenyl})$ | $d(\text{Cu})/\pi^*(\text{sal})$ | $\pi^*(\text{C-N})$ |
| LUMO+4 | $\pi^*(\text{carb})$ | $\pi^*(\text{sal})$ | $\pi^*(\text{phenyl})/\pi^*(\text{carb})$ | $\pi^*(\text{carb})$ |
| LUMO+5 | $\pi^*(\text{carb})$ | $\pi^*(\text{sal})$ | $\pi^*(\text{phenyl})/\pi^*(\text{carb})$ | $\pi^*(\text{carb})$ |
| LUMO+6 | $\sigma^*(\text{phenyl})$ | $\pi^*(\text{phenyl})$ | $\pi^*(\text{carb})/\pi^*(\text{phenyl})$ | $\pi^*(\text{phenyl})$ |
| LUMO+7 | $\sigma^*(\text{carb})$ | $\pi^*(\text{carb})$ | $\pi^*(\text{carb})/\pi^*(\text{phenyl})$ | $\pi^*(\text{phenyl})$ |

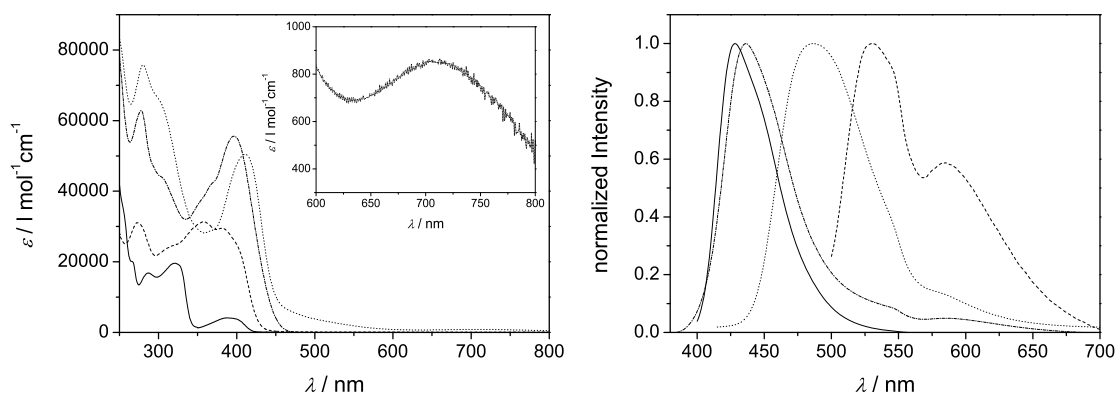


Figure 3.4: Left: Wavelength dependence of the extinction coefficient of the amine precursor in THF (solid line), the ligand H₂CarbOMe in THF (dashed line), [Cu₂(CarbOMe)₂] in dichloromethylene (dotted line) and [Zn₂(CarbOMe)₂] in dichloromethylen (dashed dotted line), inset: enlargement for [Cu₂(CarbOMe)₂] between 600 nm and 800 nm. Right: Fluorescence spectra for the amine precursor (solid line, $\lambda_{\text{ex}} = 388$ nm), the ligand H₂CarbOMe (dashed line, $\lambda_{\text{ex}} = 428$ nm), [Zn₂(CarbOMe)₂] (dotted line, $\lambda_{\text{ex}} = 375$ nm) and [Cu₂(CarbOMe)₂] (dash-dotted line, $\lambda_{\text{ex}} = 400$ nm), all measured in THF. The spectra are normalized to the maximum absorption of each compound.

weakly purple colored solid, while the use of toluene gives better yields of a dark purple solid. However, the NMR spectra show no differences. The 320 nm transition is calculated to be an $n-\pi^*$ transition from the lone pair of the central nitrogen into the aromatic backbone of the carbazole.

Upon Schiff-base condensation two new absorption bands at 271 nm ($36\,900\text{ cm}^{-1}$) with $\log \epsilon = 4.7$ and 358 nm ($27\,930\text{ cm}^{-1}$) with $\log \epsilon = 4.6$ arise, which can be attributed to transitions from the carbazole (backbone and nitrogen lone pair) into the π^* of the Schiff-base imino bond. The fluorescence band is shifted to 530 nm ($18\,870\text{ cm}^{-1}$) and contains a second band at 589 nm ($16\,980\text{ cm}^{-1}$) with Stokes-shifts of $6\,770$ and $10\,210\text{ cm}^{-1}$, respectively. These large values indicate major reorganization of the molecular structure after excitation. The intensity is strongly reduced, which is most probably due to new relaxation pathways along the salicylidene units.

While the band at 271 nm is only slightly shifted upon complexation — 278 nm ($35\,970\text{ cm}^{-1}$) for **12** with $\log \epsilon = 4.8$ versus 280 nm ($35\,710\text{ cm}^{-1}$) with $\log \epsilon = 4.9$ for **11** — the one at 358 nm is shifted to higher wavelengths by about 40 nm. It is located at 397 nm ($25\,190\text{ cm}^{-1}$) with $\log \epsilon = 4.7$ for **12** or 412 nm ($24\,270\text{ cm}^{-1}$) with $\log \epsilon = 4.7$ for **11**. The gain in intensity is easily explained by the fact, that the complex molecule contains two ligand molecules per unit. Compound **11** shows two additional broad absorption bands of low intensity: one at around 480 nm ($20\,830\text{ m}^{-1}$) with $\log \epsilon = 3.7$, which can be attributed to $n-\pi^*$ transitions from the lone pair at the nitrogen into antibonding orbitals at the carbon–nitrogen bond, and one at around 710 nm ($14\,080\text{ cm}^{-1}$) with $\log \epsilon = 2.9$, which can be attributed to $\pi^*-\pi^*$ transitions from the antibonding carbon–oxygen bond orbital into the antibonding orbitals at the carbon–nitrogen bond. The intensity of the last one scales linearly with the concentration, proving to be located on the molecule.

Compound **11** in THF shows a fluorescence maximum at around 436 nm ($22\,940\text{ cm}^{-1}$) with a Stokes-shift of $1\,330\text{ cm}^{-1}$, compound **12** shows a band at 486 nm ($20\,580\text{ cm}^{-1}$) with a Stokes-shift of $4\,610\text{ cm}^{-1}$. Additionally weak fluorescence bands at around 530 nm and 590 nm are observed, which probably belong to the free ligand, therefore indicating a partial dissociation in solution.

The formation of the complex was further investigated by UV/Vis titrations of the ligand with copper(II) and zinc(II) solutions. To a solution of the ligand $\text{H}_2\text{CarbOMe}$ in methanol/chloroform 1:1 ($c_{0,L} = 3.65 \cdot 10^{-5}\text{ mol/l}$ and $c_{0,L} = 3.08 \cdot 10^{-5}\text{ mol/l}$

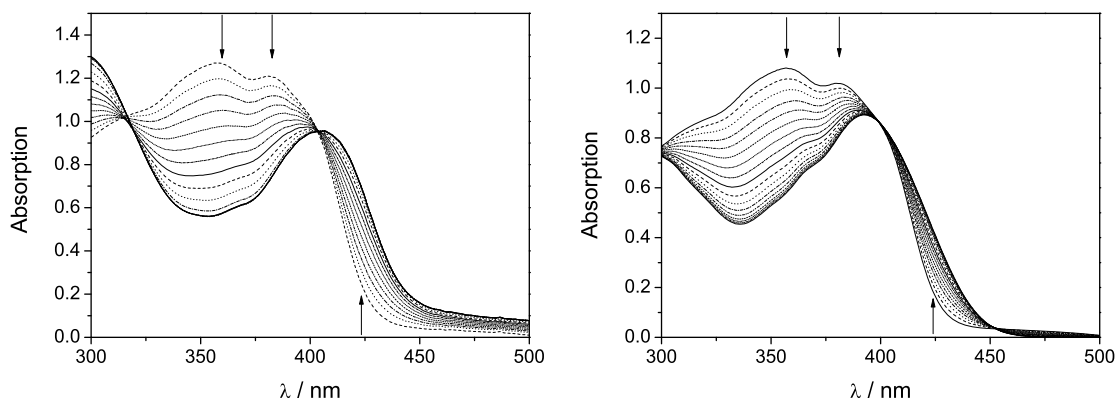
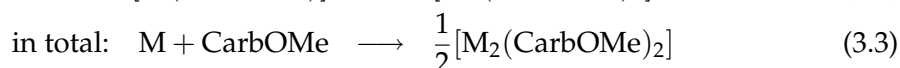
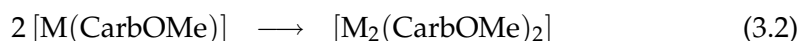


Figure 3.5: Change in the absorbance spectra of a solution of $\text{H}_2\text{CarbOMe}$ in 100 mL methanol:chloroform 1:1 upon stepwise addition of a copper(II)acetate solution (left, $c_{0,L} = 3.65 \cdot 10^{-5}$ mol/l, $c_{0,\text{Cu}} = 3.68 \cdot 10^{-3}$ mol/l, 99 μL per step, in total 1.5 equivalents) and upon addition of a zinc(II)acetate solution (right, $c_{0,L} = 3.08 \cdot 10^{-5}$ mol/l, $c_{0,\text{Zn}} = 3.62 \cdot 10^{-3}$ mol/l, 85 μL per step, in total 1.5 equivalents).

for copper and zinc, respectively) was added stepwise a solution of copper acetate ($c_{0,\text{Cu}} = 3.68 \cdot 10^{-3}$ mol/l, 99 μL per step) or zinc acetate ($c_{0,\text{Zn}} = 3.65 \cdot 10^{-3}$ mol/l, 99 μL per step) in the same solvent mixture. The spectra obtained are depicted in Figure 3.5. In both cases two absorbance bands around 358 and 380 nm decrease while the one of the corresponding metal complex increases giving rise to isosbestic points, at 404, 315, and below 300 nm for the copper compound and at 400 and 453 nm for the zinc compound. Their presence indicate a reaction of first rank. Hence there is a direct formation of the dinuclear metallacycle without a UV/Vis-detectable concentration of intermediates.

The spectra were analyzed using the program *SpecReg* (see Computational Details). Since a four component reaction is statistically improbable, the program only regards two compound reactions. In this framework, the formation of the metallacycle can be described by the following mechanism:



By fitting the equilibrium constants of these two reactions to the experimental spectra, one can obtain the equilibrium constant for the total reaction by

$$K_I = \frac{[M(\text{CarbOMe})]}{[M] \cdot [\text{CarbOMe}]} \quad (3.4)$$

$$K_{II} = \frac{[M_2(\text{CarbOMe})_2]}{([M(\text{CarbOMe})])^2} \quad (3.5)$$

$$[M(\text{CarbOMe})] = \sqrt{\frac{[M_2(\text{CarbOMe})_2]}{K_{II}}} \quad (3.6)$$

$$K_I = \frac{\sqrt{[M_2(\text{CarbOMe})_2]}}{\sqrt{K_{II}} \cdot [M] \cdot [\text{CarbOMe}]} \quad (3.7)$$

$$K_I \cdot \sqrt{K_{II}} = \frac{\sqrt{[M_2(\text{CarbOMe})_2]}}{[M] \cdot [\text{CarbOMe}]} \quad (3.8)$$

$$= K_{\text{ges}} \quad (3.9)$$

The best fit was obtained with $K_I = 1.14 \cdot 10^7$ 1/mol and $K_{II} = 9793$ 1/mol, giving $K_{\text{ges}} = 1.13 \cdot 10^9$ (1/mol)^{3/2}. Since only two species are visible in the spectra, a rather strong dependency between K_I and K_{II} is expected. This dependency can be shown by fixing one of the parameters and optimizing the other (Table 3.5). However, the values of K_{ges} remain constant. The large value shows that the copper complex has a good stability. Unfortunately, no convergence could be obtained in the case of the zinc compound.

Square-wave voltammetry of the amine precursor shows one oxidation process at around 0.69 V (Figure 3.6). It is irreversible, the offset of the reduction and oxidation peak suggesting further reactions. Measurements on the ligand and the complexes only exhib-

Table 3.5: Dependency between the two equilibrium constants K_I and K_{II} and value of the product $K_I \cdot \sqrt{K_{II}}$.

| K_I (fitted) | K_{II} (constant) | K_{ges} |
|--------------------|---------------------|-------------------|
| $2.391 \cdot 10^4$ | $1 \cdot 10^9$ | $7.56 \cdot 10^8$ |
| $7.949 \cdot 10^4$ | $1 \cdot 10^8$ | $7.95 \cdot 10^8$ |
| $3.071 \cdot 10^5$ | $1 \cdot 10^7$ | $9.71 \cdot 10^8$ |
| $1.335 \cdot 10^6$ | $1 \cdot 10^6$ | $1.34 \cdot 10^9$ |
| $3.818 \cdot 10^6$ | $1 \cdot 10^5$ | $2.21 \cdot 10^9$ |
| $1.164 \cdot 10^7$ | $1 \cdot 10^4$ | $1.16 \cdot 10^9$ |
| | mean: | $1.04 \cdot 10^9$ |

ited undefined oxidation processes at similar redox potentials. A possible explanation is the anodic coupling as described for carbazoles.^[314]

Magnetic Properties

The temperature dependence of the magnetic susceptibility of compound **11** was determined in the temperature range between 2 and 300 K. Plots of $\chi_M = f(T)$ and $\chi_M T = f(T)$ are depicted in Figure 3.7 on the left side. At high temperatures the value of $\chi_M T$ is $0.88 \text{ cm}^3 \text{K mol}^{-1}$ which corresponds well to the *spin only* value for two independent copper(II) ions ($0.75 \text{ cm}^3 \text{K mol}^{-1}$ for $g = 2$). At very low temperatures, the product decreases indicating antiferromagnetic interactions. Fitting the parameters of the Bleaney-Blowers equation^[211]

$$\chi_M T = \frac{N_A \mu_B^2}{3k_B} \left[1 + \frac{1}{3} \exp\left(\frac{-J_{\text{CuCu}}}{k_B T}\right) \right]^{-1} + \chi_{\text{TIP}} \quad (3.10)$$

to the measured data gives the best agreement with the following parameters: $g = 2.074(1)$ and $J_{\text{CuCu}} = -3.135(11) \text{ cm}^{-1}$. With $\chi_{\text{TIP}} = 0.000268(4) \text{ cm}^3 \text{K mol}^{-1}$ the agreement factor R^2 is 0.99972. This is in good accordance with values found for similar systems.^[312]

ESR spectra for **11** were recorded on powder samples at room temperature and 77 K as well as in frozen solution in chloroform at 77 K (Figure 3.7, right). It can be simulated using the rhombic g -values $[g_x, g_y, g_z] = [2.057, 2.125, 2.200]$ ($g_{\text{av}} = 2.127$), in agreement

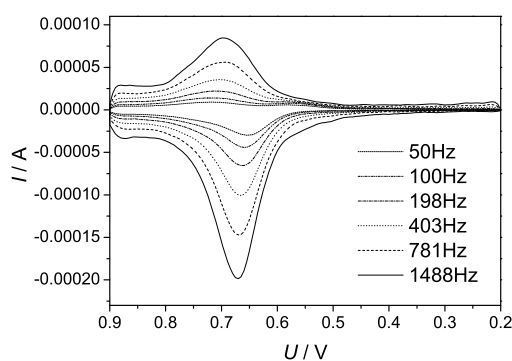


Figure 3.6: Square wave voltammogram of the amine precursor in acetonitrile.

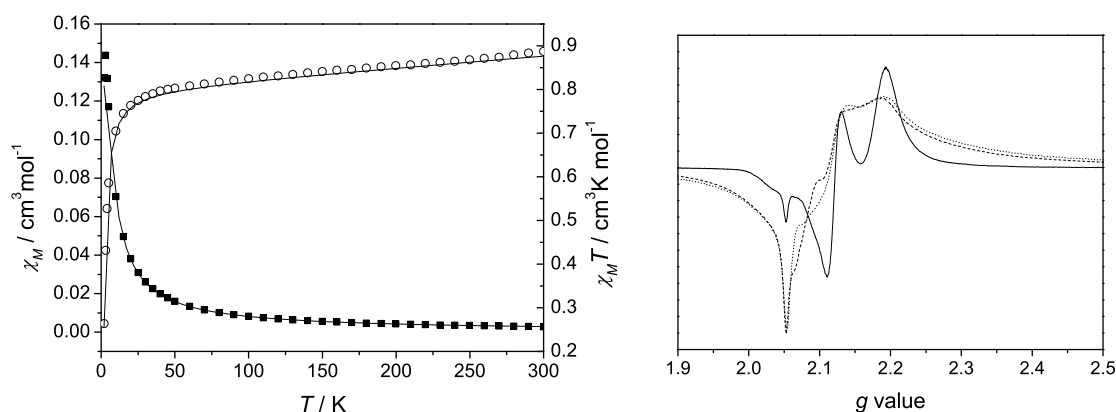


Figure 3.7: Left: Temperature dependence of the magnetic susceptibility χ_M (black squares) and the product $\chi_M T$ (open circles) of $[\text{Cu}_2(\text{CarbOMe})_2]$ (**11**) measured at an applied field of 2000 G. The solid lines represent best simulation (see text). Right: ESR spectra of $[\text{Cu}_2(\text{CarbOMe})_2]$ (**11**) recorded in a frozen solution in chloroform at 77 K (solid line) and on powder samples at 77 K (dotted line) and room temperature (dashed line).

with the measured susceptibilities. As it can be seen in Figure 3.7 the g_x -component is composed of two parts: a very sharp signal and a very broad one. This is in nice agreement with the crystal structure, if one assumes that the molecule without bonded solvent molecules (*vide supra*) gives rise to the sharp signal, whereas the disordered, hydrogen bonded solvents next to the other molecule cause the strong broadening, which mainly affects the direction along the copper-copper-axis, where the disordered molecules are located. Hence, the x -axis of the g -tensor is aligned along the copper-copper axis. Both the sharp and the broad signal are present in the frozen solution spectrum as well, although the sharp signal is less strong. This indicates the presence of an equilibrium in solution between bonded and non-bonded solvent molecules. The great excess of solvent favors the hydrogen bonding and hence causes the sharp signal to decrease, whereas the broad one gains intensity.

3.1.3 Complexes with Substituted Ligand

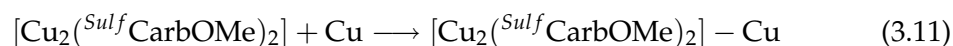
Synthesis and Spectroscopic Properties

To overcome the problems connected to the described loss of fluorescence (*vide supra*) two derivatives bearing *tert*-butyl ($\text{H}_2^{\text{tBu}}\text{CarbOMe}$, **13**) and sulfonato ($\text{H}_2^{\text{Sulf}}\text{CarbOMe}$,

15) groups were synthesized. The bulky *tert*-butyl groups might prevent the polymerization via steric repulsion, while the negatively charged sulfonates should increase the electrostatic repulsion. The *tert*-butyl group is also of great interest with respect to the magnetic anomaly discussed in Section 2.2, whereas the sulfonato group allows the incorporation of the metal complexes into polyvinylalcohol films (Section 3.3).

Since crystals suitable for X-ray crystallography were neither obtained from $[\text{Cu}_2(^{t\text{Bu}}\text{CarbOMe})_2]$ (**14**) nor from $[\text{Cu}_2(\text{SulfCarbOMe})_2]$ (**16**), the formation of the analogous structures in solution were proven by spectroscopy. Both ligands show a comparable change in the UV/Vis-absorption spectra upon addition of copper ions (Figure 3.8). Assuming the same mechanism as for **10** (Equation 3.1 to 3.9) for $^{t\text{Bu}}\text{CarbOMe}$, the best fit was obtained with the equilibrium constants $K_I = 2.39 \cdot 10^5$ l/mol and $K_{II} = 1.99 \cdot 10^5$ l/mol with a standard deviation of 0.0033, giving $K_{\text{ges}} = 1.06 \cdot 10^8$ (l/mol) $^{3/2}$. The different ratio $K_I:K_{II}$ when compared to **11** is probably due to the dependency between the two constants. However, the value for K_{ges} for the *tert*-butyl derivative is of the same magnitude as K_{ges} for the unsubstituted complex and due to the steric repulsion of the bulky substituents the complex is only slightly less stable.

In case of the sulfonate bearing ligand the absorption also changes after addition of one equivalent of copper. It is well known that sulfonate groups can coordinate metal ions (see also Section 3.2). It is therefore probable that after formation of the metallacycle the excess copper ions are coordinated by sulfonate oxygens. This coordination mode slightly decreases the electron density of the ligand and therefore shifts the absorption of the metallacycle as it is seen in the spectra at the band around 400 nm. This effect was accounted for by assuming the reaction



The corresponding equilibrium constant is defined by

$$K_{\text{add}} = \frac{[[\text{Cu}_2(\text{SulfCarbOMe})_2] - \text{Cu}]}{[[\text{Cu}_2(\text{SulfCarbOMe})_2]] \cdot [\text{Cu}]} \quad (3.12)$$

The best fit was obtained with $K_I = 4.46 \cdot 10^6$ l/mol and $K_{II} = 4210$ l/mol, giving $K_{\text{ges}} = 2.89 \cdot 10^8$ (l/mol) $^{3/2}$. With a formation constant for the adduct $K_{\text{add}} = 5.20 \cdot 10^5$ l/mol the standard deviation is 0.0023. Fluorescence spectra recorded on THF solution

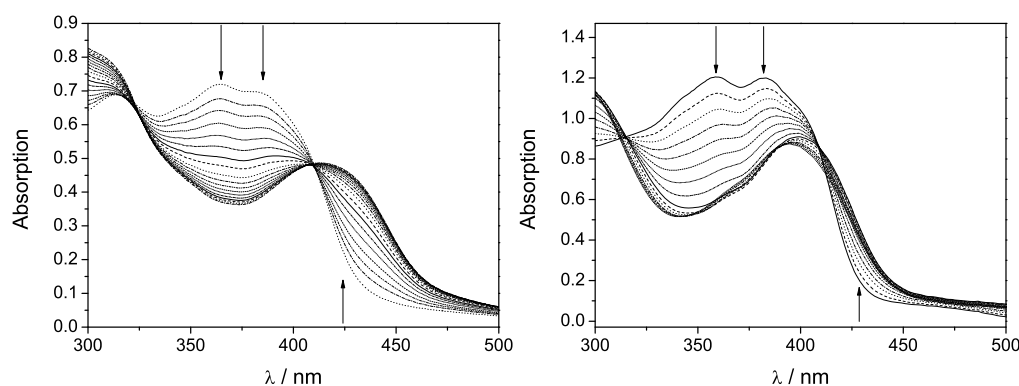


Figure 3.8: Change in the absorbance spectra of a solution of $\text{H}_2^{t\text{Bu}}\text{CarbOMe}$ in 100 mL methanol:chloroform 1:1 (left, $c_{0,\text{L}} = 2.15 \cdot 10^{-5}$ mol/l, $c_{0,\text{Cu}} = 2.35 \cdot 10^{-3}$ mol/l, $91\mu\text{L}$ per step, in total 1.5 equivalents) and SulfCarbOMe in 100 mL methanol (right) upon addition of a copper(II) acetate solution (right, $c_{0,\text{L}} = 3.94 \cdot 10^{-5}$ mol/l, $c_{0,\text{Cu}} = 3.56 \cdot 10^{-3}$ mol/l, $111\mu\text{L}$ per step, in total 1.5 equivalents).

for $\text{H}_2^{t\text{Bu}}\text{CarbOMe}$ and on methanol solution for $\text{H}_2^{\text{Sulf}}\text{CarbOMe}$ revealed a similar time dependency as found in the unsubstituted compound.

The presence of the complex $[\text{Cu}_2(\text{H}_2^{t\text{Bu}}\text{CarbOMe})_2]$ in the solid state was proved furthermore by IR spectroscopy, mass spectrometry, elemental analysis and magnetic investigations. The IR spectra are very similar to the free ligand $\text{H}_2^{t\text{Bu}}\text{CarbOMe}$, proving the presence of the ligand in the sample. The residual mass at $1000\text{ }^\circ\text{C}$ is 9.75% and therefore very close to the expected 9.97% for two remaining equivalents of copper(II) oxide per molecule. The elemental analysis is also in good agreement with the calculated values. The magnetic susceptibility shows cooperativity and proves the presence of at least two coupled copper ions while the anomaly between 50 and 150 K similar to that described in Section 2.2 indicates a distorted tetracoordinated copper(II) ion (*vide infra*). ESR spectroscopy reveals a hyperfine pattern consisting of seven lines, proving equal contributions of two copper nuclei.

Magnetic Properties

The temperature dependence of the magnetic susceptibility of compound **14** was determined in the temperature range between 2 and 250 K. Plots of $\chi_M = f(T)$ and $\chi_M T = f(T)$ are depicted in Figure 3.9 on the left side. At high temperatures the $\chi_M T$ shows a linear increase due to temperature independent paramagnetism. Upon

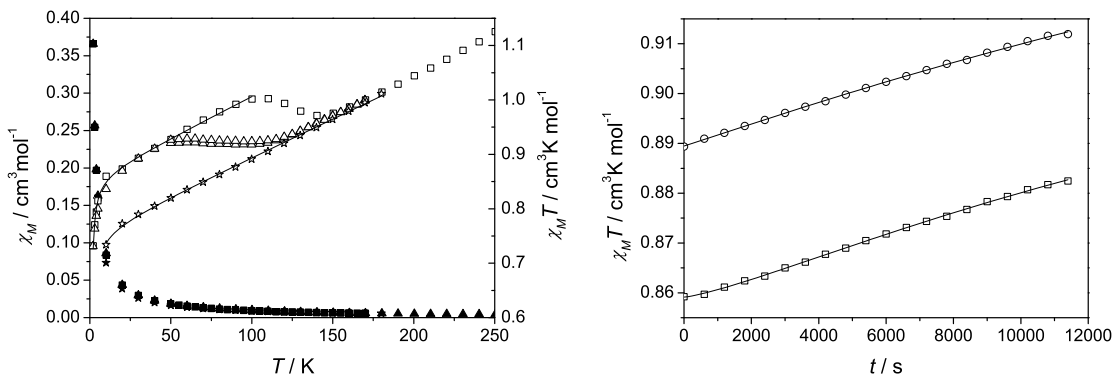


Figure 3.9: Left: Temperature dependence of the magnetic susceptibility χ_M (filled symbols) and the product $\chi_M T$ (open symbols) of $[\text{Cu}_2(\text{t}^{\text{Bu}}\text{CarbOMe})_2]$ (**14**) measured at an applied field of 2000 G. The data were recorded upon fast cooling (stars), upon slow cooling with one hour equilibration time at every temperature step (triangles, measured before and after the equilibration time) and upon heating after the slow cooling procedure (boxes). Right: Time dependence of $\chi_M T$ at 77 K (open boxes) and 100 K (open circles). The solid lines represent the simulated behavior with the parameters listed in Table 3.6 assuming logistic growth.

fast cooling the curve shows a decrease below 20 K indicating antiferromagnetic interactions. The behavior can be described by the Bleaney-Bowers equation^[211] (Equation 3.10) assuming the following parameters: $g = 2.007(3)$, $J_{\text{CuCu}} = -1.2(1) \text{ cm}^{-1}$ and $\chi_{\text{TIP}} = 0.00141(15) \text{ cm}^3 \text{ mol}^{-1}$ giving $R^2 = 0.99921$. In comparison to the unsubstituted compound **11** the g -value is quite low, however the coupling is weaker and χ_{TIP} much larger.

Rising the equilibration time at each temperature up to one hour has a major impact on the obtained magnetic susceptibility. Between 125 and 50 K the $\chi_M T$ -plot increases slightly upon lowering the temperature. As it can be seen in Figure 3.9, $\chi_M T$ increases slightly at each temperature during the equilibration time. Below 50 K it decreases linearly and below 20 K it decreases strongly, indicating antiferromagnetic interactions

Table 3.6: Best fit parameters to reproduce the time dependency of $\chi_M T$ at 77 and 100 K assuming sigmoidal growth: $\chi_M T(t) = B + (A - B)/(1 + (t/t_0)^p)$. The last column gives the values by the slow cooling procedure (1 hour equilibrium time) at the corresponding temperatures.

| T K | A $\text{cm}^3 \text{K mol}^{-1}$ | B $\text{cm}^3 \text{K mol}^{-1}$ | t_0 s | p | R^2 | $(\chi_M T)_{\text{exp}}$ $\text{cm}^3 \text{K mol}^{-1}$ |
|----------|--|--|--------------|---------|---------|--|
| 77 | 0.8591(14) | 0.93(10) | 21000(4000) | 1.28(5) | 0.99950 | 0.96 (70K) |
| 100 | 0.8895(16) | 1.02(5) | 51000(25000) | 1.04(5) | 0.99932 | 1.00 |

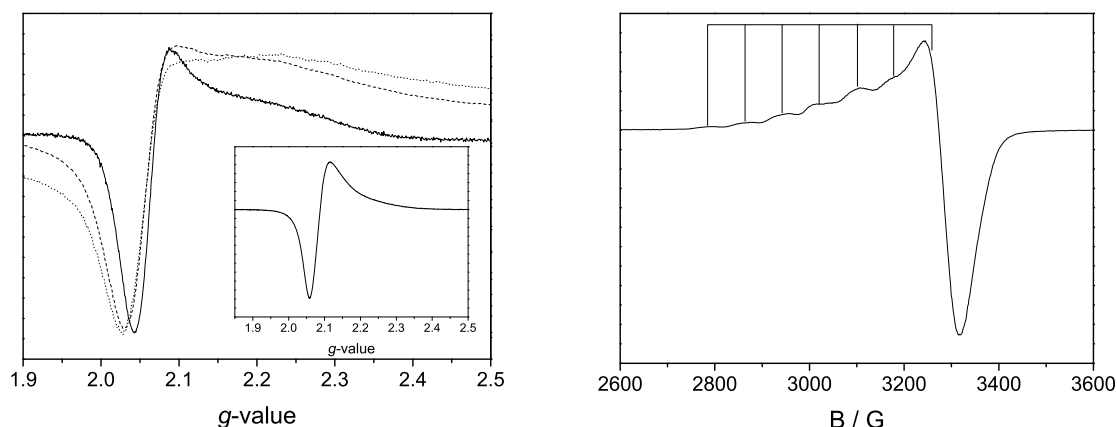


Figure 3.10: Left: ESR spectra of $[\text{Cu}_2(\text{}^t\text{BuCarbOMe})_2]$ (**14**) recorded on a powder sample at room temperature (solid line) and at 77 K just after cooling (dashed line) and after 1 hour at 77 K (dotted line). Inset: ESR spectra of $[\text{Cu}_2(\text{}^t\text{BuCarbOMe})_2]$ (**14**) recorded on a chloroform solution at room temperature. Right: ESR spectra of $[\text{Cu}_2(\text{}^t\text{BuCarbOMe})_2]$ (**14**) recorded on a frozen chloroform solution at 77 K.

as well. Upon heating $\chi_M T$ coincides with the values obtained by the slow cooling procedure up to 50 K. At higher temperatures it shows a linear increase up to 100 K followed by a sharp decrease and a linear increase afterwards. This is consistent with the mechanism proposed in Section 2.2. The temperature dependence up to 100 K can be described by the Bleaney-Bowers equation^[211] (Equation 3.10) using the following parameters: $g = 2.139(4)$, $J_{\text{CuCu}} = -0.77(3) \text{ cm}^{-1}$ and $\chi_{\text{TIP}} = 0.00151(6) \text{ cm}^3 \text{ mol}^{-1}$ giving $R^2 = 0.9965$. Despite the expected increase of g there is also a slight decrease in the coupling constant J_{CuCu} , probably caused by a different relative arrangement of the two copper ions in the two structures.

Isothermal time dependent measurements at 77 K and 100 K exhibit a comparable increase of $\chi_M T$ as described in Section 2.2 (Figure 3.9, right). Both can be reproduced very nicely using logistic growth. However, at 100 K the increase is nearly linear and the agreement factor of the logistic fit is only slightly higher than the one of the linear fit. At 77 K the curvature of the measured values is more pronounced and is reproduced very well using the logistic approach. In both cases the limit for $t \rightarrow \infty$ corresponds well to the value obtained during the heating procedure.

ESR spectra for **14** were recorded on powder samples at room temperature and 77 K (Figure 3.10, left). To elucidate the time dependence of the ESR behavior spectra at 77 K were recorded just after cooling and after another hour at 77 K. From the SQUID-

measurements performed at 77 K one can deduce a fraction of transformation of 6.1%. At room temperature an axial spectrum is observed with a perpendicular transition at $g_{\perp} = 2.069$ and a very broad parallel transition around $g_{\parallel} = 2.2$. At 77 K the spectrum broadens and the perpendicular transition loses intensity. In contrast, the axial transition seems to gain intensity and shows indications of a hyperfine structure. This change continues with time and becomes more pronounced in the spectrum recorded after 1 hour. The spectrum recorded on a chloroform solution at room temperature (Figure 3.10, inset) shows an unsymmetric single signal at $g_{av} = 2.088$. The spectrum recorded on a frozen chloroform solution at 77 K (Figure 3.10, right) exhibits no time dependence. It shows a hyperfine pattern of seven signals, which proves equal contribution from two copper nuclei as expected in the metallacycle. The distance of 78 G between the hyperfine signals gives rise to a hyperfine parameter $A_{\parallel} \approx 156$ G, which is well within the expected range for copper(II).^[8;204]

3.2 Sulfonated Mesalen-type Complexes

3.2.1 Ligand Synthesis

The Ligand $\text{Na}_2\text{H}_2^{\text{Sulf}}\text{Mesalen}$ (**21**) is easily synthesized by Schiff-base condensation of sulfonato substituted *ortho*-vaniline and ethylenediamine (Figure 3.11). The former one is synthesized according to a procedure reported for salicylaldehyde.^[290] After protection of the aldehyde group via Schiff base reaction with aniline, vaniline is sulfonated using concentrated sulfuric acid. X-ray diffraction analysis shows, that the sulfonic acid moiety accounts for the content of four molecules of water, which build up layers alternating with the hydrophobic aromatic rings stacked by π - π interactions (Appendix, Figures A.1 to A.3). The deblocking of the aldehyde group is achieved via hydrolysis in basic environment and removing the cleaved aniline from the equilibrium. The number of solvent molecules can be determined easily from thermogravimetry, showing a loss of 1.7% at $T = 100^\circ\text{C}$. Therefore a water content of 0.5 molecules per 5-sulfonato-2-hydroxy benzaldehyde (**21**) can be determined. In the final ligand $\text{Na}_2\text{H}_2^{\text{Sulf}}\text{Mesalen}$ thermogravimetric analysis shows four water molecules after drying under reduced pressure.

The ligand $\text{Na}_2\text{H}_2^{\text{Sulf}}\text{Mesalen}$ reacts readily with one equivalent of copper(II) nitrate or manganese(II) nitrate in the presence of one equivalent of ethylenediamine (en) serving as base. As known from many other examples, the manganese(II) is oxidized in the presence of air to manganese(III). For copper(II) vapor diffusion of methanol into the aqueous solution readily leads to crystals of $(\text{enH}_2)_2[\text{Cu}_2(\text{Sulf}\text{Mesalen})_2]\cdot\text{H}_2\text{O}$ (**22**), whose structure could be determined by X-ray diffraction. In the case of the manganese(III) compound the crystallization is very slow, leading to crystals of the composition $(\text{enH}_2)[\text{Mn}_2(\text{Sulf}\text{Mesalen})_2]\cdot 3\text{MeOH}\cdot 9.5\text{H}_2\text{O}$ (**24**) suitable for X-ray diffraction

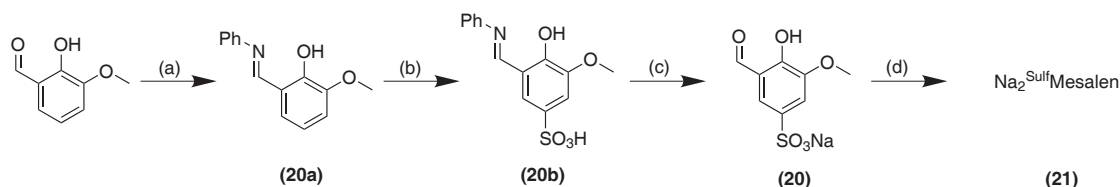


Figure 3.11: (a): Aniline, MeOH, 1h; (b): konz. H_2SO_4 , 100° , 2h; (c): Na_2CO_3 , H_2O , 100° , 2h; (d): ethylene diamine, MeOH, reflux 1h

studies. The coordination of the sulfonato group in the axial position of the metal center gives rise to the formation of metallacycles of the general formula $[M_2(\text{SulfMesalen})_2]$ with $M = \text{Mn(III)}$ and Cu(II) . By layering *iso*-propanol over an aqueous solution of $(\text{enH}_2)[\text{Cu}(\text{SulfMesalen})]$ crystals of the stoichiometry $(\text{enH}_2)[\text{Cu}(\text{SulfMesalen})] \cdot 4\text{H}_2\text{O}$ (**23**) are obtained. This compound contains monomeric $[\text{Cu}(\text{SulfMesalen})]$ entities as well as $[\text{Cu}_2(\text{SulfMesalen})_2]$ cycles. It also shows an interesting way of crystallization: at first voluminous conglomerates of very thin green needles are formed, which then recrystallize slowly to give violet flakes. However, the incorporation of the flakes into the voluminous conglomerate makes a separation very difficult.

3.2.2 Complex Structures

$(\text{enH}_2)_2[\text{Cu}_2(\text{SulfMesalen})_2] \cdot \text{H}_2\text{O}$ — Copper Dimer Chain (**22**)

The compound **22** crystallizes in the triclinic space group $P\bar{1}$. The molecular structure shows a distorted octahedral environment for the copper(II) ions. The structure is depicted in Figure 3.12 on the left; selected bond lengths and angles are summarized in Table 3.7. The equatorial positions are held by the N_2O_2 donor set of the *SulfMesalen* ligand consisting of two phenolic oxygen atoms and two imine nitrogen atoms. The distance of the copper atom from this plane is only 9 pm. The smallest angle in the plane is the N1-Cu-N2 angle with 83.6° , the largest is the O5-Cu1-O1 with 97.2° . The distances to the sulfonato oxygen atoms, which hold the axial positions are much longer (241 pm) than the equatorial ones (164–196 pm) due to the Jahn-Teller distortion. The O5-Cu-O10 angle is 176.6° and therefore very close to the ideal 180° .

While the coordination octahedron is only slightly distorted the ligand shows a rather strong bending of the two aromatic rings forming an angle of 29° . Interestingly the bending is not symmetric. The coordination plane is nearly coplanar with one of the rings ($\theta = 6^\circ$) and forms a much larger angle with the other one ($\theta = 22^\circ$). The sulfonato group of the bended ring is disordered. This asymmetry and disorder gives rise to an interesting supramolecular structure.

Since one of the sulfonato oxygens takes the axial position of an neighboring copper ion, tetragons are formed with the sulfur and copper ions on the edges. These are very regular in the case of the non-disordered sulfonate groups. The distance between the copper ion and the sulfonato oxygen is 242 pm and the benzene rings are coplanar at

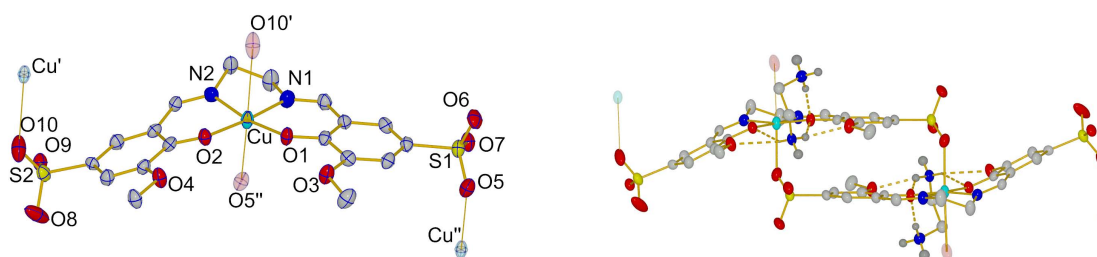


Figure 3.12: Molecular structure of $[\text{Cu}(\text{SulfMesalen})]$ (left) and metallacycle $[\text{Cu}_2(\text{SulfMesalen})_2]$ formed by coordination of the sulfonato group (right) in the crystal structure of $(\text{enH}_2)_2[\text{Cu}_2(\text{SulfMesalen})_2]\cdot\text{H}_2\text{O}$ (**22**). Carbon bound hydrogen atoms are omitted for clarity. Atoms belonging to neighboring molecules are depicted transparent. Thermal ellipsoids are drawn at 50% probability.

a distance of 360 pm, indicating π - π interactions. However, the disordered sulfonate groups shows only very weak interactions with a distance of around 280 pm for one of the disordered positions and or does not coordinate at all in the other position. This gives rise either to dimers (Figure 3.12, right) arranged in chains or to an alternating coordination polymer consisting of nearly ideal rectangles and distorted ones. The copper-copper distances are 856 pm and 794 pm, respectively.

The chains are perpendicular to the a -axis and run diagonally through the b - c -plane. A twice protonated ethylenediamin serves as the counterion to the negative charge of the complex molecule. It plays a particular role in the supramolecular structure: one of

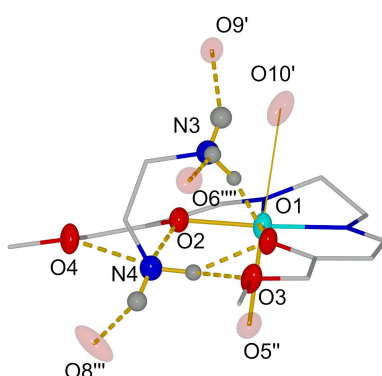


Figure 3.13: Hydrogen bonding around the diammoniummethylene in the crystal structure of $(\text{enH}_2)_2[\text{Cu}_2(\text{SulfMesalen})_2]\cdot\text{H}_2\text{O}$ (**22**). Carbon atoms around the metal center are depicted as wires, whereas the rest of the molecule and carbon bound hydrogen atoms are omitted for clarity. Atoms belonging to neighboring molecules are depicted transparent. Thermal ellipsoids are drawn at 50% probability.

the ammonium groups is located in the outer O₄ environment of ^{Sulf}Mesalen forming hydrogen bonds to the atoms O1 and O2 and to the sulfonato group of a neighboring molecule (Table 3.8). It is located 12 pm below the plane spanned by the atoms O1, O2, O3 and O4. The second ammonium group is located 250 pm above the plane and forms three hydrogen bonds, an intramolecular one to O1 and two to the sulfonato groups of a neighboring chains. The hydrogen bonding network therefore plays an important role for the supramolecular structure (Figure 3.13). An additional molecule of water is incorporated in the crystal lattice.

(enH₂)[Mn₂(^{Sulf}Mesalen)₂].3MeOH.9.5H₂O — Manganese Dimer Chain (24)

The manganese compound 24 crystallizes in the monoclinic space group *P1/n*. The molecular structure is quite similar to the one of 22. However, due to the higher oxidation state the overall metallacycle is charged only twice and needs only one molecule (enH₂)²⁺ as counter ion. However, this mainly influences the supramolecular arrangement and the intermolecular connection by diamoniummethylenes. There exist two molecules in the unit cell, however, due to the very small differences in bond lengths and angles (Table 3.9) only one will be discussed.

Complex 24 shows a distorted octahedral environment for the manganese(III) ions. The structure is depicted in Figure 3.14 on the left side; selected bond lengths and angles are summarized in Table 3.9. The equatorial positions are held by the N₂O₂ donor set of the ^{Sulf}Mesalen ligand consisting of two phenolic oxygen atoms and two imine

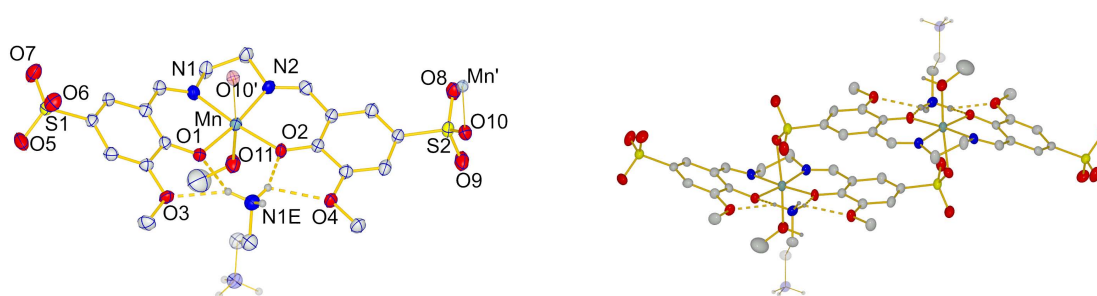


Figure 3.14: Molecular structure and numbering scheme for heteroatoms of (enH₂)_{0.5}[Mn(^{Sulf}Mesalen)] (left) and metallacycle (enH₂)[Mn₂(^{Sulf}Mesalen₂)] formed by coordination of the sulfonato group (right) in the crystal structure of (enH₂)[Mn₂(^{Sulf}Mesalen)₂].3MeOH.9.5H₂O (24). Atoms belonging to neighboring molecules are depicted transparent. Thermal ellipsoids are drawn at 50% probability.

Table 3.7: Selected bond lengths in pm and bond angles in ° for complex $(\text{enH}_2)[\text{Cu}(\text{Sulf Mesalen})]\cdot\text{H}_2\text{O}$ (22)

| bond lengths (pm) | | bond angles (°) | |
|-------------------|----------|-----------------|-----------|
| Cu – O1 | 195.1(2) | O5 – Cu1 – O1 | 97.25(11) |
| Cu – O2 | 194.1(3) | O5 – Cu1 – O2 | 87.34(11) |
| Cu – N1 | 196.0(3) | O5 – Cu1 – N1 | 94.53(13) |
| Cu – N2 | 194.2(3) | O5 – Cu1 – N2 | 91.64(12) |
| Cu – O5 | 241.8(3) | O1 – Cu1 – O2 | 92.38(10) |
| | | O1 – Cu1 – N1 | 91.77(12) |
| | | O2 – Cu1 – N2 | 91.95(12) |
| | | N1 – Cu1 – N2 | 83.58(13) |

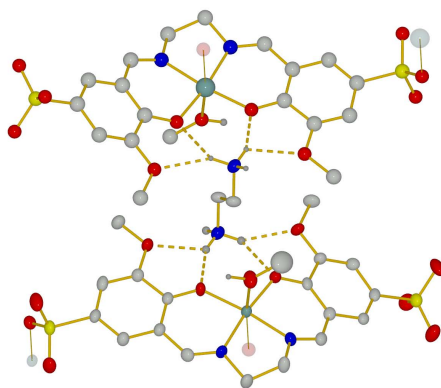
**Figure 3.15:** Bridging of two $[\text{Mn}(\text{Sulf Mesalen})]$ units by the ethylenediammonium counter ion in the crystal structure of $(\text{enH}_2)[\text{Mn}_2(\text{Sulf Mesalen})_2]\cdot 3\text{MeOH}\cdot 9.5\text{H}_2\text{O}$ (24). Carbon bound hydrogen atoms are omitted for clarity. Atoms belonging to neighboring molecules are depicted transparent. Thermal ellipsoids are drawn at 50% probability.

Table 3.8: Summary of the metric parameters for the hydrogen bonds found in the crystal structures of $(\text{enH}_2)_2[\text{Cu}_2(\text{Sulf Mesalen})_2]\cdot\text{H}_2\text{O}$ (**22**), $(\text{enH}_2)[\text{Mn}_2(\text{Sulf Mesalen})_2]\cdot 3\text{MeOH}\cdot 9.5\text{H}_2\text{O}$ (**24**) and $(\text{enH}_2)[\text{Cu}(\text{Sulf Mesalen})]\cdot 4\text{H}_2\text{O}$ (**23**). In the case of the manganese compound the two numbers correspond to the two molecules per cell ($n = 1,2$, $X = \text{B,A}$ and $Y = 4,3$).

| D-H...A | $d(\text{D-H})/\text{pm}$ | $d(\text{D}\cdots\text{H})/\text{pm}$ | $d(\text{D}\cdots\text{A})/\text{pm}$ | $\alpha(\text{D-H}\cdots\text{A})/^\circ$ |
|---|---------------------------|---------------------------------------|---------------------------------------|---|
| compound 22 (Figure 3.12) | | | | |
| N3-H...O1 | 98 | 189 | 285 | 165 |
| N3-H...O9' | 89 | 199 | 277 | 145 |
| N3-H...O6''' | 94 | 198 | 285 | 153 |
| N4-H...O1 | 98 | 202 | 287 | 143 |
| N4-H...O3 | 98 | 214 | 289 | 131 |
| N4-H...O2 | 73 | 221 | 285 | 148 |
| N4-H...O4 | 73 | 236 | 288 | 131 |
| N4-H...O8''' | 90 | 201 | 291 | 172 |
| compound 24 (Figure 3.14) | | | | |
| $Nn\text{E-H}\cdots\text{O1X}$ | 91/91 | 236/216 | 298/294 | 125/143 |
| $Nn\text{E-H}\cdots\text{O3X}$ | 91/91 | 212/215 | 295/287 | 151/135 |
| $Nn\text{E-H}\cdots\text{O2X}$ | 91/91 | 202/218 | 288/289 | 157/135 |
| $Nn\text{E-H}\cdots\text{O4X}$ | 91/91 | 227/213 | 290/291 | 126/143 |
| $Nn\text{E-H}\cdots\text{OYW}$ | 91/91 | 212/186 | 295/277 | 150/176 |
| compound 23 hydrogen bonded cycle (Figure 3.17) | | | | |
| N1E-H...O1B | 86 | 214 | 289 | 151 |
| N1E-H...O2B | 85 | 214 | 282 | 137 |
| N1E-H...O9B | 86 | 221 | 283 | 132 |
| N1E-H...O10B | 85 | 212 | 282 | 139 |
| N1E-H...O1W | 89 | 193 | 277 | 157 |
| sulfonate cycle (Figure 3.16) | | | | |
| N2E-H...O1A | 82 | 227 | 295 | 141 |
| N2E-H...O2A | 90 | 229 | 287 | 128 |
| N2E-H...O9A | 82 | 227 | 285 | 128 |
| N2E-H...O10A | 90 | 204 | 287 | 153 |

nitrogen atoms. The distance of the manganese atom from this plane is with 3 pm even shorter than in **22**. The smallest angle inside in the plane is the N1–Mn–N2 angle with 82.4° , the largest is the O5–Mn–O1 with 95.7° . The axial distances to the sulfonato oxygen atom and to the methanol oxygen atom are much longer than the distances in the coordination plane due to the Jahn-Teller distortions. The O10–Mn–O11 angle is 172.6° and therefore close to the ideal 180° .

While the coordination octahedron is only slightly distorted the ligand shows a rather strong bending of the two aromatic rings forming an angle of 23° . As in **22** the bending is not symmetric and the coordination plane is nearly coplanar with one of the rings ($\theta = 3^\circ$) while the other forms a much larger angle ($\theta = 24^\circ$).

Similar to the copper dimer chain (**22**) metallacycles are formed by axial coordination of one sulfonato oxygen to a neighboring manganese (Figure 3.14, right). These are very regular with the benzene rings being coplanar at a distance of 338 pm, indicating π – π interactions. The manganese–manganese distance inside the metallacycle is 829 pm. Due to the higher charge of the metal ion, the resulting metallacycle needs only one protonated ethylenediamine for charge compensation. In the crystal structure the diammoniummethylenes bridge the metallacycles by multiple hydrogen bonds inside the outer cavity of the *Sulf*Mesalen ligand (Figure 3.15). Using this linking mode, one-dimensional chains are build.

(enH₂)[Cu(^{Sulf}Mesalen)]·4H₂O — Alternating Copper Dimer Chain (23**)**

The supramolecular arrangement of **23** can be changed by altering the crystallization conditions. When the stock solution of (enH₂)[Cu(^{Sulf}Mesalen)] in water is covered with a layer of *iso*-propanol crystals of the composition (enH₂)[Cu(^{Sulf}Mesalen)]·4H₂O (**23**) can be obtained. In this compound, diammoniummethylenes bridge the moieties similar to the manganese compound **24**. However, there is not just one dimeric unit, but two of them.

One of these to dimers shows a similar structure scheme like **22** and **24**, that is the metallacycle formed by axial coordination of a sulfonato oxygen atom. The molecular structure and the numbering scheme are depicted in Figure 3.16 (left) together with the formed metallacycle (right), selected bond lengths and angles are summarized in Table

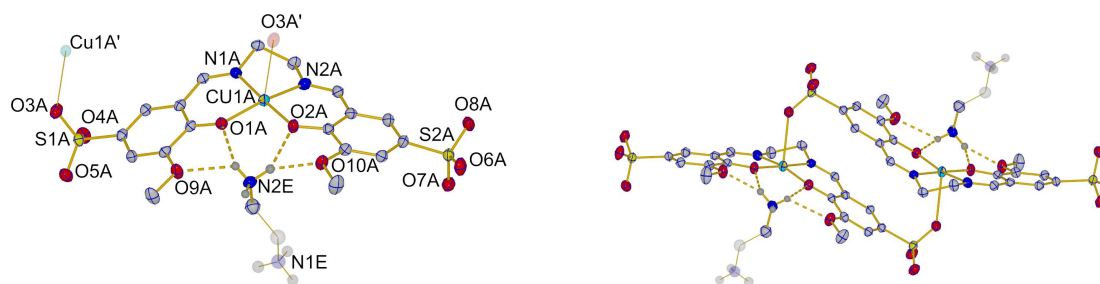


Figure 3.16: Molecular structure and numbering scheme for the $(\text{enH}_2)[\text{Cu}(\text{Sulf Mesalen})]$ unit and the formation of the metallacycle by axial coordination of the sulfonato oxygen in the crystal structure of $(\text{enH}_2)_2[\text{Cu}_2(\text{Sulf Mesalen})_2] \cdot 4\text{H}_2\text{O}$ (**23**). Ellipsoids are drawn at 50% probability. Carbon bound hydrogen atoms are omitted for clarity.

3.10. The coordination environment is similar to **22**, but the axial copper–oxygen distance is even longer. In combination with the fact, that the equatorial plane spanned by N1A, N2A, O1A and O2A is canted by 21° against the aromatic system, which constitutes the metallacycle, it leads to a much more distorted rectangular with a distance between the two aromatic rings of 323 pm. The other aromatic ring is canted only by 10° and is much better aligned with the equatorial plane. One ammonium group of the diammoniummethylene molecule is bound in the outer O_4 sphere by hydrogen bonds as it is found in **22** and **24**

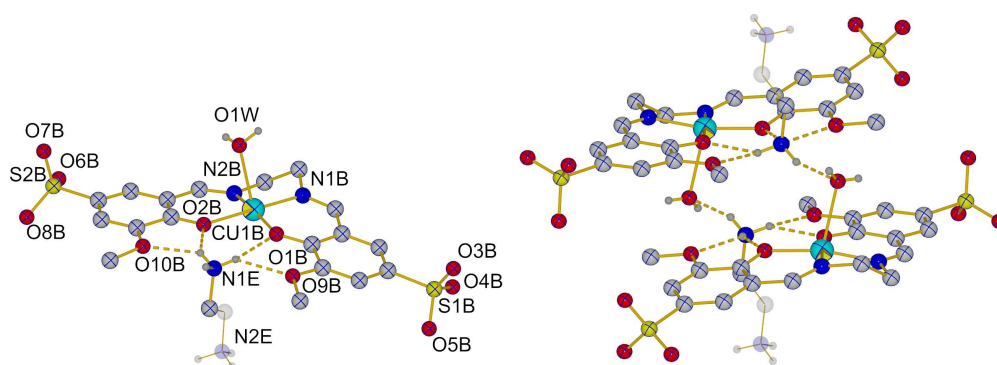


Figure 3.17: Molecular structure and numbering scheme for the $(\text{enH}_2)[\text{Cu}(\text{Sulf Mesalen})]$ unit and the formation of the metallacycle by hydrogen bonding between the ethylene diamine unit and the axial water molecule in the crystal structure of $(\text{enH}_2)_2[\text{Cu}_2(\text{Sulf Mesalen})_2] \cdot \text{H}_2\text{O}$ (**23**). Ellipsoids are drawn at 50% probability. Carbon bound hydrogen atoms are omitted for clarity.

Table 3.9: Selected bond lengths in pm and bond angles in ° complex $(\text{enH}_2)[\text{Mn}_2(\text{Sulf Mesalen})_2] \cdot 3\text{MeOH} \cdot 9.5\text{H}_2\text{O}$ (**24**) the two numbers correspond to the two molecules in the unit cell.

| bond lengths (pm) | | bond angles (°) | |
|-------------------|-------------------|-----------------|---------------------|
| Mn – O1 | 190.2(4)/190.4(4) | O1 – Mn – O10 | 89.16(14)/89.25(15) |
| Mn – O2 | 190.2(4)/190.9(3) | O2 – Mn – O10 | 96.16(15)/97.10(15) |
| Mn – N1 | 196.7(4)/197.4(4) | N1 – Mn – O10 | 84.87(16)/82.40(16) |
| Mn – N2 | 199.9(4)/198.2(4) | N2 – Mn – O10 | 88.91(16)/86.94(17) |
| Mn – O10 | 239.(4)/229.1(4) | O1 – Mn – O11 | 89.18(16)/91.49(17) |
| Mn – O11 | 219.8(4)/217.0(4) | O2 – Mn – O11 | 90.07(16)/90.14(16) |
| | | N1 – Mn – O11 | 89.05(17)/90.23(18) |
| | | N2 – Mn – O11 | 91.93(17)/91.51(18) |
| | | O1 – Mn – O2 | 95.97(15)/95.68(15) |
| | | O1 – Mn – N1 | 90.37(17)/91.02(17) |
| | | O2 – Mn – N2 | 91.71(17)/90.92(16) |
| | | N1 – Mn – N2 | 81.97(18)/82.36(17) |

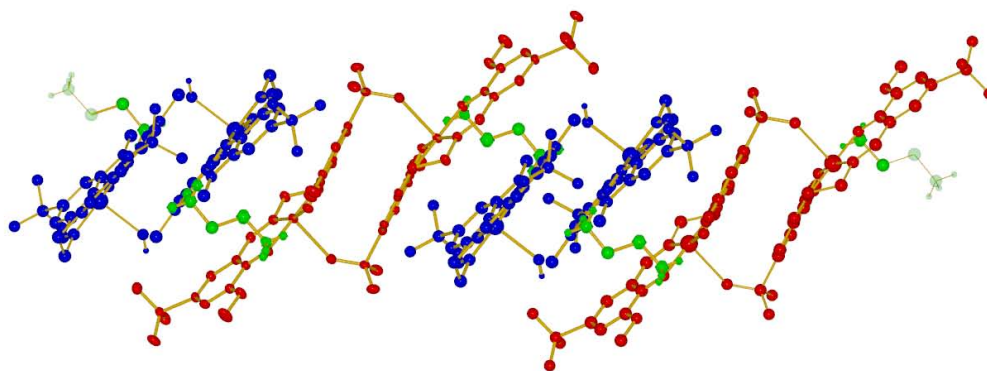


Figure 3.18: One-dimensional chain structure built by linkage of the two different metallacycles in the crystal structure of $(\text{enH}_2)_2[\text{Cu}_2(\text{Sulf Mesalen})_2] \cdot \text{H}_2\text{O}$ (**23**). The linking diamoniummethylene molecules are depicted in green, the hydrogen bond cycles in blue and the metallacycles built by axial coordination of the sulfonate oxygen in red. Ellipsoids are drawn at 50% probability. Carbon bound hydrogen atoms are omitted for clarity.

Table 3.10: Selected bond lengths in pm and bond angles in ° for complex $(\text{enH}_2)[\text{Cu}(\text{Sulf Mesalen})]\cdot 4\text{H}_2\text{O}$ (23). The first number (column A) refers to the entity with the axial coordination of a sulfonato oxygen, the second (column B) to the entity formed by hydrogen bonding (see text).

| | bond lengths (pm) | | | bond angles (°) | |
|----------|-------------------|------------|----------------------------|-----------------|-----------|
| | A | B | | A | B |
| Cu1 – O1 | 193.5(2) | 193.3(2) | N1 – Cu1 – N2 | 83.63(10) | 83.99(10) |
| Cu1 – O2 | 191.01(19) | 192.96(19) | N1 – Cu1 – O1 | 92.47(9) | 92.20(9) |
| Cu1 – N1 | 194.1(2) | 195.0(2) | N2 – Cu1 – O2 | 94.03(9) | 93.99(10) |
| Cu1 – N2 | 194.9(2) | 194.4(2) | O1 – Cu1 – O2 | 89.95(8) | 89.48(8) |
| | | | O _{1W} – Cu1 – N1 | | 94.23(10) |
| | | | O _{1W} – Cu1 – N2 | | 87.67(10) |
| | | | O _{1W} – Cu1 – O1 | | 103.21(9) |
| | | | O _{1W} – Cu1 – O2 | | 87.44(9) |

In the second dimer, the axial position is occupied by a water molecule instead of a sulfonato oxygen. The molecular structure and the numbering scheme are depicted in Figure 3.17 (left) together with the formed metallacycle (right), selected bond lengths and angles are summarized in Table 3.10. Also in this dimer an ammonium group is bound in each entity by two hydrogen bondings. The residual hydrogen forms a rather strong hydrogen bond to the axial water molecule of the other unit ($d(\text{O}_{1\text{W}}-\text{N}_{1\text{E}}) = 277$ pm). This leads to the formation of a hydrogen bonded metallacycle. Interestingly the ligand adopts a zig-zag conformation, in which the angle between the two aromatic rings (13°) is smaller than the angle between one of the aromatic rings and the equatorial plane (19°). The other aromatic ring is nearly coplanar with the equatorial plane (6°).

The resulting dinuclear units are linked by the bound diammoniummethylenes into one-dimensional chains (Figure 3.18). The copper–copper distance between the dimers (522 pm) is shorter than the distances inside the sulfonato linked dimer (759 pm) and in the hydrogen bonded dimer (693 pm). Two additional ethylenediamine molecules are located between these chains and establish an extended three dimensional hydrogen bonding network incorporating also the sulfonato oxygens and three water molecules per $(\text{enH}_2)[\text{Cu}(\text{Sulf Mesalen})]$ entity.

3.2.3 Magnetic Properties of Copper Dimer Chain

The temperature dependence of the magnetic susceptibility of the copper dimer chain (22) was determined in the temperature range between 2 and 300 K. Plots of $\chi_M = f(T)$ and $\chi_M T = f(T)$ are depicted in Figure 3.19. The $\chi_M T$ value of $0.43 \text{ cm}^3 \text{K mol}^{-1}$ is nearly temperature independent and increases slightly at very low temperatures. This indicates very weak ferromagnetic copper–copper interactions. The weakness is caused by the fact, that the exchange interactions between the magnetic $d_{x^2-y^2}$ orbitals take place along the axial sulfonato group. Therefore, the field dependence of the magnetization (inset in Figure 3.19) can be reproduced very nicely using the Brillouin function with the following parameters: $S = 0.5$, $T = 2 \text{ K}$ and $g = 2.187(2)$ giving $R^2 = 0.99988$.

Identical X-band ESR spectra were recorded on powder samples at room temperature and at 77 K (Figure 3.20, left). They show a rhombic spectrum with a very broad and unresolved g_z -component. The weak ferromagnetic interactions inside and also the interactions between the dimers cause further splitting of the copper hyperfine pattern. Together with a g -strain in z -direction due to the interactions with the disordered sulfonato group this explains the very broad g_z -component. A good agreement between the powder spectrum at 77 K and the simulated spectrum can be obtained by using $g = [2.055, 2.095, 2.210]$ with a g -strain of $[0.0, 0.05, 0.35]$. After dissolution in

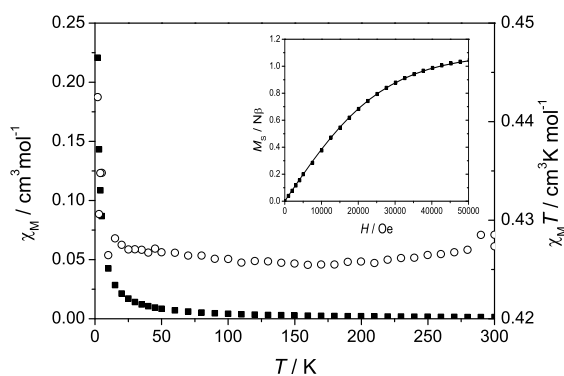


Figure 3.19: Temperature dependence of χ_M (black boxes) and $\chi_M T$ (open circles) of $(\text{enH}_2)_2[\text{Cu}_2(\text{SulfMesalen})_2]$ (22). Inset: field dependence of magnetization at 2 K and best fit using the Brillouin function with the parameters mentioned in the text.

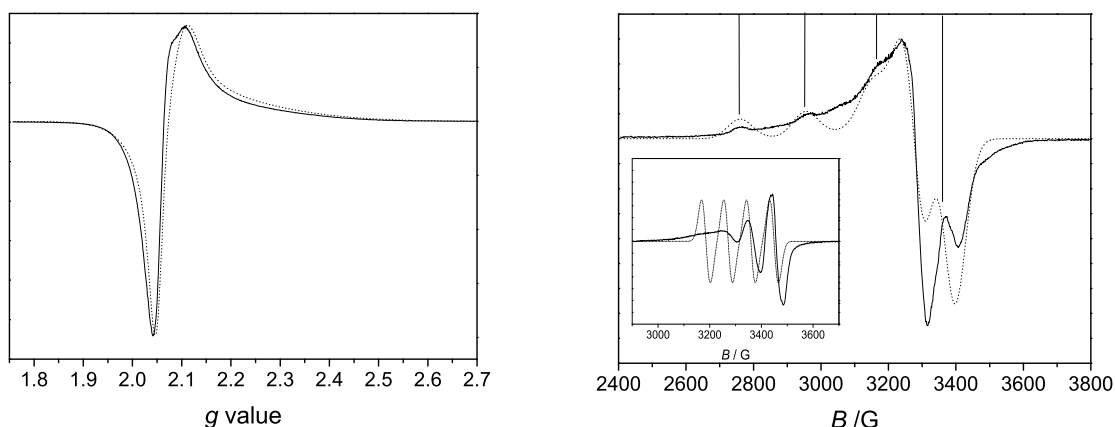


Figure 3.20: X-band ESR spectra of $(\text{enH}_2)_2[\text{Cu}_2(\text{Sulf Mesalen})_2]$ (**22**) recorded on powder samples at 77 K (left), and on a frozen MeOH/H₂O solution at 77 K (right). The inset shows the spectrum obtained on the MeOH/H₂O solution at room temperature. The dotted lines represents the corresponding simulations with the parameters mentioned in the text.

a methanol/water mixture (1:1) spectra were recorded on solution at room temperature and on the frozen solution at 77 K (Figure 3.20, right). The spectrum measured at room temperature on solution can be reproduced with $g_{\text{av}} = 2.110$ and $A_{\text{av}} = 93$ G (260 MHz). In frozen solution an axial spectrum is measured, which can be reproduced nicely using the following parameters: $g = [2.052, 2.052, 2.215]$ ($g_{\text{av}} = 2.12$) and $A_{\parallel} = 214$ G.

Due to the very long crystallization times of **23** and **24** not enough material for extended magnetic characterization could be obtained up to now.

3.3 Magnetic Properties of Substituted Triaminoguanidine Ligands

3.3.1 Properties of Unsubstituted Trinuclear Copper Complex

The synthesis and structure of the complex $[(^H\text{TAG})\text{Cu}_3(\text{bipy})_3](\text{ClO}_4)$ have been reported elsewhere.^[308] A short summary of the structural features relevant for the magnetic discussion is given in the following paragraph.

The molecular structure is depicted in Figure 3.21. The central bridging triaminoguanidine ligand offers three binding pockets to accommodate metal ions with a N_2O donor set per pocket. Because of the extended π -system delocalized over the central triaminoguanidine core, the ligand enforces a planar configuration. Each copper ion is coordinated by the two nitrogen and one oxygen donor from the triaminoguanidine as well as by two nitrogen atoms from the capping 2,2'-bipyridyl (bipy) ligand. This leads to a square pyramidal coordination mode with one of the nitrogens from the bipy ligand occupying the axial position. These rather disk shaped molecules are arranged in hexagonal layers by π - π interactions of the aromatic rings from the bipyridines. The

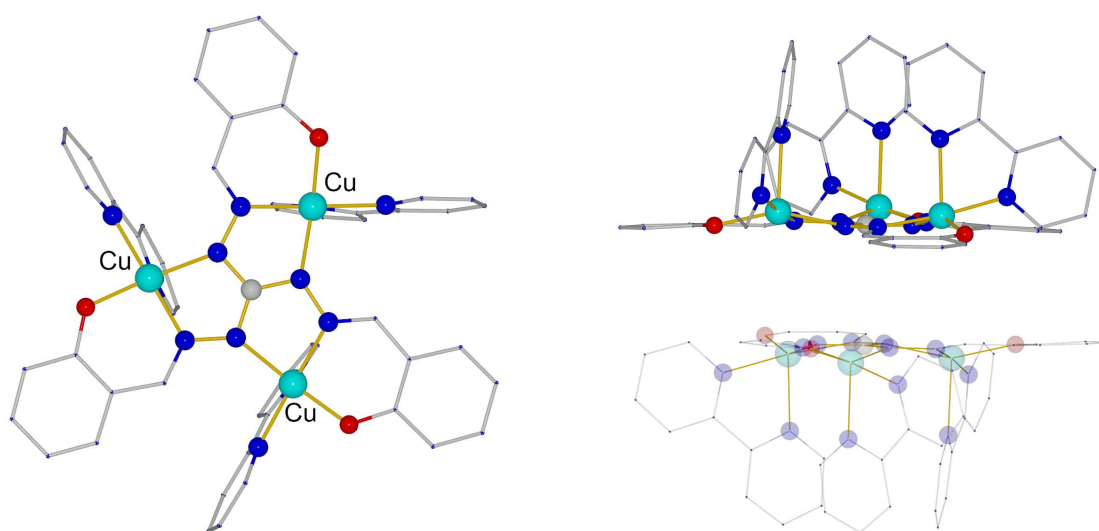


Figure 3.21: Molecular structure of $[(^H\text{L})\text{Cu}_3(\text{bipy})_3]\text{ClO}_4$ (left) and close dimer stacking in the crystal structure (right). The second complex is depicted and all hydrogen atoms have been omitted for clarity.

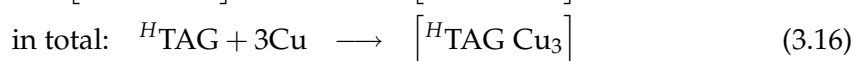
resulting layers are then stacked closely with two complex molecules oriented face-to-face without separating solvent molecules (Figure 3.21). Two stacked molecules are twisted by 60° , so that each copper has two close neighbors (511 pm) and one remote (702 pm) in the adjacent molecule.

Spectroscopic Properties

To compare the properties of substituted derivatives of the triaminoguanidine ligand scaffold, the unsubstituted complex molecule $[(^H\text{TAG})\text{Cu}_3(\text{bipy})_3](\text{ClO}_4)$ and its formation were investigated by UV/Vis spectroscopy. Absorption spectra were recorded on solid samples grinded with barium sulfate (Figure 3.22, left) and dissolved in dimethylformamide (Figure 3.22, right). The formation of the complex in dimethylformamide was investigated by UV/Vis titrations of $\text{H}_5^H\text{TAG}\cdot\text{HCl}$ with copper(II) and subsequent titration with 2,2-bipyridyl (Figure 3.23).

The results of the titration with copper(II) ions are shown in Figure 3.23 on the right side. To the solution of the ligand $\text{H}_5^H\text{TAG}\cdot\text{HCl}$ was added triethylamine as a base. To avoid side reactions (decomposition of the ligand, precipitation of copper salts), only three equivalents of triethylamine were added before addition of the copper solution and three after. No changes in the spectrum are visible upon each base addition as is depicted in Figure 3.23 on the left side.

The addition of three equivalents of copper causes significant changes in the spectrum. The band below 350 nm decreases, whereas new bands at 398, 417 and 620 nm arise. There can be seen three crossing points between 366 nm and 391 nm. In these points the spectra of the first to fourth, the fifth to eighth and the ninth to twelfth spectrum cross. These stepwise crossings strongly suggest a subsequent filling of the coordination pockets:



3.3 Magnetic Properties of Substituted Triaminoguanidine Ligands

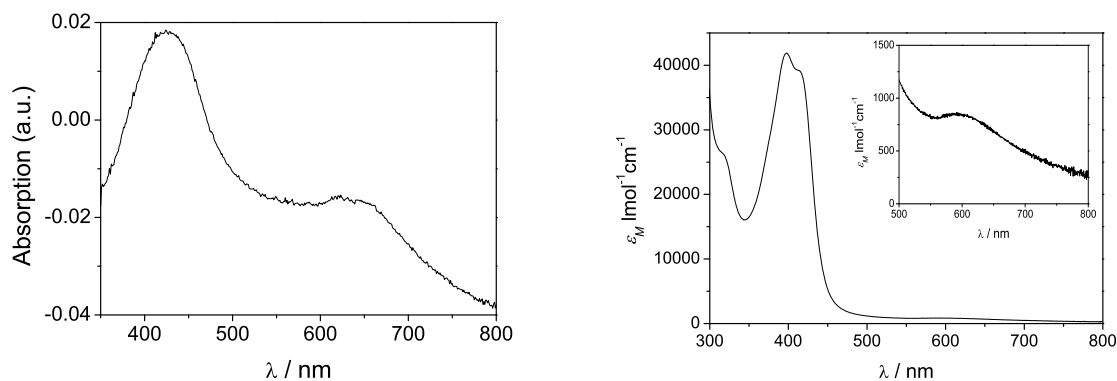


Figure 3.22: UV/Vis absorption spectra recorded on a solid sample of $[(^H\text{TAG})\text{Cu}_3(\text{bipy})_3]\text{ClO}_4$ grinded with barium sulfate (left) and in dimethylformamide solution (right). The inset enlarges the spectrum between 500 and 800 nm.

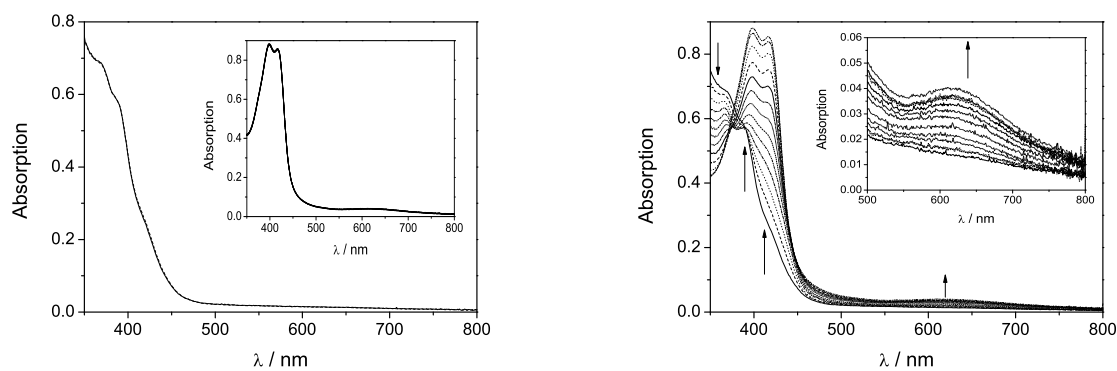


Figure 3.23: Left: UV/Vis absorption spectra recorded on 100 mL of a dimethylformamide solution of $\text{H}_5^H\text{TAG}\cdot\text{HCl}$ ($c_{0,L} = 2.13 \cdot 10^{-5}$ mol/l) upon addition of three equivalents of base. The inset shows the UV/Vis absorption spectra recorded on a dimethylformamide solution of $[(^H\text{TAG})\text{Cu}_3(\text{bipy})_3]^+$ upon addition of three equivalents of base. Right: Change in the UV/Vis absorption spectra upon addition of copper(II) ions ($c_{0,\text{Cu}} = 5.56 \cdot 10^{-3}$ mol/l, 96 μL per step, in total 3 equivalents) to 100 mL of a dimethylformamide solution of $\text{H}_5^H\text{TAG}\cdot\text{HCl}$ ($c_{0,L} = 2.13 \cdot 10^{-5}$ mol/l). Inset: enlargement of the spectrum between 500 and 800 nm.

In these equations the deprotonation has been omitted, since the addition of base had no effect on the the spectra of the ligand as well as on the final complex. The equilibrium constants read

$$K_1 = \frac{c([\text{}^H\text{TAG Cu}])}{c([\text{}^H\text{TAG}]) \cdot c(\text{Cu})} \quad (3.17)$$

$$K_2 = \frac{c([\text{}^H\text{TAG Cu}_2])}{c([\text{}^H\text{TAG Cu}]) \cdot c(\text{Cu})} \quad (3.18)$$

$$K_3 = \frac{c([\text{}^H\text{TAG Cu}_3])}{c([\text{}^H\text{TAG Cu}_2]) \cdot c(\text{Cu})} \quad (3.19)$$

$$K_{\text{ges}} = \frac{c([\text{}^H\text{TAG Cu}_3])}{c([\text{}^H\text{TAG}]) \cdot c^3(\text{Cu})} \quad (3.20)$$

$$= K_1 \cdot K_2 \cdot K_3 \quad (3.21)$$

Least square fitting of the equilibrium constants to the measured spectra assuming the above sequence of reactions gives the $K_1 = 1.30 \cdot 10^6$ l/mol, $K_2 = 6.51 \cdot 10^6$ l/mol and $K_3 = 3.39 \cdot 10^5$ l/mol with an overall constant of $K_{\text{ges}} = 2.87 \cdot 10^{18}$ l³/mol³ ($\text{p}K_{\text{ges}} = -18.5$). This shows that the trinuclear copper complex has high binding constants. To avoid polymerization^[144;145] 2,2'-bipyridyl (bipy) is used as a capping ligand. Interestingly no change in the absorption spectra was observed upon the addition of 2,2'-bipyridyl. It should be stressed here, that the double band around 400 nm only appears upon the addition of the third equivalent of copper(II) during the titration of **27** with copper ions (*vide infra*) is present in this compound as well. It therefore is a good indicator for the presence of the trinuclear core fragment $[(\text{}^H\text{TAG})\text{Cu}_3]$.

This double band is also present in the solution spectra of $[(\text{}^H\text{TAG})\text{Cu}_3(\text{bipy})_3]\text{ClO}_4$ in DMF solution (Figure 3.22, right). The powder spectrum shows only a single band around 424 nm and a second one at 627 nm, however, it is too broad and the signal-to-noise ratio is too low to exclude the presence of the double band. It is also probable, that the structure changes upon dissolution, which can be seen in the ESR spectra as well (*vide infra*).

Magnetic Properties

The temperature dependence of the molar magnetic susceptibility of $[(^H\text{TAG})\text{Cu}_3(\text{bipy})_3](\text{ClO}_4)$ was determined between 2 and 300 K on powdered samples (Figure 3.24, left).^[308] The decrease at low temperatures might be composed of intermolecular interactions between adjacent complex molecules (described by the mean field model, MF) as well as of non isotropic Dzalozinsky-Moriya interactions (DM). The appropriate hamiltonian reads:

$$\hat{H} = \sum_{i=1}^3 (g\mu_B \vec{B} \hat{S}_i) - J (\hat{S}_1 \cdot \hat{S}_2 + \hat{S}_1 \cdot \hat{S}_3 + \hat{S}_2 \cdot \hat{S}_3) + \vec{G} (\hat{S}_1 \times \hat{S}_2 + \hat{S}_2 \times \hat{S}_3 + \hat{S}_3 \times \hat{S}_1) \quad (3.22)$$

A comparison of the best fit parameters obtained by least square numerical fitting procedures is depicted in Table 3.11. A comparison of the simulated and experimental behavior is depicted in Figure 3.24 on the right side. It can be seen that the intermolecular interactions plays a more pronounced role than the antisymmetric interactions inside the molecule. Regarding only one effect, the experimental behavior is

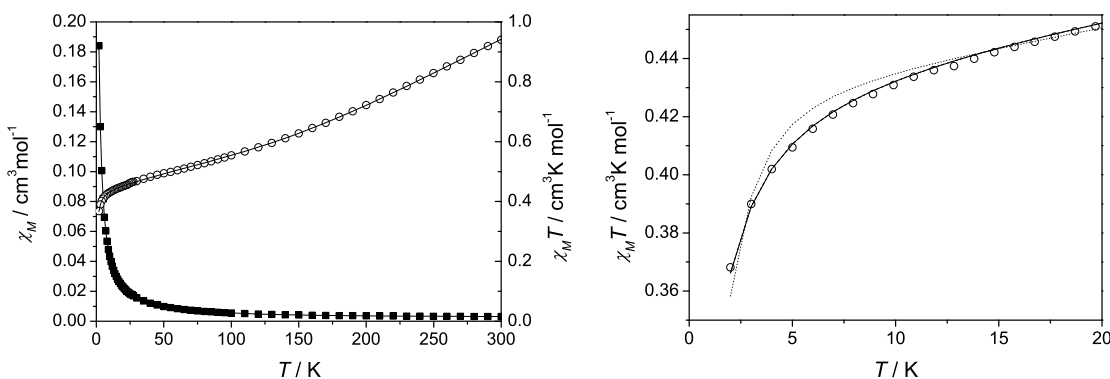


Figure 3.24: Left: Temperature dependence of χ_M (black filled boxes) and of $\chi_M T$ (open circles) between 2 and 300 K for $[(^H\text{TAG})\text{Cu}_3(\text{bipy})_3](\text{ClO}_4)$ (26). The solid lines represent the best fit regarding intermolecular interactions via the mean field model and Dzalozinsky-Moriya interactions (see text). Right: Comparison of simulated behavior regarding different effects with the experimental data in the temperature range between 2 and 20 K. The empty circles represent the measured $\chi_M T$ values, the lines the simulated behavior including intramolecular interactions (dashed, coincides with the solid curve), Dzalozinsky-Moriya interactions (dotted line) and both (solid line).

much better described by the mean-field interactions, whereas the inclusion of both effects leads to very small antisymmetric interactions. This illustrates, that a determination of the antisymmetric interactions is strongly hindered by the close dimer stacking.

X-band ESR measurements have been performed on powdered samples at 5, 10, 20, 40 and 77 K as well as at room temperature (Figure 3.25, left). In addition spectra were recorded on a solution in dimethylformamid at room temperature as well as on frozen solutions at 4.3 K (Figure 3.25, right). The solid state spectra show a perpendicular transition around $g_{\perp} = 2.10$ and a very broad axial transition around $g_{\parallel} = 2.31$. In the frozen solution the shape is similar, but the transitions are shifted to $g_{\perp} = 2.07$ and $g_{\parallel} = 2.28$, respectively. This can be explained by structural rearrangements or additional axial coordination of dimethylformamide and is in agreement with the differences in the UV/Vis-spectra. The solution spectra show an untypical signal between 2940 and 3630 G with a very broad and unresolved low-field side and a structured high-field side. The center gives $g_{av} = 2.133$ and the distance between the resolved lines on the high-field side is about 75 G.

3.3.2 Properties of Substituted Trinuclear Copper Complex

To enforce the electrostatic repulsion of the complex molecules the ligand $\text{Na}_2\text{H}_6^{\text{Sulf}}\text{TAG}$ was synthesized by reacting triaminoguanidine hydrochloride with the sodium salt of 5-sulfonato-2-hydroxybenzaldehyde (Figure 3.26). With this ligand the

Table 3.11: Comparison of best fit parameters obtained by least square numerical fitting of the hamiltonian 3.22 to the measured temperature dependence of the molar magnetic susceptibility.

| Parameter | no DM/MF | DM/MF | DM/no MF |
|---|-----------------------|-----------------------|-----------------------|
| g | 2.162 | 2.162 | 2.131 |
| J [cm^{-1}] | 324 | 324 | 345 |
| G_z [cm^{-1}] (G_z/J) | — | 0.0031 (0.001%) | -0.9 (0.3%) |
| χ_{TIP} [$\text{cm}^3\text{mol}^{-1}$] | 0.00117 | 0.00117 | 0.00128 |
| λ [K] | -0.92 | -0.92 | — |
| χ^2 | $8.843 \cdot 10^{-5}$ | $8.843 \cdot 10^{-5}$ | $6.791 \cdot 10^{-4}$ |

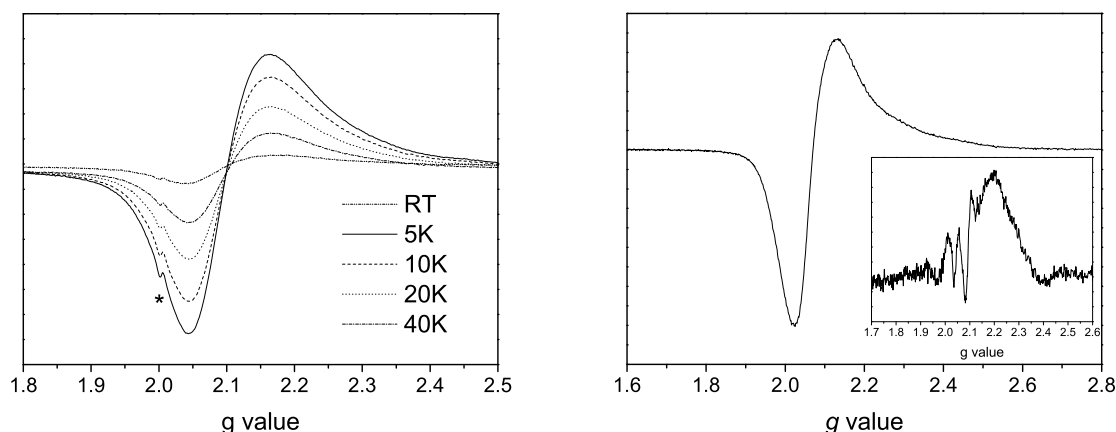


Figure 3.25: Left: X-band ESR spectra recorded on powdered samples of $[(^H\text{TAG})\text{Cu}_3(\text{bipy})_3]\text{ClO}_4$ at room temperature and at 5, 20, 20 and 40 K. The signal marked with an asterisk is a known artifact caused by the resonance cavity. Right: X-band ESR spectra recorded on a frozen solution of $[(^H\text{TAG})\text{Cu}_3(\text{bipy})_3]\text{ClO}_4$ in DMF at 4.3 K. The inset shows the spectrum recorded on a solution of $[(^H\text{TAG})\text{Cu}_3(\text{bipy})_3]\text{ClO}_4$ in DMF at room temperature.

complex anion $[(^{\text{Sulf}}\text{TAG})\text{Cu}_3(\text{bipy})_3]^{2-}$ (**28**) was synthesized *in situ*, which is soluble in methanol and water and can be either precipitated using the bulky *tris*-(2,2'-bipyridyl)ruthenium(II) dichloride ($[\text{Ru}(\text{bipy})_3]\text{Cl}_2$) or be included in the preparation of polyvinylalcohol films.

Since no crystals could be obtained from $[(^{\text{Sulf}}\text{TAG})\text{Cu}_3(\text{bipy})_3][\text{Ru}(\text{bipy})_3]$ the formation of this salt was proven by IR and UV/Vis spectroscopy, thermogravimetry, elemental analysis and mass spectrometry. The IR spectrum shows strong signals, which can be attributed to vibrations of the bipy coligand and the sulfonato group. UV/Vis spectra recorded in aqueous solution show the typical absorption bands found for the trinuclear core and additional bands, which are in good agreement with reported values for the $[\text{Ru}(\text{bipy})_3]^{2+}$ ion (*vide infra*).^[315] Thermogravimetry shows a loss of weight of 13.6% between 80 and 100 °C indicating 17 molecules of water. This is in good agreement with the elemental analysis. The residual mass of 17.1 is slightly higher than the expected, assuming a final composition of RuO and 3 CuO (16.4%) per complex moiety. However, the thermogravimetry curve is still descending at 1000 °C, indicating the final residual mass to be lower than 17.1%. Positive ESI mass spectrum shows a series of strong signals which can be attributed to the complex $[\text{Ru}(\text{bipy})_3]^{2+}$ and its fragments. The negative ESI mass spectrum is dominated by a signal at $\frac{m}{z} = 293$, which can be attributed to a rearranged fragment of $^{\text{Sulf}}\text{TAG}$ being a common fragment formed by

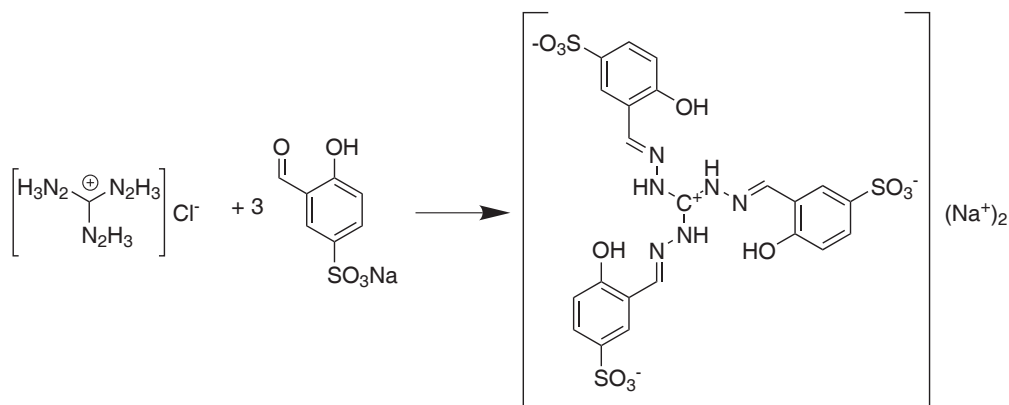


Figure 3.26: Synthesis of the Ligand $\text{Na}_2\text{H}_6^{\text{Sulf}}\text{TAG}$ via Schiff base condensation of triaminoguanidine hydrochloride and sodium 5-sulfonato-2-hydroxy benzaldehyde.

cyclization in complexes of this ligand. Also a signal at $\frac{m}{z} = 419$ is present, which can be assigned to the trimeric core $[(^{\text{Sulf}}\text{TAG})\text{Cu}_3]^{2-}$.

Spectroscopic Characterization

The formation of the complex in methanol was investigated by UV/Vis titrations of $\text{Na}_2\text{H}_6^{\text{Sulf}}\text{TAG}$ with copper(II) and subsequent titration with 2,2'-bipyridyl. The results of the titration with copper(II) ions are shown in Figure 3.27 on the right side. To the solution of the ligand $\text{Na}_2\text{H}_6^{\text{Sulf}}\text{TAG}$ triethylamine was added as base. To avoid side reactions (*vide supra*), only three equivalents were added before addition of copper solution and three after the addition of three equivalents of copper. The change in the spectrum can be seen in Figure 3.27 on the left side.

Upon the first addition of triethylamine the band at 380 nm loses in intensity, which is probably due to the removal of the hydrochloride proton, resulting in a major change of the chromophore. The addition of three equivalents of copper causes significant changes in the spectrum. The band at 340 nm decreases, whereas new bands at 394, 415 and 620 nm arise. There can be seen several crossing points, one set between 308 nm and 328 nm and one between 366 nm and 380 nm. In these points the spectra of the first to fourth, the fifth to eighth and the ninth to twelfth spectrum cross. These stepwise crossings strongly suggest a similar mechanism as it is found for the unsubstituted complex (Equations 3.13 to 3.16), though the change in the spectrum upon the addition

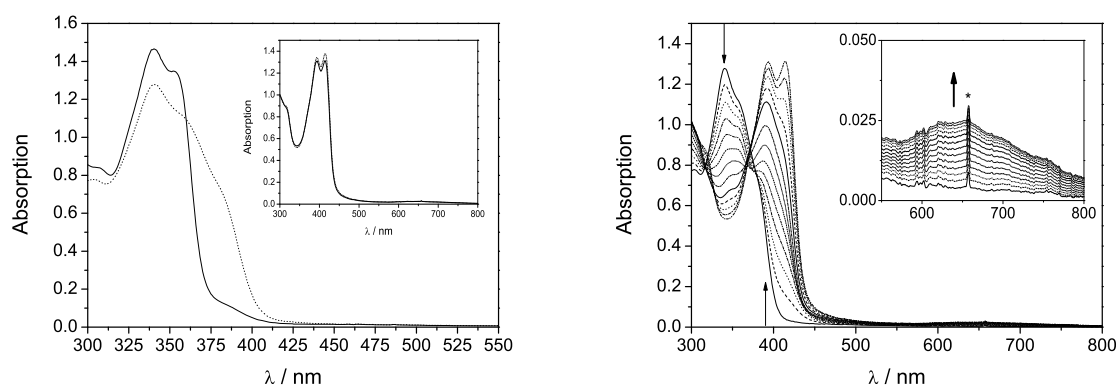


Figure 3.27: Left: Change of absorption spectrum of $\text{Na}_2\text{H}_6^{\text{Sulf}}\text{TAG}$ in 100 mL methanol ($c_{0,\text{L}} = 2.96 \cdot 10^{-5}$ mol/l) in upon addition of three equivalents of triethylamine. Inset: Change of of absorption spectrum of $[(^{\text{Sulf}}\text{TAG})\text{Cu}_3(\text{bipy})_3]^{2-}$ in 100 mL methanol ($c_{0,\text{LCu}_2} = 2.87 \cdot 10^{-5}$ mol/l) upon addition of three equivalents of triethylamine. Right: Titration of $\text{Na}_2\text{H}_6^{\text{Sulf}}\text{TAG}$ in 100 mL methanol ($c_{0,\text{L}} = 2.96 \cdot 10^{-5}$ mol/l) with copper(II)chloride ($c_{0,\text{Cu}} = 6.08 \cdot 10^{-3}$ mol/l, 122 μL per step, in total 3 equivalents). The signal marked with an asterisk is caused by the experimental setup.

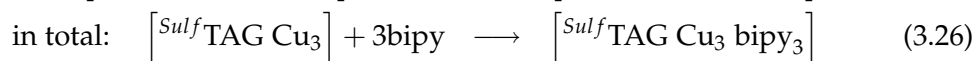
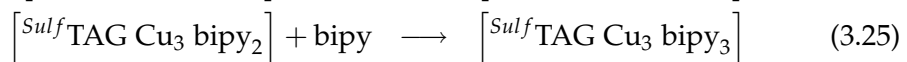
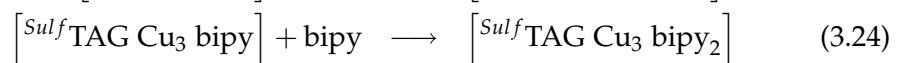
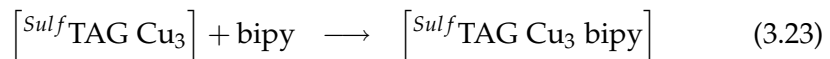
of base suggest, that the deprotonations of the ligand plays a more significant role. However, the negligible changes at the final addition of triethylamine to the solution of $[(^{\text{Sulf}}\text{TAG})\text{Cu}_3(\text{bipy})_3]^{2-}$ (Figure 3.27, left inset) suggest that the deprotonation has still only minor impact on the complex formation. This assumption is strengthened by the strong similarities of the spectra recorded during the addition of copper ions to the unsubstituted Ligand $\text{H}_5^{\text{H}}\text{TAG} \cdot \text{HCl}$ and during the addition of copper ions to the sulfonate derivative $\text{Na}_2\text{H}_6^{\text{Sulf}}\text{TAG}$.

For this reason, the same mechanism (Equations 3.13 to 3.16) and the same equilibrium constants (Equations 3.17 to 3.21) have been used to describe the experimental behavior. Least square fitting of the equilibrium constants against the measured spectra gives the equilibrium constants $K_1 = 1.09 \cdot 10^8$ l/mol, $K_2 = 9.90 \cdot 10^6$ l/mol and $K_3 = 1.32 \cdot 10^5$ l/mol leading to $K_{\text{ges}} = 1.42 \cdot 10^{20}$ l³/mol³ ($\text{p}K_{\text{ges}} = 20.2$). This shows that the sulfonato substituted copper complex has even higher binding constants than the complex based on the unsubstituted ligand. This is not surprising, since the increased negative charge of the deprotonated ligand favors the coordination of the positive metal ions.

In contrast to the results of the unsubstituted ligand $\text{H}_5^{\text{H}}\text{TAG}$ the binding constants decrease upon subsequent filling of the binding pockets. This can be explained by the

stronger basicity of the ligand. Since deprotonation is needed for “opening” a binding pocket for complexation of a copper ion, the stepwise coordination of the three copper centers is much more pronounced. This is also confirmed by the relative intensity of the two bands at 394 and 415 nm. The latter appears only during the addition of the third equivalent of the copper solution and shows, that the presence of both absorption bands is a very good indicator for the presence of the trinuclear copper core structure.

To avoid polymerization^[144;145] 2,2'-bipyridyl (bipy) is used as a capping ligand. The impact of the addition of bipy on the absorption spectra is depicted in Figure 3.28 on the left side. At the beginning, a solution containing one equivalent of ligand, three equivalents of copper(II) and six equivalents of triethylamine is used. There are only slight changes in the spectrum, but the presence of an isosbestic point at 420 nm and the increasing absorption below 320 nm indicate the coordination of the bipy ligands. The following reaction mechanism is assumed:



which gives rise to the following equilibrium constants:

$$K_1 = \frac{c([SulfTAG Cu_3 bipy])}{c([SulfTAG Cu_3]) \cdot c(bipy)} \quad (3.27)$$

$$K_1 = \frac{c([SulfTAG Cu_3 bipy_2])}{c([SulfTAG Cu_3 bipy]) \cdot c(bipy)} \quad (3.28)$$

$$K_1 = \frac{c([SulfTAG Cu_3 bipy_3])}{c([SulfTAG Cu_3 bipy_2]) \cdot c(bipy)} \quad (3.29)$$

$$K_{ges} = \frac{c([SulfTAG Cu_3 bipy_3])}{c([SulfTAG Cu_3]) \cdot c^3(bipy)} \quad (3.30)$$

$$= K_1 \cdot K_2 \cdot K_3 \quad (3.31)$$

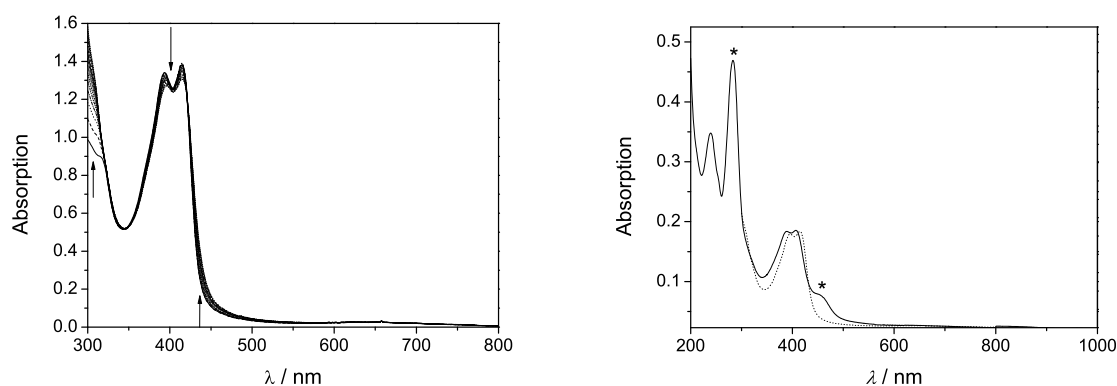


Figure 3.28: Left: Titration of $[(^{Sulf}TAG)Cu_3]$ ($c_{0,LCu_3} = 2.91 \cdot 10^{-5}$ mol/l) with 2,2'-bipyridyl ($c_{0,bipy} = 5.67 \cdot 10^{-3}$ mol/l, $131 \mu\text{L}$ per step, in total 3 equivalents) in 100 mL methanol. Right: Absorbance spectrum of $[(^{Sulf}TAG)Cu_3(bipy)_3][Ru(bipy)_3]$ recorded on an aqueous solution. The dotted line represent a scaled spectrum of the in-situ formed complex $[(^{Sulf}TAG)Cu_3(bipy)_3]^{2-}$ as obtained after the titration with three equivalents of copper and three equivalents of bipy as described in the text. The absorptions marked with asterisks are attributed to the $[Ru(bipy)_3]^{2+}$ counter ion (see text).

The equilibrium constants $K_1 = 3.66 \cdot 10^4$ l/mol, $K_2 = 1.51 \cdot 10^5$ l/mol and $K_3 = 2.57 \cdot 10^5$ l/mol can be obtained by least square fitting to the experimental UV/Vis-spectra and give rise to an overall binding constant $K_{ges} = 1.42 \cdot 10^{15}$ l³/mol³ ($pK_{ges} = 15.2$). This shows that the bipy binds to the trinuclear copper core with quite high formation constants. In conclusion, the spectral behavior of the sulfonato substituted ligand ^{Sulf}TAG is very similar to that of the unsubstituted compound $^H TAG$ and shows once more, that the double band around 400 nm is a good indicator for the presence of the trinuclear core structure.

This double band is also present in the spectrum of $[(^{Sulf}TAG)Cu_3(bipy)_3][Ru(bipy)_3]$ when dissolved in water. Due to the very low solubility only small amounts can be dissolved and the determination of the molar absorbance coefficient ϵ is very inaccurate. Therefore only a qualitative absorbance spectrum was recorded (Figure 3.28 on the right side), which shows the expected signals for the trinuclear copper complex, especially the double band around 400 nm. The slight shift can be explained by the change in the dielectrical constant when going from methanol to an aqueous solution. The strong band at 284 nm can be assigned to the coordinated bipy coligand, which is present in the trinuclear complex and in the ruthenium fragment. The shoulder at 450 nm corresponds well to the absorptions observed for $[Ru(bipy)_3]Cl_2$.^[315] These results are in very good agreement with the presence of $[(^{Sulf}TAG)Cu_3(bipy)_3]^{2-}$ and $[Ru(bipy)_3]^{2+}$ counter ions in solution.

Incorporation in Polymer-Films

Incorporation into a polymer matrix leads to well separated molecules without rotational averaging at room temperatures — and therefore without loss of spatial information. Films were prepared by adding a methanolic stock solution of $[(^{Sulf}TAG)Cu_3(bipy)_3]^{2-}$ to an aqueous polyvinylalcohol solution ($c = 100$ g/l). After homogenization the resulting solution is poured onto glass substrates and left standing for evaporation of the solvent. After few hours thin films are obtained. The presence of the trinuclear complex structure was proven by UV/Vis spectroscopy on films containing different concentrations of $[(^{Sulf}TAG)Cu_3(bipy)_3]^{2-}$. As one can see in Figure 3.29 the spectrum of the films is proportional to the volume of complex solution added and resembles very much the spectra obtained for $[(^H TAG)Cu_3(bipy)_3]^+$ in DMF and it also agrees with the spectra obtained in the UV/Vis titrations of $[(^{Sulf}TAG)Cu_3(bipy)_3]^{2-}$ and $[(^H TAG)Cu_3(bipy)_3]^+$. There are only minor shifts in the signal, as it is expected in changing the solvent/environment, and the lines are broadened.

Magnetic Properties

The temperature dependence of the magnetic susceptibility of **28** was determined on powder samples of $[(^{Sulf}TAG)Cu_3(bipy)_3][Ru(bipy)_3]$ and on polyvinylalcohol films in

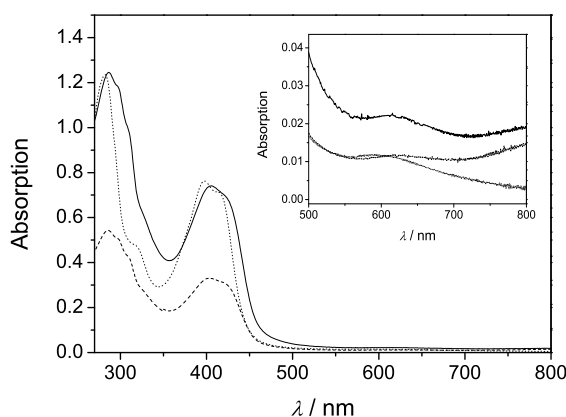


Figure 3.29: UV/Vis spectra recorded on $[(^{Sulf}TAG)Cu_3(bipy)_3]^{2-}$ incorporated in polyvinylalcohol films with two different concentrations (solid and dashed lines) The dotted line represents the spectrum recorded on $[(^H TAG)Cu_3(bipy)_3]^+$ in DMF solution. The inset enlarges the absorption band around 620 nm.

the temperature range between 2 and 300 K. Plots of $\chi_M = f(T)$ and $\chi_M T = f(T)$ are depicted in Figure 3.30. The decrease of $\chi_M T$ at low temperatures, described by intermolecular interactions in the case of $[(^H\text{TAG})\text{Cu}_3(\text{bipy})_3]\text{ClO}_4$ (Figure 3.24)^[308] is also present in the polymer based films and is even stronger than in the case of the unsubstituted trimer. Interestingly neither the polyvinylalcohol sample nor the precipitated powder of $[(^{\text{Sulf}}\text{TAG})\text{Cu}_3(\text{bipy})_3][\text{Ru}(\text{bipy})_3]$ show any sign of decoupling at high temperatures. This indicates an increase in J up to more than 400 cm^{-1} in comparison to the unsubstituted complex.

X-band ESR spectra were recorded on a methanolic solution of $[(^{\text{Sulf}}\text{TAG})\text{Cu}_3(\text{bipy})_3]^{2-}$ at room temperature (Figure 3.31, left) and on a frozen methanolic solution at 77 K (Figure 3.31, right). The solution spectrum resembles very much the one recorded for $[(^H\text{TAG})\text{Cu}_3(\text{bipy})_3](\text{ClO}_4)$. It also consists of a signal with a broad unresolved low-field side and a structured high-field side, showing a hyperfine spacing of 67 G. It is located between 2940 and 3520 G, giving an intermediate $g_{\text{av}} = 2.165$. The frozen solution spectra shows an perpendicular signal with $g_{\perp} = 2.130$, $g_{\parallel} = 2.325$ and a hyperfine spacing of $A_z = 150 \text{ G}$.

X-band ESR spectra were also recorded on powder samples of $[(^{\text{Sulf}}\text{TAG})\text{Cu}_3(\text{bipy})_3][\text{Ru}(\text{bipy})_3]$ at room temperature and at 77 K (Figure 3.32, left). While the spectrum recorded at room temperature is rather unstructured, the spectrum recorded at 77 K reveals an extended structure. The perpendicular signal at $g_{\perp} = 2.098$ shows an unstructured low-field side and an rather resolved splitting on the high-field

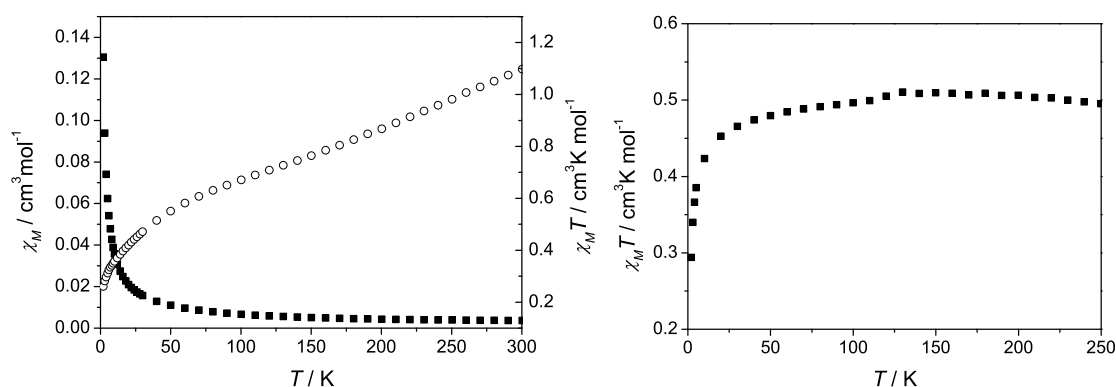


Figure 3.30: Temperature dependence of χ_M (black boxes) and $\chi_M T$ (open circles) measured on films containing $[(^{\text{Sulf}}\text{TAG})\text{Cu}_3(\text{bipy})_3]^{2-}$ (left) and on powder samples of $[(^{\text{Sulf}}\text{TAG})\text{Cu}_3(\text{bipy})_3][\text{Ru}(\text{bipy})_3]$ (right).

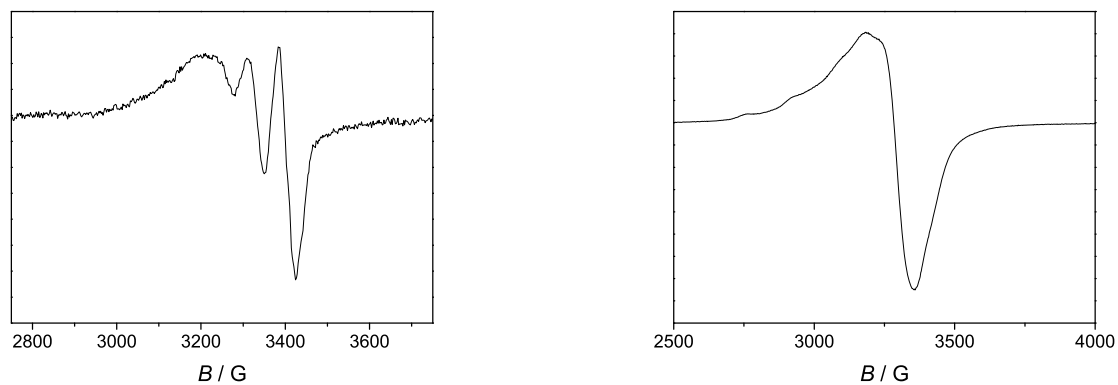


Figure 3.31: X-band ESR spectra recorded on a methanolic solution of $[(^{Sulf}TAG)Cu_3(bipy)_3]^{2-}$ at room temperature (left) and on a frozen solution at 77 K (right).

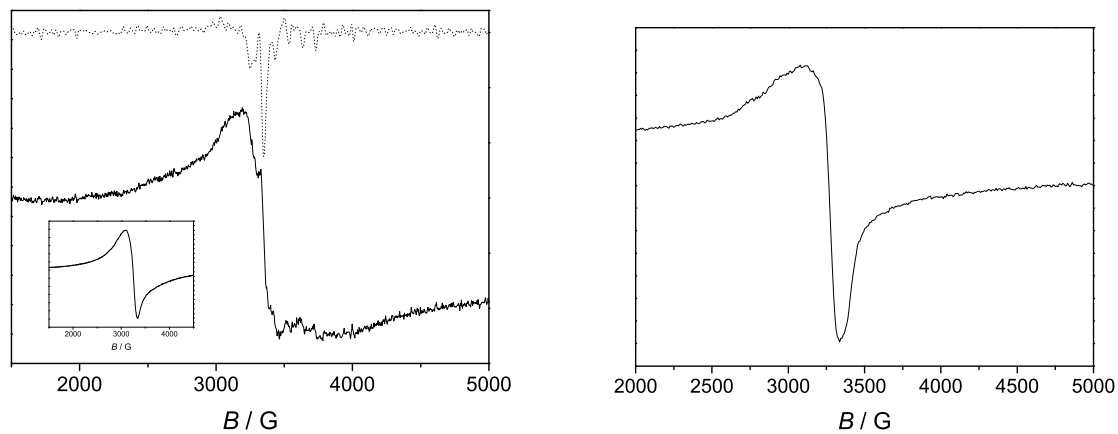


Figure 3.32: X-band ESR spectra recorded on powder samples of $[(^{Sulf}TAG)Cu_3(bipy)_3][Ru(bipy)_3]$ at 77 K (left) and room temperature (inset). The dotted line represent the first derivative of the spectrum (to reduce the noise the derivative was smoothed using a binomial algorithm with 25 points). Right: X-band ESR spectrum recorded on a polyvinylalcohol film containing $[(^{Sulf}TAG)Cu_3(bipy)_3]^{2-}$ at 77 K.

side. This effect is very similar to the observations in solution and seems to be an inherent feature of this type of molecule. The similarity of the powder spectrum of $[(^{Sulf}TAG)Cu_3(bipy)_3][Ru(bipy)_3]$ and the frozen solution spectrum of $[(^H TAG)Cu_3(bipy)_3](ClO_4)$ suggests, that the molecules are either closely stacked in solution or, more probable, that the bulky and non-coordinating counter ion $[Ru(bipy)_3]^{2+}$ leads to a rather good separation in the solid state. The ESR spectra recorded on $[(^{Sulf}TAG)Cu_3(bipy)_3]^{2-}$ incorporated in polyvinyl films is very similar to the one, which was recorded on a frozen solution of $[(^{Sulf}TAG)Cu_3(bipy)_3]^{2-}$. This is a further evidence for the presence of the trinuclear copper core in the polymeric matrix.

3.4 Outlook

The methoxy group of the amine precursor **9** can be readily removed via reaction with bortribromide to give the free hydroxy group.^[316] Because of the Lewis basicity of the two amino groups a threefold excess of bortribromide is needed. The obtained precursor **17** reacts readily with (sulfonated) salicylaldehyde to give the corresponding ligands Na₂H₂CarbOH (**18**) or H₂^{Sulf}CarbOH. Whereas the precursor and the unsubstituted ligand are obtained with rather low purity, the sulfonate substituted ligand is obtained with good purity in high yields.

The linkage of ^{Sulf}Mesalen-complexes via hydrogen bonded ammonium groups in the outer O₄ coordination environment opens up a great variety of potential applications and new molecular aggregates:

- At first one could think of replacing the ethylenediamine by functional diamines. Using a redox active spacer would give access to molecules which can be used as molecular switches. Via oxidation or reduction a radical species can be generated between two linked ^{Sulf}Mesalen-complex molecules. This will have a great impact on the overall coupling scheme.
- Besides magnetochemistry the observed structural features are also of very high interest with regard to catalysis. The Salen-type ligands are known to be highly active catalysts in a variety of reactions. Especially manganese based systems are known as superoxide dismutase and catalase analogs. On the one hand, the solubility in very polar and/or protic environments open up new conditions for the reactions.
- The binding of the ^{Sulf}Mesalen-based catalysts to an ammonium functionality might be used for separation after the reaction. Using a swellable polymer carrying ammonium groups would bind the catalyst, which then can be removed easily from the solution by filtration. Probably the catalyst could even be recovered from the polymer upon deprotonation of the ammonium groups.
- Especially the binding motive of diammoniumethylene in the copper compound **22** opens up a lot of highly interesting possibilities. Great effort is spent to position proton donating groups near the axial position of the metal.^[270] This is due to the assumption that a high valent metal species is formed during oxygen transfer

reactions with an axially bound oxygen atom. The presence of acidic protons in the environment is thought to activate this oxygen for the transfer. As one can see in Figure 3.13 the second ammonium is positioned very nicely by hydrogen bonding. Introducing an acidic group at the alpha carbon atom might indeed bring this group into the perfect position for proton donation.

The trinuclear copper complexes based on the triaminoguanidine backbone demand a detailed analysis of the magnetic structure and tests if and how these compounds perform as qubits working in a coherence free subsystem. For this reason, sophisticated ESR measurements are necessary, that means pulsed ESR techniques to determine the coherence times for the complexes. In addition, ways of preparing and manipulating entangled states of single qubits have to be developed. One possible way would be the interaction of an applied electric field with the chirality of the antisymmetric exchange.^[132]

Concerning the triaminoguanidine based systems, the obtained results show several points of contact for further research. The incorporation into a polymeric matrix is a promising way to new innovative materials for quantum computing. With the use of other bulky counter ions crystalline structures with widely separated molecules should be accessible, which then should be analyzed by single crystal magnetic studies. This would enlighten the coupling mechanisms inside the trinuclear core. However, it should be stressed, that the obtained antisymmetric exchange parameter for the unsubstituted compound $[(^H\text{TAG})\text{Cu}_3(\text{bipy})_3](\text{ClO}_4)$ are rather small even in the case of neglected intermolecular interactions. Once more, this suggests the triaminoguanidine to be an ideal candidate for quantum bit storing.

4 Linked Building Blocks

Symmetry is of great importance in many fields of chemistry. However, in the field of molecular magnetism it plays an extraordinary role. The overlap of orbitals and hence the exchange interactions between the magnetic centers crucially depend on it.^[317] In the case of orthogonality of the magnetic orbitals ferromagnetic interactions arise leading to high spin systems while symmetry-allowed overlap, antiferromagnetic interactions are achieved. They both lead to fascinating phenomena like Single Molecule Magnets (SMMs)^[39] or magnetic cooling^[98] in the first case or spin frustration in the second.^[19;99–103]

All these potential applications need appropriate symmetry. In the case of SMMs the height of the activation barrier ΔE for spin relaxation depends on the square of the total spin and the axial anisotropy (ΔE proportional to $-DS^2$ for systems with an even number of electrons and ΔE proportional to $-D(S^2 - \frac{1}{4})$ for an odd number of electrons). However, if the symmetry is lower than axial the rhombic anisotropy, characterized by the parameter E , new channels for relaxation are opened by mixing of states.^[39;66]

The simplest case for a spin frustrated system is an antiferromagnetically coupled triangular system with uneven spins. Frustration takes place in the case of three isotropic exchange interactions of the same size. If the exchange interactions differ a little bit, the degeneration of the ground state will be lifted. If the three spins are symmetry related by a three-fold rotational axis, the exchange pathways are also identical and hence the coupling strength. Lifting of the degeneracy is then only possible by structural deformation and symmetry reduction at low temperatures or by antisymmetric interactions.

To obtain polynuclear metal complexes of a certain symmetry, one way is the use symmetry inducing ligands (SIL) usually having the same symmetry. Up to now a

lot of C_3 symmetric ligands have been reported,^[58;59;144;145;197;306;308;309;318–330] but in most cases the resulting transition metal complexes have a lower symmetry. Only few examples are known, in which the symmetry is preserved in the final crystal structure.^[58;58;59;145;308;309;324;328;329] Whereas triaminoguanidine based systems^[145;308;308;329] in most cases lead to C_3 -symmetric compounds, only some examples are known among the large number of reported compounds, for example based on substituted phloroglucine. This is mainly due to the introduction of side arms to favor the coordination of the metal ions and the crystallization of the metal complex. These sidearms and their functional groups lead to additional interaction between neighboring molecules and these interactions lower the symmetry in most cases. π - π interactions, for example, are often found when the sidearms contain aromatic functionalities like pyridines. The flexibility needed for the coordination introduces additional asymmetry. The bridging SIL should therefore be very stiff and rigid.

As mentioned before, these requirements make triaminoguanidine-based ligands excellent candidates in the case of antiferromagnetic interactions. If ferromagnetic interactions are desired, the problem is a little bit more difficult. One possible mechanism to gain ferromagnetic interactions is the spin polarization. This utilizes the π -electrons in unsaturated systems and depends on the number of mediating atoms. *meta*-Substituted aromatic systems are commonly used to achieve ferromagnetic coupling and are very rigid as well. Derivatives of phloroglucine used for example by Glaser et al.^[318;321;324;326;331] have been shown to give rise to ferromagnetic interactions and they also possess C_3 -symmetry. However, in most cases the overall symmetry in the crystal is much lower. It has been shown, that the use of acetyl substituted phloroglucine itself opens a route to highly symmetric trinuclear copper complexes.^[332] The first section of this chapter deals with the effect that the overall symmetry has on the magnetic measurements performed.

The symmetry of the coordination environment is of great interest when dealing with lanthanides. Their unique properties with regard to size of spin ($S \leq \frac{7}{2}$), anisotropy (several cm^{-1}) and fluorescence make them ideal candidates for the incorporation into functional materials. In the lanthanide (and actinide) series the properties are determined by the filling of the *f*-shell and the interaction of these electrons with the coordination environment (ligand field) as well as the orbital momentum (spin-orbit coup-

ling). While the latter is rather strong and generally leads to well-separated energy levels, the former is much weaker than in the case of *d*-elements and crucially influences the properties of the system.

In most cases the spin-orbit coupling is so strong, that the analysis can be simplified by replacing the spin *S* and orbital momentum *L* by the total angular momentum *J* with the lowest energy. Due to the change in sign of the spin-orbit coupling constant λ this is the state with the smallest *J*, if the *f* shell is less than half filled and otherwise the state with the highest *J*. In the case of europium(III) and samarium(II) the energy separation between the states with different *J* is so small, that the excited levels have a major influence on the magnetic properties at room temperature. The analysis of the ligand field is hampered by several aspects:

Number of Parameters: Increasing *L* from 2 to 3 when moving from a *d* to an *f*-shell results in the inclusion of four additional parameters (B_0^6, B_3^6, B_4^6 and B_6^6).

Symmetry: In the case of higher symmetry several ligand field parameters vanish and do not have to be included. However, due to the weak coordination in combination with the high and flexible coordination number, in most cases the symmetry is rather low and hard to determine. When dealing with multinuclear compounds one has also to consider the possible relative orientation of the particular internal axis.

Structure: Lanthanides show high and flexible coordination numbers. The coordination is rather weak and due to the strong shielding of the *f*-orbitals only of minor covalent character. On the other hand, this also represents one major advantage: since also the ionic radii are rather similar along the lanthanide series and the increasing number of *f*-electrons does not affect the general bondings, different lanthanide often give isostructural compounds when reacted under similar conditions.

Basis Set: To simplify the evaluation of data, in cases with a well separated ground multiplet, the ligand field operators can be replaced by operators acting on the total angular momentum *J* (operator equivalent method). However, the size of these operators depends on the actual value of *J* and needs to be transformed when comparing isostructural complexes with different lanthanide ions. The use of several different definitions in literature makes things even more complicate.

One well-known way to incorporate rare-earth elements in coordination compounds is the use of Salen type ligands which are substituted with alkoxy groups in *ortho*-position to the hydroxy group. The methoxy derivatives are commonly called Mesalen ligands (Section 3.2) and readily react with transition metals like for instance copper(II) by filling the inner N_2O_2 coordination site. The outer O_4 cavity can then be filled by reaction with lanthanide ions to give the heterodiuuclear M–Ln-units.^[281–289] These are common building blocks for the construction of one-, two- and three-dimensional superstructures, especially since the spin–spin interactions are usually ferromagnetic and therefore provide a large spin ground state.^[333;334] The second section deals with the magnetic properties of such an one-dimensional coordination polymer containing Cu–Ln-entities with Ln = La, Pr, Sm, Eu, Gd, Tb, Dy.^[156;309]

In the case of desired antiferromagnetic interactions with C_3 -symmetry hexaazatriphenylene^[335] and triaminoguanidine^[145] are potential candidates, while the latter gives much stronger interactions. On the further way to functional materials the linkage of these molecules is crucial. The demands to be fulfilled vary from application to application, but in every case one has to search for linkage in a predefined manner. In the case of the trinuclear systems described above one can think of different ways of linkage: Two triangles could be connected edge-to-edge by a linking molecule, in an edge sharing manner or they could share a vertex.^[216;335;336] But not only the mode of junction is to be controlled but also the number of molecules connected, because only then the synthetic control over the alloy size is guaranteed.

The third section of this chapter deals with a series of heterometallic pentanuclear compounds based on a triaminoguanidine core. Complexes based on this type of ligand have been shown to give access to trinuclear metal complexes^[308;309;329] as well as metal organic frameworks (MOFs).^[144;145] The pentanuclear complexes close the gap between monomeric and polymeric compounds. In contrast to reported fused triangles, which are mainly built up by self assembly of small compartments, these new complexes are synthesized in a successive coordination approach to obtain functional molecules preserving the properties of the monomeric complexes.^[213;337] This section enlightens the magnetic properties of these molecules and the preservation of the fundamental exchange properties in these rather complex molecules.

4.1 Highly Symmetric Copper Complex

4.1.1 Synthesis and Structure

The synthesis and structure of $[(\text{phloro})\text{Cu}_3(\text{bhea})_3](\text{ClO}_4)_3$ have been reported elsewhere.^[332] A short summary of the structural features relevant for the magnetic discussion is given in the following paragraphs.

The copper precursor is prepared of $\text{Cu}(\text{ClO}_4)_2$ and *N,N*-bis-2-hydroxyethyl-ethylene diamine (bhea). Three precursor molecules react with the bridging 2,4,6-triacetyl-1,3,5-trihydroxybenzen (phloro^{3-}) to form the complex $[(\text{phloro})\text{Cu}_3(\text{bhea})_3](\text{ClO}_4)_3$ (Figure 4.1, left). The equatorial planes of the copper coordination sphere are canted against each other by an angle of 25° with copper–copper distances of 725 pm. These disk shaped molecules are stacked in columns (Figure 4.1, middle), which form a hexagonal arrangement with a intercolumn distance of $d = 1514$ pm. The symmetry of the ligand is therefore nicely transferred into the crystal structure and also the shape of

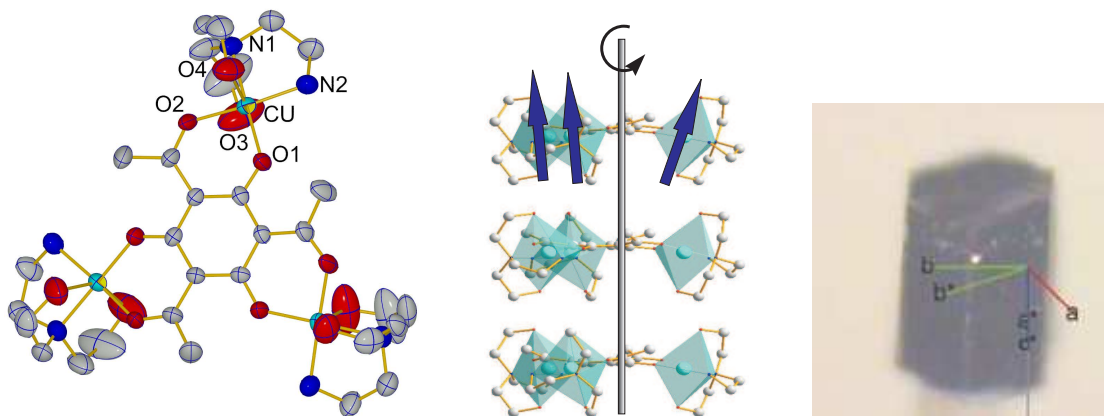


Figure 4.1: Left: Molecular structure and selected numbering scheme of the complex $[(\text{phloro})\text{Cu}_3(\text{bhea})_3](\text{ClO}_4)_3$ (**29**) as viewed along the crystallographic *c*-axis. Only the cationic core is shown; thermal ellipsoids are drawn at 50 % probability; hydrogen atoms have been omitted for clarity. Middle: Packing of $[\text{Cu}_3(\text{phloro})(\text{bhea})_3]^{3+}$ **29** as viewed along the crystallographic *b*-axis showing the stacked copper triads as seen from the side. The tilting of the individual copper octahedra is indicated by arrows as well as the threefold rotational axis. Right: Projection of crystallographic axis onto the shape of the crystal.

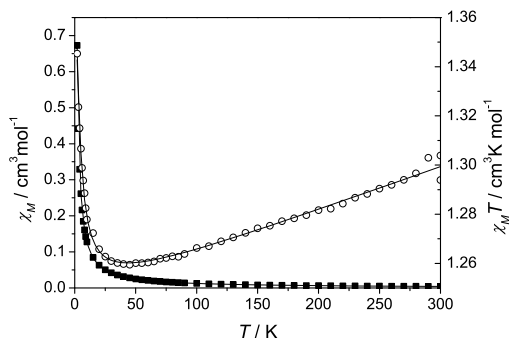


Figure 4.2: Thermal dependency of χ_M (black squares) and $\chi_M T$ (empty circles) measured on powder samples of $[(\text{phloro})\text{Cu}_3(\text{bhea})_3](\text{ClO}_4)_3$. The solid lines represent the simulation with the parameters mentioned in the text.

the crystal reflects this successful transfer, since the long axis of the obtained needles coincides with the threefold rotational axis and the crystallographic c -axis (Figure 4.1, right).

4.1.2 Magnetic Measurements

The temperature dependence of the magnetization was studied on powder samples of the trinuclear compound **29** in the 2 – 300 K range. These data are shown in Figure 4.2 in the form of $\chi_M T = f(T)$ and $\chi_M = f(T)$ plots, where χ_M is the molar paramagnetic susceptibility. At high temperature the $\chi_M T$ value increases due to a temperature independent paramagnetic susceptibility. Below 45 K the $\chi_M T$ value increases indicating ferromagnetic coupling between the three copper centers.

Even though the intermolecular copper–copper distances are shorter than the intramolecular ones, magnetic coupling mediated by spinpolarization in the phloro³⁻ ligand is assumed to be stronger than the intermolecular interactions. This is supported by the long intermolecular oxygen–oxygen distances, which make a hydrogen bonding mediated coupling improbable. The corresponding Hamiltonian

$$\hat{H} = -J_{\text{CuCu}} (\hat{S}_{\text{Cu1}}\hat{S}_{\text{Cu2}} + \hat{S}_{\text{Cu1}}\hat{S}_{\text{Cu3}} + \hat{S}_{\text{Cu2}}\hat{S}_{\text{Cu3}})$$

($S_{\text{Cu1}} = S_{\text{Cu2}} = S_{\text{Cu3}} = \frac{1}{2}$) can be solved analytically:^[7]

$$\chi_{MT} = \frac{N \cdot \beta^2 \cdot g_{\text{Cu}}^2 \cdot T}{2 \cdot k(T - \theta)} \frac{1 + 5 \exp\left(\frac{-3 \cdot J_{\text{CuCu}}}{2 \cdot k \cdot T}\right)}{1 + \exp\left(\frac{-3 \cdot J_{\text{CuCu}}}{2 \cdot k \cdot T}\right)} + \chi_{\text{TIP}} T \quad (4.1)$$

where g_{Cu} is the gyromagnetic factor of the copper centers, θ is the mean field parameter, J_{CuCu} the isotropic coupling constants and χ_{TIP} the temperature independent paramagnetism.^[7] By fitting the parameters of this expression to the experimental values, the following values are obtained: $g_{\text{Cu}} = 2.1031(6)$ and $J_{\text{CuCu}} = -1.10(4) \text{ cm}^{-1}$ with $\chi_{\text{TIP}} = 0.00018(1) \text{ cm}^3 \text{ mol}^{-1}$ and $\theta = -0.51(2)$, leading to a coefficient of determination $R^2 = 0.98892$. The calculated curve is depicted in Figure 4.2.

4.1.3 ESR Spectroscopy

X-band ESR spectra recorded on powder samples at 4.5 K exhibit an axial spectrum with $g_{\perp} = 2.074$ and $g_{\parallel} = 2.212$ (Figure 4.3 on the left side). Single crystal ESR spectra in the X-band were recorded at room temperature and at 5 K. As mentioned above the long axis of the needles coincides with the crystallographic c -axis. The spectra show no variation on rotation along this axis and a single resonance at $g = 2.076$ is observed. While rotating around an axis perpendicular to the c -axis, the g -value varies between 2.063 and 2.231 (bottom of Figure 4.4 and Figure 4.6). The recorded spectra lack any fine structure and only one signal is observed (top of Figure 4.4).

With the use of the expression

$$g = \sqrt{g_{\perp}^2 \cdot \sin^2 \alpha + g_{\parallel}^2 \cdot \cos^2 \alpha} \quad (4.2)$$

where α is the rotation angle, the g -values $g_{\perp} = 2.0633(4)$ ($g_{\perp} = 2.0815(9)$) and $g_{\parallel} = 2.2303(4)$ ($2.2343(9)$) are obtained at 4 K (room temperature) with an agreement factor of $R^2 = 0.99978$ (0.99688 , Figure 4.6). The increase at room temperature might be due to population of the excited $S = \frac{1}{2}$ levels and, probably more important, to a worse fit because of a lower signal-to-noise ratio. The average gyromagnetic ratio^[7] at 4 K

$$g_{\text{av}} = \sqrt{(2 \cdot g_{\perp}^2 + g_{\parallel}^2)/3} = 2.120 \quad (4.3)$$

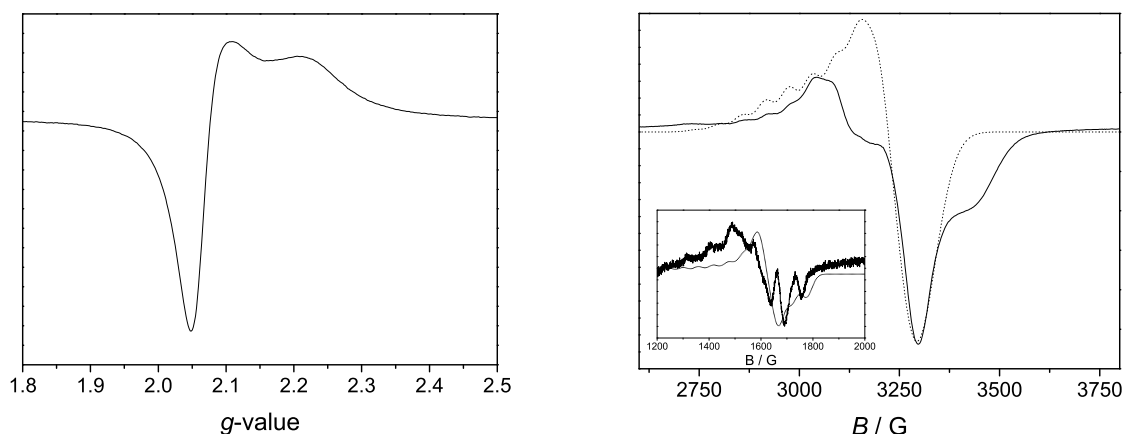


Figure 4.3: Left: X-band spectrum recorded on a powder sample of $[(\text{phloro})\text{Cu}_3(\text{bhea})_3](\text{ClO}_4)_3$ at 5 K. Right: X-Band spectrum of $[(\text{phloro})\text{Cu}_3(\text{bhea})_3](\text{ClO}_4)_3$ in a frozen solution of ethanol/acetonitrile 1:1 at 5 K, dotted line: simulated spectra (see text), inset: half field transition.

corresponds very well to the value obtained from the susceptibility measurements (*vide supra*).

In this particular compound, the presence and sign of exchange interactions can also be deduced from the ESR measurements. In the absence of any coupling one would expect a separate signal for every copper ion. The distance between the signals depends on the tilting angles between the coordination octahedra. The slope in the $g = f(\alpha)$ plot is largest around $\alpha = \pi/4$ and consequently the splitting between the g -values belonging to different tilting angles as well. This case is indicated in Figure 4.6 by the dashed lines for two angles around $\alpha = \pi/4$ differing by 0.44 (25°). This value corresponds to the tilting of the copper octahedra in the crystal structure (*vide supra*). For these angles the splitting of the g -values of the two independent copper ions would be 0.075 and hence well resolved under the experimental conditions. The presence of only one signal or the absence of line broadening around $\pi/4$ due to unresolved lines is evidence for the presence of exchange interactions. Since all the trinuclear complexes in the crystal are oriented collinear there is only one resonance per rotation angle.

The sign of the coupling constant can be derived from the hyperfine pattern. The number of lines as well as the magnitude of the splitting depend on the spin densities at the copper ions. The density is correlated to the coefficients of the wave function.

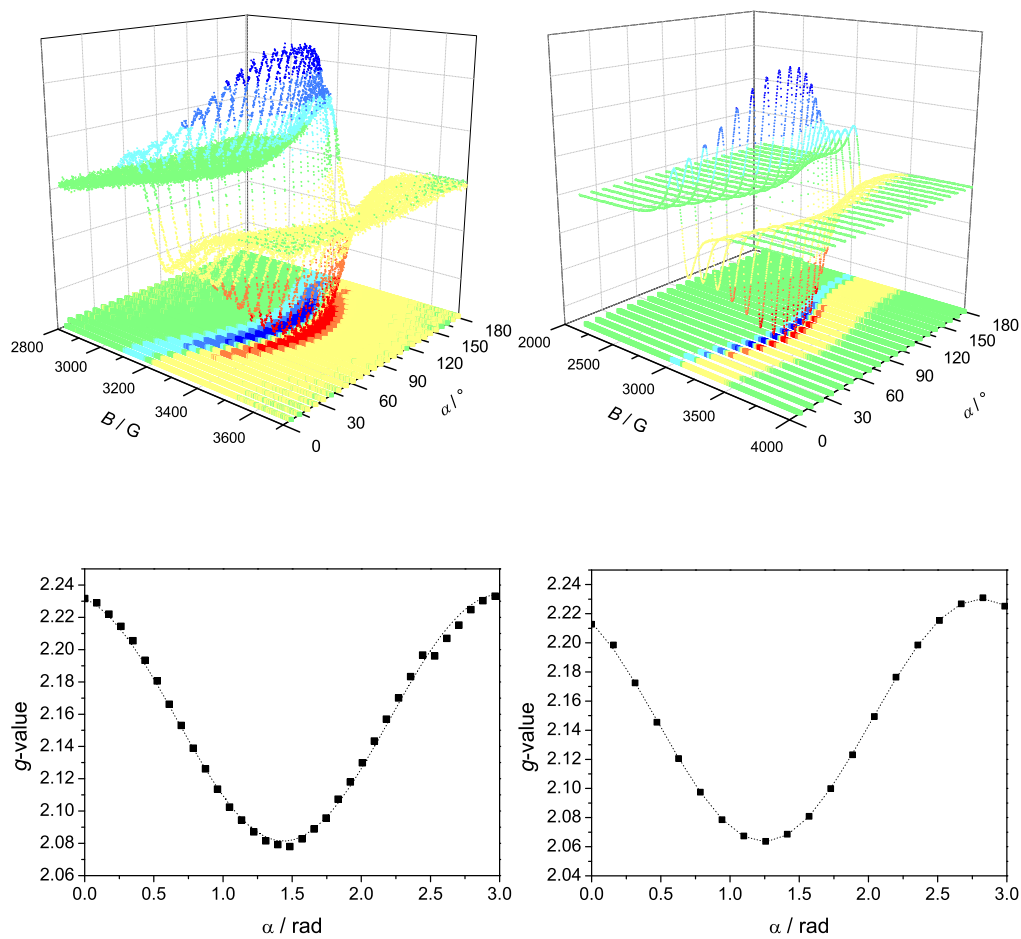


Figure 4.4: X-band spectra recorded at room temperature (top left) and 4 K (top right) at angles between 0 and 90° and angle dependence of the g -value at room temperature (bottom left) and at 4 K (bottom right) as function of the rotational angle α (black squares). The dotted lines represent the calculated values with the parameters mentioned in the text.

If the coupling is ferromagnetic, all coefficients are equal and lead to ten hyperfine lines equally spaced by an effective hyperfine splitting, which is one third of the single ion splitting.^[9] In the case of antiferromagnetic interactions the situation is more difficult due to the complex situation regarding the spin frustrated system. However, the spin density is not equally distributed and the hyperfine pattern will not be as simple as in the case of a ferromagnetic ground state. Unfortunately, the hyperfine structure cannot be resolved in the single crystal spectra because of the strong broadening due to dipolar spin–spin interactions between the closely stacked disk-shaped molecules.

To reduce these interactions in order to resolve the hyperfine structure, spectra were recorded on samples in frozen solution. Few mg of **29** were dissolved in ethanol/acetonitrile mixture (1:1) to give a blue solution, which was immediately cooled down to 5 K. The obtained spectrum (Figure 4.3, right) consists of a parallel transition split into several lines with a line distance of approximately 60 G and a structured perpendicular transition. Also the half field transition can be detected (inset in Figure 4.3) and shows the same line distance of around 60 G as the parallel transition. A simulation using the parameters $[g_x, g_y, g_z] = [2.063, 2.063, 2.230]$ and $A_{\parallel} = 64$ G on a $S = \frac{3}{2}$ system reproduces very well the hyperfine splitting (dotted line in 4.3, right) as well as the half field signal (inset in Figure 4.3). The hyperfine constant reprojected onto a single copper would be $A_{Cu} = 3 \cdot A_{\frac{3}{2}} = 192$ G^[9], which is in very good agreement with reported values for a N₂O₂ coordination environment in the equatorial plane.^[338]

However, strong deviations around the perpendicular transition are present. After re-warming the complex solution a color change could be seen and within a few hours the solution turned completely green. Most probably the free amino group of the bhea ligand and the carbonyl group of the acetyl group react to form a Schiff-base under the release of water. The presence of additional complex species would explain the deviation of the simulated spectra from the measured one as well as the color change when the octahedral environment changes to a pentacoordinated one. But the good agreement between the g -values in the simulation and the ones from the single crystal measurement indicates that the observed hyperfine splitting is due to the complex **29**, in which the copper ions are ferromagnetically coupled and can be treated as an $S = \frac{3}{2}$ system.

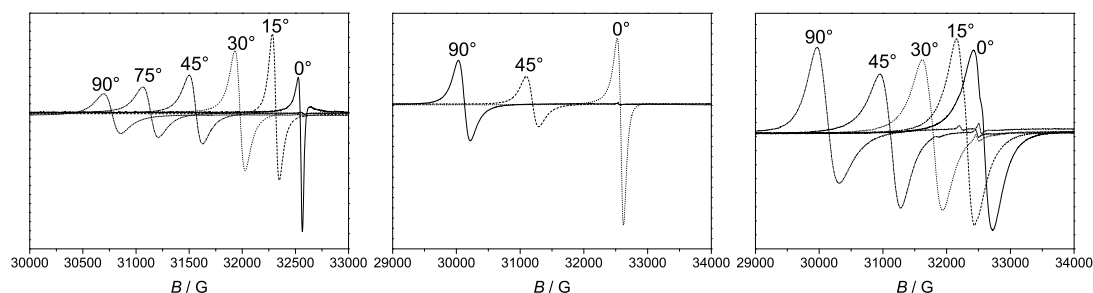


Figure 4.5: W-band spectra recorded at room temperature (left), 40 K (middle) and 10 K (right) at several angles between 0 (perpendicular to the long axis) and 90° (parallel to the long axis).

To exploit the higher separation in g -values when applying higher fields, measurements were also performed in W-band. Spectra were recorded on a single crystal by rotating around an axis perpendicular to the c -axis. The obtained spectra show no fine or hyperfine structure (Figure 4.5) and their dependence of the rotation angle fits the one obtained at X-band (Figure 4.6). They confirm the conclusions gained from the X-band analysis: the observed signals are based on the coupled system rather than on uncoupled copper ions.

Varying the temperature has no effect on the position of the signal. Spectra were recorded at 10 K, 40 K and 150 K and fit the angle dependence obtained from the X-band results. Only the line shapes change: At low temperatures the signals get broader. When the field is perpendicular to the c -axis also an asymmetry in the line shape can be observed on raising the temperatures (4.7, left).

It should be noted, that it was not possible to obtain proper powder spectra in the W-band without orientational effects, even on thoroughly grinded samples mixed with wax. The presence of only one orientation per crystallite leads to a non random distribution of orientations. The recorded spectra (Figure 4.7, right) show a series of additional signals, which are only due to not randomly oriented molecules. This shows the precaution systems with high symmetry should be handled with in powder measurements which require statistical distributions of orientations.

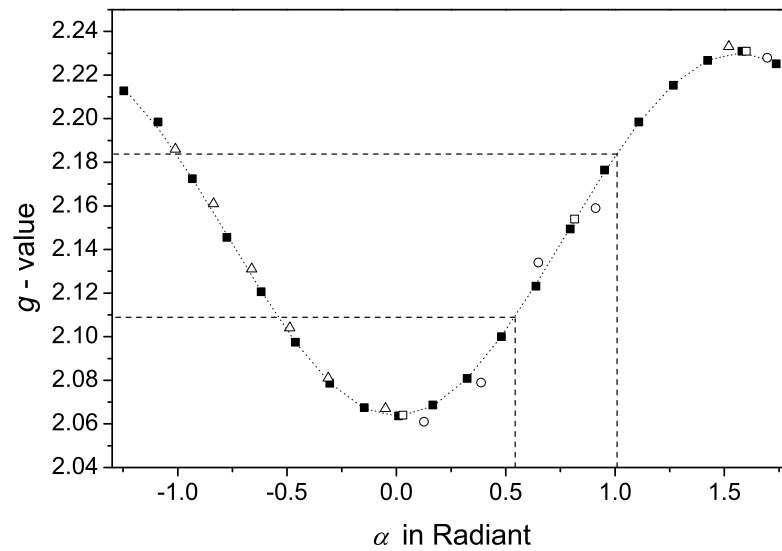


Figure 4.6: g -value at 4 K as function of the rotational angle α (black squares). The dotted line represents the calculated values with $g_{\perp} = 2.0633(4)$ and $g_{\parallel} = 2.2303(4)$. The colored squares are obtained in W-band, open triangles: room temperature, open boxes: 40 K, open circles: 10 K, dashed lines: expected distance of g -values for uncoupled copper ions, tilted by 25° , around $\alpha = \pi/2$.

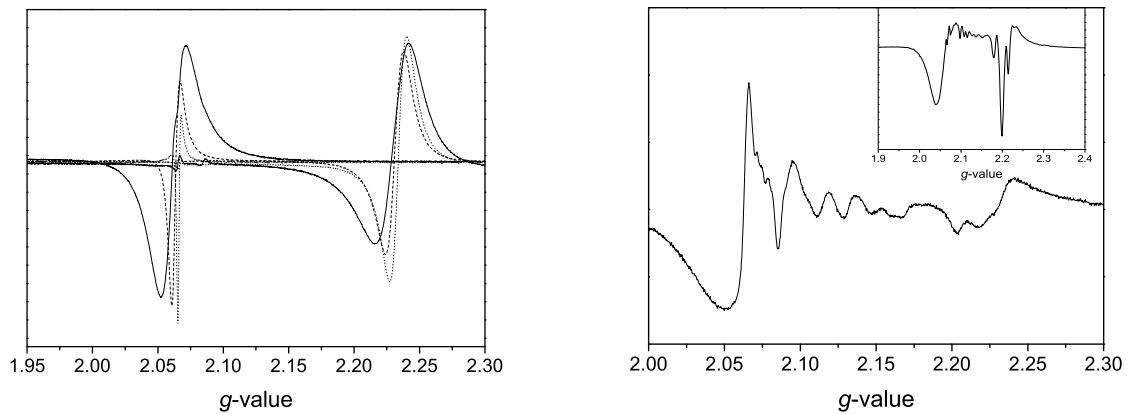


Figure 4.7: Left: Thermal dependence of the lineshape of single crystal spectra of $[(\text{phloro})\text{Cu}_3(\text{bhea})_3](\text{ClO}_4)_3$. Perpendicular and parallel transitions at 10 K (solid line), 40 K (dashed line) and room temperature (dotted line). Right: Comparison of W-band spectra recorded on a powder sample of $[(\text{phloro})\text{Cu}_3(\text{bhea})_3](\text{ClO}_4)_3$ thoroughly grinded with wax and W-band spectrum recorded on a powder sample of $[(\text{phloro})\text{Cu}_3(\text{bhea})_3](\text{ClO}_4)_3$ at 5 K without wax (Inset).

4.2 Magnetic Properties of 1-D Copper – Lanthanide Chains

4.2.1 Synthesis and Structure

The synthesis and structures of the seven isostructural compounds $[\text{Cu}(\text{OMesalen})\text{Ln}(\text{NO}_3)(\text{Pyr}(\text{COO})_2)]_n \cdot (\text{DMF})_n$ ($\text{Ln} = \text{La}, \text{Pr}, \text{Sm}, \text{Eu}, \text{Gd}, \text{Tb}, \text{Dy}$) have been reported elsewhere.^[156;309] A short summary of the structural features relevant for the magnetic discussion is given in the following paragraphs, especially concerning the symmetry of the metal centers.

A part of the polymeric chain is depicted in Figure 4.8. The 1-dimensional chain consists of copper(II)-lanthanide(III) entities bridged by 2,3-pyrazine dicarboxylic acid. The entities are formed by one copper ion occupying the inner coordination compartment of *N,N'*-bis(3-methoxysalicylidene)-1,3-diamino propane (Mesalen) and one gadolinium atom coordinated in the O_2O_2 outer cavity of the Mesalen ligand. The copper atom shows a square-pyramidal geometry with an oxygen atom of one carboxylate group of the bridging ligand occupying the apical position. The copper–oxygen distance is larger for the apical oxygen due to Jahn-Teller-distortion. Therefore one can conclude that the internal *z*-axis is along this particular copper–oxygen axis, while the *xy*-plane lies within the ligand as indicated by the red plane in Figure 4.9.

The other carboxylate oxygen and a nitrogen atoms of the pyrazine coordinate the lanthanide of the next entity, while the second carboxylate coordinates the lanthanide of

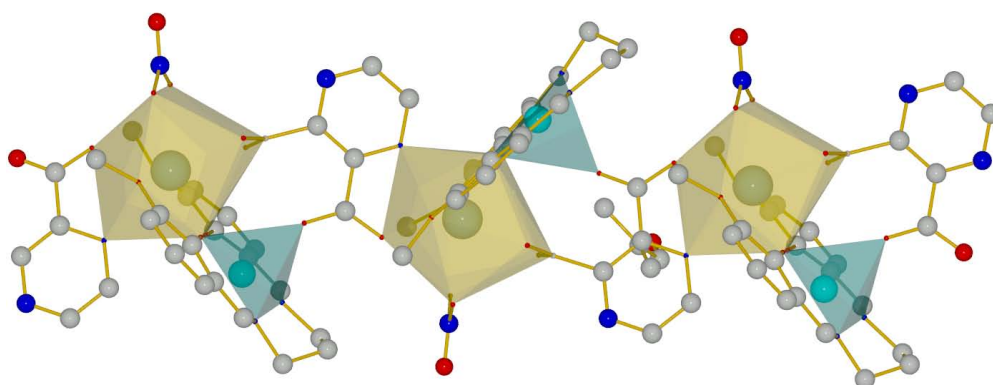


Figure 4.8: Chain structure of the general formula $[\text{Cu}(\text{OMesalen})\text{Ln}(\text{NO}_3)(\text{Pyr}(\text{COO})_2)]_n \cdot (\text{DMF})_n$

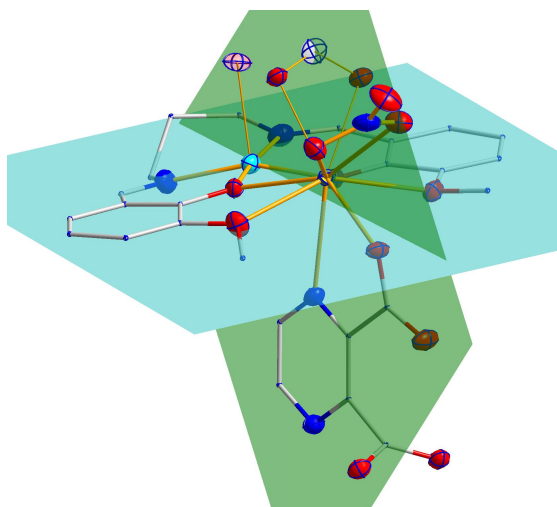


Figure 4.9: xy -plane for the copper (red) and for the lanthanide center (green) as discussed in the text. Ligand scaffold atoms are depicted as lines for clarity.

the same entity. Together with a coordinating nitrate and the salen ligand, the lanthanide yields the coordination number 10. The symmetry is rather low, but defining a mirror plane through the pyrazol ligand (green plane in Figure 4.9) gives a quite good description. The internal z -axis of the lanthanide should therefore be oriented perpendicular to this plane. This means, that the internal axis of the copper and gadolinium ions are not colinear but are canted against each other by an angle of around 90 degrees. The orientation of the x - and y -axis is not obvious from the structure.

4.2.2 Theoretical Considerations

Lanthanides possess a rich magnetochemistry. The explanation is found in the relative size of the possible effects as depicted in Table 1.1 in the Introduction. In the case of transition metal ions of the $3d$ -series the ligand field effect is stronger than the spin-orbit coupling and therefore dominates the energy pattern. In most cases the actual coordination environment quenches most of the orbital momentum. These systems therefore can be described by pure spin magnetism, which is perturbed by the residual orbital momentum via spin-orbit coupling. Only in special cases of distinct symmetry the influence of orbital momentum is strongly enhanced (Section 2.2).

In the case of the contracted and well shielded f -orbitals the ligand field is not strong enough to quench the orbital momentum. The spin-orbit coupling is much more pronounced and dominates the energy pattern. In most cases it is so strong, that the resulting total angular momentum J is a good quantum number for the description of the system. The obtained spin-orbit coupled J -states are then split by the ligand field. In addition, the shielded f -orbitals show only minor overlap with *outer* orbitals and are not capable of strong exchange coupling, so this effect does not play such an important role as it does in the case of transition metal ions. However, in several Cu(II)–Gd(III) pairs ferromagnetic exchange in the order of few cm^{-1} has been observed. The mechanism was proposed and described in particular by Dante Gatteschi^[339;340] and Olivier Kahn.^[317;341] Via charge transfer from the copper d -orbitals into the unoccupied gadolinium d -orbitals ferromagnetic spin–spin interactions due to Hund’s rule are expected. The energy pattern involving the the state structure of the ground Cu(II)–Gd(III) as well as the excited Cu(III)–Gd(II) states is depicted in Figure 4.10.^[339;340] The strength of the coupling constant $J_{\text{Cu–Gd}}$ depends on the transfer integral β_{5d-3d}^2 , the mean one site integrals k_{4f-5d}^0 (representing the averaged interaction between $5d$ - and $4f$ -orbitals) and the energy gap U' between the gravity centers of the $S = 3$ and $S = 4$ multiplets in the ground and excited state. The transfer integral involves the unoccupied d -orbitals at the lanthanide and are therefore not strongly affected by the shielded f -orbitals. The averaging in the mean one site integrals should also lead to rather similar values for the different lanthanides. And a comparison of the ionization energy (which can be used to estimate U') only shows variations in the order of some percent. The spin–spin coupling for the other lanthanides should therefore be quite similar to that found in the gadolinium system. Consequently, $J_{\text{Cu–Gd}}$ was used as first approximation in all compounds while optimizing the other parameters.

The free ion ground states are depicted in Table 4.1. Two trivalent lanthanides possess an orbital singlet ground state: lanthanum(III) with no f -electrons at all and gadolinium(III) with a half-filled f -shell. In all other cases the orbital momentum is coupled to the spin momentum. Since the spin orbit coupling constant λ changes sign when going from less than half occupied ($n_f < 7$) lanthanides to half or more than half occupied lanthanides, the alignment of orbital and spin momenta changes from antiparallel to parallel. Since the orbital part in most cases is larger than the spin part, the effective coupling between the total angular momenta changes from antiferromagnetic to ferromagnetic. This proposed change is confirmed in the series presented

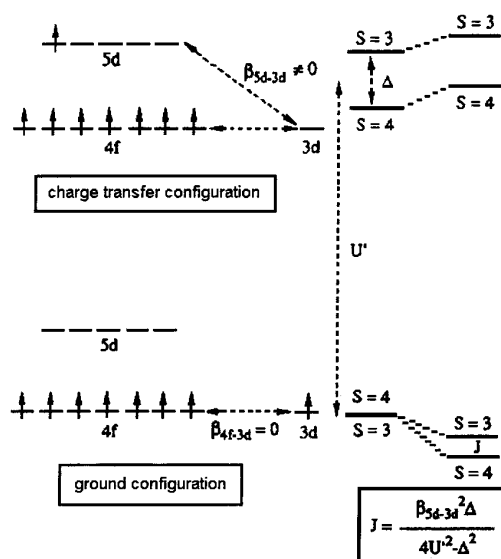


Figure 4.10: Scheme of the mechanism causing the ferromagnetic interaction in a gadolinium(III)–copper(II) pair as taken from Benelli and Gatteschi [340].

here. [156] While praseodym, samarium and europium show antiferromagnetic interactions, dysprosium and terbium show ferromagnetic interactions like gadolinium (*vide infra*).

In most cases similar compounds are described within the framework of spin-operator techniques and/or under the use of the operator-equivalent method. The ligand field operators work on the orbital momentum, that is on the basis of $\langle l m_l |$ states. These quantum numbers define the spatial expansion of the f -electrons and are hence directly affected by the ligand field. However, to reduce the complexity of the system, the projection into $\langle J M_J |$ states is used. This is valid, if only the ground spin-orbit coupled multiplet is thermally reachable. However, the obtained values also depend on the orbital ground multiplet and have to be reconverted to be comparable within a series of lanthanides. Using the orbital momentum itself increases the computational effort, but the parameters obtained should be quite similar along different lanthanides as long as the structural differences along the series are small enough.

The real symmetry of coordination at the lanthanide is usually very low and a large number of parameters is necessary to describe the ligand field splitting. To avoid over-parametrization an “ideal” symmetry can be assumed. In this case one could describe

Table 4.1: The free ion electronic ground states of the lanthanides used in this work to construct the 1-dimensional coordination polymer.

| | S | L | J | g_J | g_{ESR} | ground state |
|------------|-----|-----|------|-------|------------------|--------------|
| lanthanum | 0 | 0 | 0 | 0 | 0 | 1S_0 |
| praseodym | 1 | 5 | 4 | 4/5 | 2.002 | 3H_4 |
| samarium | 5/2 | 5 | 5/2 | 2/7 | 2.082 | $^6H_{5/2}$ |
| europium | 3 | 3 | 0 | 0 | 2.245 | 7H_0 |
| gadolinium | 7/2 | 0 | 7/2 | 2 | 1.98 | $^8S_{7/2}$ |
| terbium | 3 | 3 | 6 | 3/2 | 2.075 | 7F_6 |
| dysprosium | 5/2 | 5 | 15/2 | 4/3 | 2.080 | $^6H_{15/2}$ |

the coordination environment as a pentagonal bipyramid (D_{5h}) with the axis perpendicular to the z-axis of the copper center (*vide supra*). The parameters B_4^4 , B_4^6 and B_6^6 have to be included in addition to B_0^4 , B_0^6 and B_7^2 .

4.2.3 Magnetic Properties — In General

The thermal dependencies of the magnetic susceptibilities are determined for all compounds on powdered samples between 2 and 300 K. Several features in the preliminary measurements point towards rather strong orientational effects. The measurement were repeated in samples prepared as pressed Teflon pellets. However, analysis of the obtained data showed strong changes, which might be explained by the formation of lanthanide oxides during the application of pressure. Reliable data sets could only be obtained from samples which were mixed with grease prior to the measurement. This preparation method results in a large diamagnetic contribution, which cannot be determined unambiguously. The obtained values for χ_{TIP} are therefore not reliable and mainly account for the uncertainties in the diamagnetic correction.

The results of these measurements are depicted on the left side in Figure 4.11 and 4.12 for the compounds without orbital momentum and in Figure 4.14 and 4.15 for the compounds with orbital momentum as $\chi_M = f(T)$ and $\chi_M T = f(T)$ plots. Only for the europium and terbium compounds the oriented behavior is depicted, since insufficient amounts of substrate were available for repeating the measurements with the use of grease. For less than half filled f -shells overall antiferromagnetic interactions between

the copper spin and the lanthanide total momentum are expected. In contrast ferromagnetic interactions are expected, when the lanthanide contains seven or more f electrons. The high temperature value for the $\chi_M T$ product can be calculated according to

$$\chi_M T = \frac{N\beta^2 g_{\text{Cu}}^2}{3K} S_{\text{Cu}}(S_{\text{Cu}} + 1) + \frac{N\beta^2 g_f^2}{3K} J_{\text{Ln}}(J_{\text{Ln}} + 1) \quad (4.4)$$

if only the ground multiplett of the lanthanide is involved. However, the experimental values strongly suffer from the uncertainties of χ_{TIP} .

ESR spectroscopy might offer some additional insights. In most cases the splitting of the m_J -levels is so strong, that the lanthanide system can be handled as an artificial $S = \frac{1}{2}$ system with a large anisotropy. Another problem is very fast relaxation due to low lying excited states, which causes an enormous line broadening, so that it is not always possible to detect the expected signals. But nevertheless some information can be gained by a comparison study. From the lanthanum compound the parameters describing the copper ion are extracted. From the gadolinium compound general properties regarding the coupling and the tilting of the coordination polyhedra are obtained. These are then used to determine the parameters for the other lanthanides. However, tilting of principle axis between the copper and the lanthanide ion as well as coupling effects through the 2,3-pyrazine dicarboxylic acid make the problem very complicated.

4.2.4 Magnetic Properties — Without Angular Momentum

Lanthanum

The thermal dependency of $\chi_M T$ for $[\text{Cu}(\text{OMesalen})\text{La}(\text{NO}_3)(\text{Pyr}(\text{COO})_2)]_n \cdot (\text{DMF})_n$ (**30**) is depicted in Figure 4.11 on the left side as $\chi_M T = f(T)$ plot. At very low temperatures a small decrease of $\chi_M T$ indicates very small antiferromagnetic interactions between the copper centers.

The X-band spectra recorded on powder samples at 5 K and room temperature consist of a rhombic spectrum. It can be simulated with $[g_x, g_y, g_z] = [2.074, 2.085, 2.259]$ and a hyperfine tensor $[A_x, A_y, A_z] = [0, 19, 188]$ G (Figure 4.11, right). Interestingly also

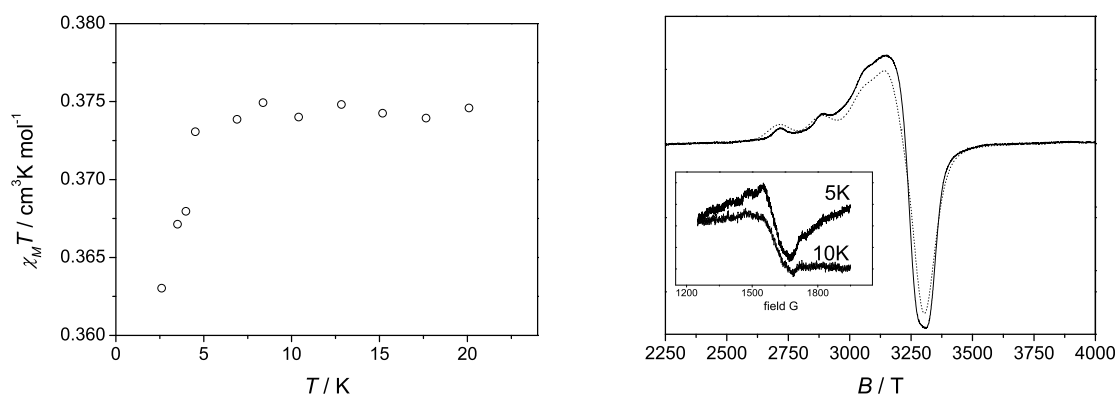


Figure 4.11: Left: Plot of thermal dependence of $\chi_M T$ for $[\text{Cu}(\text{OMesalen})\text{La}(\text{NO}_3)(\text{Pyr}(\text{COO})_2)]_n \cdot (\text{DMF})_n$ (**30**) below 30 K measured with an applied magnetic field of 1000 Oe. Right: X-band ESR spectrum for **30** recorded on powder samples at 5K. Solid line: measured spectrum, dotted line: simulated spectrum. Inset: Half field signal at 5 K and 10 K recorded on powder samples with lower attenuation.

a half field signal can be observed, showing a hyper fine structure due to two copper centers with half the line distance of the main signal (inset in Figure 4.11). This indicates, that the coupling takes place between two atoms whose internal z-axes are colinear. The shortest copper–copper distance is within the chains (≈ 940 pm), but in this case the angle of the coordination planes is 86° , which makes this exchange pathway improbable. The nearest copper atoms suitable for coupling interactions are in the adjacent chain, separated by ≈ 1000 pm and ≈ 1090 pm, respectively. In this cases the angles are 35° and 0° . The latter thus presents a nice explanation for the observed effects.

Gadolinium

The thermal dependency of the molar magnetic susceptibility measured on powder samples of $[\text{Cu}(\text{OMesalen})\text{Gd}(\text{NO}_3)(\text{Pyr}(\text{COO})_2)]_n \cdot (\text{DMF})_n$ (**34**) is depicted in Figure 4.12 on the left side as $\chi_M = f(T)$ and $\chi_M T = f(T)$. At 300 K, $\chi_M T$ is equal to $8.59 \text{ cm}^3 \text{ mol}^{-1} \text{ K}$, which roughly corresponds to the expected value for two uncoupled metal ions ($8.25 \text{ cm}^3 \text{ mol}^{-1} \text{ K}$). Lowering the temperature causes an increase of the $\chi_M T$ value reaching a maximum of $9.82 \text{ cm}^3 \text{ mol}^{-1} \text{ K}$ at 6 K. This last value is very close to the

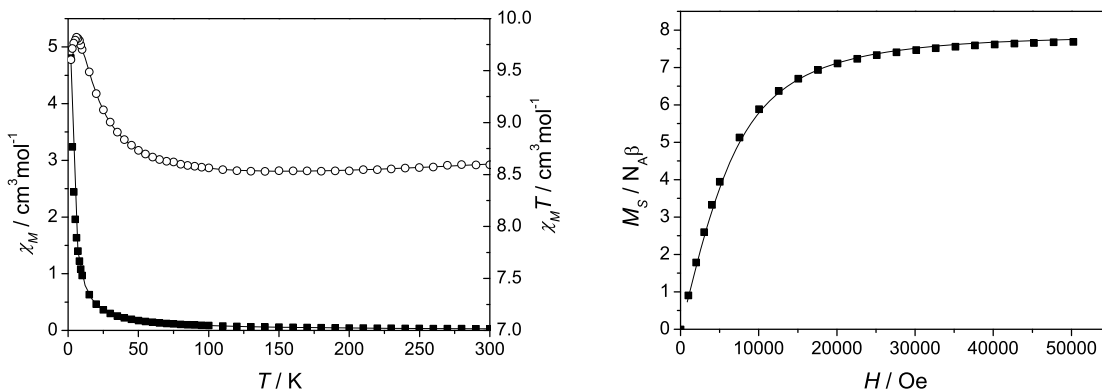


Figure 4.12: Left: Plot of thermal dependence of χ_M (empty squares) and $\chi_M T$ product (black filled circles) for (34) measured with an applied magnetic field of 2000 Oe; solid lines represent the theoretical behaviour with the parameters given in the text. Right: Plot of the field dependence of the magnetization for complex 34 measured at 2 K (black filled squares represent the experimental value; the solid line shows the theoretical curve generated using the Brillouin equation).

calculated $10.00 \text{ cm}^3 \text{ mol}^{-1} \text{ K}$ value for an $S = 4$ spin state resulting from ferromagnetic coupling within the same unit of copper(II) ($S = \frac{1}{2}$) and gadolinium(III) ($S = \frac{7}{2}$) assuming $g_{\text{Cu}} = g_{\text{Gd}} = 2$. A quantitative analysis has been performed using the spin-only Hamiltonian:

$$\hat{H} = J_{\text{Cu-Gd}} \hat{S}_{\text{Cu}} \hat{S}_{\text{Gd}} \quad (4.5)$$

leading to the equation

$$\chi_M = \frac{4N\mu_B^2}{k(T-\theta)} \frac{7g_3^2 + 15g_4^2 e^{\frac{4J_{\text{Cu-Gd}}}{kT}}}{7 + 9e^{\frac{4J_{\text{Cu-Gd}}}{kT}}} + \chi_{TIP} \quad (4.6)$$

where χ_{TIP} is the temperature independent paramagnetism, $J_{\text{Cu-Gd}}$ the isotropic coupling constant, θ the mean-field parameter and g_3 and g_4 are the g -values of the $S = 3$ and $S = 4$ states, respectively.^[7]

The best fit of the experimental data leads to an isotropic coupling constant $J_{\text{Cu-Gd}} = -4.73(5) \text{ cm}^{-1}$ for $g_4 = 1.997(1)$ and $g_3 = 1.982(3)$. The reliability factor $R^2 = 0.9998$ for $\theta = -0.078(3) \text{ K}$ shows a good agreement between calculated and experimental data sets. The small negative Weiss constant θ describes very weak antiferromagnetic exchange interactions that occur between neighboring molecules at very low temperature and it is illustrated by the decrease of $\chi_M T$ value from $9.82 \text{ cm}^3 \text{ mol}^{-1} \text{ K}$ at 6 K to around $9.60 \text{ cm}^3 \text{ mol}^{-1} \text{ K}$ at 2 K. The ferromagnetic interaction between the

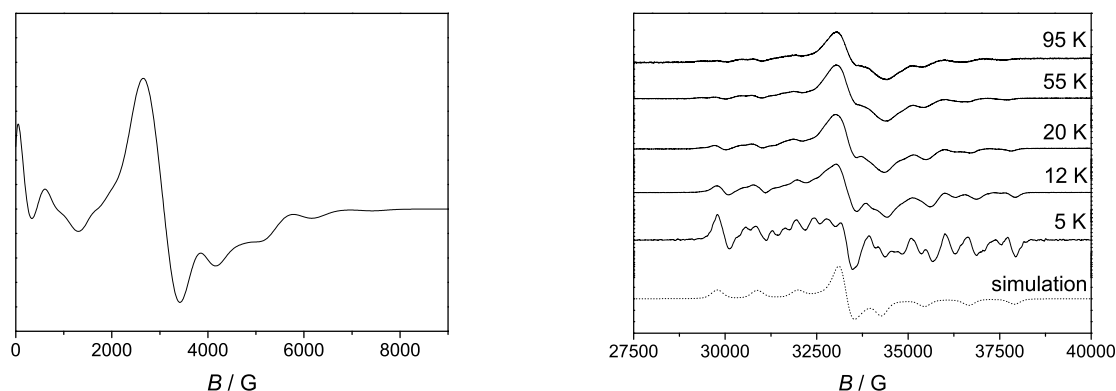


Figure 4.13: X-band for **34** 1-D chain complex measured at 5 K (left) and W-band ESR spectrum (right) measured at different temperature values.

copper and gadolinium ions is also confirmed by the field dependence of the magnetization measured at 2 K. The experimental values fit the Brillouin function assuming $g_{av} = 2.00$, resulting in a spin state $S = 3.91(1)$ with reliability factor $R^2 = 0.99888$ (Figure 4.12, right).

The X-Band ESR spectrum recorded on a powder sample of **34** consists of a strong signal with fine structure, which is not fully accessible due to limitation by the X-band frequency. To obtain better resolution and to display the whole spectrum, spectra have been recorded at the W-band on powder samples at 5, 12, 20, 55 and 95 K. The spectra recorded at temperatures above 5 K consist of a central signal with a series of signals on both sides. For simulation of these spectra the following hamiltonian for an artificial $S = 4$ system is used:

$$\hat{H} = \mu_B \vec{B} \vec{g} \hat{S} + \hat{S} \bar{D} \hat{S} \quad (4.7)$$

With $[g_x, g_y, g_z] = [2.015, 2.000, 1.995]$ and $[D, E] = [1740, 530]$ MHz a good agreement is obtained between simulated and measured spectrum. The g -components (g_x, g_y and g_z) have been chosen in a way that $E < \frac{D}{3}$ holds true.

It is worth noting that the spatial orientation of the g -tensor also favors the conclusions concerning the relative direction of the principle axis (*vide supra*). The principle axis at the gadolinium is determined by the direction of the \bar{D} tensor, while the principle axis of the Jahn Teller-distorted copper environment is determined by the largest g -component. Thus the magnitude of the g -components in the coupled state represent the tilting between copper and gadolinium environment. It can be seen that largest

component of the coupled system is in the x -direction, that means, that if the coupled system is oriented along the principle axis of the gadolinium (defined by the D -tensor), the z -axis of the copper is oriented in the x -direction. In other words: the g -tensor of the copper is tilted against the principle axis of the gadolinium approximately by the Euler angles $[\alpha, \beta, \gamma] = [90, 90, 90]$ in very good agreement with the structural discussion above.

The g -values for the system can also be calculated by projection of the copper g -values gained from the lanthanum spectrum and an isotropic $g = 1.980$ for the gadolinium onto the total spin of $S = 4$. Using the equation

$$g_S = \frac{(1+c)g_{Gd}}{2} + \frac{(1-c)g_{Cu}}{2} \quad (4.8)$$

$$c = \frac{S_{Gd}(S_{Gd}+1) - S_{Cu}(S_{Cu}+1)}{S(S+1)} \quad (4.9)$$

one gets $[g_x, g_y, g_z] = [1.992, 1.993, 2.015]$ which is in excellent agreement with the values obtained from the simulation. These values also reproduce the X-band spectrum quite nicely. Slight deviations might be due to higher order contributions, neglected coupling effects along the chain or deviation from the idealized tilting angles.

The averaged g -value calculated for the copper

$$g_{av} = \sqrt{(2.074^2 + 2.085^2 + 2.259^2)/3} = 2.140 \quad (4.10)$$

and the isotropic g -value of 1.984 for the gadolinium give rise to a $g_4 = 2.000$ for the $S = 4$ system and $g_3 = 1.960$ for the $S = 3$ system, which is in good agreement with the values obtained by the fit of the susceptibility data.

At 5 K the spectrum changes quite a lot. The number of signals rapidly increases, the relative intensity of the central signal decreases and especially the signal around 29 900 G gains much intensity. This unpredicted and surprising behavior is most likely due to the coupling along the chain and thus to an increase of the correlation length.

4.2.5 Magnetic Properties — With Angular Momentum

The thermal dependency of the magnetic susceptibility was determined between 2 and 300 K and is depicted in Figure 4.14. In order to reduce the number of parameters needed to describe the magnetic data of the other lanthanide compounds, the g -values of the copper centers were set to the values found in the lanthanum compound (Equation 4.11) and the exchange coupling was fixed to the one found in the gadolinium compound (Equation 4.12, *vide supra*). The ligand field parameters B_k^i were then determined to describe all discussed compounds (Equation 4.13). The magnetic data were thus analyzed using the total hamiltonian

$$\hat{H} = \bar{g}\mu_B\vec{B}\hat{S}_{\text{Cu}} + \gamma(\hat{L}_{\text{Ln}} + 2 \cdot \hat{S}_{\text{Ln}}) \quad (4.11)$$

$$+ J_{\text{CuLn}}\hat{S}_{\text{Cu}}\hat{S}_{\text{Ln}} \quad (4.12)$$

$$+ B_0^2\hat{C}_0^2 + B_2^2\hat{C}_2^2 + B_0^4\hat{C}_0^4 + B_4^4\hat{C}_4^4 + B_0^6\hat{C}_0^6 + B_4^6\hat{C}_4^6 + B_6^6\hat{C}_6^6 \quad (4.13)$$

A possible parameter set describing the measured data within this framework is summarized in Table 4.2. It should be noted that regarding the magnetic behavior of only one complex other data sets are possible, however, the listed numbers reproduced all data well allowing only the gyromagnetic ratio γ of the lanthanide and the diamagnetic contribution χ_{TIP} to relax. The fact that the obtained values for γ are of similar size shows once more, that this approach might indeed be a good description of the systems containing an unquenched orbital momentum.

Praseodymium

In the free-ion-approximation the splitting between the praseodym(III) ion ground state ($^3\text{H}_4$) and the first excited state ($^3\text{H}_5$) is 2000 cm^{-1} . Thus mainly the $^3\text{H}_4$ state contributes to the magnetic behavior. At room temperature the $\chi_M T$ product is $1.57 \text{ cm}^3\text{K mol}^{-1}$ which is slightly lower than the value calculated by Equation 4.4 ($2.03 \text{ cm}^3\text{K mol}^{-1}$) and decreases on lowering the temperature reaching a value of $0.38 \text{ cm}^3\text{K mol}^{-1}$ at 2 K, characteristic of an $S = \frac{1}{2}$ ground state with $g = 2.01$. The X-Band ESR spectrum recorded on powder samples at 5 K exhibits a nearly isotropic signal with a g_{eff} -value 2.002 and a large peak-to-peak distance of 325 G. This rather

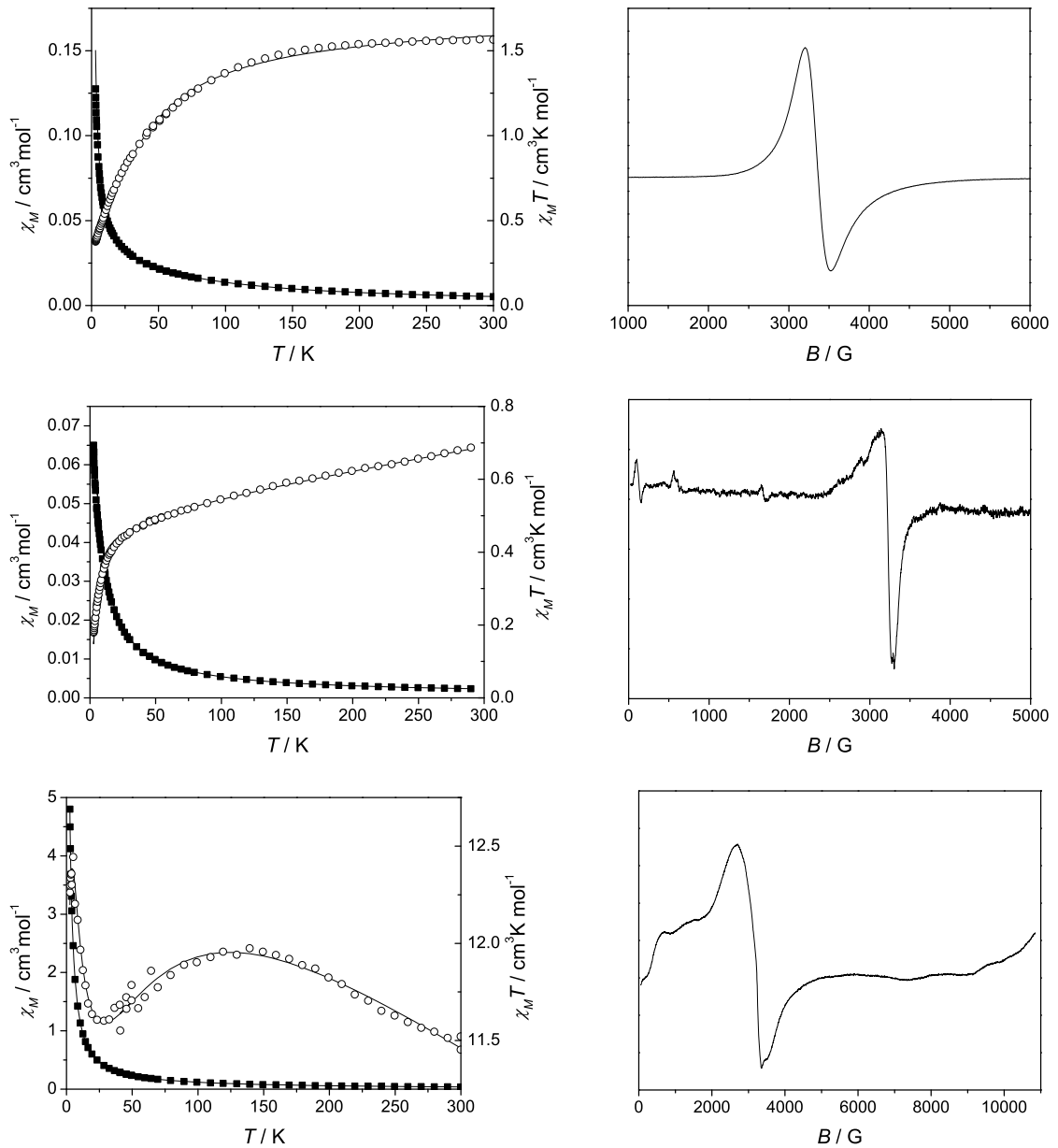


Figure 4.14: Left side: Plot of thermal dependence of χ_M (filled squares) and $\chi_M T$ (open circles) for $[\text{Cu}(\text{OMesalen})\text{Ln}(\text{NO}_3)(\text{Pyr}(\text{COO})_2)]_n \cdot (\text{DMF})_n$ (top: Pr; middle: Sm; bottom: Dy), measured with an applied magnetic field of 2000 Oe. Right side: X-band ESR spectrum for $[\text{Cu}(\text{OMesalen})\text{Ln}(\text{NO}_3)(\text{Pyr}(\text{COO})_2)]_n \cdot (\text{DMF})_n$ (top: Pr; middle: Sm; bottom: Dy), recorded on powder samples at 5K.

Table 4.2: Summary of simulations used to reproduce the magnetic behavior.

| | Pr | Sm | Eu | Tb | Dy |
|---|-------|--------|----------|---------|-------|
| γ | 0.848 | 0.734 | (1) | (1.123) | 0.936 |
| g_{Cu} | | [2.085 | 2.259 | 2.074] | |
| D_L [cm^{-1}] | | | 0.159 | | |
| E_L [cm^{-1}] | | | -0.304 | | |
| B_0^4 [cm^{-1}] | | | -0.0479 | | |
| B_4^4 [cm^{-1}] | | | -0.259 | | |
| B_0^6 [cm^{-1}] | | | 0.00079 | | |
| B_4^6 [cm^{-1}] | | | 0.000208 | | |
| B_6^6 [cm^{-1}] | | | -0.0126 | | |
| $J_{\text{Cu-Ln}}$ [cm^{-1}] | | | -4.7 | | |
| λ [cm^{-1}] | 750 | 1180 | (1360) | (-1620) | -1820 |
| χ_{TIP} [$10^{-3}\text{cm}^3\text{mol}^{-1}$] | 0.161 | 0.655 | (0) | (6.858) | 4.491 |

interesting result is in good agreement with the $S = \frac{1}{2}$ ground state deduced from the magnetic susceptibility measurement. The large peak-to-peak distance points towards an exchange broadening, which is in consistent with the small interdimer interaction mediated by the bridging dicarboxypyrazine.

Samarium

For compound [32](#) the sharp decrease of $\chi_M T$ at low temperatures down to $0.23 \text{ cm}^3\text{K mol}^{-1}$ indicates antiferromagnetic interactions between the ($J = \frac{5}{2}$) samarium(III) and the copper(II) ion as is expected for electronic configuration with less than seven f -electrons. ESR spectra have been recorded on powdered samples at 5 K. They show a rather low signal to noise ratio, which is in good agreement with a diamagnetic ground state. Although the signal to noise ratio is not very good, a series of signals can be seen in the X-Band ESR spectrum. In the case of antiferromagnetic interactions a singlet ground state is to be expected, if the ligand field splitting results in a lowest lying $m_J = \frac{1}{2}$ level. The anisotropic signal at a g_{eff} -value around 2.082 shows four lines at the low field side split by 260 G, which seem to be split again in two lines by 90 G.

The main signal is also split but only about 36 G. In addition a series of smaller signals can be observed: two signals 1550 G and 3100 G lower than the main signal another one in a distance of 2370 G from the center of the four lines.

Dysprosium

The magnetic behavior of the dysprosium compound **36** is quite interesting. Upon cooling $\chi_M T$ increases due to a negative χ_{TIP} (related to the diamagnetic contributions of the grease, *vide supra*). Below 150 K $\chi_M T$ decreases, reaching a minimum of $11.6 \text{ cm}^3\text{K mol}^{-1}$ at 28 K. On further cooling $\chi_M T$ increases to a maximum of $12.4 \text{ cm}^3\text{K mol}^{-1}$ and decreases again. This is due to three effects: first the thermal depopulation of the Stark-levels leads to the decrease, second the ferromagnetic coupling with the copper ion causes the increase and at last antiferromagnetic interactions between the dysprosium–copper dimers along the chain are responsible for the final decrease. The X-Band ESR spectrum recorded on a powder sample at 5 K shows an anisotropic signal at $g_{\text{eff}} = 2.080$ and a second signal at $g_{\text{eff}} \sim 11.4$.

Europium and Terbium

For the europium (**33**) and terbium compound (**35**) the thermal dependency of the magnetic susceptibility was determined between 2 and 300 K on powdered samples (*vide supra*). Most probably the microcrystals are not randomly oriented and the obtained data should be handled with caution. For comparison, the expected behavior with the parameters used for the praseodymium, samarium and dysprosium compound is depicted together with the simulated behavior in Figure 4.15 for the europium and terbium compound.

The X-Band ESR spectra were recorded on powdered samples at 5 K. The spectrum of the europium compound shows an isotropic signal comparable to the one measured for the praseodymium compound. It can be simulated quite nicely using a g_{eff} -value of 2.245 and an isotropic magnetic field domain line width of 8 mT Gaussian broadening and 19 mT Lorentzian broadening. Also a half-field transition can be detected which lacks any structure as well. The spectrum of the terbium compound consists of a very sharp perpendicular signal at $g_{\text{eff}} = 2.075$ and an axial component at around

4.2 Magnetic Properties of 1-D Copper – Lanthanide Chains

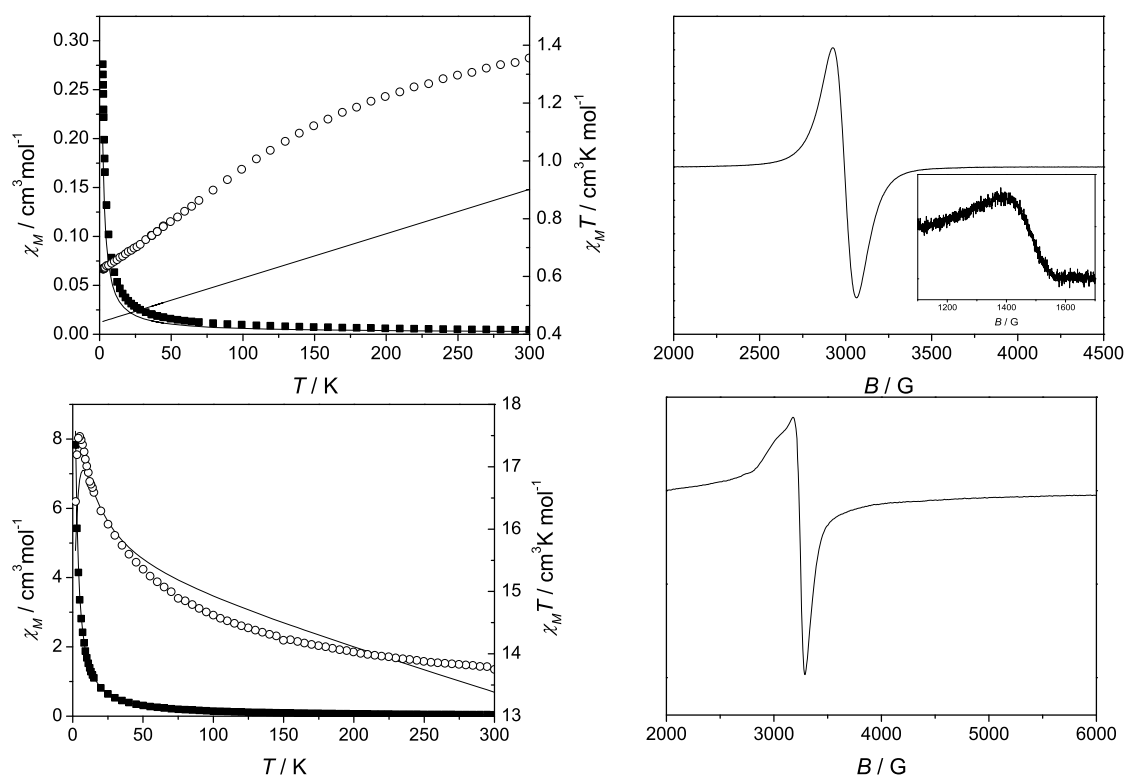


Figure 4.15: Left: Plot of thermal dependence of χ_M (filled squares) and $\chi_M T$ product (open cycles) for $[\text{Cu}(\text{OMesalen})\text{Ln}(\text{NO}_3)(\text{Pyr}(\text{COO})_2)]_n \cdot (\text{DMF})_n$ (top: Eu; bottom: Tb), measured with an applied magnetic field of 2000 Oe. Right side: X-band ESR spectrum for $[\text{Cu}(\text{OMesalen})\text{Ln}(\text{NO}_3)(\text{Pyr}(\text{COO})_2)]_n \cdot (\text{DMF})_n$ (top: Eu; bottom: Tb), recorded on powder samples at 5K. Inset: half field transition observed at higher attenuation.

$g_{\text{eff}} = 2.247$. Around zero field there are indications of another signal (not depicted), which is not accessible in the X-band. Interestingly the g -values are very close to the ones observed for the lanthanum compound, suggesting $m_J = 0$ to be the ground state of the ligand field split J -multiplet. The ligand field favors the low lying M_J -states, which is in good qualitative agreement with the results deduced for the samarium compound (*vide supra*).

4.3 Magnetic Properties of Pentanuclear Complexes

4.3.1 Synthesis and Structure

The synthesis and structure of $[\text{FeNi}_4(\text{BrTAG})_2(\text{tptz})_4]^+$ (**FeNi₄**), $[\text{CoNi}_4(\text{HTAG})_2(\text{tptz})_4]^+$ (**CoNi₄**) and $[\text{MnNi}_4(\text{HTAG})_2(\text{tptz})_4]^+$ (**MnNi₄**) have been reported elsewhere.^[213] A short summary of the structural features relevant for the magnetic discussion is given in the following paragraphs.

A sketch of the molecular structure of $[\text{FeNi}_4(\text{BrTAG})_2(\text{tptz})_4]^+$ (where *BrTAG* denotes the bridging ligand obtained by Schiff-base condensation of triaminoguanidine with 5-bromo-salicylaldehyde and tptz the capping ligand 2,4,6-*tris*-(2-pyridin)-triazin) as found in the crystal structure of $[\text{FeNi}_4(\text{BrTAG})_2(\text{tptz})_4](\text{ClO}_4)_{0.5}\text{Cl}_{0.5} \cdot 2.5\text{DMF} \cdot \text{MeOH} \cdot 9\text{H}_2\text{O}$ (**FeNi₄**) is depicted in Figure 4.16. A simplified picture, showing only the metal polyhedra and the bridging triaminoguanidine moieties is depicted in Figure 4.17. All metals are coordinated in slightly distorted octahedra. They are connected by two triaminoguanidine based ligand molecules (bromo substituted *BrTAG* for the iron com-

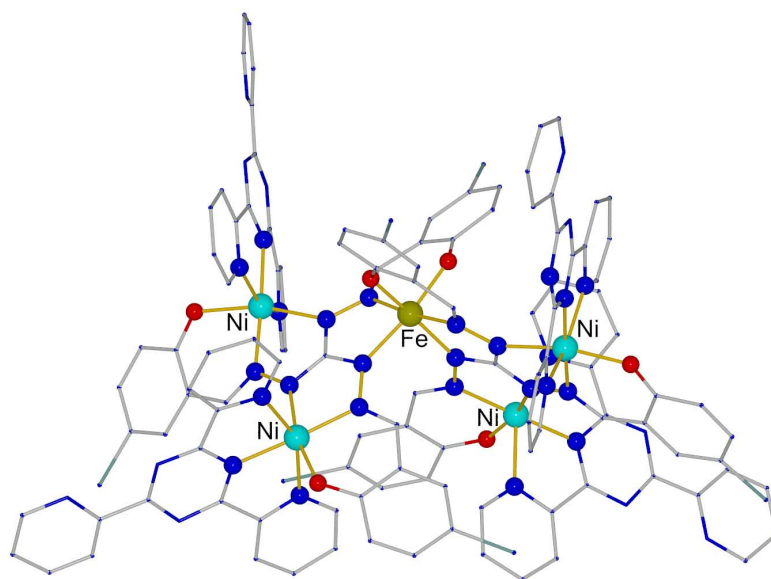


Figure 4.16: Molecular structure of the complex cation $[\text{FeNi}_4(\text{TAG}^{\text{Br}})_2(\text{tptz})_4]^+$ (**FeNi₄**) in crystals of $[\text{FeNi}_4(\text{BrTAG})_2(\text{tptz})_4](\text{ClO}_4)_{0.5}\text{Cl}_{0.5} \cdot 2.5\text{DMF} \cdot \text{MeOH} \cdot 9\text{H}_2\text{O}$ as reported by D. Plaul^[213]. All atoms are illustrated as sticks except the metal centers and the coordinating atoms. Furthermore all hydrogen atoms are omitted for clarity.

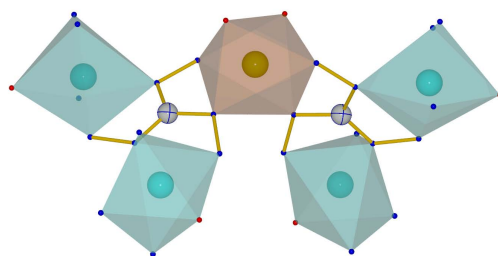


Figure 4.17: Metal polyhedra in FeNi_4 and their connection by triaminoguanidine moieties as a cutout from the molecular structure. The nickel polyhedra are depicted in blue and the iron polyhedra in brown.

plex and unsubstituted ^HTAG for the cobalt and manganese complexes) offering an N_2O donor set per binding pocket. While the coordination sphere of the iron center is filled by binding two molecules triaminoguanidine, the coordination sphere of the nickel ions is completed by the N_3 donor set of a tptz molecule. This capping ligand has also been used in the construction of homometallic trinuclear nickel complexes.^[309;329] Complexes of similar composition and structure were obtained with cobalt (CoNi_4) and manganese (MnNi_4).

4.3.2 Magnetic Properties

Variable temperature (2 – 300 K) magnetic susceptibility data were collected on powder samples for all three complexes and are shown in Figure 4.18 (CoNi_4) and on the left side of Figures 4.19 (CoMn_4) and 4.20 (FeNi_4) as $\chi_M = f(T)$ and $\chi_M T = f(T)$ plots. They all show a monotonous decline upon lowering the temperatures. This indicates antiferromagnetic interactions through the triaminoguanidine ligand scaffold as found in other reported compounds.^[144;145;213;308;309;329] The comparative study of the magnetic data shows how the magnetic insights gained from the monomeric trinuclear complexes are preserved in the oligomeric structures.

Cobalt Complex (CoNi_4)

The room temperature values of $\chi_M T$ is $3.7 \text{ cm}^3\text{K mol}^{-1}$ for the cobalt(III) complex. This is lower than the expected value for four independent nickel(II) ions with $g > 2$ and $S = 1$ (e.g. $4.4 \text{ cm}^3\text{K mol}^{-1}$ for $g = 2.1$). However, from the $\chi_M = f(T)$ plot

one can explain this deviation by the presence of a paramagnetic impurity, which is assumed to possess a spin $S = 1$. Upon cooling the $\chi_M T$ value decreases to reach $0.07 \text{ cm}^3\text{K mol}^{-1}$. This confirms that the central cobalt(III) ion is in the low spin state leading to an expected low temperature value of zero. This compound therefore can be treated as two strongly coupled nickel dimers which are coupled very weakly through the central diamagnetic ion. The remaining $0.07 \text{ cm}^3\text{K mol}^{-1}$ suggest a paramagnetic impurity of approximately 7% (with $S = 1$). The magnetic data were analyzed using the hamiltonian

$$\hat{H} = -J_{\text{NiNi}}(\hat{S}_{\text{Ni1}}\hat{S}_{\text{Ni2}} + \hat{S}_{\text{Ni3}}\hat{S}_{\text{Ni4}}) \quad (4.14)$$

with the help of a full matrix least square routine which also accounts for the paramagnetic impurity α ^[10]

$$\chi_{\text{total}} = (\alpha - 1) \cdot \chi_{\text{complex}} + \alpha \cdot \chi_{\text{impurity}} \quad (4.15)$$

The measured values could be reproduced quite nicely using the parameters $J_{\text{Ni-Ni}} = -35.8 \text{ cm}^{-1}$ and $g_{\text{Ni}} = 2.111$ with $\alpha = 7.3\%$ (solid line in Figure 4.18). Interdimer exchange as well as axial zero-field splitting at the nickel centers cannot be determined unambiguously from these data. Because of the rather strong antiferromagnetic interactions between the nickel centers inside a dimer, the ground state is an $S = 0$ and therefore is not affected by neither interdimer exchange nor zero-field splitting. Inclusion leads only to an unreasonable high D -value and a vanishing J_{dimer} . These data clearly show that the magnitude of the nickel–nickel interactions resembles very well the one found for the reported trinuclear compounds.^[309;329]

Manganese Complex (MnNi₄)

For the manganese(III) complex $\chi_M T$ is $7.96 \text{ cm}^{-1}\text{K mol}^{-1}$ at room temperature and is still raising with increasing temperature. The observed value is slightly higher than the spin only value for four independent nickel(II) ions ($S = 1$, $g > 2$) and one manganese(III) *high spin* ($S = 2$) with $g = 2$, which is $7.4 \text{ cm}^{-1}\text{K mol}^{-1}$ for $g_{\text{Ni}} = 2.1$. The

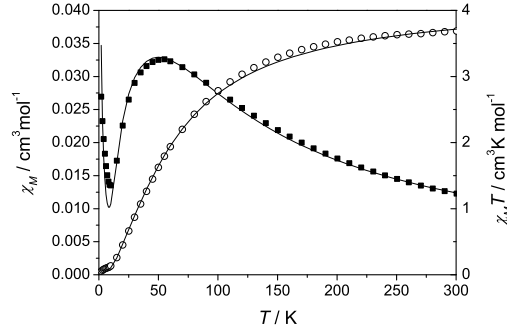


Figure 4.18: Thermal dependence of the molar magnetic susceptibility χ_M (black boxes) and $\chi_M T$ (open circles) for CoNi_4 . Solid lines: simulated behavior with the parameters mentioned in the text.

observed linear increase of $\chi_M T$ at high temperature may be attributed to a contribution from temperature independent paramagnetism (χ_{TIP}) arising from spin-orbit coupled low lying excited states. For a manganese(III) high spin ion, g_{Mn} -values slightly smaller than 2 are expected.^[8] A more pronounced decrease of $\chi_M T$ upon lowering the temperature is observed below 100 K, indicating fairly strong antiferromagnetic interactions, whereas the sharp decrease observed below 20 K should most probably be attributed to zero-field splitting effects. The appropriate hamiltonian, which accounts for the possible exchange interactions and the zero-field splitting at the metal ions, is:

$$\begin{aligned}
 \hat{H} = & -J_{\text{NiNi}}(\hat{S}_{\text{Ni1}}\hat{S}_{\text{Ni2}} + \hat{S}_{\text{Ni3}}\hat{S}_{\text{Ni4}}) \\
 & -J_{\text{MnNi}}(\hat{S}_{\text{Ni1}}\hat{S}_{\text{Mn}} + \hat{S}_{\text{Ni3}}\hat{S}_{\text{Mn}} + \hat{S}_{\text{Ni2}}\hat{S}_{\text{Mn}} + \hat{S}_{\text{Ni4}}\hat{S}_{\text{Mn}}) \\
 & + \bar{D}_{\text{Mn}}\hat{S}_{\text{Mn}}^2 + \sum_{i=1}^4 \bar{D}_{\text{Ni},i}\hat{S}_{\text{Ni},i}^2
 \end{aligned} \tag{4.16}$$

Isothermal magnetization measurements performed at 2 K (inset of Figure 4.19, right) can be fitted^[10] by assuming an isolated $S = 2$ with $g = 1.86$ and an axial zero-field splitting $D = -1.607 \text{ cm}^{-1}$. These values are in the expected range for a high spin manganese(III),^[8;342] thus suggesting that the ground state properties are essentially those of the central manganese(III). This points to nickel–nickel interactions much stronger than the nickel–manganese ones.^[8;86;342;343]

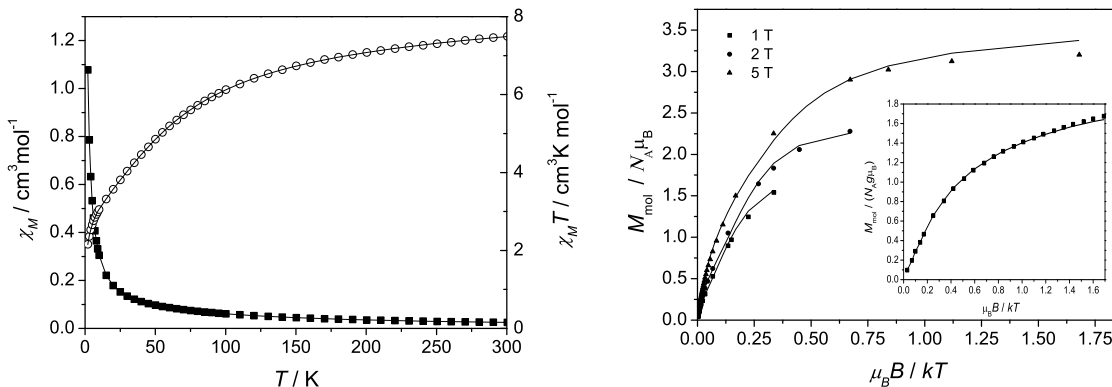


Figure 4.19: Left: Thermal dependence of χ_M (black boxes) and $\chi_M T$ (open circles) for **MnNi₄**. Solid lines: simulated behavior with the parameters mentioned in the text. Right: Variable Field Variable Temperature plots for **MnNi₄**. Solid lines: simulated behavior with the parameters mentioned in the text. Inset: Magnetization curve measured at 2 K for **MnNi₄**, the solid line represents the best fit with the parameters mentioned in the text.

On the one hand, due to the strong nickel-nickel coupling, the ground state is dominated by the properties of the manganese center and it is therefore again impossible to obtain reasonable values for the zero field splitting at the nickel ions. On the other hand, there are still a lot of parameters and one has to be very careful to avoid over-parametrization. For these reasons, the anisotropy of the nickel ions has been neglected and the anisotropy of the manganese was fixed to the values obtained by saturation measurements. Fitting the remaining parameters to the experimental data,^[11] regarding temperature independent paramagnetism and intermolecular interactions via the mean field approach (λ), gave the following results: $g_{\text{Mn}} = 1.997$ $g_{\text{Ni}} = 2.114$, $J_{\text{NiNi}} = -34.0 \text{ cm}^{-1}$, $J_{\text{MnNi}} = +1.3 \text{ cm}^{-1}$ and $\chi_{\text{TIP}} = 3.1 \cdot 10^{-3} \text{ cm}^3 \text{ mol}^{-1}$. These numbers are in accordance with the considerations above. The residual deviations at low temperatures are accounted for by the small mean field parameter $\lambda = -0.03 \text{ K}$. The g_{Mn} -value was limited to values lower than two, because it turned out to be correlated with χ_{TIP} . Furthermore, it has to be kept in mind that the g -value is strongly affected by any experimental error.

These results are also in good agreement with the obtained variable field variable temperature (VFVT) measurements. The experimental data can be simulated very nicely using the parameters obtained by the fitting procedures described above (Figure 4.19, right).

Iron Complex (FeNi₄)

At room temperature $\chi_M T$ is $5.3 \text{ cm}^{-1} \text{K mol}^{-1}$ for the iron(III) complex and still increases. For an iron(III) high spin this value is far too low ($S_{\text{Fe}} = \frac{5}{2}$, $S_{\text{Ni}} = 1$, $g_{\text{Fe}} = 2$ and $g_{\text{Ni}} = 2.1$ resulting in $\chi_M T \approx 8.79 \text{ cm}^{-1} \text{K mol}^{-1}$) and all attempts to fit these data with this configuration lead to unreasonable values for the parameters. Although the bond length suggest the iron(III) to be in the low spin state ($d(\text{Fe-O}) = 189\text{--}191 \text{ pm}$, $d(\text{Fe-N}) = 198\text{--}201 \text{ pm}$, taken from Plaul^[213]), it has to be remembered, that the crystal structure was recorded at 183 K. To exclude a spin transition at higher temperatures, Mössbauer spectra were recorded by Gabriele Spina from the Physics Department at the University in Florence to prove the electronic structure at room temperature. They also are in agreement with a low spin iron(III).^[337]

Under these circumstances the high temperature value can be explained by contributions of low lying spin-orbit coupled states of the iron(III) low spin. In first order perturbation, this leads to temperature independent paramagnetism (χ_{TIP}), which accounts for the monotonous increase of the $\chi_M T$ at higher temperatures. The low temperature value for $\chi_M T$ of $0.44 \text{ cm}^{-1} \text{K mol}^{-1}$ corresponds to an $S = \frac{1}{2}$ with $g = 2.17$. Assuming only isotropic iron–nickel and nickel–nickel exchange interactions leads to the Hamiltonian:

$$\begin{aligned} \hat{H} = & -J_{\text{NiNi}}(\hat{S}_{\text{Ni1}}\hat{S}_{\text{Ni2}} + \hat{S}_{\text{Ni3}}\hat{S}_{\text{Ni4}}) \\ & -J_{\text{FeNi}}(\hat{S}_{\text{Ni1}}\hat{S}_{\text{Fe}} + \hat{S}_{\text{Ni2}}\hat{S}_{\text{Fe}} + \hat{S}_{\text{Ni3}}\hat{S}_{\text{Fe}} + \hat{S}_{\text{Ni4}}\hat{S}_{\text{Fe}}) \end{aligned} \quad (4.17)$$

The best fit (Figure 4.20, left) was obtained using the parameters $g = 2.298$, $J_{\text{NiNi}} = -33.2 \text{ cm}^{-1}$, $J_{\text{FeNi}} = -39.9 \text{ cm}^{-1}$ and $\chi_{\text{TIP}} = 0.0017 \text{ cm}^3 \text{K mol}^{-1}$,^[11] which yield a twice degenerated $S = \frac{1}{2}$ ground state with a further $S = \frac{1}{2}$ and an $S = \frac{3}{2}$ lying 6.7 cm^{-1} and 13.2 cm^{-1} , respectively, above in energy (Figure 4.21 for the complete energy spectrum and the resulting Boltzmann population). The spin ground state is also confirmed by the isothermal (2 K) field dependence of the magnetization, which saturates to a value close to that expected for an $S = \frac{1}{2}$ system. (Figure 4.20, right) It is evident, that in contrast to the manganese derivative the exchange interaction involving the central iron atom is stronger than the nickel–nickel interactions. This yields an $S = \frac{1}{2}$ ground state which, in contrast to what is observed for the $S = 2$ ground state of

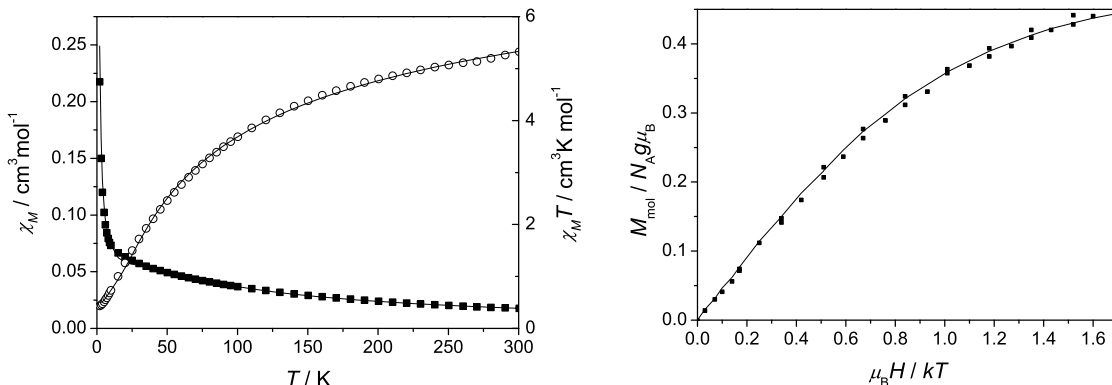


Figure 4.20: Left: Thermal dependence of the molar magnetic susceptibility χ_M (black boxes) and $\chi_M T$ (open circles) for FeNi_4 . Solid lines: simulated behavior with the parameters mentioned in the text. Right: Field dependence of the magnetization of FeNi_4 . Solid line: simulated behavior with the parameters mentioned in the text.

the manganese derivative, is not simply due to the central metal ion, but experiences relevant contributions of nickel wave functions. By contrast, the first excited doublet is completely iron centered. It is worth noting here that the assumption of purely isotropic exchange coupling made above is not at all justified when dealing with systems having unquenched orbital momentum, like low spin iron(III).^[344] However, since the agreement between the simulated behavior and the experimental one is satisfactory, and single crystal magnetic characterization is not available, the inclusion of additional parameters would not provide any relevant advancement in the knowledge of the energy pattern of the system. Yet the inclusion of anisotropic exchange may prove important in explaining the temperature and frequency dependence of the ESR spectra, as discussed in the following.

The X-Band ESR spectrum of FeNi_4 (Figure 4.22, left) consists of a dominant rhombic signal occurring at fields corresponding to g -values of [1.956, 2.123, 2.206]. On increasing temperature a reduction of the intensity of the spectrum is observed, indicating that the observed spectrum should be attributed to the ground state. The loss in intensity is accompanied by a broadening of the signal which points towards a rapidly decreasing spin-lattice relaxation time of the ground state. An analysis of the eigenvectors obtained by the best fit of magnetic data shows that the global g -value of the two degenerate $S = \frac{1}{2}$ ground states can be expressed as

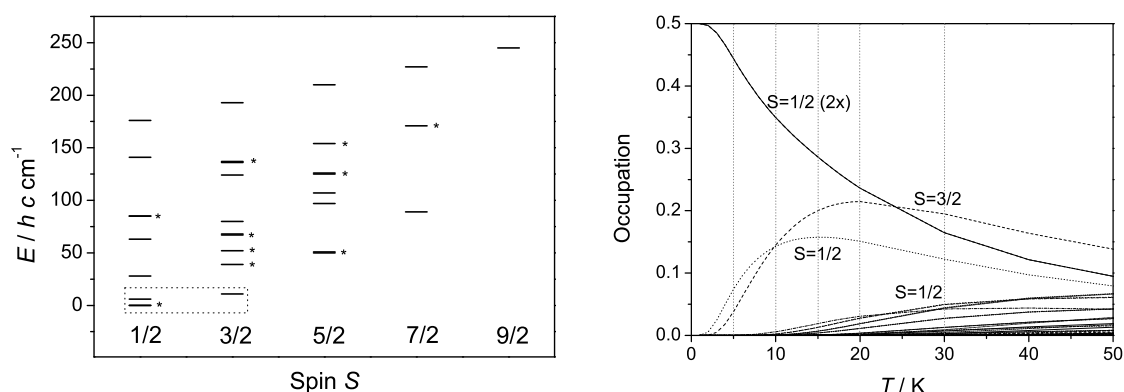


Figure 4.21: Left: Energy levels of FeNi_4 obtained with the parameters mentioned in the text. Bars with an asterisk indicate twofold degenerate levels. The dotted box contains the levels, which are thermally available in the ESR experiments. Right: Boltzmann factors of the energy levels of FeNi_4 in the temperature range between 1 and 50 K. The vertical dotted lines represent the temperatures where W-band spectra were recorded. The relevant levels are labeled according to their Spin S .

$$g_{\frac{1}{2}} = \frac{4}{3} \cdot g_{\text{Ni}} - \frac{1}{3} \cdot g_{\text{Fe}} \quad (4.18)$$

On the basis of results reported for similar trinuclear complexes^[329] and those obtained for CoNi_4 and MnNi_4 we can assume a g -value of 2.1 for the nickel ions: this gives the pattern [1.782, 2.031, 2.532] for g_{Fe} , which is within the expected range for low spin iron(III).^[345–353] Indeed, using ligand field arguments it can be shown that the observed value corresponds to a composition of the iron(III) ground doublet

$$\Psi = 0.07 \cdot d_{xy} + 0.98 \cdot d_{yz} + 0.20 \cdot d_{xz} \quad (4.19)$$

with an orbital reduction factor of $k = 0.71$.^[354] Two additional signals at around 1305 G ($g_{\text{eff}} = 5.12$) and 4020 G ($g_{\text{eff}} = 1.70$) are also observed (marked with asterisks in Figure 4.22, left). They broaden on increasing temperature and can in principle be attributed either to the first excited $S = \frac{1}{2}$ state or to the $S = \frac{3}{2}$ one.

To have a more confident assignment of the spectrum to the different low lying paramagnetic states W-band ESR spectra were recorded at variable temperature (Figure 4.22, right). The first difference which can be observed with respect to X-band, is that

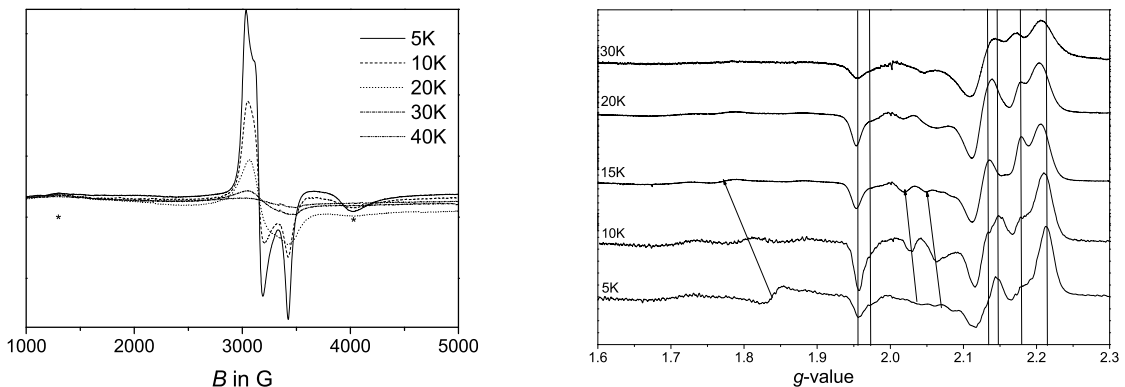


Figure 4.22: Left: X-Band ESR spectra of FeNi_4 , recorded on powder samples at different temperatures. Right: W-Band ESR spectra of FeNi_4 , recorded on powder samples at different temperatures (solid lines). The vertical lines represent the set of main signals, the arrows indicate the shifting side signals (see text).

due to the higher frequencies and fields used the spectrum is much more resolved. In particular, a doubling of the lines is seen in the rhombic signals, with the relative intensities of the two components depending on temperature. This suggests that the two $S = \frac{1}{2}$ ground states, which are degenerate in the simple assumption of isotropic coupling, are actually lying at different energies, and their wave functions are also slightly different.

A further signal is observed at about 40 000 G. Since the corresponding g -value of this signal ($g_{\text{eff}} = 1.67$) is the same observed at X-band we may assume that this is one g -component of the first excited $S = \frac{1}{2}$ level. In this framework the absence of signals due to the other components of the anisotropic g -value of the $S = \frac{1}{2}$ level should be attributed to an excessive line broadening preventing them to be observed. However, it has to be noted that in the simple isotropic coupling approach used to simulate the magnetic measurements this state should be purely iron centered, so that $g_{\frac{1}{2}} = g_{\text{Fe}}$, where g_{Fe} was obtained by the projection analysis of the ground state g -values. The fact that this is not the case indicates once more that the anisotropic exchange coupling plays a relevant role in terms of composition and energy pattern of the lowest lying states.

An additional fine structure of the spectrum, with resonant fields strongly dependent on temperature, is also observed in W-band spectra (arrows in Figure 4.22, right). On

the basis of the energy pattern obtained by magnetic measurements these signals are attributed to the $S = \frac{3}{2}$ level split in zero field. The observed shift can be explained to be due to a temperature dependence of the local anisotropy of the nickel ions, which has been described by Penrose and Stevens in 1950^[355] and is attributed to small structural distortions at low temperatures. This would be in qualitative agreement with the substantial nickel character of the first $S = \frac{3}{2}$ state obtained by the magnetic measurement analysis and with the correspondingly expected contribution of the nickel ions to the overall anisotropy. The global extension of this fine structure points to a zero-field splitting increasing from 0.85 cm^{-1} at 5 K to 1.0 cm^{-1} at 30 K. On the basis of the corresponding spin projection coefficients, and assuming collinear single ion anisotropy tensors, a D of $1.5 - 2 \text{ cm}^{-1}$ can be estimated for the nickel centers, which is in the expected range for nickel(II) in octahedral environment.^[8;356-360]

Alternatively, one may attribute the shift of the resonance fields to the coalescence of signals due to different spin states, so that changes in the thermal population of the levels would result in different contributions to the observed signal.^[361] However, this would imply that there is at least another $S = \frac{3}{2}$ state close in energy to the first one, which is apparently not the case here.

4.4 Outlook

The use of small symmetric bridging ligands is a suitable way of designing highly symmetric crystals. In avoiding conformers of side arms a more rigid orientation is enforced. This should be transferred onto other systems which are good candidates as SMMs, for example lanthanides. To achieve linking by phloro³⁻ one must first block all but two coordination sites of the metal ion. Coordination of the bridging ligand to lanthanides is further enhanced due to the oxophilicity of these metals.

In the case of the lanthanide chain compounds the isostructural series of lanthanides with orbital momentum should be extended to have a broader base for the determination of the ligand field parameters. The temperature dependence of the magnetic susceptibility of the terbium and europium compound should be measured on samples grinded with grease as well. Though the coupling by the bridging ligand is rather small, preliminary *ac*-susceptibility measurements indicate single chain magnet behavior for the dysprosium compound. Unfortunately the blocking temperature and energy barrier are too low for a quantitative evaluation. Furthermore, to avoid the interchain interactions, sulfonated Mesalen ligands (Section 3.2) should be used with large counter ions to separate the individual one-dimensional coordination polymers.

The analysis of the magnetic data recorded on the pentanuclear complexes clearly show how robust the exchange coupling inside the triaminoguanidine is. The nature and size of the exchange coupling constant between the nickel ions is perfectly preserved also in more complex structures in comparison to homometallic trinuclear complexes. This makes the triaminoguanidine a perfect candidate for quantum computing, allowing aggregation and modifications on the periphery and still maintaining the desired functionality. Replacing the iron by a transition metal ion without orbital contribution should avoid antisymmetric exchange interactions and prevent lifting of the degeneracy. These system could then also serve as qubits.

5 Summary / Zusammenfassung

5.1 Summary

This thesis shows several pioneering approaches towards new building blocks for molecular spintronics. The synthesis of new building blocks is described as well as extended analysis of final compounds. Two new ligand scaffolds are presented comprising triphenylamine derivatives as highly functional entities (Figures 5.1 and 5.2). Furthermore compounds based on triaminobenzene, triaminoguanidines (Figure 5.4), Mesalen-type ligands (Figure 5.3) and acetyl-substituted phloroglucinine are characterized carefully regarding their magnetic properties in order to elucidate their potential use for molecular spintronics. The results obtained from these evaluations are then successfully transferred to other classes of materials, hence proving the validity of the building block approach: the magnetic anomaly found in triaminobenzene compounds is incorporated in carbazole based compounds and the use of sulfonato groups in various compounds shows highly interesting properties:

1. It drastically changes the solubility of the obtained compounds. The water soluble products can be incorporated into polyvinylalcohol films. This is a promising approach for future materials.
2. It favors the formation of extended structure schemes due to the coordinating properties of the sulfonato oxygens.
3. It offers new structure schemes like the hydrogen bonding of amines.

Especially the last point is of great interest with respect to the combination of functional entities.

5.1.1 New Functionalities

Section 2.1 deals with the combination of the well-known electrochemical properties of triphenylamines with the magnetic properties of transition metal ions. Amino derivatives with triphenylamine core are synthesized and are reacted with salicylaldehyde derivatives to give the ligands HTPA (**3**) and H^{tBu} TPA (**4**). The redox chemistry of these two ligands was investigated by means of cyclic voltammetry, UV/Vis spectroscopy and theoretical calculations using DFT and semiempirical methods. The successive addition of copper(II) ions and hexafluoroacetylacetonate (Hhfac) to HTPA gives rise to the formation of the dimeric complex $[Cu_2(hfac)_2(HTPA)_2]$ (**5**). Reaction of copper(II) with two equivalents of H^{tBu} TPA yields the complex $[Cu(H^{tBu}TPA)_2]$ (**6**), in which the copper ion is tetracoordinated in a distorted tetrahedral environment. These results show nicely, that the synthesis of both homoleptic and heteroleptic complexes is possible with this type of ligands. These complexes have been characterized according to their magnetic properties. The coupling within the dimer **5** is weakly ferromagnetic as it is expected from the small Cu–O–Cu bridging angle. The ESR spectra recorded of **6** indicate strong distortions from the ideal tetrahedral structure.

Section 2.2 investigates a magnetic anomaly found in a series of dinuclear cyclic copper complexes in triaminobenzene based systems. It is shown that this effect is caused by an interplay between insufficient equilibrium times during the measurements and a very slow structural transition. The nature of this transition is explained by changes in the

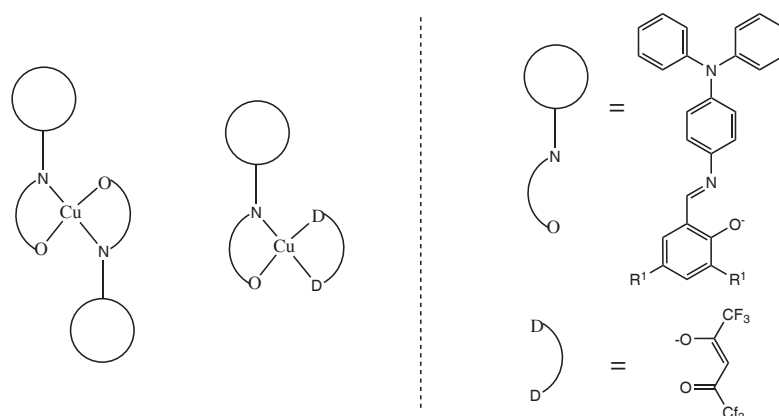


Figure 5.1: Coordination possibilities with ligands based on triphenylamines. R^1 can be either hydrogen or *tert*-butyl.

strongly distorted tetrahedral coordination environment of the copper ions. The distortions can be described by the tilting of a plane spanned by the two donor atoms of one ligand and the coordinated copper ion against the corresponding plane formed by the second ligand with the copper ion. The impact of changes in the angle between these two planes on the energy pattern was investigated theoretically using ligand field arguments. The temporal progress of the transformation was monitored with isothermal time dependent determination of the magnetic susceptibility and the limiting values for $t \rightarrow 0$ and $t \rightarrow \infty$ were deduced by extrapolation. W-band ESR spectra recorded at different temperatures on powder samples confirm structural changes.

5.1.2 New Building Blocks

Section 3.1 deals with the synthesis and characterization of dinuclear metallacycles based on carbazole containing ligands. The additional carbon–carbon bond in carbazoles reduces the flexibility compared to the triphenylamine compounds and therefore promotes the crystallization. It also accounts for a strong photoactivity and thus allows to characterize the electronic properties by means of fluorescence spectroscopy. The ligands $\text{H}_2\text{CarbOMe}$ (**10**), $\text{H}_2^{t\text{Bu}}\text{CarbOMe}$ (**13**) and $\text{H}_2^{\text{Sulf}}\text{CarbOMe}$ (**15**) have been prepared and reacted with copper(II) and zinc(II) ions forming dinuclear metallacycles, which were characterized by X-ray diffraction in the case of $\text{H}_2\text{CarbOMe}$. The formation of the complexes as well as the complexes themselves were investigated thoroughly by several spectroscopic methods in combination with theoretical calculations using DFT and semiempirical methods. The introduction of the *tert*-butyl groups in $\text{H}_2^{t\text{Bu}}\text{CarbOMe}$ leads to the occurrence of the magnetic anomaly described in the previous chapter. It was therefore successively transferred into a different class of ligands. The introduction of the very polar sulfonato groups gives rise to complexes, which are water soluble and can be incorporated in polyvinylalcohol films. This is a promising way for the fabrication of functional materials.

Section 3.2 shows how the properties of the sulfonato groups can also be used for the construction of supramolecular assemblies. The use of sulfonato substituted *ortho*-vanilline (**20**) for the synthesis of $\text{Na}_2\text{H}_2^{\text{Sulf}}\text{Mesalen}$ (**21**) leads to two major impacts in the complexes with copper(II) and manganese(III). On the one hand the sulfonato group coordinates the metal ions in an axial position leading to the formation of metal-

lacycles $[M_2(\text{SulfMesalen})_2]$. On the other hand the outer cavity of the Mesalen ligand is capable of coordinating additional metal ions and ammonium ions. Using ethylene diamine for the deprotonation of the ligand results in the binding of one protonated amine via several hydrogen bonds to the O_4 donor set, which are stabilized by the electrostatic interactions between the positively charged ammonium group and the negative charge of the complex. The second amino group is either located near the axial position of the metal center (22) or is bound by a second complex molecule leading to a 1-dimensional hydrogen bonded polymer 23 and 24 (Figure 5.3). The mode of binding can be controlled by the crystallization conditions. ESR spectra recorded on frozen H_2O solution indicate dissociation of the metallacycles in solution.

In Section 3.3 the advantages of sulfonato groups are transferred to triaminoguanidine ligands and the synthesis of the ligand $Na_2H_6\text{SulfTAG}$ (27) is described. This ligand system has been shown to transmit very strong antiferromagnetic interactions and to yield compounds with strict C_3 symmetry (mode (a) in Figure 5.4). These are very good premises for the use of such compounds as qubits with long coherence times. The reported copper(II) complex (26) based on the unsubstituted ligand (25) and its formation in solution were investigated by spectroscopic methods. The formation of the trinuclear copper complex with the sulfonated ligand 27 was investigated by means of UV/Vis-spectroscopy. Using $[Ru(\text{bipy})_3]^{2+}$ as bulky and non-coordinating precipitating agent the compound $[Ru(\text{bipy})_3][(\text{SulfTAG})Cu_3(\text{bipy})_3]$ (28) was isolated. In this molecule the antiferromagnetic coupling is even stronger than in 26. According to the magnetic susceptibility even at room temperature only the ground doublets are populated, which

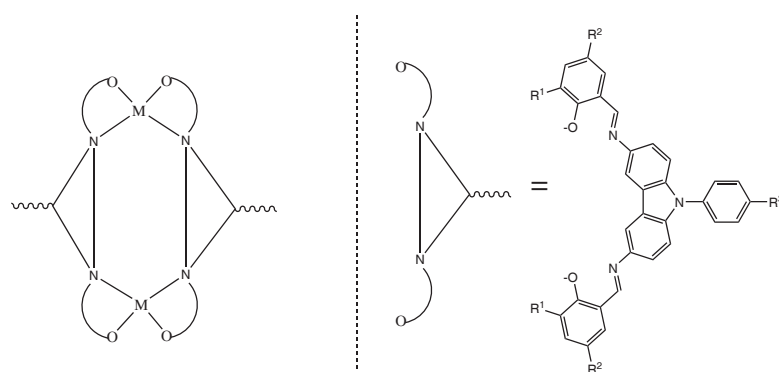


Figure 5.2: Building blocks based on carbazoles. R^1 can be either hydrogen or *tert*-butyl, R^2 hydrogen, *tert*-butyl or sulfonato and R^3 either methoxy or hydroxy.

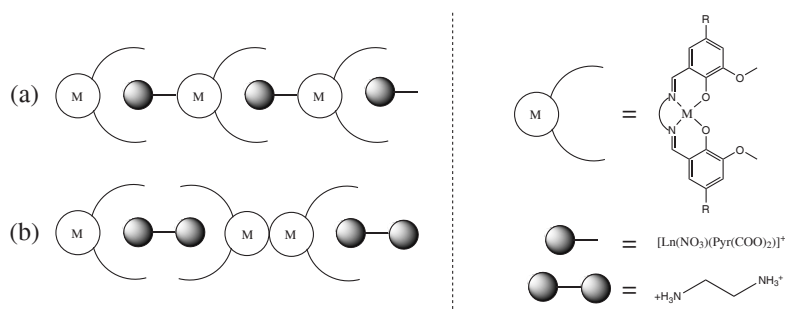


Figure 5.3: Building blocks and their linkage mode based on Mesalen-type ligand, where R can either be hydrogen or sulfonato. Linkage can occur by lanthanide ions and the use of bridging ligands (mode (a), $\text{Pyr}(\text{COO})_2$: 2,4-dicarboxy-pyrazine) as discussed in Section 4.2 or via coordination of ethylenediamine (mode (b), Section 3.2)

makes this compound even more interesting for quantum computation. Low temperature ESR measurements on powder samples of **28** reveal an extended hyperfine structure in contrast to **26**, where only broad, unresolved lines are observed. This clearly shows that the molecules are successfully separated by the use of sulfonated ligands in combination with bulky counter ions. The introduction of the sulfonato groups also allows the preparation of polyvinylalcohol films. The existence of the trinuclear compound in the polymer matrix is confirmed by UV/Vis spectroscopy. Magnetic measurements again point towards very large coupling and the ESR spectra recorded at very low temperatures are in good agreement with the ones observed for **28**. Sulfonated triaminoguanidines are therefore not only highly promising candidates for quantum bit storing but they also give easy access to final materials.

5.1.3 Linked Building Blocks

In Section 4.1 the linkage of a copper(II) precursor to a highly symmetric compound is described. The use of the small, rigid bridging ligand 2,4,6-triacetyl-phloroglucine (*phloro*) results in the formation of disk-shaped molecules, which form columns in a hexagonal arrangement. The symmetry of the bridging ligand is nicely transferred both onto the complex molecule and the crystal shape and structure. Magnetic measurements and single crystal ESR investigations both in X- and W-band show that the copper ions are coupled ferromagnetically. Due to the high symmetry, which gives only one orientation of molecules per crystallite, a uniform distribution of orientations

necessary for powder measurements can not be achieved. This emphasizes the precautions, which are necessary in the case of highly symmetric compounds.

Section 4.2 discusses the magnetic properties of a 1-dimensional coordination polymer (Figure 5.3). It is based on heterodinuclear copper-lanthanide complexes on the basis of the unsubstituted Mesalen ligand. These building blocks are linked by the bridging ligand 2,4-dicarboxy-pyrazine. Analysis of the magnetic data reveals that coupling through the bridging ligand is present, but rather weak. The measured data are analyzed including the orbital momentum and spin orbit coupling assuming an idealized pentagonal symmetry around the lanthanide ion. It is shown, that the magnetic behavior of different lanthanides can be explained using only one set of ligand field parameters. Also the exchange coupling is found to be very similar. Analysis of the W-band ESR spectra recorded on powder samples of the gadolinium compound confirm tilting of the principal axis of the metal coordination polyhedra inside the building block.

Finally, Section 4.3 presents a detailed study regarding the magnetic properties of three pentanuclear complexes $[MNi_4(RTAG)_2(tptz)_4]^+X^-$ ($M = Fe, Co, Mn$; $X = Cl^-, ClO_4^-$; $R = H, Br$). In these complexes two triaminoguanidine moieties are linked by a central trivalent metal ion (mode (b) in Figure 5.4). The other four binding pockets are filled with nickel(II) ions, whose free coordination sites are saturated with the tridentate capping ligand 2,4,6-*tris*-(2-pyridin)-triazin (tptz). In these complexes the nickel–nickel interactions along the triaminoguanidine backbone well resemble the ones found in trinuclear homometallic compounds. By contrast, the coupling to the central ion depends strongly on the nature of this metal ion. The cobalt(III) is low spin, leading to

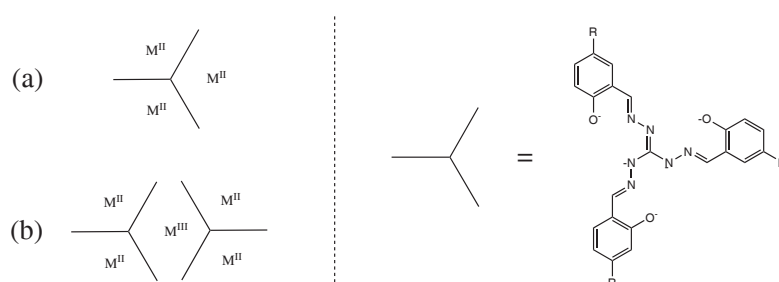


Figure 5.4: Trinuclear (a) and pentanuclear (b) complexes on the basis of triaminoguanidines. M^{II} can be copper(II) or nickel(II) and R refers to hydrogen or sulfonato.

a diamagnetic bridge. The magnetic data can therefore be reproduced assuming two isolated nickel dimers. Manganese(III) is in the high spin state with $S = 2$. Possessing electrons both of t_{2g} and e_g symmetry, a lot of exchange pathways with different sign are present which sum up to only weak overall interactions. Since the coupling inside the nickel dimers is much stronger, the behavior of the ground state can hence be described by a single $S = 2$ system. This is confirmed by isothermal magnetization measurements at 2 K. From these measurements also the zero field splitting parameters are deduced. Analysis of the thermal dependency of the magnetic susceptibility on the basis of the obtained parameters gives small ferromagnetic nickel–manganese interactions.

The magnetic data of the iron(III) compound were analyzed using isotropic exchange. The temperature dependence of the susceptibility can be reproduced very nicely with iron–nickel interactions which are stronger than the nickel–nickel interactions. Hence, the ground state is not centered on the central metal ion like in the manganese compound, but it is rather delocalized over the nickel ions. This gives rise to a degenerated ground state. ESR spectra recorded both in X- and W-band at different temperatures are in good agreement with a low spin iron(III) and confirm contributions of the nickel ions to the ground state. However, they also show several features like the splitting of the main signals with temperature dependent intensities, which clearly point towards lifting of the degeneracy by non-isotropic interactions. Yet the main characteristics of the triaminoguanidine ligand are preserved even in this rather complex structure, although the full analysis of the exchange coupling properties in the nickel–iron pairs would require single crystal experiments.

5.2 Zusammenfassung

Diese Arbeit zeigt mehrere wegweisende Ansätze auf dem Weg zu neuen Bausteinen für die Molekularelektronik. Die Synthese von neuen Bausteinen steht dabei ebenso im Fokus wie die ausgedehnte Analyse der erhaltenen Verbindungen. Zwei neue Ligandgerüste werden beschrieben, die hochfunktionale Triphenylamineinheiten enthalten (Abbildungen 5.5 und 5.6). Des Weiteren werden Verbindungen auf der Basis von Triaminobenzen, Triaminoguanidin (Abbildung 5.8), Mesalen-artigen Liganden (Abbildung 5.7) und acetylsubstituierten Phloroglucin untersucht und sorgfältig bezüglich ihrer magnetischen Eigenschaften charakterisiert, um ihr Potential für die molekulare Spintronik zu beleuchten. Die erhaltenen Ergebnisse konnten anschließend erfolgreich in andere Materialklassen übertragen werden, was die Eignung des Bausteinansatzes beweist: Die magnetische Anomalität, wie sie in Verbindungen basierend auf Triaminobenzen gefunden wurde, konnte erfolgreich in Carbazolverbindungen integriert werden. Außerdem zeigt der Einbau von Sulfonatgruppen in mehrere Verbindungen hochinteressante neue Eigenschaften:

1. Die Lösungseigenschaften der erhaltenen Verbindungen werden stark geändert. Die wasserlöslichen Produkte können in Polyvinylalkoholfolien eingebettet werden, was einen vielversprechenden Ansatz für zukünftige Materialien darstellt.
2. Er begünstigt auf Grund der Koordinationsfähigkeiten der Sulfonatgruppe die Ausbildung ausgedehnter Strukturen.
3. Er bietet neue Strukturen durch die Bindung von Ammoniumgruppen mittels mehrfacher Wasserstoffbrückenbindungen an Mesalen-artige Metallkomplexe.

Besonders der letzte Punkt ist im Bezug auf die Kombination von funktionalen Bausteinen von besonderem Interesse.

5.2.1 Neue Funktionen

Abschnitt 2.1 behandelt die Kombination der wohlbekannten elektrochemischen Eigenschaften von Triphenylaminen mit den magnetischen Eigenschaften von Übergangsmetallionen. Aminverbindungen mit Triphenylaminkern werden dargestellt und mit Salicylaldehydderivaten umgesetzt, um die Liganden HTPA (3) und H^{tBu}TPA (4) zu

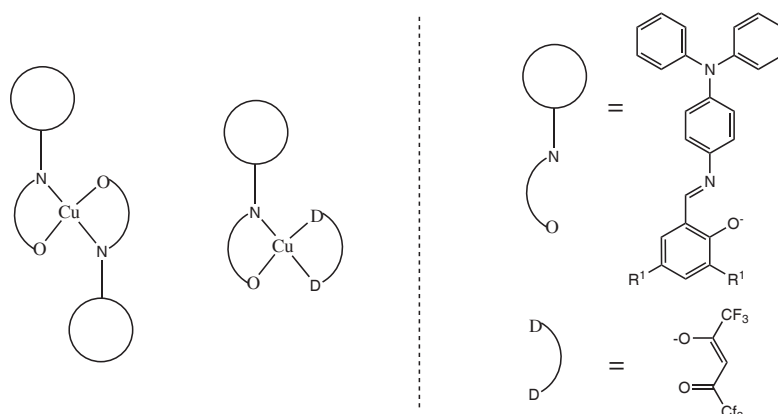


Abbildung 5.5: Möglichkeiten der Koordination bei Liganden auf der Basis von Triphenylaminen. R^1 entspricht entweder Wasserstoff oder *tert*-Butyl.

erhalten. Die Redoxchemie dieser zwei Liganden wurde mittels Cyclovoltammetrie, UV/Vis-Spektroskopie und theoretischen Berechnungen mit DFT und semiempirischen Verfahren untersucht. Die schrittweise Zugabe von Kupfer(II)ionen und Hexafluoroacetylacetonat zu HTPA führt zu der Bildung des Dimers $[\text{Cu}_2(\text{hfac})_2(\text{TPA})_2]$ (**5**). Die Reaktion von Kupfer(II) mit zwei Äquivalenten $\text{H}^{t\text{Bu}}\text{TPA}$ ergibt dagegen den Komplex $[\text{Cu}(^{t\text{Bu}}\text{TPA})_2]$ (**6**), in dem das Kupfer vierfach koordiniert in einer verzerrt tetraedrischen Struktur vorliegt. Diese Ergebnisse zeigen deutlich, dass sowohl homo- als auch heteroleptische Komplexe mit dieser Art von Liganden zugänglich sind. Die erhaltenen Komplexe wurden hinsichtlich ihrer magnetischen Eigenschaften charakterisiert. Die Wechselwirkung innerhalb des Dimeres **5** ist schwach ferromagnetisch, wie es auf Grund des kleinen Cu–O–Cu Winkels zu erwarten ist. Die ESR-Spektren, die von der Verbindung **6** aufgenommen wurden, deuten auf starke Verzerrungen von der idealen tetraedrischen Struktur hin.

Abschnitt 2.2 untersucht eine magnetische Anomalie, die in einer Serie von zweikernigen Metallzyklen mit Triaminobenzol-Liganden gefunden wurde. Es wird gezeigt, dass dieser Effekt auf einem Wechselspiel zwischen zu kurzen Gleichgewichtszeiten während der Messungen und einer sehr langsamen Strukturänderung beruht. Die Natur dieses Übergangs wird mit Änderungen in der stark verzerrten tetraedrischen Koordination der Kupferionen erklärt. Diese Verzerrungen können durch den Verdrehungswinkel der beiden Ebenen beschrieben werden, die jeweils von den zwei Donoren eines Liganden mit dem Kupferion gebildet werden. Der Einfluss von Änderungen in

diesem Winkel auf das Energieschema wurde ligandenfeldtheoretisch untersucht. Der zeitliche Verlauf der Umwandlung wurde mit zeitabhängigen isothermischen Bestimmungen der magnetischen Suszeptibilität verfolgt. Aus diesen Messungen konnten die beiden Grenzwerte $t \rightarrow 0$ und $t \rightarrow \infty$ durch Extrapolation gewonnen werden. Die strukturellen Veränderungen wurden weiterhin durch W-Band ESR-Spektren bei verschiedenen Temperaturen bestätigt.

5.2.2 Neue Bausteine

Abschnitt 3.1 handelt von der Synthese und der Charakterisierung von zweikernigen Metallzyklen basierend auf carbazolhaltigen Liganden. Die zusätzliche Kohlenstoff-Kohlenstoff-Bindung reduziert die Flexibilität verglichen mit den Triphenylaminverbindungen und begünstigt somit die Kristallisation. Sie führt auch zu starker Photoaktivität und erlaubt somit die Charakterisierung der elektronischen Eigenschaften mittels Fluoreszenzspektroskopie. Es wurden die Liganden $H_2\text{CarbOMe}$ (**10**), $H_2^{tBu}\text{CarbOMe}$ (**13**) und $H_2^{Sulf}\text{CarbOMe}$ (**15**) dargestellt und intensiv mit Hilfe verschiedener spektroskopischer Verfahren in Kombination mit theoretischen Rechnungen (DFT und semiempirische Verfahren) untersucht. Die Einführung der *tert*-Butylgruppen führt zum Auftreten der magnetischen Anomalie, wie sie im vorigen Kapitel beschrieben wurde. Sie kann somit erfolgreich in eine andere Klasse von Liganden übertragen werden. Die Einführung von Sulfonatgruppen dagegen führt zu wasserlöslichen Komplexen, die in Polyvinylalkoholfolien eingebettet werden können. Dies ist ein vielversprechender Weg zu neuen funktionalen Materialien.

Abschnitt 3.2 zeigt auf, wie die Eigenschaften der Sulfonatgruppen auch für den Aufbau von supramolekularen Strukturen genutzt werden können. Die Verwendung sulfonatsubstituierter *ortho*-Vanillins bei der Synthese des Liganden $\text{Na}_2\text{H}_2^{Sulf}\text{Mesalen}$ (**21**) zeigt zwei Haupteinflüsse auf die Struktur der Kupfer(II)- und Mangan(III)komplexe. Auf der einen Seite koordiniert die Sulfonatgruppe an das Metallion in axialer Position und führt zur Ausbildung von Metallzyklen $[\text{M}_2^{(Sulf)\text{Mesalen}}]_2$. Auf der anderen Seite ist die äußere O_4 -Bindungstasche des Mesalen-Liganden zur Koordination von zusätzlichen Metallionen oder Ammoniumionen fähig. Die Verwendung von Ethylendiamin zur Deprotonierung des Liganden resultiert in der Anbindung eines protoniertenamins durch mehrere Wasserstoffbrückenbindungen zum O_4 -Donorsatz, wel-

che zusätzlich durch die elektrostatischen Wechselwirkungen zwischen dem positiv geladenen Ammoniumion und der negativen Ladung des Komplexes stabilisiert werden. Die zweite Ammoniumgruppe befindet sich entweder nahe der axialen Position des Metallzentrums (Verbindung **22**) oder wird durch ein zweites Komplexmolekül gebunden, was zur Ausbildung von eindimensionalen wasserstoffverbrückten Polymeren **23** und **24** führt (Weg (b) in Abbildung 5.7). Die Art der Anbindung kann dabei über die Kristallisationsbedingungen gesteuert werden. In wässriger Lösung aufgenommene ESR-Spektren deuten die Dissoziation des Metallzyklus in Lösung an.

Im Abschnitt 3.3 werden die Vorteile der Sulfonatgruppen auf Triaminoguanidinliganden übertragen und es wird die Synthese des C_3 -symmetrischen, tritopen Liganden $\text{Na}_2\text{H}_6^{\text{Sulf}}\text{TAG}$ (**27**) beschrieben. Es konnte bereits gezeigt werden, dass diese Ligandensysteme sehr starke antiferromagnetische Wechselwirkung vermitteln und zu Verbindungen mit strikter C_3 -Symmetrie führen (Art (a) in Abbildung 5.8). Dies sind hervorragende Voraussetzungen um solche Verbindungen als QuBits mit langen Kohärenzzeiten einzusetzen. Der bereits beschriebene Kupfer(II)komplex (**26**) auf der Basis des unsubstituierten Liganden $\text{H}_5^{\text{H}}\text{TAG}\cdot\text{HCl}$ (**25**) sowie seine Bildung in Lösung wurden eingehend mittels spektroskopischer Methoden untersucht. Die Bildung des dreikernigen sulfonatsubstituierten Kupferkomplexes wurde mittels UV/Vis-Spektroskopie untersucht. Unter Verwendung von $[\text{Ru}(\text{bipy})_3]^{2+}$ als sperrigem und nichtkoordinierendem Fällungsmittel konnte die Verbindung $[\text{Ru}(\text{bipy})_3][(\text{Sulf}^{\text{TAG}}\text{Cu}_3(\text{bipy})_3)]$ (**28**) isoliert werden. In diesem Molekül ist die antiferromagnetische Wechselwirkung sogar noch stärker als in **26**. Den magnetischen Daten nach ist selbst bei Raumtemperatur nur das

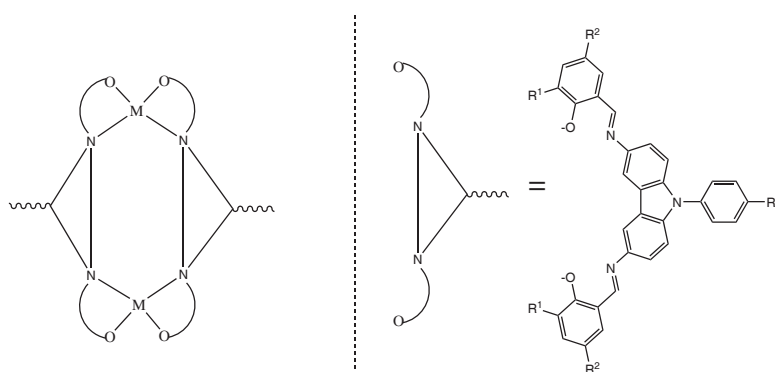


Abbildung 5.6: Bausteine auf der Basis von Carbazolen. R^1 ist entweder Wasserstoff oder *tert*-Butyl, R^2 Wasserstoff, *tert*-Butyl oder Sulfonat und R^3 entweder Methoxy oder Hydroxy.

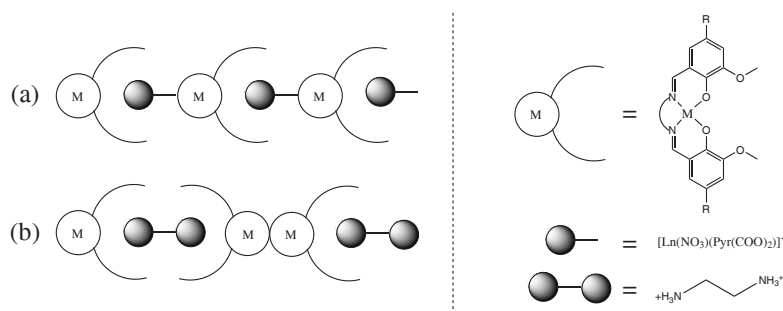


Abbildung 5.7: Bausteine und deren Verknüpfung auf der Basis von Mesalen-artigen Liganden, dabei kann R entweder Wasserstoff oder Sulfonat sein. Verknüpfungen kann durch Lanthanoide und die Verwendung von Brückenliganden erfolgen, wie sie in Abschnitt 4.2 beschrieben wird (Weg (a) $\text{Pyr}(\text{COO})_2$: 2,4-dicarboxy-pyrazine) oder durch die Koordination von Ethylendiamin (Weg b), wie sie in Abschnitt 3.2 dargestellt ist.

Grunddublett bevölkert, was diese Verbindung noch interessanter für Quantencomputer macht. Tieftemperatur ESR-Spektren von Pulverproben der Verbindung **28** zeigen eine ausgeprägte Hyperfeinstruktur, im Gegensatz zur Verbindung **26**, in deren Spektren nur unstrukturierte breite Banden beobachtet werden. Dies zeigt deutlich, dass die Einführung von Sulfonatgruppen in Verbindung mit sperrigen Gegenionen zu einer erfolgreichen Separation der Komplexmoleküle führt. Die Einführung der Sulfonatgruppen erlaubt weiterhin die Darstellung von Polyvinylalkoholfolien. Die Existenz des dreikernigen Komplexes in der Polymermatrix wird durch UV/Vis-Spektroskopie bestätigt. Magnetische Messungen deuten wiederum auf sehr starke Kopplungen hin und die ESR-Spektren, die bei tiefen Temperaturen gemessen wurden, stimmen gut mit denen der Verbindung **28** überein. Die sulfonierten Triaminogandinkomplexe sind daher nicht nur vielversprechende Kandidaten als QuBits, sie lassen sich zusätzlich auch leicht zu funktionalen Materialien verarbeiten.

5.2.3 Verbrückte Bausteine

In Abschnitt 4.1 wird die Verknüpfung von Kupfer(II)-Vorläufern zu hochsymmetrischen Verbindungen beschrieben. Die Verwendung des kleinen, starren Brückenliganden 2,4,6-Triacetylphloroglucin führt zur Bildung von scheibenförmigen Verbindungen, die sich in hexagonal angeordneten Säulen stapeln. Die Symmetrie des Brückenliganden wird somit sowohl auf das Komplexmolekül, als auch auf Kristallform und

-struktur übertragen. Messungen der magnetischen Suszeptibilität als auch Einzelkristall-ESR-Spektren in X- und W-Band zeigen, dass die Kupferzentren ferromagnetisch gekoppelt sind. Auf Grund der hohen Kristallsymmetrie, die nur eine Orientierung pro Kristallit zulässt, kann keine gleichförmige Verteilung an Orientierungen erreicht werden, wie sie für Pulvermessungen nötig ist. Dies verdeutlicht, welche große Vorsicht bei der Messung hochsymmetrischer Verbindungen angebracht ist.

Abschnitt 4.2 diskutiert die magnetischen Eigenschaften eines eindimensionalen Koordinationspolymers (Abbildung 5.7). Dieses wird durch heterodinuklear Kupfer-Lanthanoid-Komplexe aufgebaut, die mit unsubstituierten Mesalen-Liganden gebildet werden. Diese Bausteine sind durch den Brückenliganden 2,4-Dicarboxypyrazin verbunden. Die Analyse der magnetischen Daten weist darauf hin, dass eine Kopplung durch den Brückenliganden stattfindet, diese jedoch sehr schwach ist. Die Messwerte werden unter Berücksichtigung des Bahndrehimpulses analysiert, wobei eine pentagonale Bipyramide als idealisierte Symmetrie am Lanthanoidion angenommen wird. Es wird gezeigt, dass das magnetische Verhalten verschiedener Lanthanoide mit nur einem Satz an Ligandenfeldparametern beschrieben werden kann. Auch die Kupfer-Lanthanoid-Austauschwechselwirkungen sind sehr ähnlich. Die Auswertung der W-Band ESR-Spektren, die an Pulverproben der Gadoliniumverbindung aufgenommen wurden, bestätigt die Verdrehung der Hauptachsen der Metallkoordinationspolyeder innerhalb des Bausteins.

Anschnitt 4.3 präsentiert zum Abschluss eine detaillierte Analyse der magnetischen Eigenschaften in einer Serie von fünfkernigen Komplexen $[M Ni_4(RTAG)_2(tpz)_4]^+ X^-$

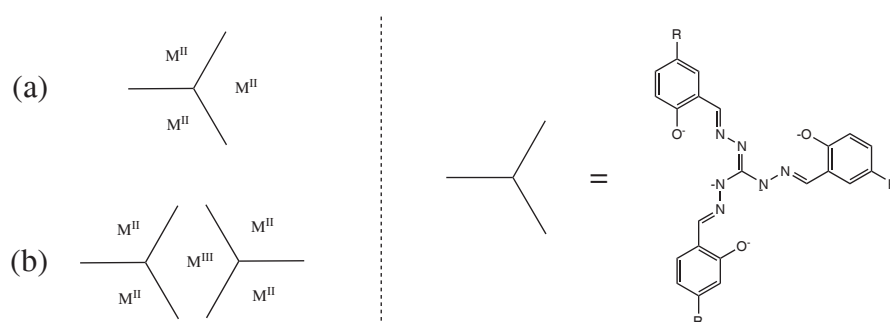


Abbildung 5.8: Dreikernige (a) und fünfkernige (b) Komplexe basierend auf Triaminoguanidinen. M^{II} kann Kupfer(II) oder Nickel(II) sein und R entweder Wasserstoff oder Sulfonat.

(M = Fe, Co, Mn; X = Cl⁻, ClO₄⁻; R = H, Br). In diesen Komplexen sind zwei Triaminoguanidineinheiten durch ein zentrales dreiwertiges Metallion verknüpft (Weg (b) in Abbildung 5.8). Die übrigen vier Bindungstaschen werden mit Nickel(II)ionen gefüllt, die wiederum mit dem Koliganden 2,4,6-tris-(2-pyridin)-triazin (tptz) koordinativ abgesättigt werden. In diesen Komplexen entspricht die Nickel–Nickel-Wechselwirkung über den Triaminoguanidinkern derjenigen, die in dreikernigen, homometallischen Nickelkomplexen gefunden wurde. Im Gegensatz dazu hängt die Kopplung zum Zentralatom stark von dessen Natur ab. Im Falle des Kobalt(III) handelt es sich um eine *low spin* Verbindung, was zu einer diamagnetischen Brücke führt. Die magnetischen Daten können daher unter Annahme zweier unabhängiger Nickeldimere nachgebildet werden. Mangan(III) dagegen befindet sich im *high spin* Zustand mit vier ungepaarten Elektronen. Da es sowohl Elektronen der Symmetrie *t_{2g}* als auch *e_g* besitzt, ergibt sich eine Vielzahl von Austauschwechselwirkungspfaden mit unterschiedlichem Vorzeichen, welche in Summe nur eine schwache Gesamtwechselwirkung ergeben. Da der Austausch innerhalb der Nickeldimere wesentlich stärker ist, wird das Verhalten des Grundzustandes daher durch ein *S* = 2 System beschrieben. Dies wird durch Magnetisierungsmessungen bei 2 K bestätigt, aus denen auch die Größe der Nullfeldaufspaltung abgeleitet werden kann. Die Analyse der Suszeptibilitätsmessungen auf der Basis der erhaltenen Parameter ergibt eine schwache ferromagnetische Nickel–Mangan-Wechselwirkung.

Die magnetischen Daten der Eisen(III)verbindung wurden im Rahmen isotroper Wechselwirkungen analysiert. Die Temperaturabhängigkeit der magnetischen Suszeptibilität kann sehr gut mit Eisen–Nickel-Wechselwirkungen wiedergegeben werden, die größer sind als die zwischen den Nickelatomen. Daher erstreckt sich die Grundzustandswellenfunktion nicht nur auf das Zentralatom, wie es in der Manganverbindung der Fall ist, sondern ist vielmehr auf die Nickelionen delokalisiert. Dies führt zu einem entarteten Grundzustand. ESR-Spektren, die sowohl im X- als auch im W-Band aufgenommen wurden, stimmen gut mit einem Eisen(III) *low spin* überein und bestätigen die Beteiligung der Nickelionen am Grundzustand. Sie zeigen jedoch auch eine Reihe von Merkmalen — zum Beispiel eine Aufspaltung der Hauptsignale mit temperaturabhängiger Intensität — die darauf hindeuten, dass die Entartung auf Grund nicht-isotroper Wechselwirkungen aufgehoben wird. Zwar werden die Haupteigenschaften des Triaminoguanidins sogar in dieser sehr komplexen Struktur erhalten, jedoch wären zur vollständigen Analyse der Austauschwechselwirkung zwischen dem Eisen- und Nickelion Einzelkristallmessungen notwendig.

— **Experimental Section** —

6 Computational Details

6.1 Simulation and Fitting Routines

Simulation of magnetic data and of ESR-spectra were performed as mentioned in the text using one of the following methods:

1. When analytical expressions are known or can be derived, the program *OriginPro* (v8.0951)^[362] was used to simulate the magnetic behavior and to fit the parameters of the expressions to the measured values by least square procedures.
2. For the simulation of the thermal variation of the magnetic molar susceptibilities as well as for the fitting of parameters of an assumed exchange model the program package *julX* (v1.41)^[10] was used. It is suitable for systems up to four spins with $S \leq 5/2$, interacting via isotropic interactions and possessing local anisotropy represented by the axial parameter D and the rhombic parameter E . It also regards temperature independent magnetism (χ_{TIP}), a fraction of paramagnetic impurities (α) and intermolecular interactions via the mean field model (θ). The energy levels of the coupling matrix are calculated by numerical diagonalization. From the energy spectrum the temperature dependence of the magnetic susceptibility is calculated using the Van-Vleck equation.
3. For the simulation of the thermal variation of the magnetic molar susceptibilities as well as for the fitting of parameters of an assumed exchange model the program package *DAVE*^[11] was used. It includes isotropic and anisotropic exchange interactions of angular momenta (spin and orbital contributions) as well as local anisotropy and/or ligand fields up to sixth order. It also allows anisotropic g values and calculates the energy spectrum by full matrix diagonalization including the Zeeman term as well. It also includes temperature independent magnetism

(χ_{TIP}) and intermolecular interactions either via the mean field model (θ) or by means of self consisting equations.

4. For the simulation of ESR spectra the program package *EasySpin* (v3.0.0)^[364] for the MatLab (version R2006a)^[365] program package was used. It includes isotropic and anisotropic exchange interactions as well as local anisotropy up to sixth order. In single spin systems also strains on the magnetic field and on the g value can be introduced. It also offers the possibility to fit experimental spectra with different fitting routines.
5. For the simulation of ESR spectra the program package *XSophe* 1.1.4^[366] was used. It includes isotropic and dipolar exchange interactions as well as local anisotropy up to sixth order.

The spectra obtained by spectroscopic titrations of ligand solutions with metal ions are evaluated using the *SpecReg* fitting software developed by Dr. Manfred Rudolph in our group.

6.2 Quantum Chemistry Calculations

All structures were optimized using the BP86 functional^[367;368] with the *ri*-approximation on the def2-TZVP basis set^[369-371] as provided by the program package TurboMole.^[372-376] Absorbance spectra were calculated on the optimized structures using the INDOS method as implemented within the ORCA program package and plotted with the *mapspc* functionality (<http://www.thch.uni-bonn.de/tc/orca/>).

7 Synthesis

7.1 Instrumentation

^1H , ^{13}C , $^1\text{H}\{^1\text{H}\}$ COSY and $^1\text{H}\{^{13}\text{C}\}$ heteronuclear correlation NMR spectra were recorded on a Bruker Avance 400 MHz spectrometer. IR spectra were measured on a Bruker IFS55/Equinox spectrometer with a Raman unit FRA 106/S on samples prepared as KBr pellets. Mass spectra were measured on a Bruker MAT SSQ 710 spectrometer. Elemental analysis (C, H, N) were carried out on a Leco CHNS-932 and El Vario III elemental analyzers. Thermogravimetric analysis (TGA) for powdered samples was performed on a NETZSCH STA409PC Luxx apparatus under constant flow of air ranging from room temperature up to 1000 °C with a heating rate of 1 °C/min. Solution UV/Vis spectra were recorded on a VARIAN CARY 5000 UV/Vis-NIR-spectrometer. Solid state UV/Vis spectra were recorded on a VARIAN CARY 5E UV/Vis-NIR-spectrometer using the praying mantis diffuse reflectance accessory. UV/Vis spectra on films were recorded on a VARIAN CARY 5000 UV/Vis-NIR-spectrometer using the solid sample holder accessory. UV/Vis titrations were performed using an AnalytikJena Specord S100 with a Hellma Standard Immersion Probe. Fluorescence spectra were recorded on a Jasco FP-6300 spectrofluorometer. ESR measurements were performed on a Bruker ESP 300E using X-Band (9 GHz) and on a Bruker E600 using W-Band (95 MHz). Magnetic susceptibilities were obtained from powdered samples in gelatin capsules using a Quantum-Design MPMSR-5S SQUID magnetometer equipped with a 5 Tesla magnet in the range from 300 to 2 K or using a Cryogenic S600 SQUID magnetometer using teflon pellets and grease to avoid orientational effects. The measured data were corrected for diamagnetism of the capsules and the intrinsic diamagnetism of the sample, estimated by measurements on a similar ligand system. Due to the need of sample fixation with diamagnetic grease in the case of lanthanide containing systems the size of the diamagnetic contributions is somewhat uncertain.

7.2 Materials

Dried solvents were prepared according to standard procedures^[377]. Tetrahydrofuran for fluorescence measurements was obtained from Roth as RotiSolv $\geq 99.9\%$ UV/IR grade and was used without further purification. *N*-(*p*-Methoxyphenyl)-carbazole,^[310] *N,N*-bis(2-Hydroxyethyl)-ethylenediamin,^[378] 2,4,6-Triacetylphloroglucinol^[379] and sulfonated salicyl aldehyd^[290] were prepared according to reported procedures. All other chemicals were used as received without further purification. Copper(I)iodide was purified and activated by THF through continuous extraction using a Sockslett extractor.

7.3 Films

All films were prepared from aqueous solutions of polyvinyl alcohol. Stock solutions of polyvinylalcohol were prepared by dissolution of 5 g of polyvinyl alcohol in 50 mL of water by heating and stirring under reflux. The complexes were prepared in methanol and poured into the still warm solution. After homogenization the resulting solution was poured onto glass plates and left standing open for evaporation of the solvent. The resulting films were detached from the glass. For ESR measurements these films were cut into slices and stacked.

7.4 Preparation

N-(4-Nitrophenyl)-diphenylamine (1)

1.69 g (10 mmol) diphenylamine, 2.02 g (10 mmol) 4-bromo-nitrobenzene and 1.44 g (14 mmol) NaO^tBu are suspended in 50 mL of dry toluene and degassed for 30 minutes. 112 mg (0.5 mmol) palladium(II)acetate and 404 mg (2 mmol) tri-*tert*-butylphosphine are added and the mixture is heated at 80° for 3.5 hours. After the solution has cooled to room temperature it is poured into 100 mL diethylether, filtrated and washed three times with glime. The organic phase is dried over sodium sulfate and the solvent is removed. The remaining oil is separated over silica gel with petrol ether/dichloromethylene 4:1. From the first fraction the solvent is removed and the remaining solid is recrystallized from *n*-hexane to give a red brown micro crystalline solid. Total yield: 1.88 g (6.4 mmol, 64 %).

m.p.: 293 °C (decomposition). **IR** (KBr, cm⁻¹): 3060w ν (C-H)^{aryl}, 3037w ν (C-H)^{aryl}, 1582s ν (C-C)^{aryl}, 1490s ν_{as} (NO₂), 1314s ν_s (NO₂), 1297s, 1287s, 1075s, 844m, 697m, 533m. **¹H-NMR** (400 MHz, CDCl₃): δ = 6,93–6,95 (m, 2H, CH²), 7.19–7.25 (m, 6H, CH^{3,5}), 7.36–7.41 (m, 4H, CH⁴), 8.04–8.07 (m, 2H, CH¹). **¹³C-NMR** (100 MHz, CDCl₃): δ = 118.2 (C²), 125.4 (C³), 125.7 (C⁸), 126.5 (C⁶), 129.9 (C⁷), 140.2 (C¹), 145.7 (C⁵), 153.5 (C⁴). **DEI-MS:** $\frac{m}{z}$ = 77 (33%, [C₆H₅]⁺), 166 (59%, [NPh₂-H]⁺), 243 (66%, [NPh₃-3H]⁺), 260 (61%, [M-2O+2H]⁺), 290 (100%, M⁺). **Analysis:** calculated for C₁₈H₁₄N₂O₂ (M = 290.32 g/mol): C, 74.47; H, 4.86; N, 9.65; found: C, 74.89; H, 5.14; N, 9.28.

N-(4-Aminophenyl)-diphenylamine (2)

300 mg (1 mmol) of *N*-(4-nitrophenyl)-diphenylamine are dissolved in 40 mL ethylacetate and some spatula of Raney-nickel are added. H₂ is applied with a pressure of 55 bar. The reaction mixture is stirred at 80° for 16 hours. The nickel is removed by filtration and washed three times with ethylacetate. The combined organic phases are dried over NaSO₄. The solvent is removed under reduced pressure to give 0.26 g crude product as a gray solid (quantitative).

m.p.: 282 °C (decomposition). **IR** (KBr, cm⁻¹): 3430w ν_{as} (NH₂), 3351w ν_s (NH₂), 3055w ν (C-H)^{aryl}, 3032m ν (C-H)^{aryl}, 1622m, 1583s ν (C-C)^{aryl}, 1510vs ν (C-C)^{aryl}, 1489vs, 1330m,

1267vs, 890m, 751s, 694s. $^1\text{H-NMR}$ (400 MHz, DMSO- D_6): $\delta = 5.08$ (s, 2H, NH_2), 6.57–6.59 (m, 2H, CH^1), 6.80–6.82 (m, 2H, CH^2), 6.86–6.91 (m, 6H, $\text{CH}^{3,5}$), 7.18–7.21 (m, 4H, CH^4). $^{13}\text{C-NMR}$ (100 MHz, DMSO- D_6): $\delta = 115.5$ (C^2), 121.5 (C^3), 122.0 (C^6), 128.6 (C^8), 129.6 (C^7), 135.7 (C^4), 146.7 (C^1), 148.1 (C^5). **EI-MS**: $\frac{m}{z} = 260$ (100%, M^+). **Analysis**: calculated for $\text{C}_{18}\text{H}_{16}\text{N}_2$ ($M = 260.33$ g/mol): C, 83.04; H, 6.19; N, 10.76; found: C, 82.96; H, 6.27; N, 10.27.

N-((2-Hydroxybenzylidene)-4-iminophenyl)-diphenylamin, HTPA (3)

500 mg (1.92 mmol) *N*-(4-aminophenyl)-diphenylamine are suspended in 25 mL methanol. 235 mg (1.92 mmol) salicylaldehyde dissolved in 2 mL methanol are added and the resulting suspension is heated under reflux for 1 h. After cooling the yellow precipitation is filtered off, washed with few mL methanol and dried under reduced pressure. Total Yield: 479 mg (1.31 mmol, 68%).

m.p.: 155 °C (decomposition). **IR** (KBr, cm^{-1}): 3460vs $\nu(\text{O-H})$, 3050w $\nu(\text{C-H})^{\text{aryl}}$, 1646s $\nu(\text{C=N})$, 1635s $\nu(\text{C-C})^{\text{aryl}}$, 1491vs, 1315s, 776s, 700s. $^1\text{H-NMR}$ (400 MHz, CDCl_3): $\delta = 6.94$ – 6.97 (1H, m, $\text{CH}^{2\text{Sal}}$), 7.04–7.09 (3H, m, $\text{CH}^{2\text{TPA},4\text{Sal}}$), 7.13–7.15 (5H, m, $\text{CH}^{3\text{TPA},3\text{Sal}}$), 7.22–7.24 (2H, m, $\text{CH}^{1\text{TPA}}$), 7.28–7.32 (6H, m, $\text{CH}^{4\text{TPA},1\text{Sal}}$), 7.36–7.41 (2H, m, $\text{CH}^{5\text{TPA}}$), 8.65 (1H, s, $\text{CH}^{6\text{Sal}}$), 13.40 (1H, s, OH). $^{13}\text{C-NMR}$ (100 MHz, CDCl_3): $\delta = 117.0$ ($\text{C}^{8\text{TPA}}$), 119.5 ($\text{C}^{3\text{Sal}}$), 119.9 ($\text{C}^{1\text{Sal}}$), 123.1 ($\text{C}^{3\text{TPA}}$), 123.8 ($\text{C}^{2\text{TPA}}$), 124.3 ($\text{C}^{5\text{Sal}}$), 124.5 ($\text{C}^{6\text{TPA}}$), 130.1 ($\text{C}^{7\text{TPA}}$), 132.8 ($\text{C}^{6\text{Sal}}$), 133.4 ($\text{C}^{4\text{Sal}}$), 142.7 ($\text{C}^{4\text{TPA}}$), 146.9 ($\text{C}^{1\text{TPA}}$), 147.5 ($\text{C}^{5\text{TPA}}$), 160.7 ($\text{C}^{2\text{Sal}}$), 162.1 ($\text{C}^{7\text{Sal}}$). **EI-MS**: $\frac{m}{z} = 364$ (100%, M^+). **Analysis**: calculated for $\text{C}_{25}\text{H}_{20}\text{N}_2\text{O}$ ($M = 364.44$ g/mol): C, 82.39; H, 5.53; N, 4.39; found: C, 82.20; H, 5.53; N, 4.69.

N-((3,5-Di-*tert*-butyl-2-hydroxybenzylidene)-4-iminophenyl)-diphenylamin, H^{tBu} TPA (4)

500 mg (1.92 mmol) *N*-(4-aminophenyl)-diphenylamine are suspended in 30 mL ethanol. 450 mg (1.92 mmol) 3,5-di-*tert*-butyl-salicylaldehyde dissolved in 5 mL ethanol are added and the resulting suspension is heated under reflux for 1 h. After cooling the reaction mixture is kept in the fridge overnight. The yellow, micro-crystalline precipitation is filtered off, washed with very few mL cold ethanol and dried under reduced pressure. Total Yield: 346 mg (0.68 mmol, 38%).

m.p.: 171 °C (decomposition). **IR** (KBr, cm^{-1}): 3436w $\nu(\text{O-H})$, 3034w $\nu(\text{C-H})^{\text{aryl}}$, 2954s $\nu_{\text{as}}(\text{CH}_3)$, 2867m $\nu_{\text{s}}(\text{CH}_3)$, 1617s $\nu(\text{C=N})$, 1793s, 1495s $\nu(\text{C-C})^{\text{aryl}}$, 1274s $\nu(\text{C-O})$, 895w. **$^1\text{H-NMR}$** (400 MHz, CDCl_3): $\delta = 1.36$ (9H, s, CH_3), 1.51 (9H, s, CH_3), 7.04–7.08 (2H, m, $\text{H}^{5\text{TPA}}$), 7.12–7.15 (6H, m, $\text{H}^{2\text{TPA},3\text{TPA}}$), 7.23–7.25 (3H, m, $\text{H}^{3\text{Sal},1\text{TPA}}$), 7.27–7.31 (4H, m, $\text{H}^{4\text{TPA}}$), 7.46–7.47 (1H, d, $\text{H}^{2\text{Sal}}$), 8.6 (1H, s, $\text{H}^{1\text{Sal}}$), 13.81 (1H, s, OH). **$^{13}\text{C-NMR}$** (100 MHz, CDCl_3): $\delta = 29.4$ ($\text{C}^{9\text{Sal},11\text{Sal}}$), 31.5 ($\text{C}^{9\text{Sal},11\text{Sal}}$), 34.2 ($\text{C}^{8\text{Sal},10\text{Sal}}$), 35.1 ($\text{C}^{8\text{Sal},10\text{Sal}}$), 118.5 ($\text{C}^{1\text{Sal}}$), 122.0 ($\text{C}^{2\text{TPA}}$), 123.0 ($\text{C}^{8\text{TPA}}$), 124.3 ($\text{C}^{6\text{TPA}}$), 124.4 ($\text{C}^{3\text{TPA}}$), 126.6 ($\text{C}^{4\text{Sal}}$), 127.7 ($\text{C}^{6\text{Sal}}$), 129.3 ($\text{C}^{7\text{TPA}}$), 136.9 ($\text{C}^{3\text{Sal}}$), 140.5 ($\text{C}^{4\text{TPA}}$), 143.0 ($\text{C}^{5\text{Sal}}$), 146.7 ($\text{C}^{1\text{TPA}}$), 147.6 ($\text{C}^{5\text{TPA}}$), 158.2 ($\text{C}^{2\text{Sal}}$), 161.8 ($\text{C}^{7\text{Sal}}$). **DEI-MS:** $\frac{m}{z} = 219$ (98%, $\text{C}_{15}\text{H}_{24}\text{O}$), 461 (82%, $(\text{M-CH}_3)^+$), 476 (100%, M^+). **Analysis:** calculated for $\text{C}_{33}\text{H}_{36}\text{N}_2\text{O}$ ($M = 476.65$ g/mol): C, 83.15; H, 7.61; N, 5.88; found: C, 82.92; H, 7.72; N, 5.84.

[Cu(hfac)(TPA)]₂ (5)

29 mg (0.17 mmol) $\text{CuCl}_2 \cdot 2\text{H}_2\text{O}$ are dissolved in 5 mL of methanol. Then a solution of 61 mg (0.17 mmol) HTPA and 26 μL (19 mg, 0.17 mmol) triethylamine in 10 mL chloroform are added. After five minutes of stirring a solution of 35 mg (0.17 mmol) hexafluoroactaylacetonate and 26 μL (19 mg, 0.17 mmol) triethylamine in 2 mL of chloroform is added. The resulting solution is stirred for additional five minutes and left for slow evaporation. After few days crystals suitable for X-ray analysis are obtained. Total yield after drying under reduced pressure: 100 mg (0.16 mmol, 94%).

m.p.: 209 °C (decomposition). **IR** (KBr, cm^{-1}): 3435m $\nu(\text{O-H})$, 3059w $\nu(\text{C-H})^{\text{aryl}}$, 3034w $\nu(\text{C-H})^{\text{aryl}}$, 2927w, 2647s, 1613vs $\nu(\text{C-C})^{\text{aryl}}$, 1494vs, 1215s, 1147vs $\nu(\text{C-F})$, 753s, 698m, 501m. **pos. ESI-MS:** $\frac{m}{z} = 812$ (100%, $[\text{L}_2\text{CuNa}]^+$). **neg. ESI-MS:** $\frac{m}{z} = 207$ (100%, hfac⁻), 363 (8%, L⁻), 437 (100%), 661 (92%), 667 (26%), 679 (18%). **Analysis:** calculated for $\text{C}_{30}\text{H}_{20}\text{CuF}_6\text{N}_2\text{O}_3$ ($M = 634.03$ g/mol): C, 56.83; H, 3.18; N, 4.42; found: C, 59.37; H, 3.92; N, 4.72.

[Cu(^tBuTPA)]₂ (6)

200 mg (0.42 mmol) $\text{H}^{\text{tBu}}\text{TPA}$ (4) are dissolved in 15 mL methanol by addition of 58 μL (42 mg, 42 mmol) triethylamine. 78 mg (0.21 mmol) $\text{Cu}(\text{ClO}_4)_2 \cdot 6\text{H}_2\text{O}$ dissolved in 2 mL methanol are added. The resulting brown solution is left to evaporate, subsequently redissolved and left to evaporate in chloroform, ethanol and acetone to give 100 mg of dark crystalline product, which was dried in air (0.10 mmol, 47%).

m.p.: 241 °C (decomposition). **IR** (KBr, cm^{-1}): 3437m $\nu(\text{O-H})$, 3058w $\nu(\text{C-H})^{\text{aryl}}$, 3032w $\nu(\text{C-H})^{\text{aryl}}$, 2924w $\nu_{\text{as}}(\text{CH}_3)$, 2853w $\nu_{\text{s}}(\text{CH}_3)$, 1612vs $\nu(\text{C-C})^{\text{aryl}}$, 1534s, 1493vs $\nu(\text{C-C})^{\text{aryl}}$, 1464s, 1448s, 1333m, 1275m, 1184m, 1147m, 751s. **ESI-MS:** $\frac{m}{z} = 1014$ (100%, $\text{M}+\text{H}^+$). **Analysis:** calculated for $\text{C}_{66}\text{H}_{70}\text{CuN}_4\text{O}_2$ ($M = 1014.83$ g/mol): C, 78.11; H, 6.95; N, 5.52; found: C, 77.82; H, 7.09; N, 5.65.

4,4'4''-Trinitrotriphenylamin (7)

4.45 g (18.4 mmol) $\text{Cu}(\text{NO}_3)_2 \cdot 3\text{H}_2\text{O}$ are suspended in a mixture of 10 mL acetic acid and 20 mL acetic acid anhydride. Then 2.50 g (10.2 mmol) triphenylamine are added slowly during 5 minutes. Nitrosic gases evolve and the mixture heats up. After addition of another 10 mL of acetic acid the resulting yellow-green suspension is stirred for 30 minutes at 100 °C. After cooling down, the suspension is poured into 200 mL of water and the yellow precipitate is filtered off. It is washed three times with 50 mL of water. After one day of drying at 100° under reduced pressure 3.61 g (9.5 mmol, 93%) of yellow powder are obtained.

m.p.: 390 °C (decomposition). **$^1\text{H-NMR}$** (400 MHz, THF-D_8): $\delta = 7.22\text{--}7.23$ (m, 6H), 8.17–8.18 (m, 6H). **IR** (KBr, cm^{-1}): 3108w $\nu(\text{CH})^{\text{aryl}}$, 3075w $\nu(\text{CH})^{\text{aryl}}$, 2919w, 2853vw, 1606m $\nu(\text{C-C})^{\text{aryl}}$, 1582vs $\nu(\text{C-C})^{\text{aryl}}$, 1508s $\nu_{\text{as}}(\text{NO}_2)$, 1494s, 1339vs $\nu_{\text{s}}(\text{NO}_2)$, 1313vs $\nu_{\text{s}}(\text{NO}_2)$, 1273vs, 1181m, 1111m, 849m, 704m. **ESI-MS:** $\frac{m}{z} = 241$ (28%), 242 (13%, $[\text{M}-3\text{NO}_2]^+$), 288 (7%, $[\text{M}-2\text{NO}_3]^+$), 304 (6%, $[\text{M}-\text{N}_2\text{O}_3]^+$), 335 (18% $[\text{M}-\text{NO}_2+\text{H}]^+$), 350 (7%, $[\text{M}-\text{NO}]^+$), 380 (100%, M^+). **Analysis:** calculated for $\text{C}_{18}\text{H}_{12}\text{N}_4\text{O}_6$ ($M = 380.31$ g/mol): C, 56.85; H, 3.18; N, 14.73; found: C, 56.80; H, 3.13; N, 14.54.

4,4'4''-Triaminotriphenylamin (8)

3.50 g (9.2 mmol) of 4,4'4''-Trinitrotriphenylamin are suspended in 40 mL of ethylacetate and some spatula of *Raney*-nickel are added. H_2 is applied with a pressure of 55 bar. The reaction mixture is stirred at 80° for 16 hours. The nickel is removed by filtration and washed three times with ethylacetate. The combined organic phases are dried over NaSO_4 . The solvent is removed under reduced pressure to give 2.00 g of crude product (gray solid, 6.9 mmol, 75%).

m.p.: 301 °C (decomposition). **IR** (KBr, cm^{-1}): 3407s $\nu_{\text{as}}(\text{NH}_2)$, 3338s $\nu_{\text{s}}(\text{NH}_2)$, 3031w $\nu(\text{C-H})^{\text{aryl}}$, 1619s $\nu(\text{C-C})^{\text{aryl}}$, 1503vs $\nu(\text{C-C})^{\text{aryl}}$, 1329s, 1261vs, 839vs, 570vs, 506s. **ESI-MS:** $\frac{m}{z} = 290$ (100%, M^+). **Analysis:** calculated for $\text{C}_{18}\text{H}_{18}\text{N}_4$ ($M = 290.36$ g/mol): C, 74.46; H, 6.25; N, 19.30; found: C, 74.04; H, 6.04; N, 18.84.

***N*-(4-Methoxyphenyl)-3,4-diaminocarbazole (9)**

7.94 g (33 mmol) $\text{Cu}(\text{NO}_3)_2 \cdot 3\text{H}_2\text{O}$ are stirred in a mixture of 15 mL acetic acid and 30 mL acetic acid anhydride for 10 minutes. Then 7.50 g (27 mmol) *N*-(4-methoxyphenyl)-carbazole are slowly added during 5 minutes. After adding another 15 mL of acetic acid the resulting solution is stirred for additional 30 minutes at 100 °C. It is poured into 250 mL of ice water, the yellow precipitation is filtered off and washed three times with 150 mL of water. The product is dried for one day under reduced pressure at 70°. It is suspended in acetylene diethyl ester and some spatula of Raney-nickel are added. H_2 is applied with a pressure of 55 bar. The mixture is stirred at 80 °C for 4 hours. After cooling the nickel is removed by filtration and washed three times with ethylacetate. After drying over Na_2SO_4 the solvent is removed to give 7.50 g of crude product. Recrystallization from toluene yielded 5.54 g of a dark solid (18 mmol, 67%).

m.p.: 320 °C (decomposition). **IR** (KBr, cm^{-1}): 3377s $\nu_{\text{as}}(\text{NH}_2)$, 3292s $\nu_{\text{s}}(\text{NH}_2)$, 2956m, 2933m, 2838m $\nu(\text{OCH}_3)$, 1613m $\nu(\text{C-C})^{\text{aryl}}$, 1580m $\nu(\text{C-C})^{\text{aryl}}$, 1514s $\nu(\text{C-C})^{\text{aryl}}$, 1218s. **$^1\text{H-NMR}$** (400 MHz, CDCl_3): $\delta = 3.84$ (s, 3H, OCH_3); 4.72 (s, 4H, NH_2); 6.69–6.71 (m, 2H, H^2); 7.00–7.02 (m, 2H, H^3); 7.13–7.15 (m, 2H, $H^{4,5}$); 7.15 (s, 2H, H^1); 7.39–7.4 (m, 2H, $H^{4,5}$). **$^{13}\text{C-NMR}$** (100 MHz, CDCl_3): $\delta = 55.9, 104.3, 110.0, 115.3, 115.5, 123.6, 127.7, 131.5, 135.5, 142.1, 157.9$. **EI-MS:** $\frac{m}{z} = 303$ (100%, M); 288 (27%, $\text{M}(\text{CH}_3)$); 31 (38%, OCH_3). **Analysis:** calculated for $\text{C}_{19}\text{H}_{17}\text{N}_3\text{O}$ ($M = 303.36$ g/mol): C, 75.23; H, 5.65; N, 13.85; found: C, 75.15; H, 5.73; N, 13.94.

***N*-(4-Methoxyphenyl)-bis-(2-hydroxybenzylidene)-3,4-diiminocarbazole, $\text{H}_2\text{CarbOMe}$ (10)**

240 μL (0.28 g, 2.3 mmol) of salicylaldehyde are added to a suspension of 0.35 g (1.15 mmol) *N*-(4-methoxyphenyl)-3,4-diaminocarbazole in 20 mL methanol. The mixture is heated for ten minutes under reflux and allowed to cool down. The yellow

precipitation is collected via filtration and washed with few mL of methanol. After drying under reduced pressure 0.48 mg of a yellow powder are obtained (0.94 mmol, 82 %).

m.p.: 300° (decomposition). **IR** (KBr, cm^{-1}): 3437s $\nu(\text{O-H})$, 3053w, 2930w, 2836w $\nu(\text{OCH}_3)$, 1618s $\nu(\text{C=N})$, 1514s $\nu(\text{C-C})^{\text{aryl}}$, 1285s, 1247s, 1149m, 1031m, 754s. **$^1\text{H-NMR}$** (400 MHz, CDCl_3): $\delta = 3.95(\text{s}, 3\text{H}, -\text{OCH}_3)$, 6.8–7.6 (m, 16H, H^{aryl}), 8.11 (s, 2H, H^7), 8.80 (s, 2H, N=CH-), 13.61 (s, 2H, $-\text{OH}$). **$^{13}\text{C-NMR}$** (100 MHz, CDCl_3): $\delta = 55.7, 110.7, 112.5, 115.3, 117.2, 119.0, 119.6, 120.6, 123.7, 128.4, 129.7, 132.0, 132.7, 141.1, 141.4, 159.2, 160.5, 161.1$. **ESI-MS:** $\frac{m}{z} = 413$ (28%), 512 (100%, $\text{M}+\text{H}^+$). **Analysis:** calculated for $\text{C}_{33}\text{H}_{25}\text{N}_3\text{O}_3 \cdot 0.07\text{H}_2\text{O}$ ($\text{M} = 512.83$ g/mol): C, 77.28; H, 4.95; N, 8.20; found: C, 77.09; H, 4.80; N, 8.03.

[Cu₂(CarbOMe)₂] (11)

To a solution of 102 mg (0.2 mmol) H₂CarbOMe in 10 mL of chloroform/methanol 1:1 are added 40 mg (0.2 mmol) of Cu(AcO)₂·H₂O dissolved in 2 mL chloroform/methanol 1:1. The resulting red solution is left to evaporate. Red crystals suitable for X-ray are obtained within one day. Total yield: 47 mg (0.04 mmol, 40%).

m.p.: 300 °C (decomposition). **IR** (KBr, cm^{-1}): 3435s $\nu(\text{O-H})$, 3052w $\nu(\text{C-H})^{\text{aryl}}$, 2988w, 2927w, 1605vs $\nu(\text{C=N})$, 1530s, 1514vs $\nu(\text{C-C})^{\text{aryl}}$, 1461s, 1444s, 1248s, 1148s, 757m. **ESI-MS:** $\frac{m}{z} = 1146$ (36%, M^+), 1167.1 (100%, $\text{M}+\text{Na}^+$). **Analysis:** calculated for $\text{C}_{66}\text{H}_{46}\text{Cu}_2\text{N}_6\text{O}_6 \cdot 0.082 \text{CHCl}_3$ ($\text{M} = 1156$ g/mol): C, 64.68; H, 3.81; N, 6.74; found: C, 64.68; H, 3.81; N, 6.78.

[Zn₂(CarbOMe)₂] (12)

To a solution of 102 mg (0.2 mmol) H₂CarbOMe in 10 mL of chloroform/methanol 1:1 are added 44 mg (0.2 mmol) of Zn(AcO)₂·2H₂O dissolved in 2 mL chloroform:methanol 1:1. The resulting brown-orange solution shows green fluorescence and is left to evaporate. Crystals suitable for X-ray are obtained within one day. Total yield: 52 mg (0.045 mmol, 45%).

m.p.: 400 °C (decomposition). **IR** (KBr, cm^{-1}): 3435m $\nu(\text{O-H})$, 3044w, 3001w, 2957w, 2933w, 2905w, 2834w $\nu(\text{OCH}_3)$, 1605vs $\nu(\text{C=N})$, 1534s, 1514vs $\nu(\text{C-C})^{\text{aryl}}$, 1463s, 1442s, 1248s, 1173s, 1025m, 757m. **DEI-MS:** $\frac{m}{z} = 28$ (HCN^+), 47 (21%), 83 (100%), 575 (0.1%, $[\text{Zn}(\text{CarbOMe})]^+$), 1151 (0.5%, $[\text{M}]^+$). **Analysis:** calculated for $\text{C}_{66}\text{H}_{46}\text{N}_6\text{O}_6\text{Zn}_2 \cdot 0.123\text{CHCl}_3$ ($M = 1165$ g/mol): C, 62.49; H, 3.69; N, 6.51; found: C, 62.50; H, 3.63; N, 6.45.

***N*-(4-Methoxyphenyl)-bis-(3,5-Di-*tert*-butyl-2-hydroxybenzylidene)-3,4-diimino-carbazole, $\text{H}_2^{\text{tBu}}\text{CarbOMe}$ (**13**)**

0.43 g (1.84 mmol) of 3,5-di-*tert*-butyl-2-hydroxy-benzaldehyd are added to a suspension of 0.28 g (0.92 mmol) *N*-(4-Methoxyphenyl)-3,4-diaminocarbazole in 20 mL methanol. The mixture is heated for 1 hour under reflux and allowed to cool down. The bright yellow precipitation is collected via filtration and washed with few mL of methanol. After drying under reduced pressure 0.56 mg of a yellow powder are obtained (0.76 mmol, 83 %).

m.p.: 375 °C (decomposition). **IR** (KBr, cm^{-1}): 3435m $\nu(\text{O-H})$, 2957s $\nu_{\text{as}}(\text{CH}_3)$, 2869m $\nu_{\text{s}}(\text{CH}_3)$, 1615s $\nu(\text{C=N})$, 1515vs $\nu(\text{C-C})^{\text{aryl}}$, 1481s, 1467s, 1285m, 1249s, 1169m, 1035w, 877w, 830w, 810w, 773w. **$^1\text{H-NMR}$** (400 MHz, CDCl_3): $\delta = 1.39$ (s, 18H, $-\text{C}(\text{CH}_3)_3$), 1.54 (s, 18H, $-\text{C}(\text{CH}_3)_3$), 3.96(s, 3H, $-\text{OCH}_3$), 7.18 (m, 2H, H^{aryl}), 7.28–7.39 (m, 4H, H^{aryl}), 7.49 (m, 6H, H^{aryl}), 8.16 (s, 2H, H^7), 8.87 (s, 2H, $\text{N}=\text{CH}-$), 14.08 (s, 2H, $-\text{OH}$). **$^{13}\text{C-NMR}$** (100 MHz, CDCl_3): $\delta = 29.5, 31.6, 34.3, 35.2, 55.7, 110.6, 112.2, 115.3, 118.7, 120.8, 123.8, 126.6, 127.5, 128.4, 129.9, 136.9, 140.5, 140.9, 141.5, 158.2, 159.1, 161.6$. **FAB-MS:** $\frac{m}{z} = 720$ (63%, $[\text{M-O}]^+$), 736 (72%, M^+). **Analysis:** calculated for $\text{C}_{49}\text{H}_{57}\text{N}_3\text{O}_3$ ($M = 736$ g/mol): C, 79.96; H, 7.81; N, 5.71; found: C, 79.72; H, 7.82; N, 5.71.

$[\text{Cu}_2(\text{H}_2^{\text{tBu}}\text{CarbOMe})_2]$ (14**)**

To a solution of 0.32 g (0.43 mmol) $\text{H}_2^{\text{tBu}}\text{CarbOMe}$ in a mixture of 12 mL methanol and 9 mL chloroform are added 121 μL (88 mg, 0.87 mmol) triethylamine. To the clear solution are added 73 mg (0.43 mmol) $\text{CuCl}_2 \cdot 2\text{H}_2\text{O}$ dissolved in 1 mL methanol. The resulting red solution is stirred for 30 min, the precipitation formed is filtered off, washed with few mL of methanol and dried under reduced pressure. 0.33 g of a brown solid are obtained (0.21 mmol, 96%).

m.p.: 280 °C (decomposition). **IR** (KBr, cm^{-1}): 3435m $\nu(\text{O-H})$, 2956s $\nu_{\text{as}}(\text{CH}_3)$, 2906m, 2869w $\nu_{\text{s}}(\text{CH}_3)$, 1613s $\nu(\text{C=N})$, 1592s, 1528s, 1515vs $\nu(\text{C-C})^{\text{aryl}}$, 1482s, 1460s, 1426s, 1385m, 1361m, 1326m, 1287m, 1253vs, 1167s, 1029m, 873m, 833m, 810m, 787m. **pos. ESI-MS:** $\frac{m}{z} = 413$ (79%), 559 (72%), 587 (100%), 613 (87%), 635 (26%), 1410 (15%). **Analysis:** calculated for $\text{C}_{98}\text{H}_{110}\text{Cu}_2\text{N}_6\text{O}_6$ ($M = 1595.05$ g/mol): C, 73.79; H, 6.95; N, 5.27; found: C, 73.47; H, 7.20; N, 5.30.

***N*-(4-Methoxyphenyl)-bis-(2-hydroxy-5-sulfonylbenzylidene)-3,4-diiminocarbazole, H_2^{Sulf} CarbOMe (15)**

A suspension of 1.00 g (3.3 mmol) *N*-(4-methoxyphenyl)-3,4-diaminocarbazole and 1.76 g (6.6 mmol) sodium 5-sulfonato-2-hydroxy-benzaldehyde in 25 mL methanol are heated under reflux for 2 h. After cooling the yellow precipitation is collected via filtration, washed with few mL of methanol and dried under reduced pressure. 2.37 g of a red-yellow solid are obtained (3 mmol, 91%).

m.p.: 344 °C (decomposition). **IR** (KBr, cm^{-1}): 3435s $\nu(\text{O-H})$, 3067w $\nu(\text{C-H})^{\text{aryl}}$, 2958w $\nu_{\text{as}}(\text{CH}_3)$, 2953w, 2853w $\nu_{\text{s}}(\text{CH}_3)$, 1617s $\nu(\text{C=N})$, 1516vs $\nu(\text{C-C})^{\text{aryl}}$, 1482s, 1292m, 1239vs, 1183vs $\nu_{\text{as}}(\text{SO}_3^-)$, 1110vs, 1037vs $\nu_{\text{s}}(\text{SO}_3^-)$, 872m, 827m, 720m, 687m, 602s. **$^1\text{H-NMR}$** (400 MHz, DMSO-D_6): $\delta = 3.89$ (s, 3H, OCH_3), 6.96 (m, 2H, CH^{aryl}), 7.25 (m, 2H, CH^{aryl}), 7.37 (m, 2H, CH^{aryl}), 7.58 (m, 2H, CH^{aryl}), 7.65–7.67 (m, 4H, CH^{aryl}), 8.02 (d, 2H, CH^{aryl}), 8.51 (s, 2H, CH^{aryl}), 9.22 (s, 2H, $-\text{N}=\text{CH}-$), 13.69 (s, 2H, OH). **$^{13}\text{C-NMR}$** (100 MHz, DMSO-D_6): $\delta = 56.0$, 111.0, 114.5, 115.9, 116.3, 118.7, 121.1, 123.8, 128.6, 129.5, 130.0, 130.8, 140.2, 140.9, 141.2, 159.2, 160.8, 161.5. **ESI-MS neg.:** $\frac{m}{z} = 334.5$ ($[\text{M}-2\text{Na}]^{2-}$), 692 ($[\text{M}-\text{Na}]^-$). **Analysis:** calculated for $\text{C}_{33}\text{H}_{23}\text{N}_3\text{Na}_2\text{O}_9\text{S}_2 \cdot 4\text{H}_2\text{O}$ ($M = 787.74$ g/mol): C, 50.31; H, 3.96; N, 5.34; S, 8.12; found: C, 50.26; H, 3.86; N, 5.35; S, 7.83.

***N*-(4-Hydroxyphenyl)-3,4-diaminocarbazole (17)**

The reaction was carried out under an argon atmosphere and the exclusion of water. 4.80 g (15.8 mmol) *N*-(4-methoxyphenyl)-3,4-diaminocarbazole are dissolved in 50 mL of dry CH_2Cl_2 . 29 mL of a 1.22 M solution of BBr_3 in CH_2Cl_2 (35.4 mmol, 2.2 eq) are added resulting in a pale blue precipitation. After stirring for 60 h a dark green suspension is formed with a pale green precipitation. Upon addition of 100 mL of methanol

a violet solution is formed under the evolution of gas. The solvent is removed and the the addition of methanol is repeated twice. Upon the addition of 100 mL of 0.5 M aqueous NaOH a red solution is formed. After filtration the solution is acidified and the precipitation is collected by centrifugation. It is redissolved in 800 mL of AcOEt and dried over Na₂SO₄. After removal of the solvent 2.74 g of a dark gray crude product are obtained.

m.p.: 320 °C (decomposition). **IR** (KBr, cm⁻¹): 3416s $\nu_{\text{as}}(\text{NH}_2)$, 3367s $\nu_{\text{s}}(\text{NH}_2)$, 3500–3000s $\nu(\text{OH})$, 1617m, 1583m, 1516vs $\nu(\text{C-C})^{\text{aryl}}$, 1493s, 1468s, 1312m, 1243s, 1213s, 834m, 804m, 578m. **¹H-NMR** (400 MHz, MeOD): $\delta = 7.08\text{--}7.11$ (m, 2H, H^2); 7.34–7.36 (m, 2H, H^3); 7.43–7.45 (m, 2H, $H^{4,5}$); 7.51–7.54 (m, 2H, $H^{4,5}$); 8.35 (m, 2H, H^1). **¹³C-NMR** (100 MHz, MeOD): $\delta = 104.8, 108.0, 114.4, 114.6, 121.8, 126.3, 128.4, 135.1, 137.4, 154.7$. **DEI-MS:** $\frac{m}{z} = 289$ (100%, M⁺). **Analysis:** calculated for C₁₈H₁₅N₃O (M = 289.33 g/mol): C, 74.72; H, 5.23; N, 14.52; found: C, 70.13; H, 5.23, N, 13.05.

***N*-(4-Hydroxyphenyl)-bis-2-hydroxybenzylidene-3,4-diiminocarbazole, H₂CarbOH (18)**

0.30 g (1.04 mmol) *N*-(4-hydroxyphenyl)-3,4-diaminocarbazole are dissolved in 10 mL of methanol and 216 μL (2.08 mmol) salicylaldehyde are added. The solution is stirred for 1 h, the precipitation collected by filtration and dried under reduced pressure to give 319 mg of a green solid (0.64 mmol, 62%).

m.p.: 320 °C (decomposition). **IR** (KBr, cm⁻¹): 3435s $\nu(\text{O-H})$, 3057w $\nu(\text{C-H})^{\text{aryl}}$, 2930w, 1616s $\nu(\text{C=N})$, 1570m, 1516vs $\nu(\text{C-C})^{\text{aryl}}$, 1480s, 1464s, 1369s, 1282s, 1237s, 1180m, 1150m, 810m, 754s. **¹H-NMR** (400 MHz, DMSO-D₆): $\delta = 6.98\text{--}7.02$ (m, 4H, $H^2 + H^9$); 7.06–7.08 (m, 2H, H^{11}); 7.34–7.44 (m, 6H, $H^{4,3,10}$); 7.60–7.62 (m, 2H, H^1); 7.66–7.68 (m, 2H, H^8), 8.47 (s, 2H, CH^7), 9.14 (s, 2H, CH^6), 9.96 (s, 1H, OH^{12}), 13.52 (s, 2H, OH^5). **¹³C-NMR** (100 MHz, DMSO-D₆): $\delta = 111.1, 114.1, 117.0, 117.2, 119.6, 120.0, 121.2, 123.7, 127.8, 128.6, 141.0, 141.1, 157.7, 160.7, 161.5$. **EI-MS:** $\frac{m}{z} = 29$ (100%, CHO), 497 (46%, M⁺). **Analysis:** calculated for C₁₈H₁₅N₃O (M = 289.33 g/mol): C, 77.25; H, 4.66; N, 8.45; found: C, 73.96; H, 4.75, N, 8.72.

***N*-(4-Hydroxyphenyl)-bis-(2-hydroxy-5-sulfonylbenzylidene)-3,4-diiminocarbazole, H₂^{Sulf} Carb^{OH} (19)**

A suspension of 0.34 g (1.12 mmol) *N*-(4-hydroxyphenyl)-3,4-diaminocarbazole and 0.60 g (2.24 mmol) sodium 5-sulfonato-2-hydroxy-benzaldehyde in 15 mL *iso*-propanol is heated under reflux for 1 h. After cooling the dark yellow precipitation is collected via filtration, washed with few mL of *iso*-propanol and dried under reduced pressure. 0.72 g of a dark-yellow solid are obtained (0.98 mmol, 88%).

m.p.: 338 °C (decomposition). **IR** (KBr, cm⁻¹): 3435s ν (O-H), 2952w, 2954w, 1617s ν (C=N), 1517vs ν (C-C)^{aryl}, 1486s, 1368m, 1325m, 1287s, 1238s, 1213s, 1181vs ν_{as} (SO₃⁻), 1107vs, 1034vs ν_s (SO₃⁻), 829m, 812m, 716m, 687m, 668m, 600s. **¹H-NMR** (400 MHz, DMSO-D₆): δ = 6.94 (m, 2H, CH^{aryl}), 7.07 (m, 2H, CH^{aryl}), 7.36 (m, 2H, CH^{aryl}), 7.45 (m, 2H, CH^{aryl}), 7.62–7.67 (m, 4H, CH^{aryl}), 7.99 (d, 2H, CH^{aryl}), 8.48 (s, 2H, CH^{aryl}), 9.21 (s, 2H, -N=CH-), 9.93 (s, 1H, OH) 13.65 (s, 2H, OH_{sal}). **¹³C-NMR** (100 MHz, DMSO-D₆): δ = 110.6, 113.9, 115.8, 116.7, 118.3, 120.6, 123.2, 126.3, 127.4, 128.1, 129.5, 130.3, 139.6, 140.5, 157.2, 160.4, 160.9. **ESI-MS neg.:** $\frac{m}{z}$ = 327.5 (100%, [M-2Na]²⁻), 678 (10%, [M-Na]⁻). **Analysis:** calculated for C₃₂H₂₁N₃Na₂O₉S₂·2H₂O (M = 737.66 g/mol): C, 52.10; H, 3.42; N, 5.70; S, 8.69; found: C, 52.58; H, 3.21; N, 6.05; S, 8.56.

Sodium-2-hydroxy-3-methoxy-5-sulfonatobenzaldehyde (20)

20a: 2.00 g (0.013 mol) *ortho*-vaniline are dissolved in 20 mL methanol and 1.2 mL (0.013 mmol) aniline are added slowly under stirring. After stirring for 1 h most of the solvent is removed to yield a red oil, from which orange crystals are gained in short time, which are filtered off, washed with methanol and dried in air. Yield: 2.4 g (81%).

20b: 2.40 g **20a** are suspended in 20 mL konz. H₂SO₄ and are stirred for 2 h at 100°C to give a dark green solution. After cooling, the solution is poured onto 300 mL ice water. The green precipitate is redissolved by heating under reflux. Two third of the solvent are removed under reduced pressure. After two days of cooling a green-yellow precipitate is formed, which is filtered off, washed with water, ethanol and acetone and dried in air. Yield: 2.24 g (64%).

20: 2.24 g **20b** are dissolved in 50 mL of water in an open beaker and 2.00g Na₂CO₃ are added. The solution is heated for 2 h. During this time the evaporated water is regularly replaced. After cooling, the dark yellow solution is concentrated by removing half

of the solvent and the same amount of ethanol is added. After two days in the fridge a yellow precipitate is formed, which is filtered off, washed three times with 5 mL of methanol and dried in air. Yield: 1.00 g (58%). Total yield over all steps: 1.00 g (30%)

m.p.: 323 °C (decomposition). **IR** (KBr, cm^{-1}): 3435s $\nu(\text{O-H})$, 3081w $\nu(\text{C-H})^{\text{aryl}}$, 3036w $\nu(\text{C-H})^{\text{aryl}}$, 1670m $\nu(\text{C=O})$, 1471s $\nu(\text{C-C})^{\text{aryl}}$, 1258s $\nu_{\text{as}}(\text{C-O-C})$, 1214s $\nu_{\text{as}}(\text{SO}_3^-)$, 1198s, 1116m $\nu(\text{C-O})$, 1092s $\nu_{\text{s}}(\text{C-O-C})$, 1045s $\nu_{\text{s}}(\text{SO}_3^-)$. **$^1\text{H-NMR}$** (400 MHz, DMSO- D_6): δ = 3.86 (s, 3H, CH_3), 7.38 (d, 1H, $J = 4\text{Hz}$, CH^{arom}), 7.53 (d, 1H, $J = 4\text{Hz}$, CH^{arom}), 10.27 (s, 1H, OH). **$^{13}\text{C-NMR}$** (100 MHz, DMSO- D_6): δ = 56.6 (OCH_3), 114.9 (C^4), 117.6 (C^6), 121.6 (C^1), 140.2 (C^5), 148.1 (C^2), 151.4 (C^3), 192.2 ($-\text{CHO}$). **EI-MS:** $\frac{m}{z}$ = 106 (23%), 122 (8%), 136 (6%), 151 (23%), 152 (100%), 232 (13%, $[\text{M-Na+H}]^+$), 256 (15%, $[\text{M+2H}]^+$). **Analysis:** calculated for $\text{C}_8\text{H}_7\text{NaO}_6\text{S}\cdot 0.5\text{H}_2\text{O}$ ($M = 263.16$ g/mol): C, 36.50; H, 3.07; S, 12.18; found: C, 36.89; H, 2.46; S, 11.61.

Disodium bis-(2-hydroxy-3-methoxy-5-sulfonatobenzylidene)-1,2-diimineethylene, $\text{H}_2\text{Na}_2^{\text{Sulf}}$ Mesalen (21)

A suspension of 0.35 g (1.3 mmol) Sodium-2-hydroxy-3-methoxy-5-sulfonatobenzaldehyde and 93 μL (67 mg, 0.66 mmol) ethylenediamine is heated under reflux for 2 h. After cooling the yellow precipitation is filtered off, washed with methanol and dried under reduced pressure. Yield: 0.36 g (0.60 mmol, 91%).

m.p.: 300° (decomposition). **IR** (KBr, cm^{-1}): 3435s $\nu(\text{O-H})$, 2940w $\nu(\text{CH}_2)$, 1636s $\nu(\text{C=N})$, 1540m, 1527m, 1457w, 1342w, 1253s $\nu_{\text{as}}(\text{C-O-C})$, 1230s, 1209s $\nu_{\text{as}}(\text{SO}_3^-)$, 1187s, 1102s $\nu_{\text{s}}(\text{C-O-C})$, 1043s $\nu_{\text{s}}(\text{SO}_3^-)$, 974w, 900w, 855w, 784w, 697w, 631s, 617s, 602m. **$^1\text{H-NMR}$** (400 MHz, DMSO- D_6): 3.77 (t, 4H, CH_2), 3.91 (s, 6H, CH_3), 7.17 (d, 2H, $J = 4\text{Hz}$, CH^{aryl}), 7.29 (d, 2H, $J = 4\text{Hz}$, CH^{aryl}), 8.63 (s, 6H, CH=N), 13.79 (s, 6H, OH). **$^{13}\text{C-NMR}$** (100 MHz, DMSO- D_6): 56.0 (OCH_3), 58.0 (CH_2), 112.3 (C^4), 116.7 (C^6), 120.8 (C^1), 138.4 (C^5), 147.9 (C^2), 153.7 (C^3), 167.6 (C=N). **neg. ESI-MS:** $\frac{m}{z}$ = 243 (100%, $[\text{M-2Na}]^{2-}$), 254.5 (24%, $[\text{M-Na}]^{2-}$), 509 (34%, $[\text{M-Na}]^-$), 541 (2%, $[\text{M-Na+MeOH}]^-$). **Analysis:** calculated for $\text{C}_{18}\text{H}_{18}\text{N}_2\text{Na}_2\text{O}_{10}\text{S}_2\cdot 4\text{H}_2\text{O}$ ($M = 604.53$ g/mol): C, 35.67; H, 4.34; N, 4.64; S, 10.61 found: C, 35.77; H, 4.10; N, 4.78; S, 10.90.

(enH₂)[Cu(^{Sulf} Mesalen)] · H₂O (22)

2.00 g (3.8 mmol) H₂Na₂^{Sulf}Mesalen are dissolved in 40 mL water and 126 μL (113 μg, 1.9 mmol) ethylenediamine are added. After adding 0.45 mg (1.9 mmol) Cu(NO₃)₂ dissolved in 1 mL water the pH is adjusted to 8 by adding 1M NaOH. Crystals suitable for X-ray diffraction are obtained by vapor diffusion of methanol into the aqueous solution. Yield: 1.80 g (2.7 mmol, 71%).

m.p.: 310°C (decomposition). **IR** (KBr, cm⁻¹): 3435m ν(O-H), 3096w ν(C-H)^{aryl}, 3067w ν(C-H)^{aryl}, 2940w ν(CH₂), 1642s, 1600m, 1549w, 1457m, 1384m, 1253s, 1193s ν_{as}(SO₃⁻), 1167s, 1111s, 1040m ν_s(SO₃⁻). **neg. ESI-MS:** $\frac{m}{z} = 255$ (37%, [L+Na+H]²⁻), 274 (100%, [L+Cu]²⁻), 570 (9%, [L+Cu+Na]⁻). **Analysis:** calculated for

C₂₀H₂₆CuN₄O₁₀S₂·3H₂O (M = 663.07 g/mol): C, 36.17; H, 4.86; N, 8.44; S, 9.66 found: C, 36.29; H, 4.13; N, 8.71; S, 10.12.

(enH₂)[Cu(^{Sulf} Mesalen)] · 4H₂O (23)

70 mg of (enH₂)[Cu(^{Sulf} Mesalen)] · H₂O are dissolved in water. The obtained solution is layered with *iso*-propanol. After few days voluminous aggregates of fibers are formed, which recrystallize very slowly during months to give violet plate-shaped crystals, which are suitable for X-ray crystallography.

(enH₂)[Mn₂(^{Sulf} Mesalen)₂]·3MeOH·9.5H₂O (24)

2.00 g (3.8 mmol) H₂Na₂^{Sulf}Mesalen are dissolved in 40 mL water and the pH is adjusted to 10 with 1M aqueous NaOH. Then 265 μL (193 mg, 1.9 mmol) ethylenediamine are added followed by 0.98 g (3.95 mmol) Mn(NO₃)₂, dissolved in few mL of water. The suspension is stirred overnight and the brown precipitate is collected by filtration. The powder is recrystallized by dissolution of small amounts in water and vapor diffusion of methanol into this aqueous solution. Octahedral shaped crystals suitable for X-ray crystallography are obtained within several weeks.

**Disodium *tris*-(5-sulfonato-2-hydroxybenzyliden)triaminoguanidine,
Na₂H₆^{Sulf}TAG (27)**

A suspension of 0.50 g (3.6 mmol) triaminoguanidine hydrochloride and 2.85 g (10.7 mmol) sodium 5-sulfonato-2-hydroxy-benzaldehyde in 20 mL water/methanol 1:1 is heated under reflux for 2 hours. After cooling the precipitation is collected via filtration and washed with ethanol. After drying under reduced pressure at 50 °C 2.60 g of colorless solid are obtained (3.36 mmol, 94%).

m.p.: 300 °C (decomposition). **IR** (KBr, cm⁻¹): 3446vs ν (O-H), 1641vs ν (C-C)^{aryl}, 1492w, 1430w, 1336w, 1294w, 1188s ν_{as} (SO₃⁻), 1085m, 1036vs ν_s (SO₃⁻), 688m, 598m. **¹H-NMR** (400 MHz, DMSO-D₆): δ = 6.90 (d, 3H, CH^{aryl}), 7.78 (d, 3H, CH_{arom}), 8.35 (d, 3H, CH^{aryl}), 9.00 (s, 3H, -N=CH-), 10.52 (s, 3H, NH₃), 12.23 (s, 3H, OH). **¹³C-NMR** (100 MHz, DMSO-D₆): δ = 115.6, 118.9, 125.1, 130.5, 140.4, 148.4, 149.2, 157.7. **neg. ESI-MS:** $\frac{m}{z}$ = 198 (100%, [C₇H₄NO₄S]⁻). **pos. ESI-MS:** $\frac{m}{z}$ = 413 (100%, [M-3SO₃⁻-H]⁺). **Analysis:** calculated for C₂₂H₁₈N₆Na₂O₁₂S₃·7H₂O (M = 826.69 g/mol): C, 31.96; H, 3.90; N, 10.17; S, 11.64; found: C, 31.99; H, 3.81; N, 10.05; S, 11.62.

[^{Sulf}TAG)Cu₃(bipy)₃][Ru(bipy)₃] (28)

100 mg Na₂H₆TAG (0.13 mmol) are dissolved in 10 mL methanol by addition of 72 μ L (53 mg, 0.52 mmol) triethylamine. A solution of 66 mg (0.39 mmol) CuCl₂·2H₂O in 1 mL methanol is added, resulting in a dark green solution. Upon addition of 61 mg (0.39 mmol) bipy in 1 mL methanol a green solid precipitates, which is redissolved with 36 μ L triethylamine (26 mg, 0.26 mmol). Then 97 mg (0.13 mmol) [Ru(bipy)₃]Cl₂ are added yielding a dark brown solution, from which a brown solid precipitates within the next hours. The precipitation is filtered off, washed with methanol and dried under reduced pressure. 73 mg of brown solid are obtained (0.03 mmol, 26%).

m.p.: 250 °C (decomposition). **IR** (KBr, cm⁻¹): 3435vs ν (O-H), 3109w, 3077w ν (C-H)^{aryl}, 1632m ν (C-C)^{aryl}, 1595s ν (C-C)^{aryl}, 1530m, 1475vs, 1445s, 1355m, 1314w, 1213m, 1189s ν_{as} (SO₃⁻), 1108s, 1030vs ν_s (SO₃⁻), 769s, 660m, 609s, 586m. **ESI-MS, neg.:** $\frac{m}{z}$ = 293 (100%, [C₉H₅N₆O₄S]⁻), 419 (5%, [L Cu₃]³⁻). **ESI-MS, pos.:** $\frac{m}{z}$ = 207 (66%, [Ru(bipy)₂]²⁺), 285 (100%, [Ru(bipy)₃]²⁺), 413 (7%, [Ru(bipy)₂]⁺). **Analysis:** calculated for C₈₂H₆₀Cu₃N₁₈O₁₂RuS₃·17H₂O (M = 2183.63 g/mol): C, 45.10; H, 4.34; N, 11.55; S, 4.41; found: C, 45.04; H, 4.65; N, 11.63; S, 4.59.

8 X-ray Crystallography

The crystallographic data were collected on a Nonius KappaCCD diffractometer using graphite-monochromated Mo-K α radiation (71.073 pm). A summary of crystallographic and structure refinement data for the investigated structures is given in the appendix. The structure was solved by direct methods with SHELXS-97 and was full-matrix least-squares refined against F^2 using SHELXL-97^[380,381]. All non-hydrogen atoms were refined anisotropically. Hydrogen atoms were calculated and treated as riding atoms with fixed or refined thermal parameters.

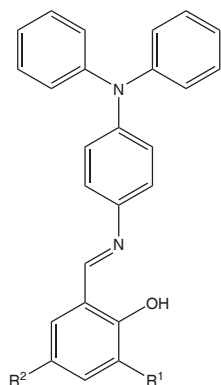
9 Electrochemical Measurements

Cyclic square-wave voltammetric measurements have been carried out by a three-electrode technique using a home-built computer-controlled instrument based on the PCI 6110-E data acquisition board (National Instruments). The experiments were performed in acetonitrile solutions containing 0.25 M tetra-*n*-butylammonium hexafluorophosphate under a blanket of solvent saturated with argon. The ohmic resistance that had to be compensated for was determined by measuring the impedance of the system at potentials where the faradaic current was negligible. Background corrections were applied only for cyclic voltammograms by subtracting the current curves of the blank electrolyte containing the same concentration of the supporting electrolyte from the experimental cyclic voltammograms. Ag/AgCl was used as the reference electrode in acetonitrile containing 0.25 M tetra-*n*-butylammonium chloride. All potentials reported in this paper refer to the ferrocenium/ferrocene couple, which has been measured at the end of each experiment. The working electrode was a hanging mercury drop ($m_{\text{Hg-drop}} = 4 \text{ mg}$) generated by a CGME instrument from Bioanalytical Systems Inc., West Lafayette, USA. Theoretical square-wave voltammograms were simulated using the *Digi-Elch* simulation software developed in our group (available via www.elchsoft.de).

— Appendix —

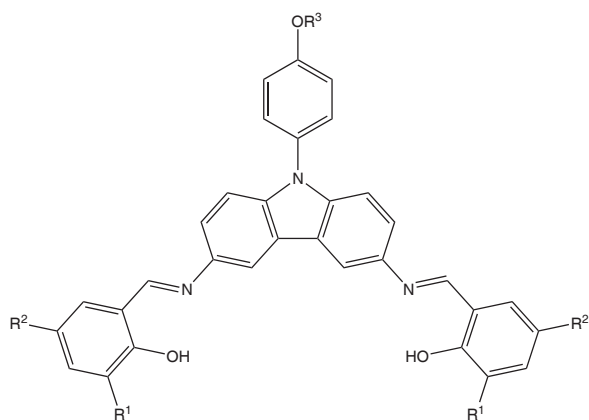
A.1 Synthesized Ligands

Triphenylamine-based ligands



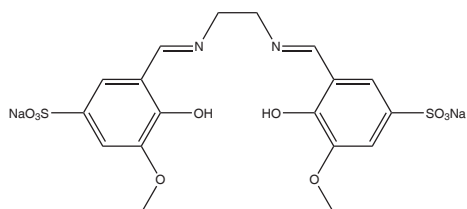
| Ligand | R ¹ | R ² |
|----------------------|-----------------|-----------------|
| HTPA | H | H |
| H ^{tBu} TPA | ^t Bu | ^t Bu |

Carbazole-based ligands



| Ligand | R ¹ | R ² | R ³ |
|--|-----------------|--------------------|----------------|
| H ₂ CarbOMe | H | H | Me |
| H ₂ ^{tBu} CarbOMe | ^t Bu | ^t Bu | Me |
| H ₂ ^{Sulf} CarbOMe | H | SO ₃ Na | Me |
| H ₂ CarbOH | H | H | H |
| H ₂ ^{Sulf} CarbOH | H | SO ₃ Na | H |

Sulf-Mesalen ligand



A.2 Synthesized Complexes

Complexes with triphenylamine-based ligands (Section 2.1)

[Cu(hfac)(TPA)]₂ 5

[Cu(^tBuTPA)₂]₂·2.5CH₃COCH₃ 6

Complexes with carbazole-based complexes (Section 3.1)

[Cu₂(CarbOMe)₂]₂·1.75CHCl₃·1.25MeOH·5.25H₂O 11

[Zn₂(CarbOMe)₂]₂·MeOH·CHCl₃ 12

[Cu₂(^tBuCarbOMe)₂]₂ 14

Complexes with sulfonated Mesalen-type ligands (Section 3.2)

(enH₂)[Cu(^{Sulf}Mesalen)]·H₂O 22

(enH₂)[Cu(^{Sulf}Mesalen)]·4H₂O 23

(enH₂)_{0.5}[Mn(^{Sulf}Mesalen)]·1.5MeOH·4.75H₂O 24

Complexes with triaminoguanidine-based ligands (Section 3.3)

[(^{Sulf}TAG)Cu₃(bipy)₃][Ru(bipy)₃] 28

Complexes with phloroglucine-based ligands (Section 4.1)

[(phloro)Cu₃(bhea)₃](ClO₄)₃ 29¹

¹The synthesis is described by the author in his Diploma Thesis^[332]

A.3 Investigated Complexes

Complexes with phloroglucine-based ligands (Section 2.2)

$[\text{Cu}_4(\text{L}2^{\text{Busal}})_2(\text{hfac})_2(\text{MeOH})_2] \cdot 5\text{CHCl}_3 \cdot 3\text{MeOH}$ **Cu₄** D. Plaul^[213]

Complexes with triaminoguanidine-based ligands (Section 3.3)

$[(^{\text{H}}\text{TAG})\text{Cu}_3(\text{bipy})_3](\text{ClO}_4)$ **26** A. Zharkouskaya^[308]

Complexes with Mesalen-type ligands (Section 4.2)

$[\text{Cu}(\text{OMesalen})\text{La}(\text{NO}_3)(\text{Pyr}(\text{COO})_2)]_n \cdot (\text{DMF})_n$ **30**

$[\text{Cu}(\text{OMesalen})\text{Pr}(\text{NO}_3)(\text{Pyr}(\text{COO})_2)]_n \cdot (\text{DMF})_n$ **31**

$[\text{Cu}(\text{OMesalen})\text{Sm}(\text{NO}_3)(\text{Pyr}(\text{COO})_2)]_n \cdot (\text{DMF})_n$ **32**

$[\text{Cu}(\text{OMesalen})\text{Eu}(\text{NO}_3)(\text{Pyr}(\text{COO})_2)]_n \cdot (\text{DMF})_n$ **33**

A. E. Ion^[309]

$[\text{Cu}(\text{OMesalen})\text{Gd}(\text{NO}_3)(\text{Pyr}(\text{COO})_2)]_n \cdot (\text{DMF})_n$ **34**

$[\text{Cu}(\text{OMesalen})\text{Tb}(\text{NO}_3)(\text{Pyr}(\text{COO})_2)]_n \cdot (\text{DMF})_n$ **35**

$[\text{Cu}(\text{OMesalen})\text{Dy}(\text{NO}_3)(\text{Pyr}(\text{COO})_2)]_n \cdot (\text{DMF})_n$ **36**

Complexes with triaminoguanidine-based ligands (Section 4.3)

$[\text{CoNi}_4(\text{TAG}^{\text{H}})_2(\text{tptz})_4]\text{ClO}_4$ **CoNi₄**

$[\text{MnNi}_4(\text{TAG}^{\text{H}})_2(\text{tptz})_4]\text{ClO}_4$ **MnNi₄**

D. Plaul^[213]

$[\text{FeNi}_4(\text{TAG}^{\text{Br}})_2(\text{tptz})_4](\text{ClO}_4)_{0.5}\text{Cl}_{0.5}$ **FeNi₄**

A.4 Crystallographic Data

Table A.1: Crystallographic data and structure-refinement parameters for complex [Cu(hfac)(TPA)]₂ (5)

| | 5 |
|--|---|
| Formula | C ₃₀ H ₂₀ CuF ₆ N ₂ O ₃ |
| Formula weight | 634.02 |
| Crystal size (mm) | 0.04 x 0.04 x 0.03 |
| Crystal system | triclinic |
| Space group | <i>P</i> $\bar{1}$ |
| Lattice parameters | |
| a (pm) | 9.4010(7), α 76.921(4) |
| b (pm) | 11.8037(9), β 82.519(4) |
| c (pm) | 13.0631(8), γ 78.781(4) |
| Cell volume (10 ⁶ pm ³) | 1379.34(17) |
| Z | 2 |
| Temperature (K) | 183(2) |
| Δ_{calc} (g cm ⁻³) | 1.527 |
| F(000) | 642 |
| μ (Mo K α) (mm ⁻¹) | 0.71073 |
| Data collection range (°) | 3.04 \leq Θ \leq 27.51 |
| Index range | -12 \leq <i>h</i> \leq 10 -15 \leq <i>k</i> \leq 14 -16 \leq <i>l</i> \leq 16 |
| Reflection measured | |
| total | 9279 |
| unique | 6185 (<i>R</i> _{int} =0.0588) |
| Goodness-of-fit | 1.028 |
| R ₁ | 0.0825 |
| wR ₂ | 0.1855 |

Table A.2: Crystallographic data and structure-refinement parameters for complex $[\text{Cu}(\text{}^t\text{BuTPA})_2]\cdot 2.5\text{CH}_3\text{COCH}_3$ (**6**)

| 6 | |
|---|--|
| Formula | $\text{C}_{71.5}\text{H}_{82}\text{CuN}_4\text{O}_{4.5}$ |
| Formula weight | 1132.95 |
| Crystal size (mm) | 0.05 x 0.05 x 0.05 |
| Crystal system | monoclinic |
| Space group | $P2/n$ |
| Lattice parameters | |
| a (pm) | 19.2683(3), α 90 |
| b (pm) | 9.8704(2), β 93.650(1) |
| c (pm) | 34.5533(7), γ 90 |
| Cell volume (10^6pm^3) | 6558.2(2) |
| Z | 4 |
| Temperature (K) | 183(2) |
| Δ_{calc} (g cm^{-3}) | 1.147 |
| F(000) | 2416 |
| $\mu(\text{Mo K}\alpha)$ (mm^{-1}) | 0.71073 |
| Data collection range ($^\circ$) | $1.18 \leq \Theta \leq 27.49$ |
| Index range | $-25 \leq h \leq 22$ $-12 \leq k \leq 11$ $-29 \leq l \leq 44$ |
| Reflection measured | |
| total | 32006 |
| unique | 14740 ($R_{int} = 0.0496$) |
| Goodness-of-fit | 1.151 |
| R_1 | 0.0977 |
| w R_2 | 0.2754 |

Table A.3: Crystallographic data and structure-refinement parameters for complex
 $[\text{Cu}_2(\text{CarbOMe})_2] \cdot 1.75\text{CHCl}_3 \cdot 1.25\text{MeOH} \cdot 5.25\text{H}_2\text{O}$ (**11**)

| 11 | |
|---|---|
| Formula | $\text{C}_{69}\text{H}_{63.25}\text{Cl}_{5.25}\text{Cu}_2\text{N}_6\text{O}_{12.5}$ |
| Formula weight | 1489.70 |
| Crystal size (mm) | 0.04 x 0.04 x 0.04 mm |
| Crystal system | triclinic |
| Space group | $P\bar{1}$ |
| Lattice parameters | |
| a (pm) | 15.6401(9), α 63.449(3) |
| b (pm) | 15.9390(8), β 71.314(2) |
| c (pm) | 16.8759(9), γ 77.162(2) |
| Cell volume (10^6pm^3) | 3549.4(3) |
| Z | 2 |
| Temperature (K) | 183(2) |
| Δ_{calc} (g cm^{-3}) | 1.394 |
| F(000) | 1533 |
| $\mu(\text{Mo K}\alpha)$ (mm^{-1}) | 0.71073 |
| Data collection range ($^\circ$) | $1.70 \leq \Theta \leq 27.47$ |
| Index range | $-20 \leq h \leq 20$ $-19 \leq k \leq 20$ $-19 \leq l \leq 21$ |
| Reflection measured | |
| total | 24816 |
| unique | 16007 ($R_{int}=0.0505$) |
| Goodness-of-fit | 1.019 |
| R_1 | 0.0866 |
| wR_2 | 0.2730 |

Table A.4: Crystallographic data and structure-refinement parameters for complex $[\text{Zn}_2(\text{CarbOMe})_2]\cdot\text{MeOH}\cdot\text{CHCl}_3$ (**12**)

| 12 | |
|---|--|
| Formula | $\text{C}_{68}\text{H}_{51}\text{Cl}_3\text{N}_6\text{O}_7\text{Zn}_2$ |
| Formula weight | 1301.24 |
| Crystal size (mm) | 0.05 x 0.05 x 0.05 |
| Crystal system | triclinic |
| Space group | $P\bar{1}$ |
| Lattice parameters | |
| a (pm) | 14.3107(3), α 112.754(1) |
| b (pm) | 14.9621(6), β 96.694(2) |
| c (pm) | 16.9319(5), γ 112.014(2) |
| Cell volume (10^6pm^3) | 2950.92(16) |
| Z | 2 |
| Temperature (K) | 183(2) |
| Δ_{calc} (g cm^{-3}) | 1.464 |
| F(000) | 1336 |
| $\mu(\text{Mo K}\alpha)$ (mm^{-1}) | |
| Data collection range ($^\circ$) | $2.36 \leq \Theta \leq 27.47$ |
| Index range | $-18 \leq h \leq 19$ $-16 \leq k \leq 19$ $-21 \leq l \leq 21$ |
| Reflection measured | |
| total | 21454 |
| unique | 13413 ($R_{int} = 0.0369$) |
| Goodness-of-fit | 1.009 |
| R_1 | 0.0494 |
| wR_2 | 0.10215 |

Table A.5: Crystallographic data and structure-refinement parameters for
2-hydroxy-3-methoxy-5-sulfonato-benzyl-phenylimine trihydrate (**21b**)

| 21b | |
|--|--|
| Formula | C ₁₄ H ₁₉ NO ₈ S |
| Formula weight | 361.36 |
| Crystal size (mm) | 0.05 x 0.05 x 0.05 |
| Crystal system | triclinic |
| Space group | <i>P</i> $\bar{1}$ |
| Lattice parameters | |
| a (pm) | 8.3274(17), α 76.36(3) $^\circ$ |
| b(pm) | 9.1052(18), β 82.13(3) $^\circ$ |
| c (pm) | 11.565(2), γ 68.36(3) $^\circ$ |
| Cell volume (10 ⁶ pm ³) | 790.8(3) |
| Z | 2 |
| Temperature (K) | 183(2) |
| Δ_{calc} (g cm ⁻³) | 1.518 |
| F(000) | 380 |
| μ (Mo K $_{\alpha}$) (mm ⁻¹) | 0.71073 |
| Data collection range ($^\circ$) | 2.64 \leq Θ \leq 27.43 |
| Index range | -9 \leq <i>h</i> \leq 10 -11 \leq <i>k</i> \leq 11 -14 \leq <i>l</i> \leq 15 |
| Reflection measured | |
| total | 5602 |
| unique | 3582 (R_{int} = 0.0277) |
| Goodness-of-fit | 1.037 |
| R ₁ | 0.0455 |
| wR ₂ | 0.1204 |

Table A.6: Crystallographic data and structure-refinement parameters for complex (enH₂)[Cu(^{Sulf}Mesalen)]·H₂O (**22**)

| 22 | |
|--|---|
| Formula | C ₂₀ H ₂₈ CuN ₄ O ₁₁ S ₂ |
| Formula weight | 628.12 |
| Crystal size (mm) | 0.05 x 0.05 x 0.04 |
| Crystal system | triclinic |
| Space group | <i>P</i> $\bar{1}$ |
| Lattice parameters | |
| a (pm) | 8.8819(6), α 77.036(3) |
| b (pm) | 9.6972(7), β 80.879(4) |
| c (pm) | 15.3085(12), γ 79.609(4) |
| Cell volume (10 ⁶ pm ³) | 1254.21(16) |
| Z | 2 |
| Temperature (K) | 183(2) |
| Δ_{calc} (g cm ⁻³) | 1.663 |
| F(000) | 650 |
| μ (Mo K α) (mm ⁻¹) | 1.105 |
| Data collection range (°) | 2.33 \leq Θ \leq 27.48 |
| Index range | -11 \leq <i>h</i> \leq 11 -12 \leq <i>k</i> \leq 12 -19 \leq <i>l</i> \leq 19 |
| Reflection measured | |
| total | 8983 |
| unique | 5689(R _{int} = 0.0386) |
| Goodness-of-fit | 1.028 |
| R ₁ | 0.0524 |
| wR ₂ | 0.1255 |

Table A.7: Crystallographic data and structure-refinement parameters for complex (enH₂)[Cu(^{Sulf}Mesalen)]·4H₂O (**23**)

| 23 | |
|--|---|
| Formula | C ₂₀ H ₃₄ CuN ₄ O ₁₄ S ₂ |
| Formula weight | 682.17 |
| Crystal size (mm) | 0.05 x 0.05 x 0.02 |
| Crystal system | triclinic |
| Space group | <i>P</i> $\bar{1}$ |
| Lattice parameters | |
| a (pm) | 13.5239(4), α 84.331(2) |
| b (pm) | 13.6325(4), β 73.876(2) |
| c (pm) | 15.8700(5), γ 85.794(2) |
| Cell volume (10 ⁶ pm ³) | 2793.80(15) |
| Z | 4 |
| Temperature (K) | 183(2) |
| Δ_{calc} (g cm ⁻³) | 1.622 |
| F(000) | 1420 |
| μ (Mo K α) (mm ⁻¹) | 0.71073 |
| Data collection range (°) | 2.75 to 27.47 |
| Index range | -16 $\leq h \leq$ 17 -17 $\leq h \leq$ 17 -18 $\leq h \leq$ 20 |
| Reflection measured | |
| total | 19317 |
| unique | 12673(R _{int} = 0.0311) |
| Goodness-of-fit | 1.017 |
| R ₁ | 0.0458 |
| wR ₂ | 0.1214 |

Table A.8: Crystallographic data and structure-refinement parameters for complex (enH₂)_{0.5}[Mn(^{Sulf}Mesalen)]·1.5MeOH·4.75H₂O (**24**)

| 24 | |
|--|--|
| Formula | C _{20.5} H _{36.5} MnN ₃ O _{16.25} S ₂ |
| Formula weight | 704.09 |
| Crystal size (mm) | 0.05 x 0.05 x 0.05 |
| Crystal system | monoclinic |
| Space group | <i>P1/n</i> |
| Lattice parameters | |
| a (pm) | 23.4849(6), α 90 |
| b (pm) | 11.8540(3), β 117.3410(10) |
| c (pm) | 24.3020(7), γ 90 |
| Cell volume (10 ⁶ pm ³) | 6009.7(3) |
| Z | 8 |
| Temperature (K) | 183(2) |
| Δ_{calc} (g cm ⁻³) | 1.556 |
| F(000) | 2940 |
| μ (Mo K α) (mm ⁻¹) | 0.71073 |
| Data collection range (°) | 2.38 to 27.48 |
| Index range | -30 $\leq h \leq$ 25 -13 $\leq h \leq$ 15 -29 $\leq h \leq$ 31 |
| Reflection measured | |
| total | 33990 |
| unique | 13524(R _{int} = 0.0965) |
| Goodness-of-fit | 1.028 |
| R ₁ | 0.0781 |
| wR ₂ | 0.2261 |

A.5 Structure of 2-Hydroxy-3-methoxy-5-sulfonato-benzyl-phenylimine (**20b**)

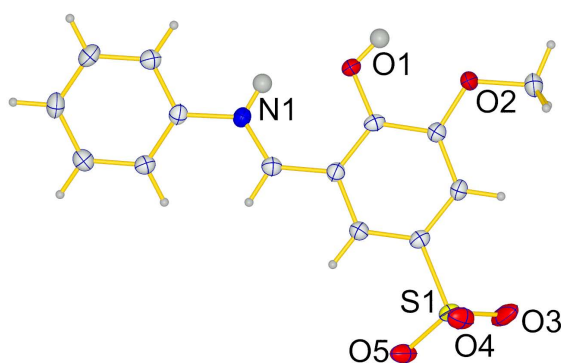


Figure A.1: Molecular structure and numbering scheme for heteroatoms of 2-hydroxy-3-methoxy-5-sulfonato-benzyl-phenylimine (**20b**). Thermal ellipsoids are drawn at 50% probability.

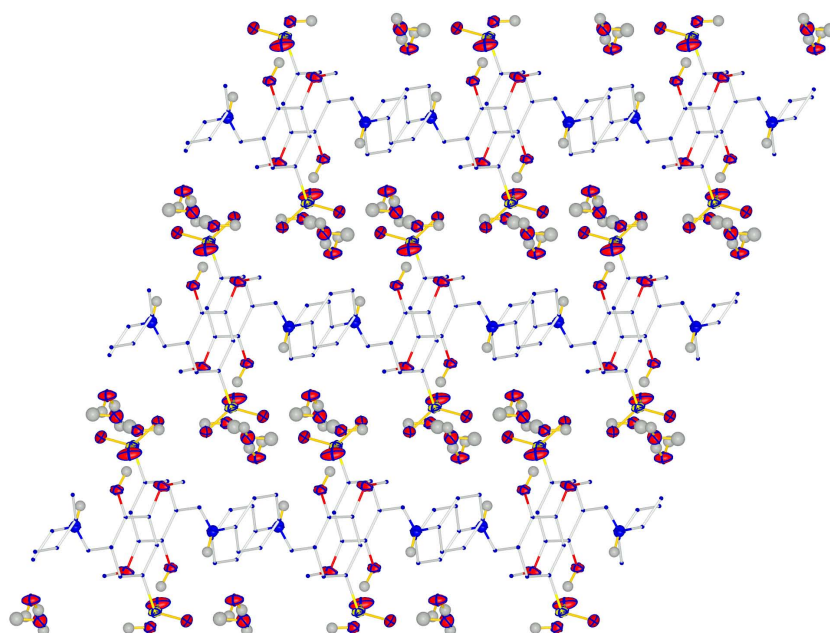


Figure A.2: Packing diagram of **20b** as viewed along the *c*-axis. Carbon atoms are depicted as sticks and carbon bound hydrogen atoms are omitted for clarity.

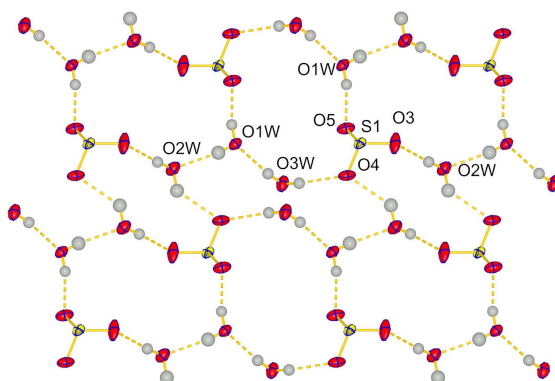


Figure A.3: Hydrogen bonding layers formed by crystal water and sulfonato groups in the *a*-*c*-plane.

Table A.9: Summary of the metric parameters for the hydrogen bonds found in the crystal structures of 2-hydroxy-3-methoxy-5-sulfonato-benzyl-phenylimine (**20b**).

| D-H...A | <i>d</i> (D-H)/pm | <i>d</i> (D...H)/pm | <i>d</i> (D...A)/pm | α (D-H...A)/ $^{\circ}$ |
|-------------|-------------------|---------------------|---------------------|--------------------------------|
| O1W-H...O5 | 87 | 192 | 278 | 169 |
| O2W-H...O3 | 85 | 205 | 290 | 173 |
| O2W-H...O4 | 96 | 220 | 294 | 134 |
| O3W-H...O4 | 88 | 207 | 290 | 155 |
| O1W-H...O2W | 80 | 200 | 280 | 172 |
| O3W-H...O1W | 85 | 207 | 292 | 173 |

A.6 Deconvolution and Calculation of UV/Vis- and ESR-Spectra

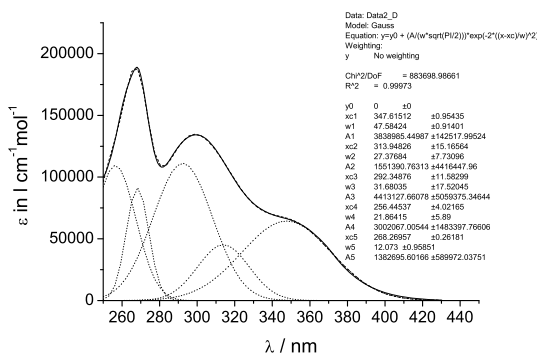


Figure A.4: Deconvolution of absorption bands in the UV/Vis absorption spectrum of H^{tBu} TPA in chloroform assuming Gaussian line shapes. The solid line represents the measured spectrum, the dashed line the sum of the simulated absorption bands and the dotted the individual absorption bands.

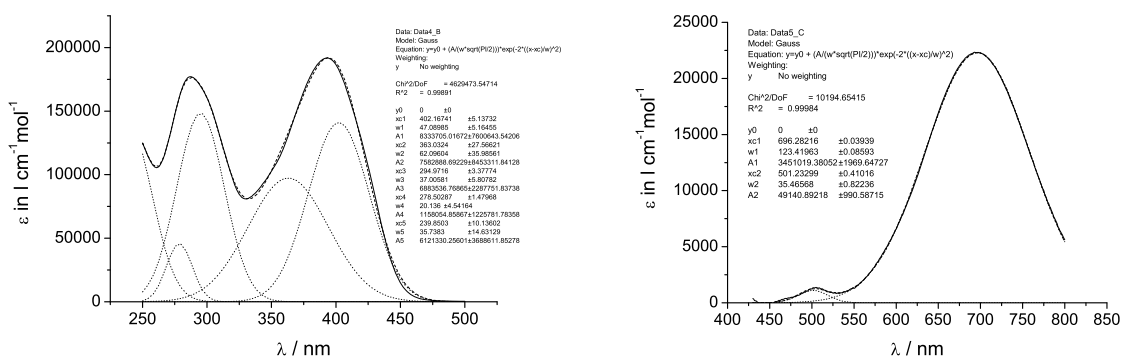


Figure A.5: Deconvolution of absorption bands in the UV/Vis absorption spectrum of H^{tBu} TPA in chloroform recorded 6 weeks after preparation assuming Gaussian line shape. For clarity the spectrum is divided in the low wavelength part (left) and the high wavelength (right). The solid line represents the measured spectrum, the dashed line the sum of the simulated absorption bands and the dotted the individual absorption bands.

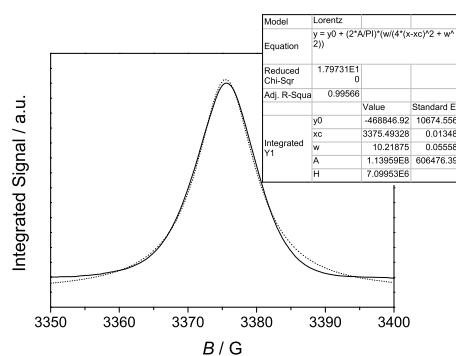


Figure A.6: Deconvolution of integrated ESR spectrum of H^tBuTPA in chloroform assuming Lorentzian line shape. The solid line represents the integrated experimental ESR-spectrum, the dotted the simulated one.

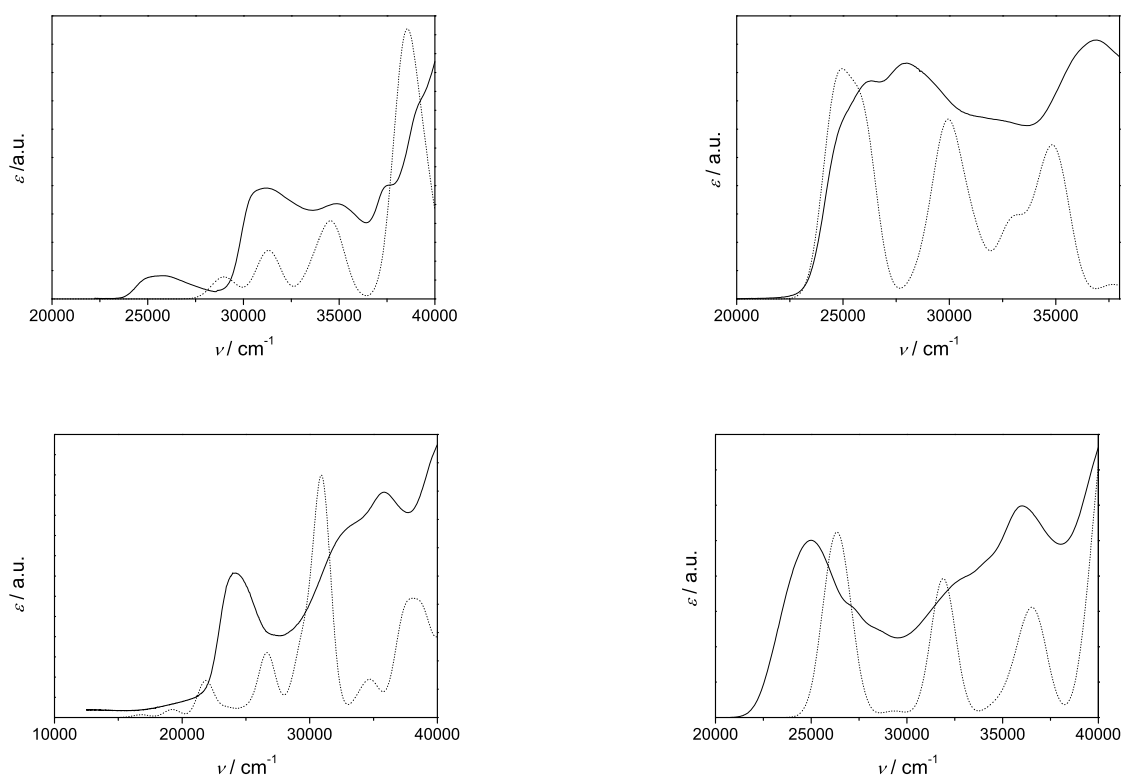


Figure A.7: Comparison between measured and computed absorption spectra of the amine precursor **9** (top left), H₂CarbOMe **10** (top right), [Cu₂(CarbOMe)₂] **11** (bottom left) and [Zn₂(CarbOMe)₂] **12** (bottom right).

A.7 Atom Numbering Scheme

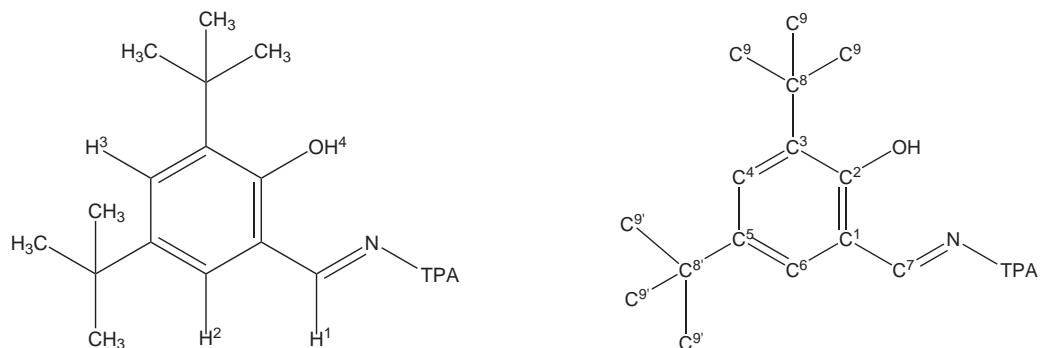


Figure A.8: Numbering scheme of hydrogen atoms (left) and carbon atoms (right) in the salicylidene moiety.

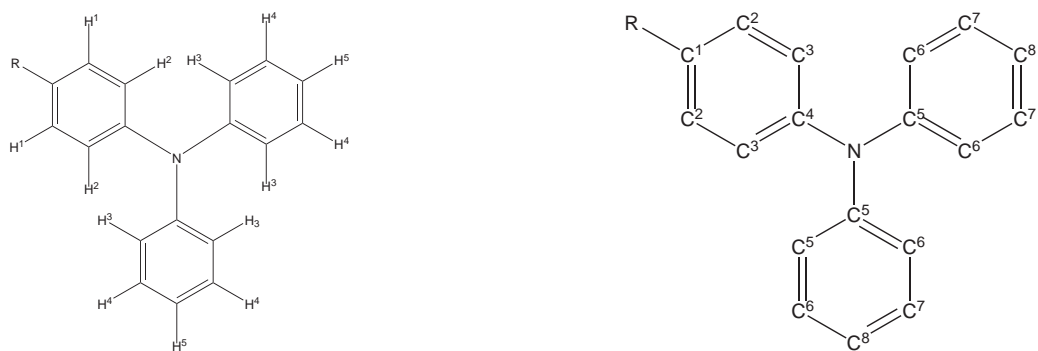


Figure A.9: Numbering scheme of hydrogen atoms (left) and carbon atoms (right) in the triphenyl amine residue.



Figure A.10: Numbering scheme of hydrogen atoms (left) and carbon atoms (right) in the salicylidene moiety.

Bibliography

- [1] S. I. Newton: *Opticks, or, A treatise of the reflections, refractions, inflections, and colours of light*, Oxford University 1730.
- [2] P. Dirac, *Proceedings of the Royal Society of London, Series A: Mathematical, Physical and Engineering Sciences* **1927**, 117, 610–624.
- [3] P. A. M. Dirac, *Proceedings of the Royal Society of London, Series A: Mathematical, Physical and Engineering Sciences* **1928**, 118, 351–361.
- [4] C. Brevard, R. W. Briggs, S. Forsén, R. Goodfellow, R. Harris, J. Hinton, J. Kennedy, R. Kidd, J. Kintzinger, B. Lindman, B. Mann, H. McFarlane, W. MacFarlane, C. Roger, G. Schrobilgen, D. Shaw, N. Sheppard, G. Webb: *NMR and the Periodic Table*, Academic Press 1978.
- [5] A. Hollemann, E. Wiberg: *Lehrbuch der Anorganischen Chemie*, Nils Wiberg 1995.
- [6] H. Lueken: *Magnetochemie*, B.G. Teubner 1999.
- [7] O. Kahn: *Molecular Magnetism*, Wiley-VCH Int., Weinheim 1993.
- [8] A. Abragam, B. Bleaney: *Electron Paramagnetic Resonance of Transition Ions*, Oxford, England: Oxford University Press 1975.
- [9] A. Bencini, D. Gatteschi: *Electron Paramagnetic Resonance of Exchange Coupled Systems*, Springer-Verlag 1990.
- [10] julX (v1.41), E. Bill, 2008, <http://ewww.mpi-muelheim.mpg.de/bac/logins/bill/julX.en.php>.
- [11] DAVE (1.5), NIST Center for Neutron Research, 2008, <http://www.ncnr.nist.gov/dave/index.html>.
- [12] T. G. Castner, M. S. Seehra, *Physical Review B* **1971**, 4, 38.
- [13] L. Banci, A. Bencini, D. Gatteschi, *Journal of the American Chemical Society* **1983**, 105, 761–764.
- [14] I. Yamada, H. Fujii, M. Hidaka, *Journal of Physics - Condensed Matter* **1989**, 1, 3397–3408.
- [15] I. Yamada, M. Nishi, J. Akimitsu, *Journal of Physics - Condensed Matter* **1996**, 8, 2625–2640.
- [16] N. Kato, I. Yamada, *Journal of the Physical Society of Japan* **1994**, 63, 3515–3521.
- [17] A. Bouwen, A. Caneschi, D. Gatteschi, E. Goovaerts, D. Schoemaker, L. Sorace, M. Stefan, *The Journal of Physical Chemistry B* **2001**, 105, 2658–2663.

Bibliography

- [18] J. Yoon, L. M. Mirica, T. D. P. Stack, E. I. Solomon, *Journal of the American Chemical Society* **2004**, *126*, 12586–12595.
- [19] J. Yoon, E. I. Solomon, *Coordination Chemistry Reviews* **2007**, *251*, 379 – 400. A Special Issue Highlighting the Many Aspects of the Electronic Spectroscopy of Inorganic Compounds.
- [20] L. M. B. Napolitano, O. R. Nascimento, S. Cabaleiro, J. Castro, R. Calvo, *Physical Review B* **2008**, *77*, 214423.
- [21] A. Ozarowski, *Inorganic Chemistry* **2008**, *47*, 9760–9762.
- [22] W. Wernsdorfer, K. Hasselbach, A. Benoit, W. Wernsdorfer, B. Barbara, D. Mailly, J. Tuaillon, J. Perez, V. Dupuis, J. Dupin, G. Guiraud, A. Perex, *Journal of Applied Physics* **1995**, *78*, 7192–7195.
- [23] J. P. Cleuziou, W. Wernsdorfer, V. Bouchiat, T. Ondarcuhu, M. Monthieux, *Nature Nanotechnology* **2006**, *1*, 53–59.
- [24] A. Fert, *Angewandte Chemie - International Edition* **2008**, *47*, 5956–5967.
- [25] T. Xu, R. Lu, X. Liu, X. Zheng, X. Qiu, Y. Zhao, *Organic Letters* **2007**, *9*, 797–800.
- [26] X. Li, J. Gui, H. Yang, W. Wu, F. Li, H. Tian, C. Huang, *Inorganica Chimica Acta* **2008**, *361*, 2835 – 2840.
- [27] Y.-G. Kim, B. C. Thompson, N. Ananthakrishnan, G. Padmanaban, S. Ramakrishnan, J. R. Reynolds, *Journal of Materials Research* **2005**, *20*, 31883198.
- [28] C. Dimitrakopoulos, P. Malenfant, *Advanced Materials* **2002**, *14*, 99+.
- [29] H. E. Katz, *Chemistry of Materials* **2004**, *16*, 4748–4756.
- [30] Y. Song, C.-a. Di, Z. Wei, T. Zhao, W. Xu, Y. Liu, D. Zhang, D. Zhu, *Chemistry - A European Journal* **2008**, *14*, 4731–4740.
- [31] W.-Y. Wong, L. Liu, D. Cui, L. M. Leung, C.-F. Kwong, T.-H. Lee, H.-F. Ng, *Macromolecules* **2005**, *38*, 4970–4976.
- [32] W.-Y. Wong, C.-L. Ho, Z.-Q. Gao, B.-X. Mi, C.-H. Chen, K.-W. Cheah, Z. Lin, *Angewandte Chemie - International Edition* **2006**, *45*, 7800–7803.
- [33] L. Liu, W.-Y. Wong, J.-X. Shi, K.-W. Cheah, T.-H. Lee, L. M. Leung, *Journal of Organometallic Chemistry* **2006**, *691*, 4028 – 4041.
- [34] S. Grigalevicius, *Synthetic Metals* **2006**, *156*, 1 – 12.
- [35] D. Velasco, S. Castellanos, M. Lopez, F. Lopez-Calahorra, E. Brillas, L. Julia, *The Journal of Organic Chemistry* **2007**, *72*, 7523–7532.
- [36] C. C. Lu, E. Bill, T. Weyhermuller, E. Bothe, K. Wieghardt, *Inorganic Chemistry* **2007**, *46*, 7880–7889.
- [37] S. Roy, M. Sieger, P. Singh, M. Niemeyer, J. Fiedler, C. Duboc, W. Kaim, *Inorganica Chimica Acta* **2008**, *361*, 1699 – 1704. Protagonists in Chemistry: Piero Zanello.

- [38] K. Nakabayashi, Y. Ozaki, M. Kawano, M. Fujita, *Angewandte Chemie - International Edition* **2008**, *47*, 2046–2048.
- [39] D. Gatteschi, R. Sessoli, *Angewandte Chemie - International Edition* **2003**, *42*, 268–297.
- [40] S. Wang, J. Zuo, H. Zhou, H. Choi, Y. Ke, J. Long, X. You, *Angewandte Chemie - International Edition* **2004**, *43*, 5940–5943.
- [41] M. D. Godbole, O. Roubeau, R. Clrac, H. Kooijman, A. L. Spek, E. Bouwman, *Chemical Communications* **2005**, 3715–3717.
- [42] S. Koizumi, M. Nihei, M. Nakano, H. Oshio, *Inorganic Chemistry* **2005**, *44*, 1208–1210.
- [43] S. Maheswaran, G. Chastanet, S. J. Teat, T. Mallah, R. Sessoli, W. Wernsdorfer, R. E. P. Winpenny, *Angewandte Chemie - International Edition* **2005**, *117*, 5172–5176.
- [44] H. Miyasaka, T. Nezu, K. Sugimoto, K. Sugiura, M. Yamashita, R. Clerac, *Chemistry - A European Journal* **2005**, *11*, 1592–1602.
- [45] M. Murugesu, F. Wernsdorfer, K. A. Abboud, G. Christou, *Angewandte Chemie - International Edition* **2005**, *44*, 892–896.
- [46] H. Oshio, M. Nihei, A. Yoshida, H. Nojiri, M. Nakano, A. Yamaguchi, Y. Karaki, H. Ishimoto, *Chemistry - A European Journal* **2005**, *11*, 843–848.
- [47] E.-C. Yang, C. Kirman, J. Lawrence, L. N. Zakharov, A. L. Rheingold, S. Hill, D. N. Hendrickson, *Inorganic Chemistry* **2005**, *44*, 3827–3836.
- [48] A. M. Ako, V. Mereacre, I. J. Hewitt, R. Clerac, L. Lecren, C. E. Anson, A. K. Powell, *Journal of Materials Chemistry* **2006**, *16*, 2579–2586.
- [49] C. Aronica, G. Pilet, G. Chastanet, W. Wernsdorfer, J.-F. Jacquot, D. Luneau, *Angewandte Chemie - International Edition* **2006**, *45*, 4659–4662.
- [50] D. Li, R. Clerac, S. Parkin, G. Wang, G. T. Yee, S. M. Holmes, *Inorganic Chemistry* **2006**, *45*, 5251–5253.
- [51] J. Martinez-Lillo, D. Armentano, G. De Munno, W. Wernsdorfer, M. Julve, F. Lloret, J. Faus, *Journal of the American Chemical Society* **2006**, *128*, 14218–14219.
- [52] A. Sieber, D. Foguet-Albiol, O. Waldmann, S. T. Ochsenein, G. Carver, H. Mutka, F. Fernandez-Alonso, M. Mezouar, H. P. Weber, G. Christou, H. U. Gudel, *Physical Review B* **2006**, *74*, 024405.
- [53] D. Venegas-Yazigi, E. Ruiz, J. Cano, S. Alvarez, *Dalton Transactions* **2006**, 2643–2646.
- [54] J. H. Yoon, J. H. Lim, H. C. Kim, C. S. Hong, *Inorganic Chemistry* **2006**, *45*, 9613–9615.
- [55] Y.-Z. Zhang, W. Wernsdorfer, F. Pan, Z.-M. Wang, S. Gao, *Chemical Communications* **2006**, 3302–2006.
- [56] Y.-Z. Zheng, M.-L. Tong, W.-X. Zhang, X.-M. Chen, *Angewandte Chemie - International Edition* **2006**, *45*, 6310–6314.

Bibliography

- [57] A. K. Boudalis, Y. Sanakis, J. M. Clemente-Juan, A. Mari, J.-P. Tuchagues, *European Journal Of Inorganic Chemistry* **2007**, 2409–2415.
- [58] A. Ferguson, A. Parkin, J. Sanchez-Benitez, K. Kamenev, W. Wernsdorfer, M. Murrie, *Chemical Communications* **2007**, 3473–3475.
- [59] T. Glaser, M. Heidemeier, R. Frohlich, *Comptes Rendus Chimie* **2007**, 10, 71–78.
- [60] H. Hiraga, H. Miyasaka, K. Nakata, T. Kajiwara, S. Takaishi, Y. Oshima, H. Nojiri, M. Yamashita, *Inorganic Chemistry* **2007**, 46, 9661–9671.
- [61] S. Koizumi, M. Nihei, T. Shiga, M. Nakano, H. Nojiri, R. Bircherrl, O. Waldmann, S. T. Ochsenbein, H. U. Guedel, F. Fernandez-Alonso, H. Oshio, *Chemistry - A European Journal* **2007**, 13, 8445–8453.
- [62] M. Manoli, A. Prescimone, R. Bagai, A. Mishra, M. Murugesu, S. Parsons, W. Wernsdorfer, G. Christou, E. K. Brechin, *Inorganic Chemistry* **2007**, 46, 6968–6979.
- [63] C. J. Milios, I. A. Gass, A. Vinslava, L. Budd, S. Parsons, W. Wernsdorfer, S. P. Perlepes, G. Christou, E. K. Brechin, *Inorganic Chemistry* **2007**, 46, 6215–6217.
- [64] A. Prescimone, J. Wolowska, G. Rajaraman, S. Parsons, W. Wernsdorfer, M. Murugesu, G. Christou, S. Piligkos, E. J. L. McInnes, E. K. Brechin, *Dalton Transactions* **2007**, 5282–5289.
- [65] M.-H. Zeng, M.-X. Yao, H. Liang, W.-X. Zhang, X.-M. Chen, *Angewandte Chemie - International Edition* **2007**, 46, 1832–1835.
- [66] Y.-Z. Zheng, W. Xue, W.-X. Zhang, M.-L. Tong, X.-M. Chen, *Inorganic Chemistry* **2007**, 46, 6437–6443.
- [67] D. E. Freedman, D. M. Jenkins, A. T. Iavarone, J. R. Long, *Journal of the American Chemical Society* **2008**, 130, 2884–2885.
- [68] S. Kanegawa, S. Karasawa, M. Maeyama, M. Nakano, N. Koga, *Journal of the American Chemical Society* **2008**, 130, 3079–3094.
- [69] L. Bogani, C. Sangregorio, R. Sessoli, D. Gatteschi, *Angewandte Chemie - International Edition* **2005**, 44, 5817–5821.
- [70] F. He, M.-L. Tong, X.-M. Chen, *Inorganic Chemistry* **2005**, 44, 8285–8292.
- [71] N. Ishikawa, M. Sugita, W. Wernsdorfer, *Journal of the American Chemical Society* **2005**, 127, 3650–3651.
- [72] K. Bernot, L. Bogani, A. Caneschi, D. Gatteschi, R. Sessoli, *Journal of the American Chemical Society* **2006**, 128, 7947–7956.
- [73] J.-P. Costes, F. Dahan, W. Wernsdorfer, *Inorganic Chemistry* **2006**, 45, 5–7.
- [74] J. Tang, I. Hewitt, N. Madhu, G. Chastanet, W. Wernsdorfer, C. Anson, C. Benelli, R. Sessoli, A. Powell, *Angewandte Chemie - International Edition* **2006**, 45, 1729–1733.
- [75] C. Aronica, G. Chastanet, G. Pilet, B. Le Guennic, V. Robert, W. Wernsdorfer, D. Luneau, *Inorganic Chemistry* **2007**, 46, 6108–6119.

- [76] N. Ishikawa, *Polyhedron* **2007**, *26*, 2147 – 2153. Proceedings of the 10th International Conference on Molecule-based Magnets (ICMM 2006) - Victoria, B.C., Canada, August 13-17, 2006, ICMM 2006.
- [77] S. Takamatsu, T. Ishikawa, S.-y. Koshihara, N. Ishikawa, *Inorganic Chemistry* **2007**, *46*, 7250–7252.
- [78] A. Okazawa, T. Nogami, H. Nojiri, T. Ishida, *Inorganic Chemistry* **2008**, *47*, 9763–9765.
- [79] V. Mereacre, A. M. Ako, R. Clérac, W. Wernsdorfer, I. J. Hewitt, C. E. Anson, A. K. Powell, *Chemistry - A European Journal* **2008**, *14*, 3577–3584.
- [80] A. L. Barra, A. Caneschi, A. Cornia, F. Fabrizi de Biani, D. Gatteschi, C. Sangregorio, R. Sessoli, L. Sorace, *Journal of the American Chemical Society* **1999**, *121*, 5302–5310.
- [81] A. Cornia, A. Fabretti, P. Garrisi, C. Mortalo, D. Bonacchi, D. Gatteschi, R. Sessoli, L. Sorace, W. Wernsdorfer, A. Barra, *Angewandte Chemie - International Edition* **2004**, *43*, 1136–1139.
- [82] M. Moragues-Canovas, P. Riviere, L. Ricard, C. Paulsen, W. Wernsdorfer, G. Rajaraman, E. Brechin, T. Mallah, *Advanced Materials* **2004**, *16*, 1101+.
- [83] N. Madhu, J.-K. Tang, I. J. Hewitt, R. Clrac, W. Wernsdorfer, J. van Slageren, C. E. Anson, A. K. Powell, *Polyhedron* **2005**, *24*, 2864 – 2869. Proceedings of the 9th International Conference on Molecule-based Magnets (ICMM 2004).
- [84] R. W. Saalfrank, A. Scheurer, I. Bernt, F. W. Heinemann, A. V. Postnikov, V. Schuenemann, A. X. Trautwein, M. S. Alam, H. Rupp, P. Mueller, *Dalton Transactions* **2006**, 2865–2874. 9th Dalton Discussion Meeting, Manchester, ENGLAND, APR 19-21, 2006.
- [85] G. G. Condorelli, A. Motta, G. Pellegrino, A. Cornia, L. Gorini, L. L. Fragala, C. Sangregorio, L. Sorace, *Chemistry of Materials* **2008**, *20*, 2405–2411.
- [86] A. Barra, D. Gatteschi, R. Sessoli, *Physical Review B* **1997**, *56*, 8192–8198.
- [87] E. Coronado, A. Torment-Aliaga, A. Gaita-Arino, C. Giminez-Saiz, F. Romero, W. Wernsdorfer, *Angewandte Chemie - International Edition* **2004**, *43*, 6152–6156.
- [88] M. Cavallini, J. Gomez-Segura, D. Ruiz-Molina, M. Massi, C. Albonetti, C. Rovira, C. Veciana, F. Biscarini, *Angewandte Chemie - International Edition* **2005**, *117*, 910–914.
- [89] D. Foguet-Albiol, T. O'Brien, W. Wernsdorfer, B. Moulton, M. Zaworotko, K. Abboud, G. Christou, *Abstracts of Papers of the American Chemical Society* **2005**, *230*, U2206–U2207. 230th National Meeting of the American-Chemical-Society, Washington, DC, AUG 28-SEP 01, 2005.
- [90] E. M. Rumberger, S. J. Shah, C. C. Beedle, L. N. Zakharov, A. L. Rheingold, D. N. Hendrickson, *Inorganic Chemistry* **2005**, *44*, 2742–2752.
- [91] Y. Li, W. Wernsdorfer, R. Clerac, I. J. Hewitt, C. E. Anson, A. K. Powell, *Inorganic Chemistry* **2006**, *45*, 2376–2378.
- [92] J. T. Brockman, T. C. Stamatatos, W. Wernsdorfer, K. A. Abboud, G. Christou, *Inorganic Chemistry* **2007**, *46*, 9160–9171.

Bibliography

- [93] C. J. Milios, A. Vinslava, W. Wernsdorfer, S. Moggach, S. Parsons, S. P. Perlepes, G. Christou, E. K. Brechin, *Journal of the American Chemical Society* **2007**, *129*, 2754–2755.
- [94] E. Cremades, J. Cano, E. Ruiz, G. Rajaraman, C. J. Milios, E. K. Brechin, *Inorganic Chemistry* **2009**, *48*, 8012–8019.
- [95] J.-P. Costes, J. M. Clemente-Juan, F. Dahan, J. Milon, *Inorganic Chemistry* **2004**, *43*, 8200–8202.
- [96] J. Ge, Y. Hu, Y. Yin, *Angewandte Chemie - International Edition* **2007**, *46*, 7428–7431.
- [97] O. Waldmann, A. M. Ako, H. U. Güdel, A. K. Powell, *Inorganic Chemistry* **2008**, *47*, 3486–3488.
- [98] K. A. G. Jr., V. K. Pecharsky, A. O. Tsokol, *Reports on Progress in Physics* **2005**, *68*, 1479–1539.
- [99] D. DiVincenzo, *Science* **1995**, *270*, 255–261.
- [100] M. Leuenberger, D. Loss, *Nature* **2001**, *410*, 789–793.
- [101] V. Cerletti, W. Coish, O. Gywat, D. Loss, *Nanotechnology* **2005**, *16*, R27–R49.
- [102] F. H. L. Koppens, C. Buizert, K. J. Tielrooij, I. T. Vink, K. C. Nowack, T. Meunier, L. P. Kouwenhoven, L. M. K. Vandersypen, *Nature* **2006**, *442*, 766–771.
- [103] J. Berezovsky, M. H. Mikkelsen, N. G. Stoltz, L. A. Coldren, D. D. Awschalom, *Science* **2008**, *320*, 349–352.
- [104] J. Lehmann, A. Gaita-Arino, E. Coronado, D. Loss, *Journal of Materials Chemistry* **2009**, *19*, 1672–1677.
- [105] F. Wang, Z. V. Vardeny, *Journal of Materials Chemistry* **2009**, *19*, 1685–1690.
- [106] M. Mas-Torrent, N. Crivillers, V. Mugaini, I. Ratera, C. Rovira, J. Veciana, *Journal of Materials Chemistry* **2009**, *19*, 1691–1695.
- [107] J. Ferrer, V. M. G. Suárez, *Journal of Materials Chemistry* **2009**, *19*, 1696–1717.
- [108] P. C. Stamp, A. Gaita-Arino, *Journal of Materials Chemistry* **2009**, *19*, 1718–1730.
- [109] M. Affronte, *Journal of Materials Chemistry* **2009**, *19*, 1731–1737.
- [110] T. Sugawara, M. M. Matsushita, *Journal of Materials Chemistry* **2009**, *19*, 1738–1753.
- [111] A. Ardavan, S. Blundell, *Journal of Materials Chemistry* **2009**, *19*, 1754–1760.
- [112] L. K. Grover, *Physical Review Letters* **1997**, *79*, 4709.
- [113] G. Burkard, A. Imamoglu, *Physical Review B* **2006**, *74*, 041307.
- [114] L. Bogani, W. Wernsdorfer, *Nature Materials* **2008**, *7*, 179–186.
- [115] C. Schlegel, J. van Slageren, M. Manoli, E. K. Brechin, M. Dressel, *Physical Review Letters* **2008**, *101*, 147203.
- [116] D. P. DiVincenzo, *Physical Review A* **1995**, *51*, 1015–.

- [117] S. Carretta, P. Santini, G. Amoretti, F. Troiani, M. Affronte, *Physical Review B* **2007**, *76*, 024408.
- [118] G. A. Timco, S. Carretta, F. Troiani, F. Tuna, R. J. Pritchard, C. A. Muryn, E. J. L. McInnes, A. Ghirri, A. Candini, P. Santini, G. Amoretti, M. Affronte, R. E. P. Winpenny, *Nature Nanotechnology* **2009**, *4*, 173–178.
- [119] J. Kempe, D. Bacon, D. Lidar, K. Whaley, *Physical Review A* **2001**, *6304*, 042307.
- [120] P. Chaudhuri, I. Karpfenstein, M. Winter, C. Butzlaff, E. Bill, A. X. Trautwein, U. Florke, H. J. Haupt, *Chemical Communications* **1992**, 321–322.
- [121] D. Gatteschi, R. Sessoli, W. Plass, A. Muller, E. Krickemeyer, J. Meyer, D. Solter, P. Adler, *Inorganic Chemistry* **1996**, *35*, 1926–1934.
- [122] J. Padilla, D. Gatteschi, P. Chaudhuri, *Inorganica Chimica Acta* **1997**, *260*, 217–220.
- [123] S. Ferrer, F. Lloret, I. Bertomeu, G. Alzuet, J. Borrás, S. Garcia-Granda, M. Liu-Gonzalez, J. G. Haasnoot, *Inorganic Chemistry* **2002**, *41*, 5821–5830.
- [124] T. Yamase, E. Ishikawa, K. Fukaya, H. Nojiri, T. Taniguchi, T. Atake, *Inorganic Chemistry* **2004**, *43*, 8150–8157.
- [125] O. Cador, D. Gatteschi, R. Sessoli, F. Larsen, J. Overgaard, A. Barra, S. Teat, G. Timco, R. Winpenny, *Angewandte Chemie - International Edition* **2004**, *43*, 5196–5200.
- [126] M. I. Belinsky, *Inorganic Chemistry* **2008**, *47*, 3521–3531.
- [127] M. I. Belinsky, *Inorganic Chemistry* **2008**, *47*, 3532–3539.
- [128] P. W. Shor, *Physical Review A* **1995**, *52*, R2493.
- [129] E. Knill, R. Laflamme, *Physical Review A* **1997**, *55*, 900.
- [130] D. Gottesman, *Physical Review A* **1996**, *54*, 1862.
- [131] A. M. Steane, *Physical Review Letters* **1996**, *77*, 793.
- [132] M. Trif, F. Troiani, D. Stepanenko, D. Loss, *Physical Review Letters* **2008**, *101*, 217201.
- [133] M. Duckheim, D. Loss, *Nature Physics* **2006**, *2*, 195–199.
- [134] M. Trif, V. N. Golovach, D. Loss, *Physical Review B* **2008**, *77*, 045434.
- [135] A. Ardavan, O. Rival, J. J. L. Morton, S. J. Blundell, A. M. Tyryshkin, G. A. Timco, R. E. P. Winpenny, *Physical Review Letters* **2007**, *98*, 057201.
- [136] D. Reilly, J. Taylor, J. Petta, C. Marcus, M. Hanson, A. Gossard, *Science* **2008**, *321*, 817–821.
- [137] L. M. Mirica, T. D. P. Stack, *Inorganic Chemistry* **2005**, *44*, 2131–2133.
- [138] Y.-Z. Zheng, M.-L. Tong, W. Xue, W.-X. Zhang, X.-M. Chen, F. Grandjean, G. J. Long, *Angewandte Chemie - International Edition* **2007**, *46*, 6076–6080.

Bibliography

- [139] C. P. Raptopoulou, V. Tangoulis, V. Psycharis, *Inorganic Chemistry* **2000**, *39*, 4452–4459.
- [140] I. Gautier-Luneau, D. Phanon, C. Duboc, D. Luneau, J. Pierre, *Dalton Transactions* **2005**, 3795–3799.
- [141] H. Y. Wei, Z. C. Hu, Z. D. Chen, *Journal Of Molecular Structure-Theochem* **2005**, *713*, 145–151.
- [142] G. Mezei, R. G. Raptis, J. Telsler, *Inorganic Chemistry* **2006**, *45*, 8841–8843.
- [143] B. Sarkar, M. S. Ray, M. G. B. Drew, A. Figuerola, C. Diaz, A. Ghosh, *Polyhedron* **2006**, *25*, 3084–3094.
- [144] A. Zharkouskaya, A. Buchholz, W. Plass, *European Journal Of Inorganic Chemistry* **2005**, *24*, 4875–4879.
- [145] A. Zharkouskaya, H. Görls, G. Vaughan, W. Plass, *Chemical Communications* **2005**, *8*, 1145–1148.
- [146] S. Decurtins, R. Pellaux, G. Antorrena, F. Palacio, *Coordination Chemistry Reviews* **1999**, *190-192*, 841 – 854.
- [147] B. J. Holliday, C. A. Mirkin, *Angewandte Chemie - International Edition* **2001**, *40*, 2022–2043.
- [148] G. Maruccio, R. Cingolani, R. Rinaldi, *Journal of Materials Chemistry* **2004**, *14*, 542–554.
- [149] B. D. Koivisto, R. G. Hicks, *Coordination Chemistry Reviews* **2005**, *249*, 2612 – 2630. Magnetism - Molecular and Supramolecular Perspectives.
- [150] K. Heinze, M. Beckmann, K. Hempel, *Chemistry - A European Journal* **2008**, *14*, 9468–9480.
- [151] M. Schmittel, K. Mahata, *Angewandte Chemie - International Edition* **2008**, *47*, 5284–5286.
- [152] N. Robertson, L. Cronin, *Coordination Chemistry Reviews* **2002**, *227*, 93 – 127.
- [153] D. L. Melton, D. G. VanDerveer, R. D. Hancock, *Inorganic Chemistry* **2006**, *45*, 9306–9314.
- [154] H. Miyasaka, A. Saitoh, S. Abe, *Coordination Chemistry Reviews* **2007**, *251*, 2622 – 2664. Chemistry of Coordination Space.
- [155] D. P. Arnold, J. Blok, *Coordination Chemistry Reviews* **2004**, *248*, 299 – 319.
- [156] A. E. Ion, E. T. Spielberg, L. Sorace, A. Buchholz, W. Plass, *Solid State Sciences* **2009**, *11*, 766 – 771.
- [157] D. G. Brnzea, L. Sorace, C. Maxim, M. Andruh, A. Caneschi, *Inorganic Chemistry* **2008**, *47*, 6590–6592.
- [158] M. Mikuriya, D. Yoshioka, M. Handa, *Coordination Chemistry Reviews* **2006**, *250*, 2194 – 2211. 20th International Conference on Coordination and Bioinorganic Chemistry.
- [159] B. Sieklucka, R. Podgajny, P. Przychodzen, T. Korzeniak, *Coordination Chemistry Reviews* **2005**, *249*, 2203 – 2221. Coordination Chemistry in Poland.
- [160] S. J. Wezenberg, A. W. Kleij, *Angewandte Chemie - International Edition* **2008**, *47*, 2354–2364.
- [161] J. K. H. Hui, Z. Yu, M. J. MacLachlan, *Angewandte Chemie - International Edition* **2007**, *46*, 7980–7983.

- [162] M. Haga, E. S. Dodsworth, G. Eryavec, P. Seymour, A. B. P. Lever, *Inorganic Chemistry* **1985**, *24*, 1901–1906.
- [163] J. P. Colin, S. Guillerez, J. P. Sauvage, F. Barigelletti, L. D. Cola, L. Flamigni, V. Balzan, *Inorganic Chemistry* **1991**, *30*, 4230–4238.
- [164] E. Baranoff, I. M. Dixon, J. P. Collin, J.-P. Sauvage, B. Ventura, L. Flamigni, *Inorganic Chemistry* **2004**, *43*, 3057–3066.
- [165] B. Rybtchinski, L. E. Sinks, M. R. Wasielewski, *Journal of the American Chemical Society* **2004**, *126*, 12268–12269.
- [166] S. Chakraborty, T. J. Wadas, H. Hester, R. Schmehl, R. Eisenberg, *Inorganic Chemistry* **2005**, *44*, 6865–6878.
- [167] E. Constable, R. Handel, C. Housecroft, A. Morales, B. Ventura, L. Flamigni, F. Barigelletti, *Chemistry - A European Journal* **2005**, *11*, 4024–4034.
- [168] Y. Pellegrin, A. Quaranta, P. Dorlet, M. Charlot, W. Leibl, A. Aukauloo, *Chemistry - A European Journal* **2005**, *11*, 3698–3710.
- [169] F. De Biani, A. Dei, C. Sangregorio, L. Sorace, *Dalton Transactions* **2005**, 3868–3873.
- [170] J. H. Alstrum-Acevedo, M. K. Brennaman, T. J. Meyer, *Inorganic Chemistry* **2005**, *44*, 6802–6827.
- [171] A. Boisdenghien, C. Moucheron, A. Kirsch-De Mesmaeker, *Inorganic Chemistry* **2005**, *44*, 7678–7685.
- [172] C. Lambert, J. Schelter, T. Fiebig, D. Mank, A. Trifonov, *Journal of the American Chemical Society* **2005**, *127*, 10600–10610.
- [173] M.-S. Yuan, Z.-Q. Liu, Q. Fang, *The Journal of Organic Chemistry* **2007**, *72*, 7915–7922.
- [174] P. Leriche, P. Frere, A. Cravino, O. Aleveque, J. Roncali, *The Journal of Organic Chemistry* **2007**, *72*, 8332–8336.
- [175] A. P. Kulkarni, Y. Zhu, A. Babel, P.-T. Wu, S. A. Jenekhe, *Chemistry of Materials* **2008**, *20*, 4212–4223.
- [176] Q. He, C. He, Y. Sun, H. Wu, Y. Li, F. Bai, *Thin Solid Films* **2008**, *516*, 5935 – 5940.
- [177] L. Hagopian, G. Köhler, R. I. Walter, *Journal of Physical Chemistry* **1967**, *71*, 2290–2296.
- [178] J. Higuchi, K. Hayashi, M. Yagi, H. Kondo, *The Journal of Physical Chemistry A* **2002**, *106*, 8609–8618.
- [179] A. Ito, M. Urabe, K. Tanaka, *Angewandte Chemie - International Edition* **2003**, *42*, 921+.
- [180] K. Lancaster, S. A. Odom, S. C. Jones, S. Thayumanavan, S. R. Marder, J.-L. Bre?das, V. Coropceanu, S. Barlow, *Journal of the American Chemical Society* **0**, *0*,
- [181] H. Murata, Y. Yonekuta, H. Nishide, *Organic Letters* **2004**, *6*, 4889–4892.
- [182] K. Peter, M. Thelakkat, *Macromolecules* **2003**, *36*, 1779–1785.

Bibliography

- [183] A. Aranyos, D. W. Old, A. Kiyomori, J. P. Wolfe, J. P. Sadighi, S. L. Buchwald, *Journal of the American Chemical Society* **1999**, *121*, 4369–4378.
- [184] M. G. Banwell, D. W. Lupton, *Organic Biomolecular Chemistry* **2005**, 213–215.
- [185] M. Beller, C. Breindl, T. H. Riermeier, A. Tillack, *Journal of Organic Chemistry* **2001**, *66*, 1403–1412.
- [186] Q. Cai, W. Zhu, H. Zhang, Y. Zhang, D. Ma, *Synthesis* **2005**, *3*, 496–499.
- [187] S. H. Cheng, S. H. Hsiao, T. H. Su, G. S. Liou, *Macromolecules* **2005**, *38*, 307–316.
- [188] A. A. Kelkar, N. M. Patil, R. V. Chaudhari, *Tetrahedron Lett.* **2002**, *43*, 7143–7146.
- [189] P. Laine, F. Bedioui, P. Ochsenbein, V. Marvaud, M. Bonin, E. Amouyal, *Journal of the American Chemical Society* **2002**, *124*, 1364–1377.
- [190] G. Lamanna, C. Faggi, F. Gasparrini, A. Ciogli, C. Villani, P. L. Stephens, F. L. Devlin, S. Menichetti, *Chemistry - A European Journal* **2008**, *14*, 5747–5750.
- [191] M. G. Organ, M. Abdel-Hadi, S. Avola, I. Dubovyk, N. Hadei, E. A. B. Kantchev, C. J. O'Brien, M. Sayah, C. Valente, *Chemistry - A European Journal* **2008**, *14*, 2443–2452.
- [192] A. Ouali, J. Spindler, H. Cristau, M. Taillefer, *Advanced Synthesis & Catalysis* **2006**, *348*, 499–505.
- [193] M. Taillefer, N. Xia, A. Ouali, *Angewandte Chemie - International Edition* **2007**, *46*, 934–936.
- [194] L. Zhu, P. Guo, G. Li, J. Lan, R. Xie, J. You, *The Journal of Organic Chemistry* **2007**, *72*, 8535–8538.
- [195] T. P. Bender, J. F. Graham, J. M. Duff, *Chemistry of Materials* **2001**, *13*, 4105–4111.
- [196] G. Casalbore-Miceli, A. D. Esposti, V. Fattori, G. Marconi, C. Sabatini, *Physical Chemistry Chemical Physics* **2004**, *6*, 3092–3096.
- [197] B. Conerney, P. Jensen, P. Kruger, C. MacGloinn, *Chemical Communications* **2003**, 1274–1275.
- [198] S. Worl, D. Hellwinkel, H. Pritzkow, M. Hofmann, R. Kramer, *Dalton Transactions* **2004**, 2750–2757.
- [199] W. Zhou, S. M. Kuebler, D. Carrig, J. W. Perry, S. R. Marder, *Journal of the American Chemical Society* **2002**, *124*, 1897–1901.
- [200] M. Lor, J. Thielemans, L. Viaene, M. Cotlet, J. Hofkens, T. Weil, C. Hampel, K. Mullen, J. W. Verhoeven, M. Van der Auweraer, F. C. De Schryver, *Journal of the American Chemical Society* **2002**, *124*, 9918–9925.
- [201] A. S. D. Sandanayaka, H. Sasabe, Y. Araki, Y. Furusho, O. Ito, T. Takata, *The Journal of Physical Chemistry A* **2004**, *108*, 5145–5155.
- [202] J. Gažo, I. B. Bersuker, J. Garaj, M. Kabešová, J. Kohout, H. Langfelderová, M. Melník, M. Serátor, F. Valach, *Coordination Chemistry Reviews* **1976**, *19*, 253 – 297.
- [203] M. Kato, Y. Muto, *Coordination Chemistry Reviews* **1988**, *92*, 45 – 83.
- [204] S. K. Hoffmann, J. Goslar, *Journal of Solid State Chemistry* **1982**, *44*, 343 – 353.

- [205] E. I. Solomon, J. W. Hare, D. M. Dooley, J. H. Dawson, P. J. Stephens, H. B. Gray, *Journal of the American Chemical Society* **1980**, *102*, 168–178.
- [206] R. J. Dudley, B. J. Hathaway, P. G. Hodgson, *Journal of the Chemical Society - Dalton Transactions* **1972**, 882–&.
- [207] K. Dyrek, J. Goslar, S. A. Hodorowicz, S. K. Hoffmann, B. J. Oleksyn, A. Weselucha-Birczynska, *Inorganic Chemistry* **1987**, *26*, 1481–1487.
- [208] A. Weselucha-Birczynska, B. Oleksyn, S. Hoffmann, J. Sliwinski, B. Borzecka-Prokop, J. Goslar, W. Hilczer, *Inorganic Chemistry* **2001**, *40*, 4526–4533.
- [209] I. H. Parker, *Journal of Physics Part C - Solid State Physics* **1971**, *4*, 2967–&.
- [210] R. E. Dietz, H. Kamimura, M. D. Sturge, A. Yariv, *Physical Review* **1963**, *132*, 1559–1569.
- [211] B. Bleaney, K. Bowers, *Proceedings of the Royal Society of London, Series A: Mathematical, Physical and Engineering Sciences* **1952**, *214*, 451–465.
- [212] F. Pan, Z.-M. Wang, S. Gao, *Inorganic Chemistry* **2007**, *46*, 10221–10228.
- [213] D. Plaul: *33d-Transition Metal Complexes of C₃ symmetric Ligands: Directed Syntheses of Trinuclear Compounds and Higher Nuclearity Aggregates*, Ph.D. thesis, Friedrich-Schiller-Universität Jena **2009**.
- [214] O. Temme, T. Dickner, S. Laschat, R. Frohlich, S. Kotila, K. Bergander, *European Journal Of Organic Chemistry* **1998**, 651–659.
- [215] P. M. Van Calcar, M. M. Olmstead, A. L. Balch, *Chemical Communications* **1996**, 2597–2598.
- [216] X. Ottenwaelder, J. Cano, Y. Journaux, E. Riviere, C. Brennan, M. Nierlich, R. Ruiz-Garcia, *Angewandte Chemie - International Edition* **2004**, *43*, 850–852.
- [217] M.-C. Dul, X. Ottenwaelder, E. Pardo, R. Lescouëzec, Y. Journaux, L.-M. Chamoreau, R. Ruiz-Garcia, J. Cano, M. Julve, F. Lloret, *Inorganic Chemistry* **2009**, *48*, 5244–5249.
- [218] C. E. Baxter, O. R. Rodig, R. K. Schlatzer, E. Sinn, *Inorganic Chemistry* **1979**, *18*, 1918–1921.
- [219] E. M. Gouge, J. F. Geldard, *Inorganic Chemistry* **1978**, *17*, 270–275.
- [220] L. P. Battaglia, A. Bonamartini Corradi, G. Marcotrigiano, L. Menabue, G. C. Pellacani, *Inorganic Chemistry* **1979**, *18*, 148–152.
- [221] O. R. Rodig, T. Brueckner, B. K. Hulburt, R. K. Schlatzer, T. L. Venable, E. Sinn, *Journal of the Chemical Society - Dalton Transactions* **1981**, 196–199.
- [222] J. Anderson, H. Pearson, D. Rawson, *Journal of the American Chemical Society* **1985**, *107*, 1446–1447.
- [223] J. G. Jewett, J. J. Breeyear, J. H. Brown, C. H. Bushweller, *Journal of the American Chemical Society* **2000**, *122*, 308–323.
- [224] P. A. Beckmann, C. Paty, E. Allocco, M. Herd, C. Kuranz, A. L. Rheingold, *The Journal of Chemical Physics* **2004**, *120*, 5309–5314.

Bibliography

- [225] A. H. Brunetti, *Journal of Molecular Structure* **2004**, 690, 83 – 88.
- [226] S. Hinchley, H. Robertson, K. Borisenko, A. Turner, B. Johnston, D. Rankin, M. Ahmadian, J. Jones, A. Cowley, *Dalton Transactions* **2004**, 2469–2476.
- [227] G. Gill, D. M. Pawar, E. A. Noe, *The Journal of Organic Chemistry* **2005**, 70, 10726–10731.
- [228] S. G. Essiz, R. D. Coalson, *The Journal of Chemical Physics* **2007**, 127, 104109.
- [229] A. Kyrychenko, S. Gawinkowski, N. Urbanska, M. Pietraszkiewicz, J. Waluk, *The Journal of Chemical Physics* **2007**, 127, 134501.
- [230] Y. Zheng, F. Cardinali, N. Armaroli, G. Accorsi, *European Journal Of Inorganic Chemistry* **2008**, 12, 2075–2080.
- [231] M.-J. Li, Z. Chen, V. W.-W. Yam, Y. Zu, *ACS Nano* **2008**, 2, 905–912.
- [232] Y. Zhang, S. Pan, X. Teng, Y. Luo, G. Li, *The Journal of Physical Chemistry C* **2008**, 112, 9623–9626.
- [233] R.-S. Zhou, L. Ye, H. Ding, J.-F. Song, X.-Y. Xu, J.-Q. Xu, *Journal of Solid State Chemistry* **2008**, 181, 567 – 575.
- [234] L.-Q. Yu, R.-D. Huang, Y.-Q. Xu, T.-F. Liu, W. Chu, C.-W. Hu, *Inorganica Chimica Acta* **2008**, 361, 2115 – 2122.
- [235] C. A. Black, J. S. Costa, W. T. Fu, C. Massera, O. Roubeau, S. J. Teat, G. Aromí, P. Gamez, J. Reedijk, *Inorganic Chemistry* **2009**, 48, 1062–1068.
- [236] A.-C. Ribou, T. Wada, H. Sasabe, *Inorganica Chimica Acta* **1999**, 288, 134 – 141.
- [237] O. Paliulis, J. Ostrauskaite, V. Gaidelis, V. Jankauskas, P. Strohriegl, *Macromolecular Chemistry and Physics* **2003**, 204, 1706–1712.
- [238] J. Morin, M. Leclerc, D. Ades, A. Siove, *Macromolecular Rapid Communications* **2005**, 26, 761–778.
- [239] K. Albrecht, K. Yamamoto, *Journal of the American Chemical Society* **2009**, 131, 2244–2251.
- [240] W. Rettig, M. Zander, *Chemical Physics Letters* **1982**, 87, 229–234.
- [241] F. Evers, J. Giraud-Girard, S. Grimme, J. Manz, C. Monte, M. Oppel, W. Rettig, P. Saalfrank, P. Zimmermann, *The Journal of Physical Chemistry A* **2001**, 105, 2911–2924.
- [242] S. Kapelle, W. Rettig, R. Lapouyade, *Chemical Physics Letters* **2001**, 348, 416 – 424.
- [243] T. Xu, R. Lu, X. Liu, P. Chen, X. Qiu, Y. Zhao, *The Journal of Organic Chemistry* **2008**, 73, 1809–1817.
- [244] A. Samanta, S. Saha, R. W. Fessenden, *The Journal of Physical Chemistry A* **2001**, 105, 5438–5441.
- [245] B. J. Kennedy, G. Brain, E. Horn, K. S. Murray, M. R. Snow, *Inorganic Chemistry* **1985**, 24, 1647–1653.
- [246] T. Storr, P. Verma, R. C. Pratt, E. C. Wasinger, Y. Shimazaki, T. D. P. Stack, *Journal of the American Chemical Society* **2008**, 130, 15448–15459.

- [247] M. Wang, H. Zhu, D. Huang, K. Jin, C. Chen, L. Sun, *Journal of Organometallic Chemistry* **2004**, 689, 1212 – 1217.
- [248] C. Baleizao, H. Garcia, *Chemical Reviews* **2006**, 106, 3987–4043.
- [249] M. Bermejo, A. Castineiras, J. GarciaMonteagudo, M. Rey, A. Sousa, M. Watkinson, C. McAuliffe, R. Pritchard, R. Beddoes, *Dalton Transactions* **1996**, 2935–2944.
- [250] C. Borriello, R. D. Litto, A. Panunzi, F. Ruffo, *Tetrahedron: Asymmetry* **2004**, 15, 681 – 686.
- [251] S. M. Bruno, S. S. Balula, A. A. Valente, F. A. A. Paz, M. Pillinger, C. Sousa, J. Klinowski, C. Freire, P. Ribeiro-Claro, I. S. Goncalves, *Journal of Molecular Catalysis A: Chemical* **2007**, 270, 185 – 194.
- [252] T. Chattopadhyay, S. Islam, M. Nethaji, A. Majee, D. Das, *Journal of Molecular Catalysis A: Chemical* **2007**, 267, 255 – 264.
- [253] A. Chellamani, S. Harikengaram, *Journal of Molecular Catalysis A: Chemical* **2006**, 247, 260 – 267.
- [254] E. F. DiMauro, M. C. Kozlowski, *Organometallics* **2002**, 21, 1454–1461.
- [255] T. Katsuki, *Coordination Chemistry Reviews* **1995**, 140, 189 – 214.
- [256] G. Kim, J. Shin, *Catalysis Letters* **1999**, 63, 83–90.
- [257] M.-H. Lin, T. V. RajanBabu, *Organic Letters* **2002**, 4, 1607–1610.
- [258] T. Luts, R. Frank, W. Suprun, S. Fritzsche, E. Hey-Hawkins, H. Papp, *Journal of Molecular Catalysis A: Chemical* **2007**, 273, 250 – 258.
- [259] M. Maneiro, M. Bermejo, M. Fondo, A. Gonzalez, M. Rey, J. Sanmartin, *Transition Metal Chemistry* **2001**, 26, 120–126.
- [260] M. Maneiro, M. R. Bermejo, A. Sousa, M. Fondo, A. M. Gonzalez, A. Sousa-Pedrares, C. A. McAuliffe, *Polyhedron* **2000**, 19, 47 – 54.
- [261] K. Matsumoto, B. Saito, T. Katsuki, *Chemical Communications* **2007**, 3619–3627.
- [262] A. Panja, N. Shaikh, M. Ali, P. Vojtsek, P. Banerjee, *Polyhedron* **2003**, 22, 1191 – 1198.
- [263] J. Park, K. Lang, K. A. Abboud, S. Hong, *Journal of the American Chemical Society* **2008**, 130, 16484–16485.
- [264] P. Pietikäinen, A. Haikarainen, *Journal of Molecular Catalysis A: Chemical* **2002**, 180, 59 – 65.
- [265] P. Plitt, H. Pritzkow, T. Oeser, R. Kraemer, *Journal of Inorganic Biochemistry* **2005**, 99, 1230 – 1237.
- [266] Y.-M. Shen, W.-L. Duan, M. Shi, *The Journal of Organic Chemistry* **2003**, 68, 1559–1562.
- [267] T. Storr, M. Merkel, G. X. Song-Zhao, L. E. Scott, D. E. Green, M. L. Bowen, K. H. Thompson, B. O. Patrick, H. J. Schugar, C. Orvig, *Journal of the American Chemical Society* **2007**, 129, 7453–7463.
- [268] W. Sun, X. Wu, C. Xia, *Helvetica Chimica Acta* **2007**, 90, 623–626.

Bibliography

- [269] S. Wu, S. Lu, *Journal of Molecular Catalysis A: Chemical* **2003**, *197*, 51 – 59.
- [270] J. Y. Yang, D. G. Nocera, *Journal of the American Chemical Society* **2007**, *129*, 8192–8198.
- [271] S. M. Malinak, D. T. Rosa, D. Coucouvanis, *Inorganic Chemistry* **1998**, *37*, 1175–1190.
- [272] M. Kondo, K. Nabari, T. Horiba, Y. Irie, M. K. Kabir, R. P. Sarker, E. Shimizu, Y. Shimizu, Y. Fuwa, *Inorganic Chemistry Communications* **2003**, *6*, 154 – 156.
- [273] Y. Abe, H. Akao, Y. Yoshida, H. Takashima, T. Tanase, H. Mukai, K. Ohta, *Inorganica Chimica Acta* **2006**, *359*, 3147 – 3155.
- [274] E. Libra, M. Scott, *Chemical Communications* **2006**, 1485–1487.
- [275] C. Meermann, P. Sirsch, K. Tornroos, R. Anwander, *Dalton Transactions* **2006**, 1041–1050.
- [276] P. Mukherjee, C. Biswas, M. G. Drew, A. Ghosh, *Polyhedron* **2007**, *26*, 3121 – 3128.
- [277] C.-Y. Wong, W.-L. Man, C. Wang, H.-L. Kwong, W.-Y. Wong, T.-C. Lau, *Organometallics* **2008**, *27*, 324–326.
- [278] B. Clarke, N. Clarke, D. Cunningham, T. Higgins, P. McArdle, M. N. Cholchin, M. O’Gara, *Journal of Organometallic Chemistry* **1998**, *559*, 55 – 64.
- [279] X. Yang, R. Jones, V. Lynch, M. Oye, A. Holmes, *Dalton Transactions* **2005**, 849–851.
- [280] X. Yang, R. Jones, W. Wong, V. Lynch, M. Oye, A. Holmes, *Chemical Communications* **2006**, 1836–1838.
- [281] J.-P. Costes, F. Dahan, A. Dupuis, J.-P. Laurent, *Inorganic Chemistry* **1996**, *35*, 2400–2402.
- [282] J.-P. Costes, F. Dahan, A. Dupuis, J.-P. Laurent, *Inorganic Chemistry* **1997**, *36*, 3429–3433.
- [283] J.-P. Costes, F. Dahan, A. Dupuis, J.-P. Laurent, *Inorganic Chemistry* **1997**, *36*, 4284–4286.
- [284] J. Costes, F. Dahan, A. Dupuis, J. Laurent, *new Journal of Chemistry* **1998**, *22*, 1525–1529.
- [285] J.-P. Costes, F. Dahan, A. Dupuis, *Inorganic Chemistry* **2000**, *39*, 165–168.
- [286] J.-P. Costes, G. Novitchi, S. Shova, F. Dahan, B. Donnadiou, J.-P. Tuchagues, *Inorganic Chemistry* **2004**, *43*, 7792–7799.
- [287] G. Novitchi, S. Shova, A. Caneschi, J. Costes, M. Gdaniec, N. Stanica, *Dalton Transactions* **2004**, 1194–1200.
- [288] R. Koner, G. Lee, Y. Wang, H. Wei, S. Mohanta. *European Journal Of Inorganic Chemistry* **2005**, 1500–1505,
- [289] J.-P. Costes, M. Auchel, F. Dahan, V. Peyrou, S. Shova, W. Wernsdorfer, *Inorganic Chemistry* **2006**, *45*, 1924–1934.
- [290] K. J. Berry, F. Moya, K. S. Murray, A. M. B. Vandenberg, B. O. West, *Journal of The Chemical Society-Dalton Transactions* **1982**, 109–116.

- [291] M. Botsivali, D. F. Evans, P. H. Missen, M. W. Upton, *Journal of the Chemical Society - Dalton Transactions* **1985**, 1147–1149.
- [292] D. F. Evans, P. H. Missen, *Journal of The Chemical Society-Dalton Transactions* **1985**, 1451–1454.
- [293] B. J. Siwick, H. J. Bakker, *Journal of the American Chemical Society* **2007**, *129*, 13412–13420.
- [294] E. Profft, E. Geisler, *Journal für Praktische Chemie* **1959**, *9*, 136–143.
- [295] W.-W. Sun, A.-L. Cheng, Q.-X. Jia, E.-Q. Gao, *Inorganic Chemistry* **2007**, *46*, 5471–5473.
- [296] D. Salazar-Mendoza, S. A. Baudron, M. W. Hosseini, *Inorganic Chemistry* **2008**, *47*, 766–768.
- [297] T. Z. Forbes, S. C. Sevov, *Inorganic Chemistry* **0**, 0,
- [298] M. Li, J. Huang, X. Zhou, H. Fang, L. Ding, *Acta Crystallographica Section C - Crystal Structure Communication* **2008**, *64*, M250–M253.
- [299] E. T. Papish, M. T. Taylor, F. E. Jernigan, M. J. Rodig, R. R. Shawhan, G. P. A. Yap, F. A. Jove, *Inorganic Chemistry* **2006**, *45*, 2242–2250.
- [300] B. Sreenivasulu, M. Vetrichelvan, F. Zhao, S. Gao, J. Vittal, *European Journal Of Inorganic Chemistry* **2005**, 4635–4645.
- [301] Y. Yu, Y. Wei, R. Broer, R. Sa, K. Wu, *Journal of Solid State Chemistry* **2008**, *181*, 539 – 551.
- [302] F. Meier, J. Levy, D. Loss, *Physical Review B* **2003**, *68*, 134417.
- [303] M. S. Ray, S. Chattopadhyay, M. G. B. Drew, A. Figuerola, J. Ribas, C. Diaz, A. Ghosh, *European Journal Of Inorganic Chemistry* **2005**, 4562–4571.
- [304] M. I. Belinsky, *Inorganic Chemistry* **2006**, *45*, 9096–9106.
- [305] S. Khanra, B. Biswas, C. Golze, B. Buechner, V. Kataev, T. Weyhermueller, P. Chaudhuri, *Dalton Transactions* **2007**, 481–487.
- [306] M. J. Prushan, N. K. Privette, M. Zeller, A. D. Hunter, S. Lofland, S. D. Preite, *Inorganic Chemistry Communications* **2007**, *10*, 631–635.
- [307] A. Tarantul, B. Tsukerblat, A. Müller, *Inorganic Chemistry* **2007**, *46*, 161–169.
- [308] A. Zharkouskaya: *Mehrkernige Übergangsmetallkomplexe als Basis für neue Klassen magnetischer Materialien*, Ph.D. thesis, Friedrich-Schiller-Universität Jena **2006**.
- [309] A. E. Ion: *Magneto-structural characterization of polynuclear complexes with supramolecular architectures*, Ph.D. thesis, Friedrich-Schiller-Universität Jena **2006**.
- [310] H. Zhang, Q. Cai, D. Ma, *Journal of Organic Chemistry* **2005**, *70*, 5164–5173.
- [311] J. P. Chen, A. Natansohn, *Macromolecules* **1999**, *32*, 3171–3177.
- [312] A. R. Paital, A.-Q. Wu, Guo, G. Aromi, J. Ribas-Arino, D. Ray, *Inorganic Chemistry* **2007**, *46*, 2947–2949.

Bibliography

- [313] J. Ambrose, L. Carpenter, R. Nelson, *Journal of the Electrochemical Society* **1975**, *122*, 876–894.
- [314] J. Ambrose, R. Nelson, *Journal of the Electrochemical Society* **1968**, *115*, 1159–1164.
- [315] U. Lachish, P. P. Infelta, M. Grätzel, *Chemical Physics Letters* **1979**, *62*, 317 – 319.
- [316] D. T. Rosa, R. A. Reynolds, S. M. Malinak, D. Coucouvanis, *Inorganic Syntheses* **2002**, *33*, 112–119.
- [317] O. Kahn, *Angewandte Chemie - International Edition* **1985**, *24*, 834–850.
- [318] T. Glaser, M. Gerenkamp, R. Frohlich, *Angewandte Chemie - International Edition* **2002**, *41*, 3823–3825.
- [319] J. Pang, Y. Tao, S. Freiberg, X. P. Yang, M. D'Iorio, S. N. Wang, *Journal of Materials Chemistry* **2002**, *12*, 206–212.
- [320] T. Glaser, H. Heidemeier, T. Lügger, *Dalton Trans.* **2003**, 2381–2383.
- [321] T. Glaser, M. Heidemeier, S. Grimme, E. Bill, *Inorganic Chemistry* **2004**, *43*, 5192–5194.
- [322] E. Kroke, M. Schwarz, *Coordination Chemistry Reviews* **2004**, *248*, 493 – 532. 14th Main Group Chemistry.
- [323] J. Leveque, C. Moucheron, A. Kirsch-De Mesmaeker, F. Loiseau, S. Serroni, F. Puntoriero, S. Campagna, H. Nierengarten, A. Van Dorselaerc, *Chemical Communications* **2004**, 878–879.
- [324] T. Glaser, M. Heidemeier, R. Frohlich, P. Hildebrandt, E. Bothe, E. Bill, *Inorganic Chemistry* **2005**, *44*, 5467–5482.
- [325] P. E. Hansen, S. Bolvig, K. Wozniak, *Journal of Molecular Structure* **2005**, *749*, 155 – 168.
- [326] T. Glaser, M. Heidemeier, T. Weyhermueller, R.-D. Hoffmann, H. Rupp, P. Mueller, *Angewandte Chemie - International Edition* **2006**, *45*, 6033–6037.
- [327] M. Quesada, P. de Hoog, P. Gamez, O. Roubeau, G. Aromi, B. Donnadieu, C. Massera, M. Lutz, A. L. Spek, J. Reedijk, *European Journal Of Inorganic Chemistry* **2006**, 1353–1361.
- [328] T. Glaser, M. Heidemeier, J. B. H. Strautmann, H. Bogge, A. Stammler, E. Krickemeyer, R. Huenerbein, S. Grimme, E. Bothe, E. Bill, *Chemistry - A European Journal* **2007**, *13*, 9191–9206.
- [329] A. E. Ion, E. T. Spielberg, H. Gorls, W. Plass, *Inorganica Chimica Acta* **2007**, *360*, 3925–3931.
- [330] H. Theil, C.-G. F. von Richthofen, A. Stammler, H. Bögge, T. Glaser, *Inorganica Chimica Acta* **2008**, *361*, 916 – 924. Protagonists in Chemistry: Professor Edward I Solomon.
- [331] T. Glaser, M. Heidemeier, T. Lügger, *Dalton Transactions* **2003**, 2381–2383.
- [332] E. T. Spielberg: *Magnetische Eigenschaften mehrkerniger Übergangsmetallkomplexe*, Master's thesis, Friedrich-Schiller-Universität Jena **2005**.
- [333] A. Bencini, C. Benelli, A. Caneschi, R. L. Carlin, A. Dei, D. Gatteschi, *Journal of the American Chemical Society* **1985**, *107*, 8128–8136.
- [334] C. Benelli, A. Caneschi, D. Gatteschi, O. Guillou, L. Pardi, *Inorganic Chemistry* **1990**, *29*, 1750–1755.

- [335] S. Kitagawa, S. Masaoka, *Coordination Chemistry Reviews* **2003**, 246, 73 – 88. Structure, Properties and Applications of Inorganic Polymers.
- [336] J.-M. Herrera, S. J. A. Pope, A. J. H. M. Meijer, T. L. Easun, H. Adams, W. Z. Alsindi, X.-Z. Sun, M. W. George, S. Faulkner, M. D. Ward, *Journal of the American Chemical Society* **2007**, 129, 11491–11504.
- [337] E. T. Spielberg, D. Plaul, L. Sorace, G. Spina, W. Plass, Directed Synthesis of Polynuclear Heterometallic Transition Metal Complexes and their Magnetic Properties, *in preparation*.
- [338] J. Peisach, W. E. Blumberg, *Archives of Biochemistry and Biophysics* **1974**, 165, 691–708.
- [339] M. Andruh, I. Ramade, E. Codjovi, O. Guillou, O. Kahn, J. C. Trombe, *Journal of the American Chemical Society* **1993**, 115, 1822–1829.
- [340] C. Benelli, D. Gatteschi, *Chemical Reviews* **2002**, 102, 2369–2388.
- [341] C. Kollmar, O. Kahn, *Accounts of Chemical Research* **1993**, 26, 259–265.
- [342] M. L. Cofield, P. S. Bryan, *Inorganica Chimica Acta* **1986**, 112, 1 – 4.
- [343] D. Goldberg, J. Telsler, J. Krzystek, A. Montalban, L. Brunel, A. Barrett, B. Hoffman, *Journal of the American Chemical Society* **1997**, 119, 8722–8723.
- [344] L. Sorace, C. Sangregorio, A. Figuerola, C. Benelli, D. Gatteschi, *Chemistry - A European Journal* **2009**, 15, 1377–1388.
- [345] P. Comba, *Inorganic Chemistry* **1994**, 33, 4577–4583.
- [346] L. Duellund, H. Toftlund, *Spectrochimica Acta Part A: Molecular and Biomolecular Spectroscopy* **2000**, 56, 331 – 340.
- [347] T. Ikeue, Y. Ohgo, T. Saitoh, M. Nakamura, H. Fujii, M. Yokoyama, *Journal of the American Chemical Society* **2000**, 122, 4068–4076.
- [348] D. Lefevre-Groboillot, S. Dijols, J.-L. Boucher, J.-P. Mahy, R. Ricoux, A. Desbois, J.-L. Zimmermann, D. Mansuy, *Biochemistry* **2001**, 40, 9909–9917.
- [349] G. Simonneaux, M. Kobeissi, L. Toupet, *Journal of the Chemical Society - Dalton Transactions* **2002**, 4011–4016.
- [350] M. Kobeissi, G. Simonneaux, *Inorganica Chimica Acta* **2003**, 343, 18 – 26.
- [351] T. Teschner, L. Yatsunyk, V. Schunemann, H. Paulsen, H. Winkler, C. Hu, W. R. Scheidt, F. A. Walker, A. X. Trautwein, *Journal of the American Chemical Society* **2006**, 128, 1379–1389.
- [352] M. S. Shongwe, B. A. Al-Rashdi, H. Adams, M. J. Morris, M. Mikuriya, G. R. Hearne, *Inorganic Chemistry* **2007**, 46, 9558–9568.
- [353] J.-J. Girerd, M.-L. Boillot, G. Blain, E. Riviere, *Inorganica Chimica Acta* **2008**, 361, 4012 – 4016. Protagonists in Chemistry: Dante Gatteschi (Part II).
- [354] B. R. McGarvey, *Coordination Chemistry Reviews* **1998**, 170, 75 – 92.

Bibliography

- [355] R. P. Penrose, K. W. H. Stevens, *Proceedings of the Physical Society of London Section A* **1950**, *63*, 29–36.
- [356] K. Park, E.-C. Yang, D. N. Hendrickson, volume 97. AIP **2005** 10M522.
- [357] G. Charron, F. Bellot, F. Cisnetti, G. Pelosi, J.-N. Rebilly, E. Riviere, A.-L. Barra, T. Mallah, C. Policar, *Chemistry - A European Journal* **2007**, *13*, 2774–2782.
- [358] D. Mal, R. Sen, C. Adhikary, A. Bhattacharjee, P. Gütllich, Y. Miyashita, K.-I. Okamoto, S. Koner, *Inorganica Chimica Acta* **2008**, *361*, 183 – 187.
- [359] J.-N. Rebilly, G. Charron, E. Riviere, R. Guillot, A.-L. Barra, M. D. Serrano, J. van Slageren, T. Mallah, *Chemistry - A European Journal* **2008**, *14*, 1169–1177.
- [360] R. Herchel, R. Boča, J. Krzystek, A. Ozarowski, M. Durán, J. van Slageren, *Journal of the American Chemical Society* **2007**, *129*, 10306–10307.
- [361] P. Fleischhauer, S. Gehring, C. Saal, W. Haase, Z. Tomkowicz, C. Zanchini, D. Gatteschi, D. Davidov, A. L. Barra, *Journal of Magnetism and Magnetic Materials* **1996**, *159*, 166 – 174.
- [362] OriginPro (v8.0951 (B951)), OriginLab Corporation, **1991**, www.OriginLab.com.
- [363] J. Borrás-Almenar, J. Clemente-Juan, E. Coronado, B. Tsukerblat, *Journal of Computational Chemistry* **2001**, *22*, 985–991.
- [364] S. Stoll, A. Schweiger, *Journal of Magnetic Resonance* **2006**, *178*, 42 – 55.
- [365] MatLab (v7.2.0.232), The MathWorks, Inc. **1984**, www.mathworks.com.
- [366] XSophe (Version 1.1.4), developed in the Centre for Magnetic Resonance and Department of Mathematics, The University of Queensland, Brisbane, Queensland, Australia 4072 and Bruker Biospin (formerly Bruker Analytik), Rheinstetten, Germany, GmbH, **1993**, <http://www.cmr.uq.edu.au/XSopheTitle.htm>.
- [367] J. P. Perdew, *Physical Review B* **1986**, *33*, 8822–8824.
- [368] A. D. Becke, *Physical Review A* **1988**, *38*, 3098–3100.
- [369] A. Schäfer, H. Horn, R. Ahlrichs, *Journal of Chemical Physics* **1992**, *97*, 2571.
- [370] F. Weigend, R. Ahlrichs, *Physical Chemistry Chemical Physics* **2005**, *7*, 3297.
- [371] F. Weigend, *Physical Chemistry Chemical Physics* **2006**, *8*, 1057.
- [372] R. Ahlrichs, M. Bär, M. Häser, H. Horn, C. Kölmel, *Chemical Physics Letters* **1989**, *162*, 165–169.
- [373] O. Treutler, R. Ahlrichs. *Journal of Chemical Physics* **1995**, *102*, 346.
- [374] M. von Arnim, R. Ahlrichs, *Journal of Computational Chemistry* **1998**, *19*, 1746.
- [375] M. von Arnim, R. Ahlrichs, *Journal of Chemical Physics* **1999**, *111*, 9183.
- [376] R. Ahlrichs, *Physical Chemistry, Chemical Physics* **2004**, *6*, 5119.

- [377] H. Becker, W. Berger, G. Domschke, E. Fanghänel, J. Faust, M. Fischer, F. Gentz, K. Gewalt, R. Gluch, R. Mayer, K. Müller, D. Pavel, H. Schmidt, S. K, K. Schwetlick, E. Seiler, G. Zeppenfeld, *Organikum*, Wiley-V C H Verlag Gmbh **2000**,
- [378] J. Rautengarten: *Untersuchungen ein- und zweikerniger Komplexe des Kupfers, Kobalts und Zinks als Modelle für die Phosphatesterspaltung*, Ph.D. thesis, Universität Bielefeld **1997**.
- [379] S. R. Gupta, K. K. Malik, T. R. Seshadri, *Indian Journal of Chemistry* **1968**, 6, 481–484.
- [380] G. Sheldrick, T. Schneider, *Macromolecular Crystallography, Part B* **1997**, 277, 319–343.
- [381] G. Sheldrick, *Acta Crystallographica Section A* **1990**, 46, 467–473.

Declaration of Originality

I certify that the work presented here is, to the best of my knowledge and belief, original and the result of my own investigations, except as acknowledged, and has not been submitted, either in part or whole, for a degree at this or any other university.

Ich erkläre, dass ich die vorliegende Arbeit selbstständig und nur unter Verwendung der angegebenen Hilfsmittel, persönlichen Mitteilungen und Quellen angefertigt habe und dass ich nicht die gleiche, eine in wesentlichen Teilen ähnliche oder eine andere Abhandlung bei einer anderen Hochschule als Dissertation eingereicht habe.

Jena, October, 13th 2009

Eike T. Spielberg